Optical and electrical characteristics of erbium doped solids for quantum technology applications

By

NAFSIKA THEODOROPOULOU

Thesis

Submitted in partial fulfillment of the requirements for the Degree of

Doctor of Philosophy in the Department of PHYSICS at Salford University

SALFORD, GREATER MANCHESTER

February 2023

ACKNOWLEDGMENTS

This thesis would not be completed without the invaluable help and support of many people over the course of my PhD studies.

Firstly, I would like to thank my supervisor, Dr. Mark Hughes for trusting me through this journey and for encouraging my independence.

Secondly, my office colleagues from the various locations we ended up moving. In particular, thank you to the 'original' G50 crew: Bwebum, Hamid, Heather, Jamie, Laila for the nice distractions and enlightening conversations. Thanks to Vijay and Ahmed for providing a fresh perspective and plenty of breaks during my write-up.

Thank you to my favourite brew providers; Lincoln and Linda, Sarah, Sammy and Nichola; your cuppas really made my mornings better.

Thank you to all members of the Physics Department in Salford, with whom I shared many discussions; special thanks to Richard and Bruce for the endless amount of caffeine and support.

My appreciation extends to Aidan from the University of Salford Maker Space facilities and to Mr. Mike Clegg and his amazing machining skills.

Jason, thank you for encouraging my early research steps in Toledo, and for showing me what constitutes 'proper winter weather'.

Nick, thank you for (not) answering your phone over the past 18 years. I promise I will visit Sweden now I have submitted!

Stuart, thank you for being there all days, good and bad and for introducing me to 'contemporary' jazz.

Finally, thank you to my parents; for your care, love and support. Mum, even after 4 years, you still mix erbium with air-bee and it makes me smile.

Abstract

This thesis explores the potential of Er:Si for quantum technology applications. The unique optical transitions of erbium in the 1.5 μm region make it a suitable candidate for both telecommunication and silicon photonics applications and the properties of the $^4I_{13/2} \rightarrow {}^4I_{15/2}$ optical transition in Er:Si have been extensively studied. However, despite improvements on excitation efficiency and device fabrication there is limited understanding on the origin and role of defects in the interaction with the silicon matrix and its effects in the overall material properties. In this work, we investigate the optical and electrical characteristics of 166-Erbium implanted in intrinsic silicon. The site structure of the Er:Si ions is analysed and the existence of at least two sites, one of cubic and one of orthorhombic symmetry is determined. For a series of different concentrations and annealing recipes variation in photoluminescence (PL) is reported and linked to different ratios of the two erbium symmetry sites in the samples. Further evidence of unreported negative thermal quenching of the PL of erbium in any material is presented. In addition this work reports the first recording of ultra-fast nanosecond relaxation measurements of erbium in a bulk semiconductor with lifetime $\tau < 5$ ns. Formation of a new electronic defect state with activation energy $E_a \approx 0.6$ eV acting as a middle state between erbium's upper excited and ground state is proposed. The optimal temperature for luminescence emission and maximum lifetime is found to be 850 °C. Seebeck measurements indicate n-type behaviour in the samples with typical coefficient values in the range of - 1.2 mVK^{-1}. Conductivity is found to reach a maximum for annealing temperatures of 750 °C. No correspondence between optical and electrical measurements was made. These findings combined with previous optically modulated magnetic resonance and electron spin resonance studies open new questions on the nature of erbium defect centre formation and suggest a potential optical spin manipulation which could pave the way for high temperature quantum platform and sensing applications. Finally, this study is complemented with proof-of-concept two-pulse photon echo experiments on an Er^{3+}:Y_2SiO_5 crystal. Low magnetic field wavelength dependent photon-echo was performed following Zeeman-splitting observation using the photon-echo sequence. Optical coherence of two energy transitions of site 1 yielded $T_2 = (2.53 \pm 0.3)$ μs and $T_2 = (1.14 \pm 0.21)$ μs for two sites at B = 0.1 T.

LIST OF PUBLICATIONS

[1] M. A. Hughes, H. Li, N. Theodoropoulou, and J. D. Carey, "Optically modulated magnetic resonance of erbium implanted silicon," *Scientific reports*, vol. 9, no. 1, pp. 1–10, 2019. DOI: https://doi.org/10.1038/s41598-019-55246-z.

[2] M. A. Hughes, N. A. Panjwani, M. Urdampilleta, N. Theodoropoulou, I. Wisby, K. P. Homewood, B. Murdin, T. Lindström, and J. D. Carey, "Erbium implanted silicon for solid-state quantum technologies," *arXiv:2006.00225(preprint)*, 2020. DOI: https://doi.org/10.48550/arXiv.2006.00225.

[3] M. A. Hughes, N. A. Panjwani, M. Urdampilleta, N. Theodoropoulou, I. Wisby, K. P. Homewood, B. Murdin, T. Lindström, and J. D. Carey, "Coupling of erbium-implanted silicon to a superconducting resonator," *Physical Review Applied*, vol. 16, no. 3, 2021. DOI: https://doi.org/10.1103/PhysRevApplied.16.034006.

CONTENTS

LIST OF FIGURES

LIST OF TABLES

1.INTRODUCTION

This thesis focuses on the optical characterisation of erbium in silicon, with the aim to examine whether its properties are suitable for quantum technology applications. Erbium is unique amongst the rare earths in that its optical transitions fall in the 1550 nm region. This is significant since it lies within the transparency window for silicon and silica fibres, making erbium an ideal candidate for linking information in the future quantum internet. This chapter briefly addresses the motivation of silicon based quantum computation, and how erbium can play a role in this development.

1.1 Research motivation

Despite microelectronics being an established technology, the constantly increasing demand for higher data rates is driving silicon microelectronics to its fundamental limits asserting the need for new technologies capable of better performance. Such technologies include silicon photonics, an area that has received a lot of interest in recent years under the premise of photons achieving much higher data transfer rates between logic devices when compared to electrons [1], [2]. One of the main issues impeding the development of the next generation of silicon processors involves propagation delays and bandwidth limitations in on-chip electrical interconnects resulting from strong capacitance effects taking place as integrated devices scale down [3]. Photonic devices lack these effects making them suitable candidates for high-bandwidth, high-density communications. As a result, numerous silicon-photonics based systems have been proposed with the majority being demonstrated on the mature complementary-metal-oxide-semiconductor (CMOS) fabrication technology compatible silicon-on-insulator (SOI) platform [4], [5]. Nevertheless, an efficient optical source is yet to be created although a lot of promising results have recently emerged [6]–[9].

Its dominance in microelectronics notwithstanding, silicon (Si) has so far proved to be a poor material choice for optical sources for numerous reasons. This is because existing telecommunication systems operate predominantly between 1500-1600 nm since this is the region in which the combined losses in silica fibres are at a minimum. Silicon however is an indirect band gap material with strong non-radiative recombination pathways and band edge luminescence at 1.1 μm, making it incompatible with fibre optic communication systems. Existing optoelectronic sources for use in the near infrared utilise mainly tuneable direct band gap group III-V semiconductors; however these have limited CMOS compatibility and remain costly. In order for silicon photonics to be a lucrative candidate for integration with already existing long-haul communication systems strong emission

in the 1.55 μm spectral region is required.

A promising technique involves doping silicon with erbium (Er) as the trivalent erbium ion has a communications wavelength compatible optical transition at 1535 nm. This concept has already materialised in optical fibre systems, where population inversion of the erbium ion in order to produce optical amplification is applied in erbium-doped fibre amplifiers (EDFAs). Nonetheless, introducing optically active erbium in silicon without degrading erbium's electronic properties remains a technological challenge that needs to be overcome for a CMOS-compatible optical source to be produced. Silicon's luminescence limitations are however of little relevance in quantum technological applications, where Si is a suitable quantum platform candidate owing to advanced manufacturing capabilities of extremely pure silicon crystals that can eliminate nuclear spins responsible for quantum noise. Moreover, the advanced industrial know-how makes any quantum computing application developed in silicon scalable. Generally, a set of requirements known as DiVincenzo conditions has been proposed in identifying criteria that need to be met by an experimental setup aiming to construct a quantum computer [10]. These criteria include:

1. The system must be scalable with well-characterised qubits.
2. One must be able to initialise the system to a well-defined state.
3. There should be long decoherence times
4. The set of quantum gates should be 'universal'.
5. A means to read-out individual qubits should exist.

Two further rules were introduced as necessary for quantum communication, requiring [11]:

6. There should be a way to inter-convert stationary and flying qubits.
7. There should be a way of transmitting flying qubits between specified locations.

Silicon's suitability in satisfying a lot of these criteria has already been met through incorporation of phorphorous dopants [12]–[14]. In fact, ^{28}Si isotopically enriched P:Si has demonstrated a 3 hour coherence time for a hyperfine transition of ^{31}P [15]. Nonetheless, the issue of telecom compatibility for this platform remains unresolved. Investigations in optically addressing single erbium ions have been successful in obtaining an electrical readout [16], whilst recently the first single shot optical readout of a spin state of a single Er ion in Y_2SiO_5 was achieved [17]. Despite these advances, one of the obstacles in practical quantum computing architecture -namely the need for the majority of solid-state

quantum technology platforms to be cryogenically cooled to ≈ 0 K in order to achieve sufficiently long optical coherence times (T_2)- persists. Exception to this is the nitrogen vacancy (NV) centre in diamond which can be uniquely optically spin polarised to give an effective spin temperature of ≈ 0 K whilst the surrounding lattice is at room temperature. However, this technology is incompatible with large scale IC integration; furthermore it requires operation in the visible regime thus making it incompatible with DiVincenzo's 7^{th} criterion. A viable alternative would be a telecommunications compatible system analogous to the NV centre where selective excitation of ground and excited states can occur. If this system could be silicon integrated with common incorporation methods, long-range silicon quantum computing architecture could be a step closer to realisation. In this thesis, erbium (and oxygen) co-implanted pure silicon is investigated having in mind the sought after quantum material characteristics.

1.2 Aims and Objectives

This thesis addresses the points mentioned in section 1.1 and aims to investigate the suitability of erbium doped solids, in particular erbium in silicon's potential for future quantum applications. To this end, erbium in silicon samples manufactured under different doping concentrations, as well as annealing conditions will be optically characterised via photoluminescence spectroscopy in order to establish the optimal processing parameters for maximum erbium luminescence emission. Correlation between post-implantation annealing of samples aiming to recrystallise the silicon matrix and luminescence intensity will be made through Raman spectroscopy. Moreover, realisation of a two-level quantum system requires knowledge of the energy structure of the material. This work aims to address that through identification of optically active centres in Si and determination of their site symmetry through crystal field splitting simulations. These findings are accompanied by fluorescence lifetime measurements intending to distinguish the longer lifetime emitting centres and elucidate sample energy transfer dynamics. Finally, coherence properties of the Er ions are a major performance factor in some quantum applications, such as creating optical buses. Demonstration of sufficiently long coherence times have been shown using Er^{3+}:Y_2SiO_5 (erbium in yttrium orthosilicate), but not Er:Si; as such, some techniques applied to Y_2SiO_5 might be applicable to Er:Si. The final experimental photon echo chapter in this work will further discuss this point.

1.3 Thesis outline

The thesis is organised as follows:

Chapter 2 introduces some elements of rare earth spectroscopy relevant to the rest of the thesis. Specifically, derivation of optical and electronic structure in rare earth

ions is presented, alongside a summary of system dynamic interaction that can affect the coherence times of these transitions. These interactions will be of relevance in the context of photon echo measurements. Energy transfer in the Er:Si system is briefly explained.

Chapters 3 to 5 detail the main experimental results of the thesis. In chapter 3, crystal field analysis is applied on a photoluminescence (PL) spectrum for an erbium implanted silicon sample. Chapter 4 examines the effect of implantation doping and thermal annealing conditions on the spectroscopic properties of Er:Si. Furthermore, the temperature dependence of the PL is investigated. Chapter 5 presents population lifetime measurements of Er:Si.

Thermopower and resistivity electrical characterisation are included in chapter 6. Chapter 7 shows proof-of concept photon echo measurements in Er^{3+}:Y_2SiO_5. Finally, chapter 8 provides a summary and future outlook from this work.

2.SPECTROSCOPIC PRINCIPLES OF RARE EARTH IONS

2.1 Physical and chemical properties

As an ion, erbium can be found in both Er^{2+} and Er^{3+} oxidation states. In solids however, lanthanides tend to become highly electro-positive and often assume the 3+ charge configuration; this holds for Er in both Si and Y_2SiO_5 [18], [19]. Ions in the trivalent oxidation state have valence electrons exclusively occupying the $4f$ shell due to their separate low-lying electronic configurations. As a result, trivalent rare earths in crystalline hosts take on the [Xe]$4f^N$ electron configuration, where N is the number of valence electrons varying from 0 to 14. While the $4f$ orbitals are the valence orbitals, the f-electrons are shielded from the coordination environment by the filled $5s$ and $5p$ orbitals, which have greater radial extension [20]. As the optical transitions of rare earths are intra $4f$, this screening leads to very sharp $4f^N \rightarrow 4f^N$ transitions characteristic of RE^{3+} doped crystals. The ligand field pertubation upon the $4f$ orbitals is minimal so the radiative transitions in solid hosts resemble those of the free ion, with some variation due to Stark splitting as will be discussed below.

2.2 Trivalent rare-earth ion energy levels in solids

An important consequence of the ultra-narrow nature of the intra $4f$ radiative transitions is that they can be modelled quite accurately using the quantum theory of atomic spectroscopy [21]–[23]. The observed energy levels of a solid-state rare-earth-ion material can be described by the total Hamiltonian:

$$\hat{H} = \hat{H}_I + \hat{H}_A + \hat{H}_D \tag{2.2.1}$$

Here, $\hat{H}_I$ represents the leading terms intrinsic to the rare-earth center ($4f$ shell), $\hat{H}_A$ relates to the perturbations to the intrinsic structure due to externally applied magnetic (Zeeman term) or electric (Stark term) fields, or applied stress. Finally, $\hat{H}_D$ denotes the frequency shifts due to dynamic interactions (treated as homogenous broadening).

2.2.1 Intrinsic structure of the $4f$ shell

The intrinsic part of the Hamiltonian $\hat{H}_I$ can be expressed as:

$$\hat{H}_I = \hat{H}_{FI} + \hat{H}_{CF} + \hat{H}_{MH} + \hat{H}_Q, \tag{2.2.2}$$

where terms (from left to right) represent energy contributions from the free ion, crystal field, magnetic hyperfine interaction and quadrupole interaction respectively. The last two terms become significant for ions with nuclear structure, such as ^{167}Er. For Er:Si related experiments inclusion of those terms is not necessary due to sole usage of the ^{166}Er isotope.

Development of the $\hat{H}_I$ has been documented extensively elsewhere. Here, we will briefly discuss this standard approach to better understand the origin of the $4f$-shell Hamiltonian used in chapter 3 to discuss the site symmetry of Er ions in silicon. We will be using the SPECTRE software suits to perform automated fits to $\hat{H}_I$ using observed optical transition energies.

Free Ion Hamiltonian

Following eq. (2.2.2), derivation of the Hamiltonian modelling the electronic states of the $4f$ shell then starts with the potential of a free ion H_{FI}. For the standard N-electron (or ion) system, this Hamiltonian is described in Chapter 5 of [24]:

$$\hat{H}_{FI} = \hat{H}_0 + \hat{H}_{so} + \hat{H}_C = \sum_{i=1}^{N} \left[\underbrace{\frac{p_i^2}{2m}}_{\text{kinetic}} - \underbrace{\frac{Ze^2}{r_i}}_{\text{nuclear}} + \underbrace{\xi(r_i) l_i \dot{s}_i}_{\text{spin orbit}} \right] + \sum_{i<j}^{N} \underbrace{\frac{e^2}{r_{i,j}}}_{\text{Coulomb}} \tag{2.2.3}$$

where p, m, e and r are the momentum, mass, charge and position of each electron and Z stands for the atomic number. The parameter $\xi(r)$ is the spin-orbit coupling constant as a function of electron position, while l and s are angular momentum operators for electron orbit and electron spin respectively. The final term $\hat{H}_C$ relates to the repulsive Coulomb interactions between electrons.

Since $\hat{H}_0$ is spherically symmetric, only $\hat{H}_C$ and $\hat{H}_{so}$ can break the degeneracy of the $4f$ energy levels. The inter-electron Coulomb repulsion splits the $4f^N$ configuration into terms separated by approximately 10^4 cm^{-1}. Spin-orbit interaction further splits each term into $2J+1$ degenerate manifolds with splittings of the order 10^3 cm^{-1}. These degenerate multiplets of the free-ion are commonly described using Russel-Saunders formalism:

$$^{2S+1}L_J$$

In this notation, $S = \sum_i^N s_i$ is the total spin angular momentum, $L = \sum_i^N l_i$ is the total orbital angular momentum and $|L - S| \leq J \geq L + S$ is the total angular momentum. The total orbital angular momentum L is traditionally specified using the spectroscopic notation, where $L = 0, 1, 2, 3...$ is denoted by S, P, D, F respectively. There are 41 distinct $|L, S, J\rangle$ multiplets for Er^{3+}, seen in the Dieke diagram in fig. 2.1.

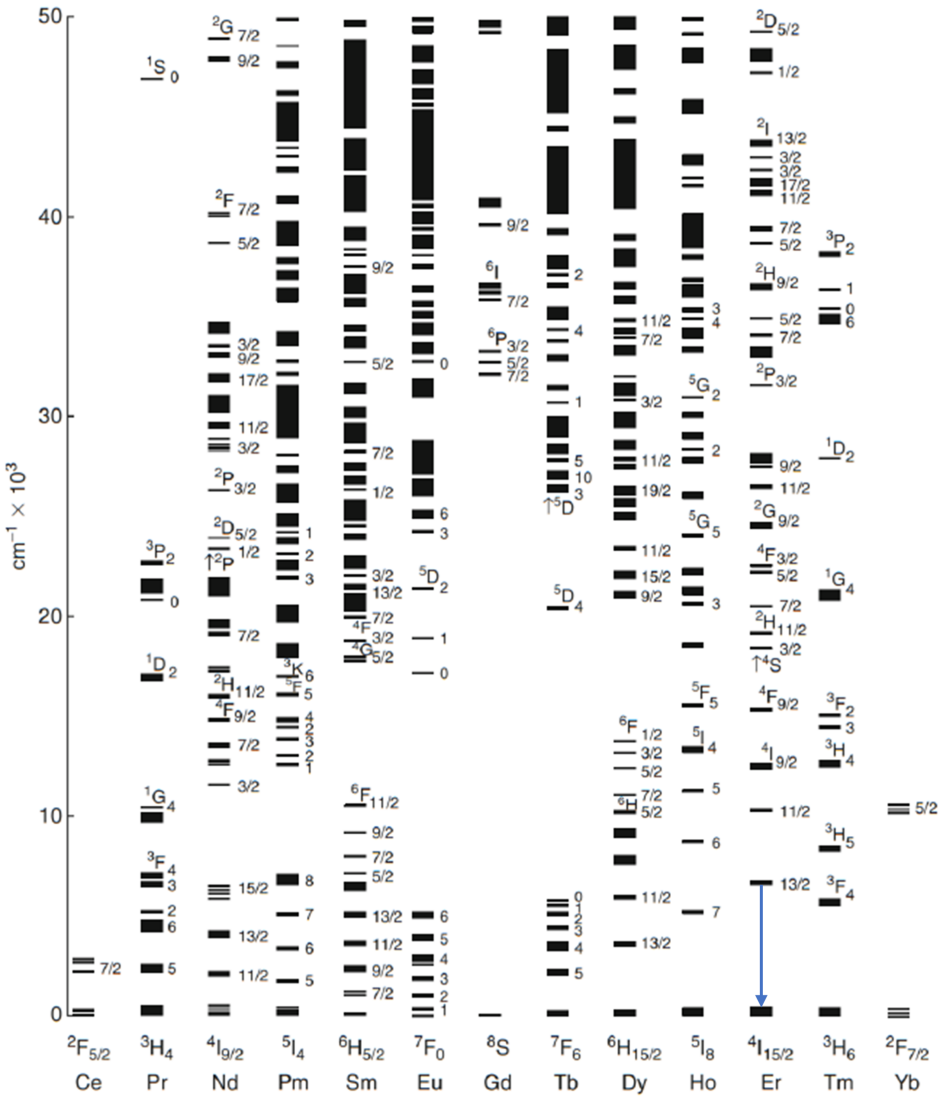

Figure 2.1: Theoretical Dieke diagram showing the $4f$ electronic levels of trivalent rare earths in LaF_3 based on theoretical free ion and crystal field splittings [25]. The erbium transition relevant in this thesis is marked with a blue arrow. Figure modified from [26].

Finally, we know that each electron is described by the wave function ψ which is a solution to the Schrödinger equation. We can see that ignoring relativistic corrections, the Hamiltonian for each electron in eq. (2.2.3) can be represented with four physical parameters with the kinetic, nuclear, and spin orbit terms being functions of the individual electrons i. However, the last term $\hat{H}_C$ depends on the coordinates of two electrons; this does not allow for separation of variables in order to represent the eigenstates as tensor products of single-electron wavefunctions. To account for this, the Central Field Approximation (CFA) was developed, see section 2.2.2 below.

2.2.2 Central Field Approximation

The aim of the Central Field Approximation is to allow the Coulomb and spin-orbit terms to be treated as perturbations [27]. This is achieved through re-expression of the Coulomb potential as a sum of centro-symmetric and asymmetric contributions:

$$H_C = \sum_{i<j}^{N} \frac{e^2}{r_{i,j}} = \underbrace{\left\langle \sum_{i<j}^{N} \frac{e^2}{r_{i,j}} \right\rangle}_{\text{symmetric}} + \underbrace{H'_C}_{\text{asymmetric}} \tag{2.2.4}$$

In CFA, each electron is assumed to move independently in a spherically symmetric potential $U(r_i)/e$ formed through averaging of the potentials of all other electrons. The Hamiltonian $\hat{H}_{CFA}$ is defined as [28]:

$$\hat{H}_{CFA} = \sum_{i=1}^{N} \left[\frac{p_i^2}{2m} + U(r_i) \right] \tag{2.2.5}$$

The Schrödinger equation can be expressed as:

$$\sum_{i=1}^{N} \left[\frac{-\hbar^2}{2m} \nabla^2 + U(r_i) \right] \Psi = E_{CFA} \Psi \tag{2.2.6}$$

Solutions to eq. (2.2.6) can be chosen such that the overall wavefunction and energy of the system is a result of N single-electron systems, yielding:

$$\Psi = \sum_{i=1}^{N} \psi_i(\alpha^i) \tag{2.2.7}$$

$$E_{CFA} = \sum_{i=1}^{N} E_i \tag{2.2.8}$$

Here, a^i stands for the quantum numbers n, l and m_l that describe the state of the electron in the central field. Separation of individual one-electron wavefunctions into their radial $R_n l$ and angular Y_{lm_l} components can now take place using polar coordinates, shown as:

$$\psi_i(\alpha^i) = \frac{1}{r} R_{nl}(r) Y_{lm_l}(\theta, \phi) \tag{2.2.9}$$

Analytical solution of r dependent R_{nl} depends on the central field potential $U_{(r_i)}$. In contrast, the angular wave functions are Laplacian spherical harmonics similar to the one-electron wave function and the well-known Hydrogen system. Extensive derivation of the Hydrogen harmonics is found elsewhere [29]. The resulting standard Laplacian spherical harmonics are [28]:

$$Y_{lm_l}(\theta, \phi) = (-1)^m \left[\frac{(2l+1)(l-|m_l|)!}{4\pi(l+|m_l|)!} \right]^{\frac{1}{2}} P_l^{m_l}(\cos\theta) e^{im_l\phi} \tag{2.2.10}$$

Where $P_l^{m_l} \cos\theta$ are the associated Legendre functions:

$$P_l^{m_l}(\cos\theta) = \frac{(1-\cos^2\theta)^{m_l/2}}{2^l l!} \frac{d^{m_l+l}}{d\cos^{m_l+l}\theta} (\cos^2\theta - 1)^l \tag{2.2.11}$$

The need to introduce a spin function $\delta(m_s, \sigma)$ arises after relativistic corrections to the Schrödinger equation. For a single electron there exist only two possible spin states with spin-projections $m_s = \pm 1/2$. Incorporation of this spin coordinate σ and quantum number m_s to the one electron wave function in eq. (2.2.9) gives:

$$\psi(n, l, m_l, m_s) = \delta(l, n, m_l, m_s) R_{nl}(r) Y_{lm_l}(\theta, \phi) \tag{2.2.12}$$

We can now re-express eq. (2.2.7) as:

$$\Psi = \sum_{i=1}^{N} \psi_i(\alpha^i) \tag{2.2.13}$$

Whilst appearing similar, the α^i term in eq. (2.2.13) stands for the four quantum numbers n,l,m_l and m_s describing the state of each i of the N electrons. Permutations amongst the quantum numbers yield anti-symmetric wave functions in the central field, which are solutions to the Schrödinger equation. These wavefunctions are commonly expressed by the use of Slater determinants [24], yielding:

$$\Psi(\lambda_1, \lambda_2 ..., \lambda_N) = \frac{1}{\sqrt{N!}} \begin{vmatrix} \psi_1\lambda_1 & \psi_2\lambda_1 & \dots & \psi_N\lambda_1 \\ \psi_1\lambda_2 & \psi_2\lambda_2 & \dots & \psi_N\lambda_2 \\ \vdots & \vdots & & \vdots \\ \psi_1\lambda_N & \psi_2\lambda_N & \dots & \psi_N\lambda_N \end{vmatrix} \tag{2.2.14}$$

where i and λ_j correspond to the (n, l, m_l, m_s) components of electron i and the polar co-ordinates of electron j respectively.

Recall that our original goal was to express the eigenstates of the free ion Hamiltonian as products of single-electron wavefunctions. Our eq. (2.2.13) result applies only

to the central spherically symmetric field with hydrogenic potential. We are therefore successful in solving the zero-order problem and it now remains to account for the asymmetric Coulomb perturbation potential and the spin-orbit interaction. These perturbations introduce off-diagonal matrix elements into the free-ion Hamiltonian breaking the degeneracy of the f electron configurations that would otherwise exist in the CFA Hamiltonian.

2.2.3 Coupling basis states

Calculation of the matrix elements H'_C and H_{so} commonly involves the use of a suitable angular momentum basis. The selected basis helps with simplification of the Hamiltonian and eigenstate vectors by reducing the amount of off-diagonal Hamiltonian parameters. To this end, several distinct bases have been developed, referred to as 'coupling' schemes. The two most known schemes are namely LS (or Russell-Saunders) coupling, and jj coupling. Generally, the relative size of the inter-electron repulsion and the spin-orbit interaction determine the choice of coupling. For example, in jj coupling one has to sum over the individual electron orbital and spin angular momenta such that:

$$j_i = l_i + s_i \tag{2.2.15}$$

$$[H_{so}, j_i] = 0 \tag{2.2.16}$$

The resulting operator j is further used to obtain the total angular momentum according to:

$$J = \sum_j j_i \tag{2.2.17}$$

$$[H_{so}, J] = 0 \tag{2.2.18}$$

Whilst H_{so} commutes with the electronic momentum of each electron j and the total momentum of the ion J, H'_C does not. Instead, it commutes with the atomic spin, orbital, and total momenta making the jj coupling scheme suitable for heavier elements where the effect of the Coulomb perturbation potential decreases. The alternate LS coupling scheme involves summing individually the orbital and spin angular momentum operators such that:

$$L = \sum_{i=1}^{N} l_i \quad \text{and} \quad S = \sum_{i=1}^{N} s_i. \tag{2.2.19}$$

The total angular momentum J is then obtained through summation of L and S:

$$J = L + S \tag{2.2.20}$$

For the LS coupling scheme, the following commutation relationships hold true for H'_C and H_{so} [24]:

$$[H'_C, L] = 0, \quad [H'_C, S] = 0, \quad \text{and} \quad [H'_C, J] = 0. \tag{2.2.21}$$

Contrarily:

$$[H_{so}, L] \neq 0 \quad \text{and} \quad [H_{so}, S] \neq 0. \tag{2.2.22}$$

From the above we can see that the LS coupling scheme would be a suitable choice for systems where $H_{so} \ll H'_C$. However, in rare earths $H_{so} \approx H'_C$ so neither L,S or j are 'good' quantum numbers [27]. As a result, the 'intermediate' LS coupling scheme is employed. Here, an effective Hamiltonian in LS coupled basis is constructed. Diagonalisation of the Hamiltonian leads to formation of a new set of eigenstates which are linear combinations of the LS eigenstates, expressed as:

$$\Psi(n, l, J, m_J) = \sum_{\tau, L, S} \alpha_{\tau, L, S} \left| n, l, \tau, L, S, J, m_J \right\rangle \tag{2.2.23}$$

Here, the coupling coefficients $\alpha_{L,S,J}$ are a result of diagonalising the effective Hamiltonian in the LS basis and τ is an extra term referred to as the seniority number. The need to include τ arises from the observation that for a given $4f^N$ configuration, breaking down the $4f$ states might lead to degenerate states with equivalent L and S labels. To uniquely identify these states, τ is used [27].

2.2.4 Free ion matrix

The last step prior to calculating the free-ion energy levels is to express the perturbation H'_C and H_{so} in operator form. We note that the perturbation potential is effectively the difference $H_{FI} - H_{CFA}$ where:

$$H_{FI} - H_{CFA} = \sum_{i=1}^{N} \left[\frac{-Ze^2}{r_i} - U(r_i) \right] + \sum_{i<j}^{N} \frac{e^2}{r_{ij}} + \sum_{i=1}^{N} \xi(r_i)(l_i \dot{s}_i) \tag{2.2.24}$$

Excluding the spin-orbit component, we see that the first summation term shifts the configuration as a whole; since we are interested in intra-configuration structure these terms can be dropped and H'_C can be parametrised using the same components as H_C. Recasting H_C in tensor form leads to [22]:

$$H_C = e^2 \sum_k \frac{r_<^k}{r_>^{k+1}} \left(\sum_{i>j}^{N} C_i^{(k)} \cdot C_j^{(k)} \right) \tag{2.2.25}$$

where for each electrons pair (i, j) the $r >$ (or $r <$) correspond to the lesser or greater element of $\{r_i, r_j\}$ respectively. The $C_i^{(k)}$ terms are spherical tensor operators functions of the ith electron, and $C_q^{(k)}$ are the Wybourne tensor operators proportional to the spherical harmonics $Y_{k,q}(\theta, \phi)$, and are given by:

$$C_q^k = \sqrt{\frac{4\pi}{2k+1}} Y_{k,q}(\theta, \phi) \tag{2.2.26}$$

Since section 2.2.4 has only radial and angular dependence, it is customary to express it as a sum of such functions:

$$\langle n, l, \tau, L, S, J, m_j | H_C | n, l, \tau', L', S', m'_J \rangle = \sum_{k=2,4,6} f_k F^k. \tag{2.2.27}$$

Here, f_k are coefficients representing the angular part of the wave function [23] and F^k are the electrostatic Slater two-electron radial integral defined as:

$$F^K = (4\pi)^2 e^2 \int_0^\infty \int_0^\infty \frac{r_<^k}{r_>^{k+1}} R_{nl}^2(r_i) R_{n'l'}^2(r_j) r_i^2 r_j^2 dr_i dr_j \tag{2.2.28}$$

The constants F^k are experimentally determined by fitting to the free-ion levels. This method has allowed the calculation of Slater parameters for Er^{3+} in different materials [30], [31].

Finally, the f_k angular coefficients are hydrogen-like and can be determined from [28]:

$$f_k = \frac{(2l+1)(l-|m_l|)!}{2(l+|m_l|)!} \frac{(2l'+1)(l'-|m'_l|)!}{2(l'+|m'_l|)!} \int_0^\pi \{P_l^{m_l}(\cos\theta_i)\}^2 P_0^k(\cos\theta_i) \sin\theta_i d\theta_i \times \int_0^\pi \{P_{l'}^{m_{l'}}(\cos\theta_i)\}^2 P_0^k(\cos\theta_i) \sin\theta_i d\theta_i \tag{2.2.29}$$

where $P_l^{m_l}$,$P_{l'}^{m'_l}$ and P_0^k are Legendre polynomials.

Similarly, the matrix elements of H_{so} can be split into radial and angular component shown as:

$$\langle l^n \alpha L S J | \sum_i \xi(r_i) s_i \cdot l_i | l^n \alpha' L' S' J' \rangle = \zeta_{nl} (-1)^{L+S'+J} \sqrt{(2l+1)(l+1)} \delta_{JJ'} \times \begin{Bmatrix} L & S & J \\ S' & L' & 1 \end{Bmatrix} \langle l^n \alpha L S || V^{11} || l^n \alpha' L' S' \rangle \tag{2.2.30}$$

where δ_{ij} are the Kronecker delta symbols and α stands for all additional quantum numbers describing the initial and final states of l^n. Terms between the curly brackets are referred to as the six-j symbol and describe coupling of three momenta L, S and J [32]. Values for the doubly reduced matrix elements containing the spin-orbit operator V^{11} have been tabulated by Nielson and Koster [33].

Whilst there can be additional corrective terms to account for relativistic effects and inter-configuration interactions, this concludes the matrix element formation for H_{FI}.

2.2.5 Crystal field interaction

Incorporation of lanthanide ions in inorganic lattices or compounds leads to each electron i feeling the effect of the crystal field generated by the ligands surrounding the metal ion, in addition to H_C and H_{so}. This effect is analogous to that first described by Stark of an the shifting of the spectral hydrogen lines due to the presence of an electric field [34]. This lifts the $2J+1$ degeneracy generating new levels with M_J quantum numbers. The resulting energy shifts are significantly weaker than the Coulomb interaction and spin-orbit equivalents, allowing the crystal field to be treated as a perturbation to the free-ion Hamiltonian. Despite the smaller splits, H_{CF} is the sole determinant of spin-lattice dynamics, optical transition strengths and spin-state mixing, thus being of critical importance to identifying key properties for quantum information processing in rare-earth systems [31].

The crystal field Hamiltonian can be expressed as a function of the crystal field parameters B_q^k as:

$$H_{CF} = \sum_{i,k,q} B_q^k C_q^k(i) \tag{2.2.31}$$

where C_q^k is as previously defined in eq. (2.2.26) and B_q^k are parameters that are in general determined by fitting the crystal field Hamiltonian eigenvalues to experimental results.

Estimation of the crystal field energy levels can be obtained via diagonalisation of the Hamiltonian:

$$\left\langle \psi_{l^n SLJM_J} \middle| H_{CF} \middle| \psi_{l^n S'L'J'M_{J'}} \right\rangle \tag{2.2.32}$$

Substitution of eq. (2.2.31) into eq. (2.2.32) it can be shown that the matrix elements can be described by [28]:

$$\sum_{k,q} B_q^k \left\langle \psi_{l^n SLJM_J} \middle| \sum_i (C_q^k)_i \middle| \psi_{l^n S'L'J'M_{J'}} \right\rangle = (-1)^{2J-M_J+S+L+k+3} 7(2J+1) \times \begin{pmatrix} 3 & k & 3 \\ 0 & 0 & 0 \end{pmatrix} \begin{pmatrix} J & k & J \\ -M_J & q & M_{J'} \end{pmatrix} \begin{Bmatrix} J & J & k \\ L & L & S \end{Bmatrix} \langle \psi_{l^n SL} || U^k || \psi_{l^n SL} \rangle \quad (2.2.33)$$

Parentheses terms correspond to 3-j symbols while bracketed terms to 6-j symbols. These values as well as doubly reduced matrix elements U^k have been tabulated in [32] and [33] respectively. As a result, only B_q^k needs to be determined to evaluate the energy level splitting due to crystal field and its symmetry.

Crystal field parameters B_q^k and symmetry

The crystal field parameters B_q^k can be considered as describing the strength of the field acting on the rare-earth ion and as such can provide an insight into the nature of distortions that reduce the site symmetry. The integer k takes values between 0-7: even k values are responsible for the crystal field splitting whilst odd values influence the intensity of the induced electronic dipole transitions [35], [36]. The integer q is symmetry as well as k magnitude dependent, with $|q| \leq k$. In the absence of symmetry there are 27 independent crystal-field parameters. Lower symmetry sites require a larger amount of parameters to describe their crystal field interaction. The reader is directed to table 1.7 in [28] for complete list of parameters for various point group symmetries.

The effect of the crystal field heavily relies on whether the ion has an odd (Kramers) or even (non-Kramers) number of electrons. In the case of Kramers' ions J is half-integer and therefore the degeneracy is not completely removed resulting in two-fold degeneracy of each sub-level (Kramers' doublet). The lifting of the degeneracy relates to the symmetry around the metal ion and so does the number of new M_J sublevels.

2.2.6 Zeeman effect

We now briefly examine the third term in our intrinsic Hamiltonian H_I, namely the magnetic and nuclear interactions. As previously mentioned, in the case of Kramer's ions where J is a non-integer, the crystal field does not result in complete lift of the J level degeneracy. However, in the presence of an external magnetic field, this degeneracy can be lifted; this is referred to as the Zeeman effect. The splitting magnitude is proportional to the strength of the applied magnetic field, with the equivalent Hamiltonian H_Z described as:

$$H_Z = g\mu_B B \cdot J \quad (2.2.34)$$

where μ_B is the Bohr Magneton, B the magnitude of the external magnetic field and g is Landé's factor in the LS coupling scheme:

$$g = 1 + \frac{J(J+1) - L(L+1) + S(S+1)}{2J(J+1)} \tag{2.2.35}$$

2.3 Spectral broadening

The linewidth of a transition can be broadened through effects categorised as either homogenous or inhomogenous. For a typical single dipole, the emission line is not infinitely sharp, but has a finite width in frequency of roughly $1/T$, where T refers to the finite natural radiative lifetime of every excited dipole moment. This width is the same for each dipole and is referred to as the "homogenous linewidth", denoted by $\delta_{\omega_H} \sim \frac{1}{T}$. Due to the dipole moment's exponential decay nature, the shape of the spectral line is Lorentzian. In a perfectly ordered crystal, each ion would experience identical crystal fields resulting in degenerate transition energies of the ensemble. However in reality, resonant atoms find themselves in slightly different local environments for reasons such as strain fields, impurities or dislocations. This random or 'inhomogenous' disorder gives rise to different effective resonance frequencies for differently positioned but otherwise identical atoms. Thus the actual emission line can be thought of as a superposition of a large number of homogenously broadened Lorentzian lines of width $1/T$ and each with a distinct centre frequency ω_a [37]. An illustration can be seen in fig. 2.2. In chapter 7 the studied sample was grown as high-quality single crystal, in which the dominant defects were usually zero or one dimensional.

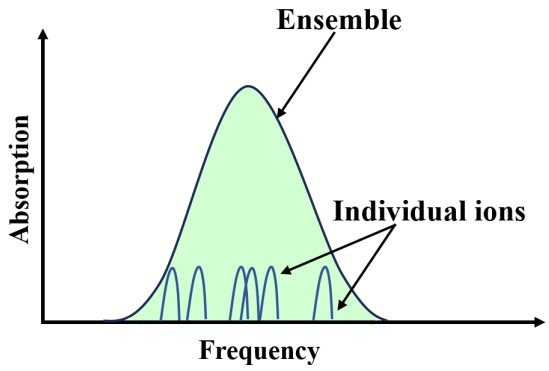

Figure 2.2: Inhomogenously broadened absorption spectrum of a rare-earth ion. Arrows indicate the homogeneous linewidths of the individual ions and the ensemble's inhomogenous broadening.

2.4 Homogenous Broadening and Coherence Lifetime

Dynamical processes have a statistically identical influence on indistinguishable ions and cause homogenous broadening, which in turn leaves the ions with the same dynamically perturbed transition energy. There are several mechanisms cumulatively contributing to the homogenous linewidth in Er^{3+}- doped crystals so that:

$\Gamma_h = \frac{1}{2}\Gamma_{pop} + \Gamma_{Er-host} + \Gamma_{Er-Er} + \Gamma_{phonon}$,

where Γ_{pop} is the population decay from the excited state, $\Gamma_{Er-host}$ refer to contributions from nuclear and electronic spin fluctuations of the host crystal, Γ_{Er-Er} is the contribution from mutual flip-flop transitions between Er^{3+} ions, and Γ_{phonon} represents a variety of phonon contributions [38]. The lower bound on the homogenous linewidth is set by population decay. Decays from the lowest crystal field level of the Er^{3+} $^4I_{13/2}$ multiplet are almost purely radiative with insignificant contributions from spontaneous phonon emission due to the large energy gap to lower levels. For Er^{3+}:Y_2SiO_5, the $\Gamma_{Er-host}$ contribution is minimal since as will be later discussed in chapter 7, the host (Y_2SiO_5) consists of elements with nuclear magnetic moments of zero (^{16}O), very small values (^{89}Y) or low isotopic abundance (^{29}Si and ^{17}O). The phonon contribution, Γ_{phonon} includes both direct phonon driven transitions and inelastic or Raman scattering of phonons [39], [40]. At room temperature homogenous linewidths in rare-earth doped crystals are dominated by phonon contributions however at low temperatures those contributions become insignificant as a result of the low phonon density of states at the resonant energy and the low available phonon energy.

The Γ_{Er-Er} contribution includes the mutual Er-Er resonant "flip-flop" transition that is quite significant and highly dependent on choice of temperature, Er^{3+} concentration, and applied magnetic field direction and strength. Even at liquid helium temperatures, thermal population of the upper Zeeman level is possible for a weakly split Kramers doublet. As a result, ions undergoing spontaneous "flip" transition from the upper to lower Zeeman component can resonantly drive another ion through a lower to upper component transition, a "flop". The resulting fluctuating magnetic field dephases the ion of interest by suddenly shifting its energy levels [41]. At liquid helium temperatures homogenous linewidths as narrow as 10s to 100s of Hz have been observed in rare earth doped crystals [42] [43]. These narrow linewidths cannot be measured directly in the frequency domain because readily available lasers have jitter-limited linewidths of a few hundred kHz; linewidths are derived from measurements of a material's coherence lifetime, T_2 through the relation $T_2 = 1/\pi\Gamma_h$ using photon echo.

2.5 Electronic properties of impurities in semiconductors

2.5.1 Defects in semiconductors

There exist numerous crystallographic defects formed during growth or subsequent processing (including doping) of crystalline semiconductors. These defects play a crucial role in the final attributes of the semiconductor device. Understanding their origin and characteristics is therefore paramount to the realisation of controlled defect incorporation into the semiconductor crystal that leads to favourable properties. An ideal single crystal semiconductor's band diagram consists of a valance and a conduction band, separated by the band gap E_g. Introduction of crystal defects or foreign atoms perturbs the periodicity of the single crystal leading to the formation of discrete energy levels in the band gap. This effect can be intentional (i.e. dopants forming shallow-level impurities) or unintentional (i.e. defects arising from device processing conditions such as radiation damage from ion implantation). Their nature could be structural (i.e. dislocations), crystallographic (i.e. point defects such as vacancies and interstitials) or foreign impurities (i.e. metals). Depending on the location of the introduced energy levels, defects can be categorised into shallow or deep level.

Shallow level defects

Shallow level defects are formed through introduction of a new atom as a dopant replacing the original atom. In silicon, shallow dopants could be atoms from groups III and V of the periodic table, such as boron (B) and phosphorus (P) respectively. These atoms lead to the creation of new energy levels close to the valence band (group III) or close to the conduction band (group V). Shallow defects can be donors or acceptors, are fully ionised at room temperature, and are of great technological importance since they determine the carrier type and conductivity of the semiconductor [44]. Many of shallow defect properties including ionisation energy and state wave functions can be calculated using the hydrogen atom model, where an electron orbits around a charged centre of the impurity's net core (i.e. a positive charge of a donor core) in a long-range Coulomb potential [45].

Deep level defects

Deep level defects consist of states within the forbidden gap of a semiconductor. They behave differently than shallow impurities, and their energy levels can not be calculated using the effective mass approximation. Many deep levels are located closer to the centre of the bandgap than to either of the band edges and are referred to as midgap centres

[46]. They can be formed by point or spatially extended defects such as dislocations. Characteristically, deep levels' ability to capture free electrons and holes has led to the alternate name of traps or deep traps. They are classified according to their charge state (i.e. neutral and positively charged states are named donor-like states). When their excitation is significant, deep level centres can act as effective recombination pathways by forming a bridge between conduction and valance band for nonradiative recombination [47]. Transition metal impurities and lattice defects such as vacancies (i.e. Chromium in GaAs, Fe in InP, Cu in Si) are examples of deep level defects.

2.6 Energy transfer of Er:Si

As discussed in section 2.1, an attractive characteristic of rare-earth ion doped semiconductors is the possibility of predictable atomic-like sharp temperature independent emissions from internal transitions of the incompletely filled $4f$ electron shell. However, the same screening of the $4f$ electron shell from the outer lying $5s$ and $5p$ electrons that leads to these ultra narrow emissions is also responsible for effectively preventing bonding of the $4f$ electrons to the host electrons. In turn, this excludes standard mechanisms of impurity luminescence excitation, with nonradiative energy transfer being the only efficient mechanism in the excitation of the $4f$ shell [48]. In rare earth (RE) doped ionic hosts and molecular systems, the excitation transfer occurs through energy exchange between a RE ion and a radiative recombination centre (i.e. a defect with allowed optical transitions). Optical excitation of the energy donor centre is followed by nonradiative energy transfer to the $4f$ shell of the RE ion. Any energy mismatch is covered by phonon emission.

It is then clear that finding an appropriate bound state near the RE ion is critical in the optimisation of the excitation process since introduction by the rare earth of a level within the band gap of the host material (silicon) influences the energy transfer to and from the $4f$ electron core. Therefore, properties of the RE ion semiconductor matrix system greatly depend on the characteristics of this RE-related level, which is crucial in understanding the energy transfer mechanisms [48].

2.6.1 Erbium incorporation into silicon

Numerous techniques have been employed to introduce optically active erbium into silicon [49]. However, a combination of ionic radii mismatch in conjunction to the sp^3 bonding of silicon result in low solubility of erbium and the need to utilise non-equilibrium methods such as ion implantation. Moreover, ion implantation has the advantage of allowing the erbium concentration depth profile to be tailored through varying the ion energy and fluence. Even so, the high stopping cross-section of Si results in relatively small

Er penetration depth in the material and implantation energies spanning several MeV are required to reach projected ion range in the micron depth [50]. To add to that, ion implantation at high fluxes introduces significant damage to the silicon matrix by amorphising the upper layers of silicon above the implanted region [51]. The majority of the damage can be recovered through high temperature annealing yet at the cost of erbium ions aggregating together and forming optically inactive clusters and silicides [52], [53].

Co-doping with impurities has been proven to change the situation [54]–[56]. Primarily oxygen, through the formation of oxygen solvation shells around erbium ions, decreases their diffusivity thus slowing the segregation process whilst significantly increasing the maximum erbium concentration. Furthermore, the presence of oxygen impurities enhances the erbium luminescence and reduces problematic quenching effects. At the same time, it promotes radiative transitions and forms Er-O complexes that can act as efficient electronic traps [57].

2.6.2 Rare earth introduction of electronic states in Si

Generally, the trivalent character of the incorporated RE ion indicates the formation of isoelectronic traps in group III-V compounds. Whilst an exact formation mechanism for these states is unknown [58], they have been experimentally identified in RE-doped InP crystals where, in the case of the InP:Yb system there is consensus on the substitutional Yb^{3+} ion generating a shallow donor level with ≈30-40 meV ionisation energy [59]–[61]. Upon optical excitation the electrons generated are trapped at this state. This negatively charged trap attracts a hole forming an isoelectronic bound exciton [62], [63]. Energy transfer from this centre to the inner $4f$ shell then occurs via a process similar to the nonradiative Auger type quenching of excitons bound to neutral donors (three particle process) [48], [64] with the excess energy emitted as phonons. The reverse of this step in the excitation process is referred to as energy back transfer [65]. Possibly a similar excitation process occurs for Er:c-Si [66]. However the substitutional Er^{3+} can in theory only introduce an acceptor level. In silicon, the 3+ charge state of the core suggests the presence of a Coulombic potential making the formation of effective mass hydrogenic donor or acceptor states possible; yet no such states have been experimentally identified.

The existence of a donor state is implied from the fact that following erbium doping the silicon crystal usually converts to n-type. Deep level transient spectroscopy studies (DLTS) in oxygen rich Cz-Si:Er have detected a donor level located around 150 meV below the silicon conduction band [67]. Total energy calculations proposed this level could be a result of mixing of the d states of the Er^{3+} ion with the conduction band states of the silicon crystal [58], whilst others associate this donor level with the formation of

erbium oxygen complexes or silicides [67], [68]. Unfortunately the link between donor level formation and Er^{3+} photon emission is indirect since electrical measurements do not discern between optically and electrically active dopants.

2.6.3 Optical excitation of Er:Si

Optical excitation of Er:Si is a multi-step process. As mentioned in section 2.6.2, in RE-doped ionic hosts the excitation transfer likely occurs by energy exchange between a radiative recombination centre acting as an energy donor, and a RE ion acting as an energy acceptor. The first step in this process in a semiconducting host such as silicon involves photo-generation of carrier pairs which in turn form free excitons. These excitons get 'trapped' by defect centres forming a bound exciton state in the vicinity of the Er^{3+} ions. Energy is subsequently nonradiatively transferred via an exchange or multipolar mechanism to the intra $4f$ shell of the Er^{3+} ions, with phonon emission accommodating any energy mismatch (see section 2.6). This mechanism, alongside competing nonradiative relaxation pathways are schematically indicated in fig. 2.3. There have been numerous investigations into this excitation mechanism, both theoretical and experimental. Notably, the role of excitons and the crucial role of Er-related donor states were established with certainty [66], [69]–[72]. Further evidence on the importance of excitons was provided through Er PL investigations following laser illumination both on the implanted as well as the substrate side of the sample. It was found that the efficiency was dependent on the distance between the exciton generating photon absorption region, and the Er^{3+} ions [73], [74].

2.6.4 De-excitation of Er:Si

As seen in section 2.2.5, transitions between different multiplets from the $4f$ electron shell are parity forbidden for a RE ion in vacuum. Incorporation of the RE ion into a host matrix introduces non-zero transition elements yet this crystal field perturbation is very small. In turn, radiative transitions are highly improbable and lifetime of the excited state is long, typically in the millisecond range. Non-radiative excitation processes and other competing Er related trap levels can shorten the lifetime.

For Er:Si luminescence monotonically decreases as temperature increases, a phenomenon referred to as PL thermal quenching. In particular, for temperatures T > 100 K rapid quenching is observed, arising from a reduction in Er luminescence efficiency or excitation efficiency. This is accompanied by a reduction in effective lifetime as well. Previous investigations in c-Si:Er reported two activation energies of ≈15 meV and 150 meV. It has been suggested that the former relates to a bound exciton state ionisation or

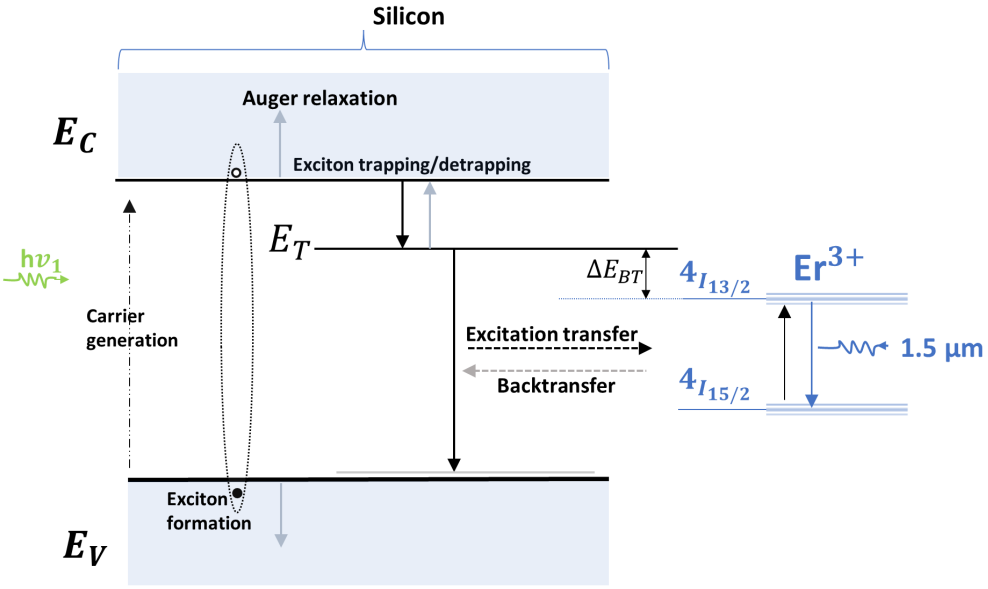

Figure 2.3: Conventional energy-band diagram for the excitation process. E_C, E_V and E_T correspond to conduction band, valence band and trap (donor) level respectively. The energy levels of Er^{3+} ions do not participate in the energy scheme of Si. The generation of excitons is followed by binding from erbium related trap levels and subsequent nonradiative energy transfer to the erbium ions. Any energy mismatch is compensated by phonons (not shown).

dissociation whilst the latter relates to the back-transfer process in a similar manner to the InP:Yb system mentioned in section 2.6.2. A final recombination pathway involves an Auger-type energy transfer where energy of an excited Er^{3+} ions dissipates to free carriers which are promoted to higher band-states.

Back-transfer process

The back-transfer process is deemed to be the primary cause of high temperature quenching of both RE photoluminescence intensity and lifetime. Originally proposed for InP:Yb [65], back-transfer can be thought of as the reverse of the last step of the excitation process where upon nonradiative relaxation of a RE ion the bound-exciton state is recreated. The recombination energy of the electron-hole pair is $E_g - E_T - E_b$, where E_g is the bandgap energy, E_T is the depth of the carrier trap level and E_b the binding energy of the donor centre [75]. Successful excitation of the Er $4f$ shell requires a recombination energy greater than or equal to Δ_{ff} which is the erbium transition energy. This energy difference $E_0 = E_g - E_T - E_b - \Delta_{ff}$ needs to be compensated whilst excitation occurs. During the back-transfer process E_0 is absorbed. Therefore, the back-transfer activation energy (ΔE_{BT}) is equal to the energy mismatch E_0 that needs to be accounted for during

excitation and relates to the location of the previously mentioned RE related donor state within the host's energy gap. This extra energy is compensated by phonons; as a result back-transfer is a thermally activated process requiring the annihilation (simultaneous absorption) of several lattice phonons. For Er:Si in particular, the back-transfer activation energy has been found to be $E_{\mathrm{BT}} \approx 0.15$ eV, correlating to the deep level located 0.15 eV below the bottom of the conduction band (see section 2.6.2). For this value, theoretical modelling predictions postulate the involvement of at least three optical phonons [76].

Auger type-quenching processes

The role of shallow centres is not limited to the excitation, with their availability having a significant influence on the number of nonradiative relaxation pathways. Notably, an impurity Auger nonradiative recombination process exists involving energy transfer to the conduction band electrons [77]. For the Er:Si system, direct evidence of such an energy transfer has been obtained after the investigation of the photoluminescence intensity temperature quenching in samples of different doping backgrounds [71], where the ionisation process of shallow dopants (B and P for p- and n- type respectively) was pinpointed as responsible for the quenching.

In addition, previous research has indicated that the effective lifetime of the excited state of Er:Si is governed by free carriers. In an experiment where there was continuous equilibrium background provision of free carriers, shortening of the lifetime proportional to the square root of power of the background illumination was observed [78]. Seeing as exciton recombination dominated the relaxation, this result was indicative of the role of free carrier concentration in the efficiency of lifetime quenching.

Finally, confirmation on the role of free carriers was further provided by two-colour spectroscopy experiments in the visible-mid IR where optically induced ionisation of shallow traps was shown to result in quenching of the Er luminescence [79].

Exciton dissociation

A decrease in the concentration of localised excitons can lead to a subsequent decrease in the Er excitation efficiency via lowering the fraction of bound excitons that result to Er excitation. This process requires an activation energy and is phonon-assisted, therefore the dissociation rate increases with temperature. As previously mentioned in Er:Si this activation energy is thought to be 15 meV.

2.7 Chapter summary

This chapter introduced several key theoretical concepts required for further understanding the results in this thesis. Section 2.2 presented the relevant to rare earth ions intrinsic $4f$-shell and crystal field parameters. These parameters will be employed to perform crystal field analysis of Er:Si in chapter 3. Section 2.3 and section 2.4 conferred some key principles for inhomogeneously broadened ensembles applicable primarily for Er^{3+}:Y_2SiO_5 in chapter 7. Moreover, section 2.5 listed necessary basic information on defects on semiconductors in order to understand the Er:Si energy structure shown in section 2.6. This included common excitation and de-excitation mechanisms in sections 2.6.3 and 2.6.4 which will be useful for understanding the photoluminescence (PL) spectra presented in chapter 4 and in particular the PL temperature dependence in section 4.4. The de-excitation principles will be further employed in the analysis of lifetime measurements in chapter 5.

3.CRYSTAL FIELD ANALYSIS OF ER:SI

In the context of crystal site symmetry, erbium is not a considered a 'good' dopand in silicon since it does not occupy well-defined substitutional sites. Instead, it forms multiple centres having different local environments and affiliated crystal fields. Thus, whilst individual erbium ion transitions are well defined, incorporated erbium in crystalline (c-) Si shows an inhomogeneously broadened spectrum.

Knowledge of the relationship between annealing recipes and preferential erbium centre formation can impact both photonic and quantum technology applications. In the case of the former, inhomogenous broadening can result in mismatched energies between the emission of a photon from one Er centre and the energy level from another Er centre, hindering absorption and further stifling the realisation of optical gain in c-Si [64]. In terms of quantum platforms, creation of a two-level quantum bus requires the ability to control and interact with the assigned qubit centres [80]. In this chapter, crystal field analysis of Er:Si is performed using the computational simulation software package SPECTRE.

3.1 The existing knowledge base on centre formation

Existing literature has yet to reach uniform agreement on actual symmetry of optically active erbium centres in silicon. It appears that centre formation is subject to the presence of co-dopants and the interaction of these co-dopants with the erbium ions [3]. The earliest centre identification came through PL studies of the 1.5 μm erbium emission in silicon and suggested the existence of a site of tetrahedral (T_d) symmetry, without further postulating on the substitutional or interstitial nature of it [81]. This was followed by a very high resolution PL study that located over 100 emission lines, assigning them to a multitude of different Er-related centres [82]. Specifically, following the earlier model of [81], isolated Er^{3+} was located in tetrahedral interstitial as well as lower symmetry sites. Moreover, sites relating to Er-O complexes were proposed, in addition to a large number of residual radiation defects. Further analysis using Extended X-ray Absorption Fine Structure Spectroscopy (EXAFS) discovered that in CZ-Si:Er the local site of an Er atom is surrounded by six oxygen atoms resembling Er_2O_3 [83]. In contrast, float-zones (FZ) silicon included 12 neighbouring silicon atoms at a mean distance of 3 Å similar to the structure of $ErSi_2$ [83], [84]. These results were backed by electron paramagnetic resonance (EPR) studies and Rutherford back-scattering [85], [86].

The nature of the main centre generated in ion implanted Er:Si is still under debate. Theoretical calculations agree on the prediction of a tetrahedral location of an isolated

Er^{3+} ion in Si; however some [58], [84], [87]–[90] suggest the tetrahedral interstitial (T_i) centre is most favourable, whilst others [19], [89] postulate the tetrahedral substitutional site (T_s) is more stable. Such is contrasted by groups calculating that the lowest energy belongs to a hexagonal interstitial site (H_i) [84], [87]. This inconsistency reflects on experimental outcomes too, with some channeling experiments having identified the T_i centre [91], whilst more recent spot the substitutional equivalent T_s [92] (preprint at the time of writing).

To add to the above, relating centre information to luminescent behaviour proves quite difficult. This is because most of the aforementioned techniques do not distinguish between optically active and non-optically active centres. Furthermore, they observe the majority component and so if a different centre is present in relatively low concentrations it might not be accounted for [93]. Until recently, the EPR studies had failed to detect optically active erbium centres in c-Si. This changed with the introduction of a specially grown multilayer structure of Si/Si:Er grown by MBE which appeared to incorporate erbium ions at a single site of non-cubic symmetry [94], [95]. This well defined site produced narrow linewidth emissions therefore allowing the observation of Zeeman effect splitting, leading to the identification of an orthorhombic-I (C_{2v}) centre. This is significant, yet the outcome remains to be generalised to more conventional ion implanted samples [96]. Very recently, erbium doping in nanophotonic silicon waveguides showed very narrow erbium related emission lines [97]; further experimentation by the same group led to the direct identification of some energy levels of the 13/2 manifold for two sites, however these were not ascribed to a particular symmetry [98]. To this end, this chapter aims to directly investigate the site symmetry of ion implanted optically active erbium in bulk silicon co-doped with oxygen using photoluminescence spectra and a crystal field simulation package, SPECTRE. The results will be compared to existing models, with suggestions and further hypotheses on the erbium centre formation.

3.2 Experimental results

Measurements of the erbium $^4I_{13/2} \rightarrow ^4 I_{15/2}$ transition were conducted between 65-250 K using the setup described in section 4.2. Figure 3.1 presents a selection of temperature dependent PL spectra for sample B3a with 1×10^{19} Er and 1×10^{20} O concentration (in cm^{-3}). The sample followed a two step annealing process with a longer (base recipe) 450 °C anneal for 30 min followed by a 620 °C anneal for 180 minutes and a rapid anneal (RA) at 850 °C for 30 seconds.

The spectrum contains many peaks, the majority of which have relatively broad linewidths. At 65 K, emission centered at 6510 cm^{-1} dominates. Peak centres do not appear to change in temperature. A closer inspection reveals the existence of multiple

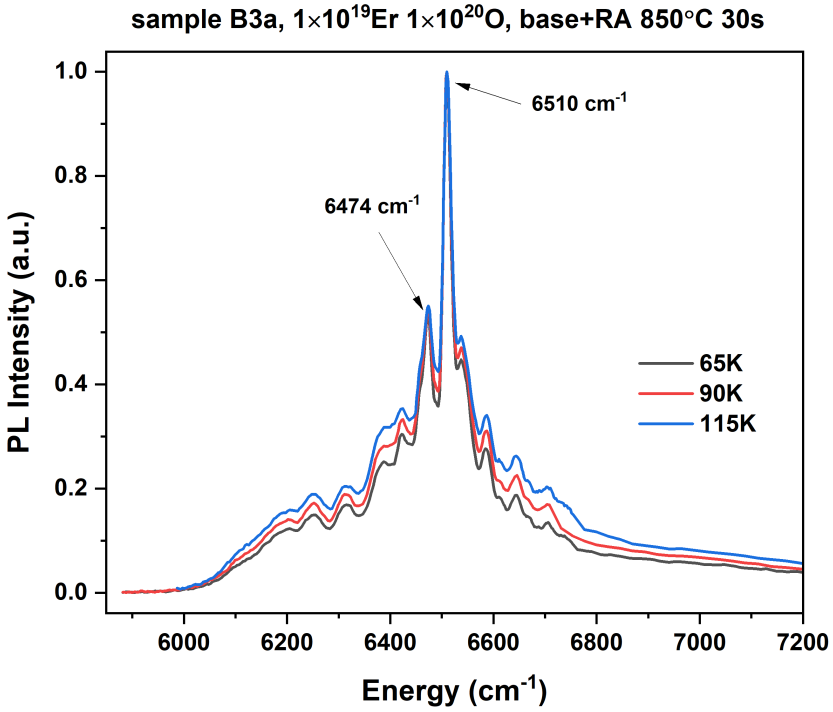

Figure 3.1: PL spectra of Er:Si sample B3a at over band gap excitation with 462 nm laser. All spectra are normalised with respect to the maximum point.

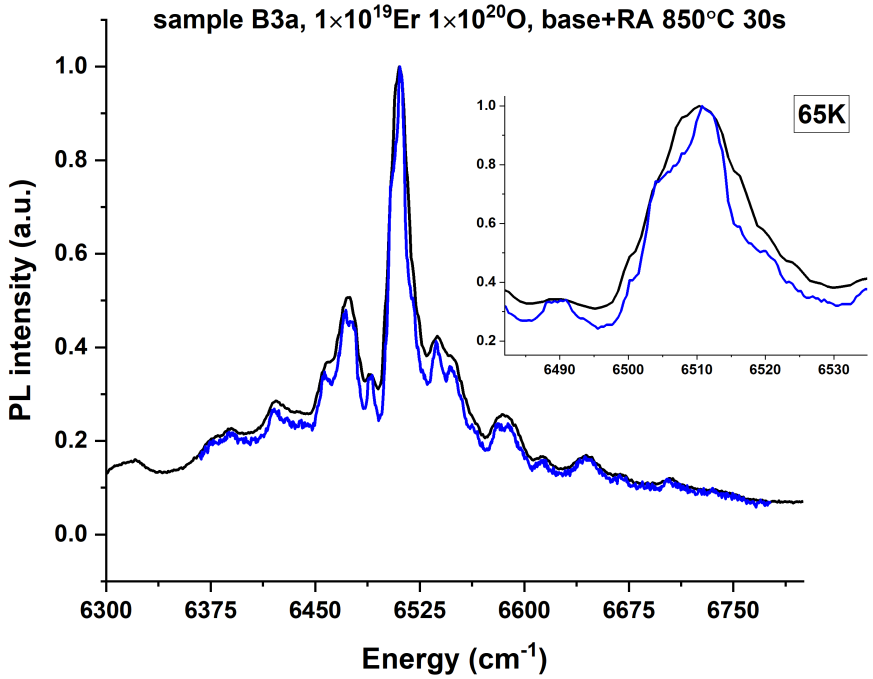

Figure 3.2: Detailed 1.6 nm (black) and sub-1 nm resolution (blue) spectra overlap for sample B3a. Inset shows the main emission line. Measurements were taken at 65 K and spectra are normalised with respect to the maximum point.

convoluted peaks, shown in fig. 3.2. In particular, the main emission line appears to contain at least four closely spaced narrow transitions. Some broader peaks also include numerous sub-nanometer transitions. This observation hints at the existence of multiple optically active symmetry centres. The broad emission linewidths could thus be attributed to a convolution of emissions from these centres as well as contributions from satellite 'hot lines', originating from the next lowest excited state of the crystal-field split $J = 13/2$ multiplet. Increased temperature would result in higher thermal population of the sub-levels of the 13/2 manifold, and thus increased emission intensity. The remaining inhomogeneity could be due to random strain fields introduced through annealing.

Identification of the centres of the 65 K depicted in fig. 3.2 PL emission is tabulated in table 3.1. Notation B refers to broad peaks while N refers to narrow peaks. In order to assign energy levels from the transitions observed in the infrared spectrum a computational crystal field analysis was performed. To begin with, fitting was obtained for the cubic centre, whose splitting had been previously investigated [81], [82], [99]. Selected cubic centre peaks are marked with C (see section 3.2.2).

Table 3.1: Observed peaks at 65 K for sample B3a.

Observed peaks			
Energy (cm^{-1})	Energy (meV)	Assignment	Notes
6735.00	834.99		B
6705.61	831.34		B
6668.00	826.68		
6644.20	823.73		B
6613.51	819.92		B
6585.68	816.47		B
6554.65	812.63		
6548.00	811.80		B
6537.53	810.50		B
6523.90	808.82		B
6520.51	808.39		B
6516.26	807.87		
6510.70	807.18		N
6508.00	806.84	C	N
6504.00	806.35		N
6500.19	805.88		
6490.08	804.62		
6480.80	803.47		
6476.00	802.88		N
6471.20	802.28		N
6467.00	801.76		N
6462.80	801.24		N
6457.40	800.57		N
6451.00	799.78		N, buried
6421.01	796.06	C	N
6388.24	792.00		
6376.85	790.58		N
6320.70	783.62	C	B
6255.70	775.56	C	B
6210.70	769.99		B
6201.50	768.84		N
6180.80	766.28		N
6163.00	764.07		B

Observed peaks continued			
Energy (cm^{-1})	Energy (meV)	Assignment	Notes
6130.00	759.98		B
6107.00	757.12	C	B,unclear
End of table			

3.2.1 SPECTRE program

SPECTRE is a program used in the calculation of spectroscopic and magnetic properties of rare-earth ions in crystals [100]. The program employs intermediate-coupling basis states (refer to section 2.2.3) whilst mixing of all terms within the f^n configuration is allowed. Free ion Hamiltonian parameters such as electrostatic and spin-orbit components are taken from [25] and stored internally in a file called upon each calculation. These are held constant during our simulations.

The user inputs the energy level splitting of their selected manifold(s) following the configuration of their assumed site symmetry. Afterwards, initial crystal field parameters are inserted. In SPECTRE, H_{CF} follows the Wybourne tensor representation as shown in eq. (2.2.31). The crystal field parameters to be varied are selected and the program iterates until a local energy minimum is found. The 'goodness' of the fit is obtained as the deviation between the input (observed) and output (calculated) values for the selected symmetry. The fitting process is repeated iteratively until the 'best' fit is obtained. In this work, input was selected based on the observed PL spectrum lines corresponding to ${}^4I_{13/2} \rightarrow {}^4I_{15/2}$ transitions. This method was further followed for fitting performed on experimental published PL values where the splitting of the 15/2 manifold (and hot lines) was given. Exception to this applies to fits of the Zeeman-observed orthorhombic-I centre (Er-1) as well as the two sites namely (A), (B) in [98] where splitting of the 13/2 manifold was seen (and as such the 13/2 values were used during simulation). Finally, following a transition energies fit, SPECTRE can calculate a list of eigenvalues of the CF Hamiltonian in order of increasing energy. This feature will be used to estimate the 13/2 level for a given centre.

3.2.2 The cubic centre

It is known that for erbium on cubic lattices the 16-fold degenerate ground state ${}^4I_{15/2}$ is split into three quartet states Γ_8 and into two doublet states Γ_6,Γ_7 [99], [101]. Correspondingly the $4^I_{13/2}$ state is split into $2\times\Gamma_8$, Γ_7 and $2\times\Gamma_6$ states [102]. The parametric Hamiltonian takes the form:

$$H_{CF} = B_0^4 C_0^{(4)} + B_0^6 C_0^{(6)} + B_4^4 C_4^{(4)} + B_4^6 C_4^{(6)}$$

For cubic symmetry, the ratio of some B_q^k parameters was fixed according to [27]:

$$B_4^4 = \frac{5}{\sqrt{70}} B_0^4, \quad B_4^6 = -\sqrt{\frac{7}{2}} B_0^6$$

Due to the amount of peaks shown in table 3.1 and the number of possible combinations in the five emission line selection, fits were firstly performed for the splitting identified in [82] and [81]. Additionally, five peaks combinations from the B3a spectrum (fig. 3.2) were selected (labelled as C in table 3.1) as potentially belonging to the cubic centre based on a similar to published values energy difference. Fitting ensued for the suggested splitting of the $^4I_{15/2}$ manifold. Finally, results were compared to a previous selection of transitions assigned to the cubic centre for the same sample (B3a) (shown in [103]). Table 3.2 summarises this selection: Columns 1-2 are fits performed on as-obtained published crystal field splittings, whilst column 4 and 5 are fits for the transitions marked as C in table 3.1. Column 3 denotes the previously suggested ground state manifold splitting for the same sample (B3a).

Table 3.2: Comparison of previously selected peaks by other groups and the resulting $^4I_{15/2}$ manifold split with current selection. The function χ^2 indicates the statistical quality of the fit. It is worth noting that the lowest ground state manifold is always denoted as 0 (cm^{-1}) and input as such in the simulation package. The remaining energy levels distances are calculated with respect to that '0' ground state. In the spectrum, '0' corresponds to the central selected peak, i.e. the 6504.8 cm^{-1}

.

$^4I_{15/2}$ splitting comparison based on peak selection (cm^{-1})				
Przybylinska[82]	Tang[81]	Hughes[103]	This work^a	This work^b
0	0	0	0	0
78.8	77.4	93.5	82.97	86.4
156.8	154.8	186.8	182.8	186.3
248.8	244.4	250.94	254.7	255.2
417.8	406.5	400.5	397.5	401
$\chi^2 = 2.65$	2.16	0.6	0.208	0.099
Central peak: a=6504.8 cm^{-1} b=6508.3cm^{-1}				

It is clear that there seems to be fit improvement with our selected peaks compared to the 'classical' assignments for a cubic crystal field. Additionally, there appears to be

further χ^2 reduction upon choosing the lowest ${}^4I_{13/2} \rightarrow {}^4I_{15/2}$ manifold transition energy as 6508.3 cm^{-1} instead of the most conventional 6504.8 cm^{-1}. Taking the better fitting assumption with central emission at 6508.3 cm^{-1} results in the calculated splitting for the ${}^4I_{15/2}$ shown in table 3.3. Similar deviation in central peak selection is not unusual and can be seen in earlier measurements as well [104]. This highlights the difficulty in making a unique identification of the five cubic lines from photo-luminescence data alone lacking further information.

Table 3.3: Comparative table of calculated (in SPECTRE) versus observed (in the PL spectrum) 15/2 splitting for cubic symmetry for sample B3a.

Observed (cm^{-1})	Calculated (cm^{-1})	$\Delta = E_{exp} - E_{calc}$ (cm^{-1})
0.00	0.00	0.00
86.47	91.44	-4.97
186.3	181.15	5.15
255.19	255.93	-0.75
401.08	400.72	0.36

The next step involved calculation of eigenvalues for the predicted splitting of the ${}^4I_{13/2}$ manifold. It was noted that the fitting algorithm had a tendency to converge to a value of 6638.32 cm^{-1} for the lowest energy level of that manifold. This deviation is not fully understood, but could be due to the integrated free ion matrix parameters in SPECTRE, which remained unchanged during the fitting process. Nonetheless, upon readjusting the calculated energy level to the selected central 6508 cm^{-1} transition the required upper excited crystal field level values can be obtained as shown in fig. 3.3. Here, transitions labelled A1-A5 correspond to the assigned observed peaks from the lowest 13/2 manifold to the ground state. Similarly, B1 is the equivalent transition from the 1^{st} excited 13/2 to the lowest 15/2, C1 from the 2^{nd} excited 13/2 and so on. This in turn enables calculation of hot line positions. Locations of all transitions for the predicted 13/2 splitting, including hot lines, are shown in fig. 3.4:

At liquid nitrogen temperatures only a small percentage of thermal population on level D and almost no population of level E is expected; as a result these levels transitions' contributions can be discounted. Few of the remaining possible transitions, marked with a blue circle in fig. 3.4, were tentatively assigned to hot lines. These are: 6529 cm^{-1} and 6457.4 cm^{-1}.

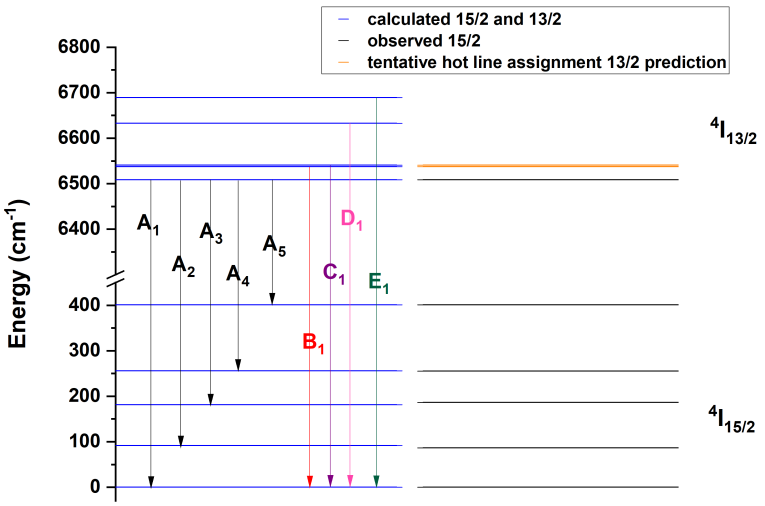

Figure 3.3: Calculated and observed energy level splitting for T_d symmetry. The 13/2 lowest manifold has been shifted to match the assigned transition at 6508 cm^{-1}. The second and third 13/2 levels are too close to be resolved. The observed 15/2 manifold A1-A5 equivalents are the peaks marked as C in table 3.1. The further 13/2 hot line assignments are 6529 cm^{-1} and 6457.4 cm^{-1}.

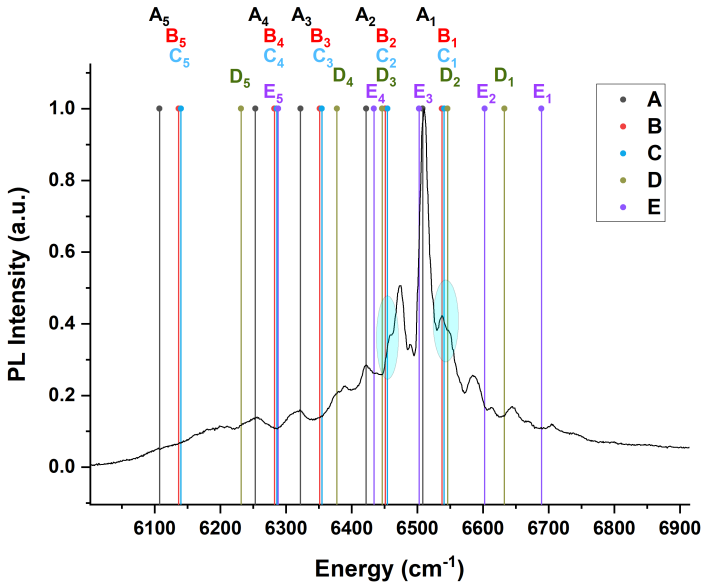

Figure 3.4: Sample B3a depicting hot lines energy calculation based on the predicted 13/2 splitting for cubic symmetry. The blue circle indicates potential emission lines to be assigned as hot lines.

Selection rules

Knowing whether a $\Gamma_a \rightarrow \Gamma_b$ transition is allowed or forbidden requires the evaluation of a set of matrix elements $\langle \Gamma_a | K | \Gamma_b \rangle$, where coupling states $|\Gamma_a\rangle, |\Gamma_b\rangle$ are eigenvectors of a particular Hamiltonian, and K is some system associated quantum operator. From group theory considerations, it can be shown that the matrix element $\langle \Gamma_a | K | \Gamma_b \rangle$ is non-zero only if the reduction of $\Gamma_K \otimes \Gamma_b$ contains Γ_a [105]. In cubic symmetry, $\Gamma_K = \Gamma_5$ [106].

In our selection 5 lines are visible with the lowest energy transition present but unclear due to detector's reduced sensitivity at that region. This is in contrast to the previous selection for the same sample at [103], where the A3 transition (as labelled in fig. 3.3, denoted with dashed red lines in section 3.2.2) is unseen. It is suggested that the proposed peak selection in this work, shown as solid black lines in section 3.2.2, is an improvement.

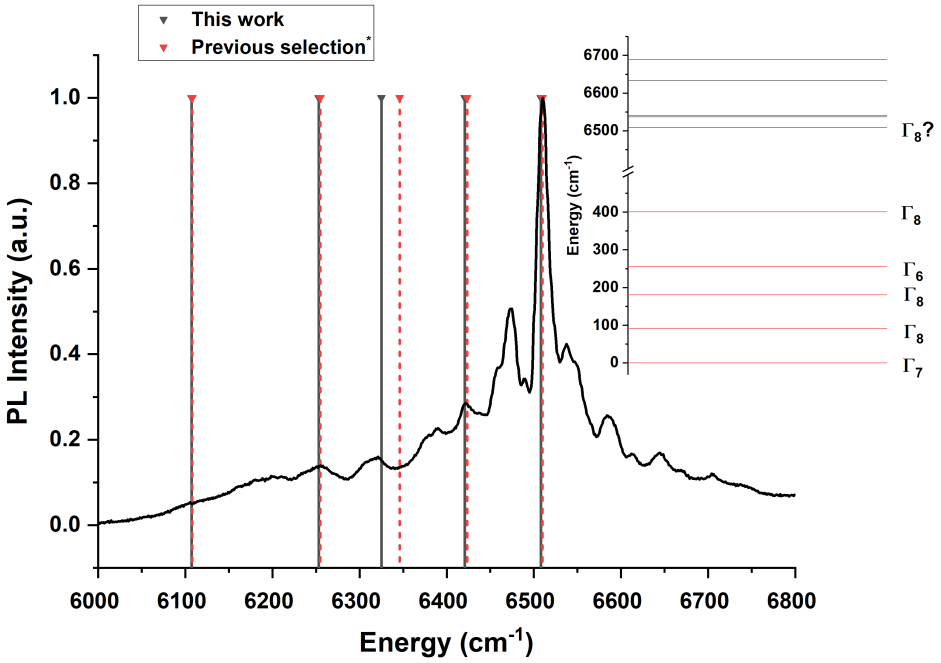

Figure 3.5: Comparison between the current peak selection for T_d symmetry and previous selection for the same sample (B3a). Inset shows the energy diagram for 15/2 and 13/2 levels with corresponding 15/2 irreducible representation notation based on similar literature reports ([81], [82]). The question-mark with relation to the irreducible representation of the lowest 13/2 manifold (Γ_8?) is deliberate and acts as a precursor to the next section.

According to Table 1 of ref.[101], the ground state of Er^{3+} should be either Γ_6 or Γ_7 for cubic symmetry. In literature, Γ_6 representation is agreed; however, observation of all 5 lines requires the lower 13/2 manifold to have Γ_8 representation [107]. Based on group-

theoretical de-compositions of the dipole times the possible excited state representations, one obtains [107]:

$$\Gamma_5 \otimes \Gamma_6 = \Gamma_7 \otimes \Gamma_8$$
$$\Gamma_5 \otimes \Gamma_7 = \Gamma_6 \otimes \Gamma_8$$
$$\Gamma_5 \otimes \Gamma_8 = \Gamma_6 \otimes \Gamma_7 \otimes 2\Gamma_8$$

Therefore, in all scenarios the third ground state manifold of Γ_8 symmetry is allowed and should be observed, unless unresolved. This confirms the previous suggestion that this work's cubic peak selection is a better candidate than the set previously identified in [103], yet brings to surface further questions on the nature of Γ_i of the lowest 13/2 manifold.

Peak selection for cubic fit; a paradox

The above observation on selection rule requirements introduces a paradox in the currently established methodology of peak choice. Previous investigations of cubic symmetry follow the notation of ref.[101] (abbreviated as LLW notation), where the cubic crystal field Hamiltonian is expressed as:

$$H = B_4 \left(O_4^0 + 5O_4^4\right) + B_6 \left(O_6^0 - 21O_6^4\right) \tag{3.2.1}$$

with O_n^m being equivalent crystal-field operators expressed as functions of the components of J, and where B_4, B_6 are parameters determining the scale of the splittings. Two further parameters x and W relating to B_4 and B_6 have been defined so that:

$$Wx = B_4 F(4), \quad W\left(1 - |x|\right) = B_6 F(6), \tag{3.2.2}$$

where $F(4) = 60$ and $F(6) = 13800$ (for $J = 15/2$) are factors to keep the ratio between 4^{th} and 6^{th} term constant. The relative splittings are solely determined by x, with W being a scaling constant. The range of x spans across $-1 \leq x \leq 1$ with positive values corresponding to octahedral coordination and negative values to tetrahedral coordination.

Looking at the $J = 13/2$ energy diagram in fig. 3.6 one notices that Γ_8 can only be the lowest 13/2 manifold for $x < -0.4$. However, this would result in a different splitting and Γ_i representation of the $J = 15/2$ manifold. On the contrary, the well-accepted configuration that we also adopted earlier (shown as inset in fig. 3.5) works for the positive x region where the ground state configuration in increasing energy is: $\Gamma_7 - \Gamma_8 - \Gamma_8 - \Gamma_6 - \Gamma_8$. Here, Γ_6 and Γ_7 have interchanged indices compared to labelling of

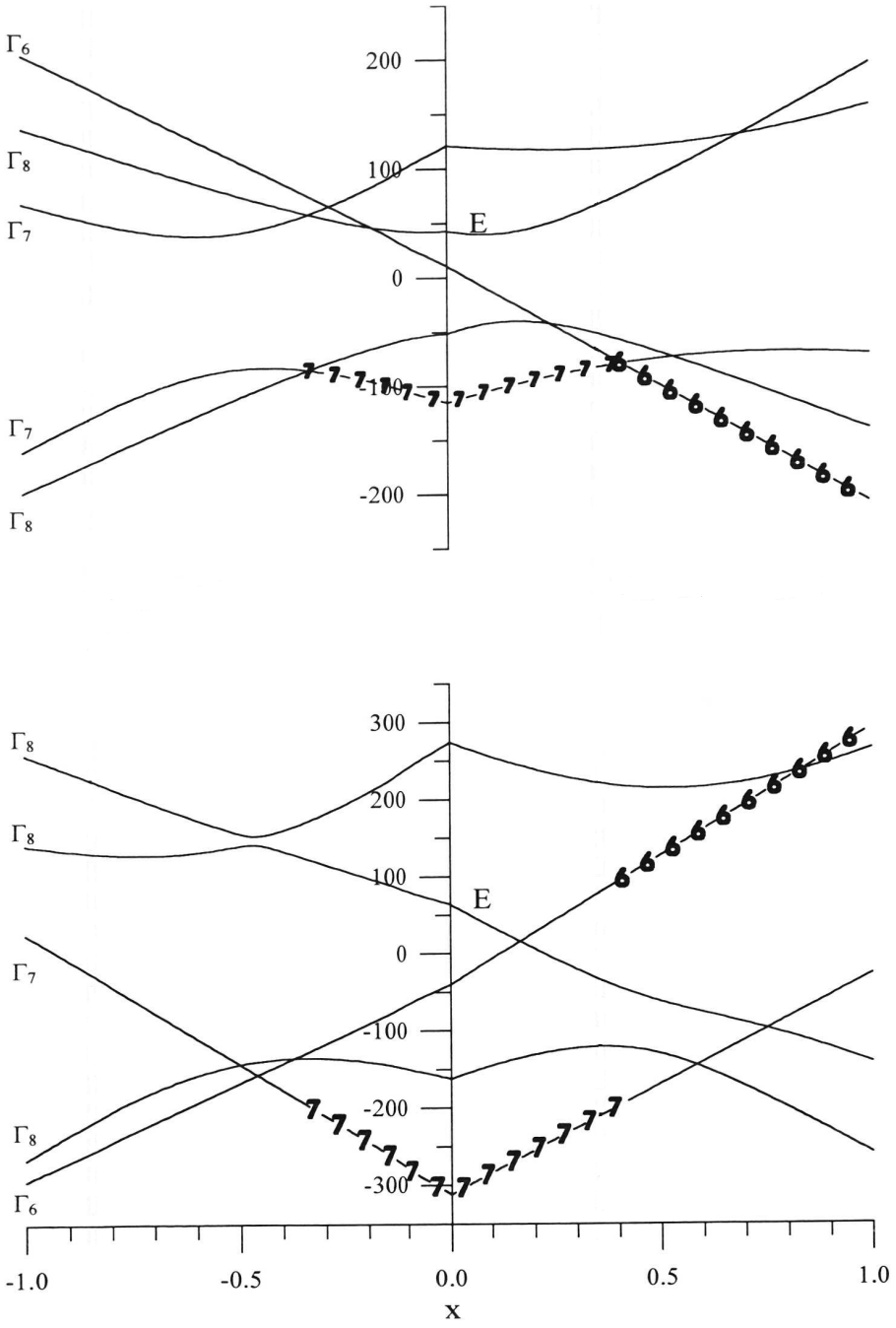

Figure 3.6: Energy level diagram for cubic crystal field splitting of $J = 15/2$ and $J = 13/2$ ground and excited states for erbium in silicon. The number labelling denotes forbidden transitions between $\Gamma_6 \rightarrow \Gamma_6$ and $\Gamma_7 \rightarrow \Gamma_7$. Figure modified from [108].

the 'Tang' model (in [81]) and following work that label according to the convention for T_d symmetry ([82]). As a result of the selection rules, for $x > 0$ there would be at least one forbidden transition. For the established model with $x \approx 0.35$ and its equivalent 15/2 energy splitting ([81], [82], columns 1 and 2 in table 3.2), the 6504.8 cm^{-1} line should be forbidden; yet it is observed as the strongest in the spectrum. This contradiction has been very briefly addressed in [107] and [108]; in the former ([107]), they suggested that achieving the required Γ_8 symmetry called for the parameter x in the excited state to be different from that of the ground state, with $|x| \approx 1$. A similar approach was adopted by [74] in their proposal for a possible J=13/2 energy level splitting. However, the computational prediction for the 13/2 splitting in our case results in levels whose energy difference does not match the equivalent splitting observed in the energy level diagrams in fig. 3.6 for $x < 0$, but is compatible for $x \approx 0.4$, the range used previously in adopted models. In another work [108], the same x value for 13/2 and 15/2 manifolds was assumed and numerous fits were performed for a combination of a given set of emission lines; they concluded that all these combinations gave a 'good' fitting result for both $x > 0$ and $x < 0$. Nonetheless, a common factor in all previous methodologies is the lack of 13/2 splitting calculations. To address this and compare the x value between 15/2 and 13/2 levels, this work performs fits based on several other 15/2 possible configurations using sets of observed transitions from table 3.1. These results are summarised in table 3.4.

Table 3.4: T_d symmetry fitting for various 15/2 Γ_i representations. Labels follow the LLW [101] notation.

Fit label	15/2 Γ_i representation	1st 13/2 level	x range	χ^2
a	$\Gamma_7 - \Gamma_8 - \Gamma_6 - \Gamma_8 - \Gamma_8$	Γ_7	$x \approx 0.15$	0.32
b	$\Gamma_7 - \Gamma_6 - \Gamma_8 - \Gamma_8 - \Gamma_8$	Γ_8	$x \approx -0.4$	0.03
c	$\Gamma_7 - \Gamma_8 - \Gamma_8 - \Gamma_6 - \Gamma_8$	Γ_7	$x \approx 0.3$	0.1
d	$\Gamma_7 - \Gamma_8 - \Gamma_8 - \Gamma_6 - \Gamma_8$	Γ_7	$x \approx 0.35$	2.65

Fits labelled a-c were performed based observed peaks from table 3.1 centered at 6508.3 cm^{-1}. The last row (d) includes a fitting from T_d attributed emission lines in [82]. The second column shows the assumed ground level manifold Γ_i representation, whose energies in sequences of doublet and quartet states were input in the SPECTRE program. The third and fourth columns are the projected lowest 13/2 manifold and x range respectively if x kept the same value for ground and excited state, based on the calculated LLW diagrams in fig. 3.6. Cross checking the relative energy level differences between these diagrams and the SPECTRE obtained calculated energy levels in fig. 3.7, there is a very good match. This is further confirmed from the output format of the

SPECTRE predicted values, where the resulting energies linked to doublets or quadruplets follow the 13/2 representation projected from 15/2 for a given x. These results suggest that the value of x should be shared amongst ground and first excited state, and that for spectra where multiple transitions are seen there can be many combinations resulting in good fits (see i.e. fig. 3.8). Moreover, for the previously established model fit (labelled d), following this cross-examination method results in the same $x \approx 0.35$, further confirming the validity of the model and adding to our earlier statement on the requirement of Γ_7 symmetry of the lower 13/2 manifold leading to forbidden transitions. For this fit (labelled d), calculations of W and x were also performed using eq. (3.2.2) and SPECTRE's output crystal field parameters. The x value was found to be identical to the 0.35 reported in [82] whilst W was slightly increased from the reported 0.88 W to 0.96 W, indicating less stretching of the energy levels. However, in addition to the main transition for this x value being forbidden as previously mentioned, the predicted splitting of the 13/2 manifold contradicts the same group's 'hot' line assignment for the cubic symmetry centre [82]. The only combination with no forbidden lines is (b) with $x < 0$. A possible interpretation of this is shown in fig. 3.8 for our sample B3a. Considering the range of projected x values, these results imply there are numerous possible cubic centres that are sample dependent and it could be that erbium co-exists both in tetrahedral or octahedral coordination arrangement. Finally, given the selection rules for tetrahedral symmetry and assuming the 13/2 computation is correct, previous observations solely based on 'goodness of fit' factors could be flawed resulting in improper peak labelling. Whilst further understanding on the theoretical implications of such a fit are outside the scope of this work, the above underscore once again the difficulty of clear cubic peak assignment from PL studies alone.

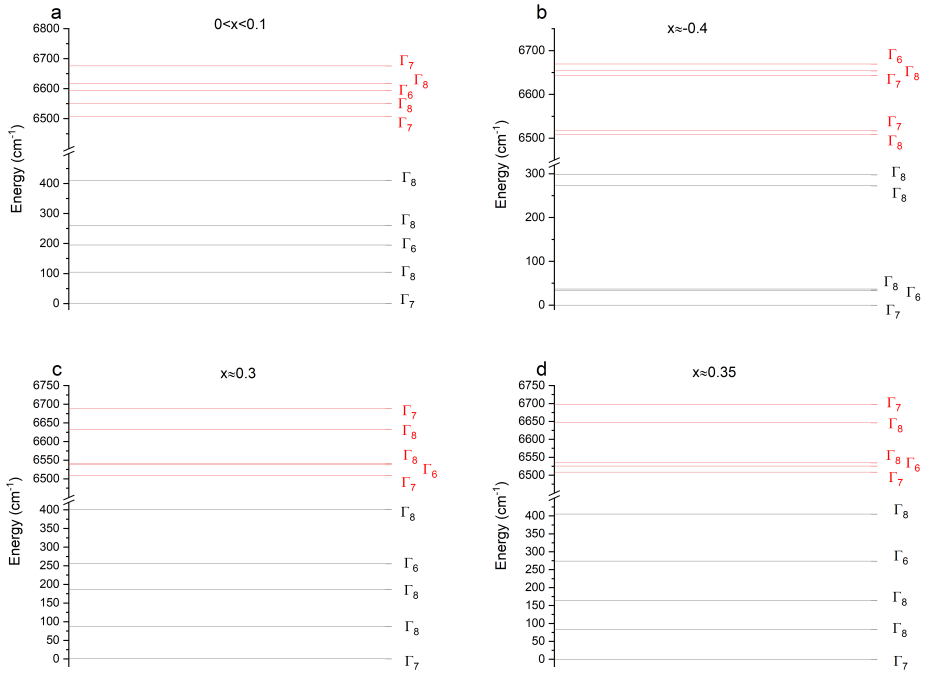

Figure 3.7: Calculated energy levels for 15/2 and 13/2 manifolds for the various 15/2 configurations in table 3.4

3.2.3 Lower than cubic symmetry

Si:Er-1 centre

Previous photoluminescence investigations in Si/Si:Er multinanolayer structures grown by sublimation molecular beam epitaxy (SMBE) had led to the identifications of another eight-lines, including some closely spaced pairs of lines [74], [95], [109]. As discussed in section 3.1, this centre, labelled Si:Er-1 (or Er-1), was unique in offering the possibility of preferential formation of a singular optically active Er-related site. The narrow lines originated from the splitting of the Γ_8 quartet levels in centres of near-cubic symmetry and consequent magneto-optical studies revealing this centre to be of orthorhombic-I symmetry (C_{2v}) [74], [94], [110]. It was suggested this site arose from a distortion of tetrahedrally coordinated Er^{3+} ions, with minimal distortion from T_d symmetry resulting in optical transitions following selection rules for the T_d, rather than the C_{2v} group. The orthorhombic symmetry was further confirmed in [111], where a scheme for the numerical calculation of energy levels of lower than cubic symmetry centres based on the tetragonal distortion of the cubic centre was presented, and for which Si:Er-1 centre was used as a case study.

In this section the observed lines and energy level splitting of the $^4I_{15/2}$ state for

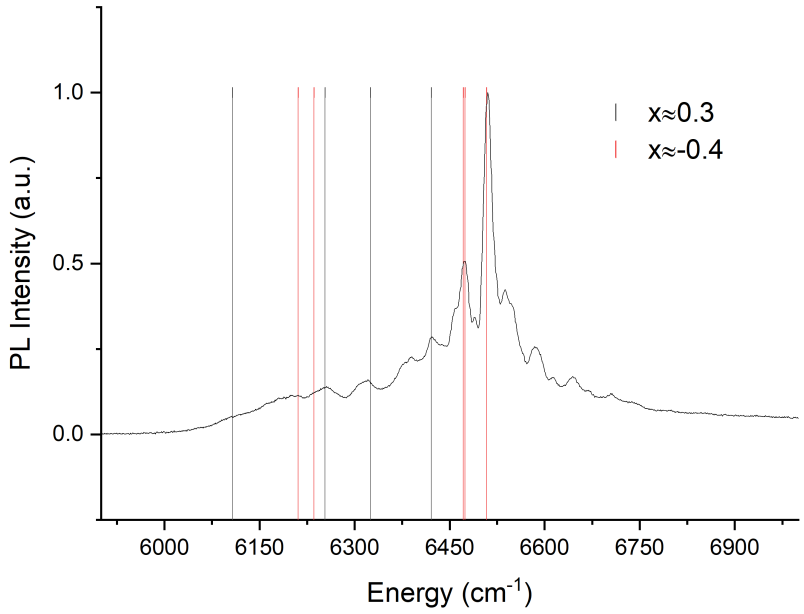

Figure 3.8: Simple comparison of the possibility of co-existence of both cubic centres with $x > 0$ and $x < 0$, with peaks shown excluding the forbidden lower 13/2 manifold to ground transition for $x > 0$.

sample B3a are compared with those of the Si:Er-1 centre. The ground state energy levels for the Si:Er-1 centre provided in [109] are input in SPECTRE alongside crystal field parameters for orthorhombic symmetry. The outcome of this fit is presented in fig. 3.9. It is shown that whilst the calculated ground state is in very good agreement with the experimental values ($\chi^2 = 0.07$), the splitting of the $^4I_{13/2}$ state does not match the hot line assignment by [74]. It is unclear whether this is a result of selection rule differences due to the aforementioned very small distortion from T_d symmetry or something else. In any case, the ground state splitting does not correspond to PL lines in the spectrum of the ion implanted sample B3a. Formation of the Si-Er-1 centre is thought to occur for annealing temperatures over 800°C; our sample fulfilled that criteria and so absence of these lines suggests the existence of a different axial symmetry site.

Er:Si implanted waveguide lower symmetry centre

Recently, a group has identified the $^4I_{13/2}$ splitting of two lower symmetry centres, namely A and B, of an Er implanted Si waveguide [98] but no particular symmetry was attributed to these centres. Here, computational fittings in SPECTRE were performed for various symmetries for both of these sites. The best fit was found to be for orthorhombic symmetry, shown in fig. 3.10.

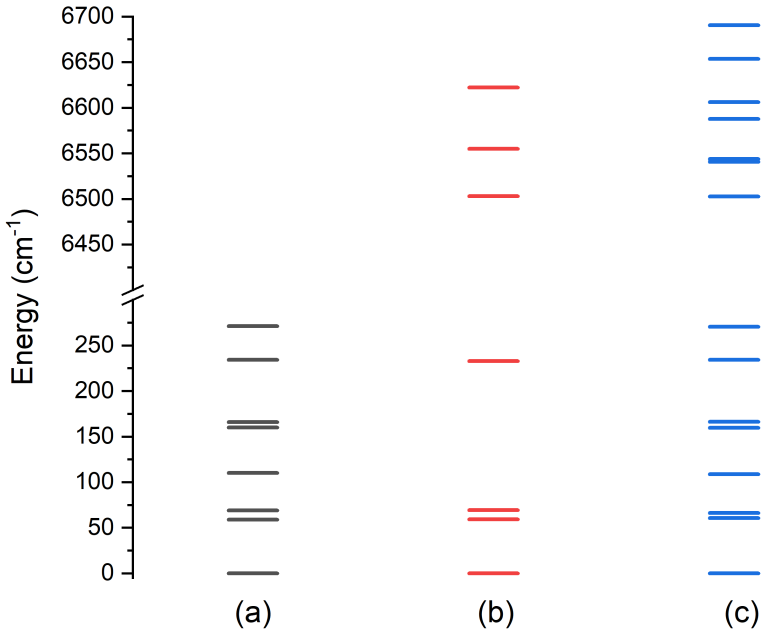

Figure 3.9: Crystal field energy levels for the $^4I_{15/2}$ and $^4I_{13/2}$ states of the Si-Er-1 centre. (a) the eight levels derived from the PL spectrum in [109] (b) the lines observed by [74] with allocated $^4I_{13/2}$ levels from hot lines, (c) SPECTRE calculated fit following same ground level splitting as [109] with predicted $^4I_{13/2}$ levels. The B_q^k parameters were (in meV): $B_0^2 = -33.76$, $B_0^4 = 93.8$, $B_0^6 = -3.35$, $B_2^2 = -32.62$, $B_2^4 = 52.52$, $B_4^4 = -67.65$, $B_2^6 = -8.1$, $B_4^6 = 7.2$, $B_6^6 = -19.4$.

The fitting output shows excellent agreement for the $^4I_{13/2}$ levels, and is mostly in agreement with the higher manifolds of $^4I_{15/2}$. There is some discrepancy in the lower levels. The calculated splitting were next compared to the observed spectra of sample B3a. The central transition was varied between 6503 cm^{-1} and 6510 cm^{-1} to coincide with the primary emission lines. The results are presented in fig. 3.11.

Interestingly, plots (a) and (b) for site A show very good agreement with observed emission lines, with (a) being an excellent match. The same is true for site B when the primary emission is set at 6510 cm^{-1}. It is therefore possible, that the ion implanted sample in this work has either one, or two identical centres to those reported in fig. 3.11.

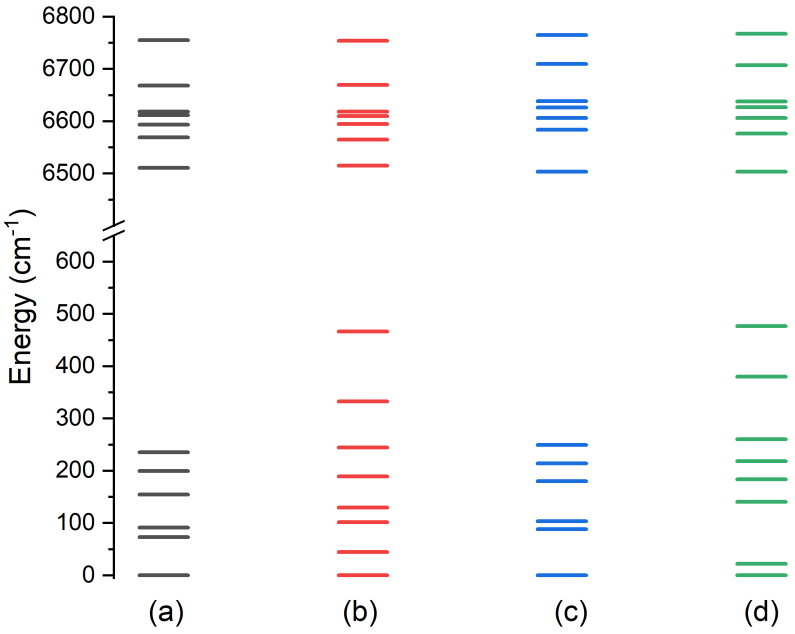

Figure 3.10: Crystal field splitting using orthorhombic CFPs using the reported $^4I_{13/2}$ manifold splitting in [98]. In (a), reported transitions for site A and (b) calculated orthorhombic fit using $^4I_{13/2}$ values and predicting $^4I_{15/2}$. In (c), reported values for site B with (d) the calculated orthorhombic fit.

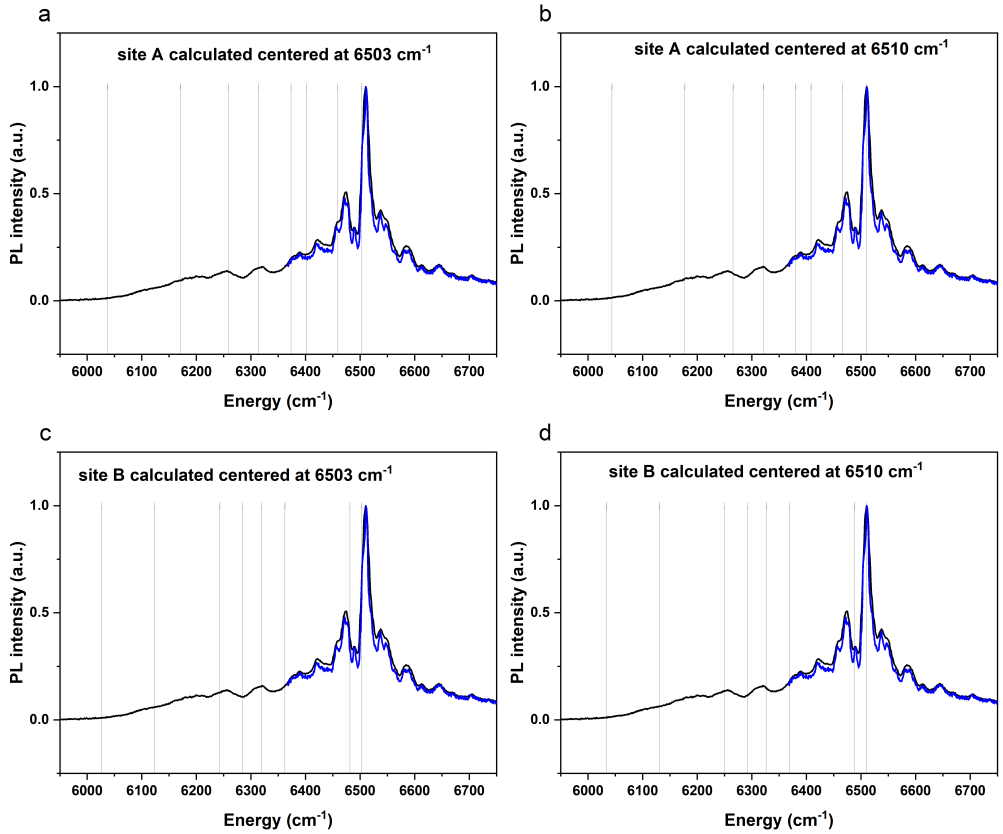

Figure 3.11: Calculated $^4I_{15/2}$ levels for an orthorhombic fit shown as vertical lines on top of sample B3a. In (a), site A as denoted in [98] with transitions centered at 6503 cm^{-1}. In (b) the same site centered at 6510 cm^{-1}. Similarly in (c) site B centered at 6503 cm^{-1} and (d) centered at 6510 cm^{-1}.

3.2.4 OMMR measurements (preliminary)

Optically modulated magnetic resonance (OMMR) is an optical characterisation technique conceptualised by Dr. Mark Hughes in the University of Salford. It involves the modulation of an electron paramagnetic resonance (EPR) signal from a sample by a tuneable laser resonant with the under investigation centre's electron dipole transition. This is in contrast to the more traditional optically detected magnetic resonance (ODMR), detailed in [112], where a microwave field modulates the absorption signals. As a result, characterisation of materials with low absorption cross-sections which could otherwise be extremely challenging, such as Er, becomes reachable. This technique was used for one of the Er:Si samples in this work (sample B3a) with the aim of probing the crystal field splitting of the first excited state of Er implanted Si.

Firstly, the Er:Si sample's typical EPR spectrum at 10 K was obtained at a microwave frequency of 9.37 Hz, and its three strong narrow resonances were attributed to Er at different sites. Of particular importance here, the EPR line at 950 G was attributed to the OEr-1' monoclinic centre based on previous studies [55], [85], [113]. Secondly, the sample was illuminated under 1565 nm laser irradiation which resulted in the EPR spectrum broadening. Following such, contour plots of laser illumination under different magnetic fields were created, and the OMMR spectrum with the strongest resonance was identified for 1173 G, shown as top left in fig. 3.12. Rotation of the sample in the (110) plane resulted in a shift in magnetic field of both the EPR and broad optically generated resonances. Small angle adjustments were made to align the zero-crossing point at 961 G of the initial illuminated EPR spectrum of the non-rotated sample with the 950 G EPR line of the monoclinic centre. In turn, the 961 G OMMR spectrum consisted of seven narrow less intense peaks. This spectrum became featureless upon different sample orientations when the zero-crossing point was not at the EPR resonance line and therefore suggested that the 961 G OMMR was related to the 950 G OEr-1' EPR line. It was proposed that the peaks observed in the OMMR spectrum were an indirect measurement of the crystal field splitting of the $^4I_{13/2}$ manifold and that the two distinct spectra (broad at 1173 G and narrow at 961 G) correspond to two different Er centres. Crystal field splitting was performed on known energies of the $^4I_{15/2}$ determined by PL and compared to the OMMR spectra. For the 1173 G plot, predictions on PL crystal field splitting for a cubic centre did not agree with the OMMR experimental results, whilst the latter 961 G spectrum's splitting was a good fit for an orthorhombic C_{2v} centre. However, agreement between the PL and OMMR splitting required the assignment of the ground state to ≈ 6588 cm^{-1}, which is quite far from the previously assumed centres at 6502-6510 cm^{-1}. For more details, the reader is referred to [103]. In this work, we

will re-evaluate this assignment and show that it is possible for the 1173 G spectrum to be a result of an Er centre with cubic symmetry or the broadened spectrum of the same peaks as those present in the 961 G plot.

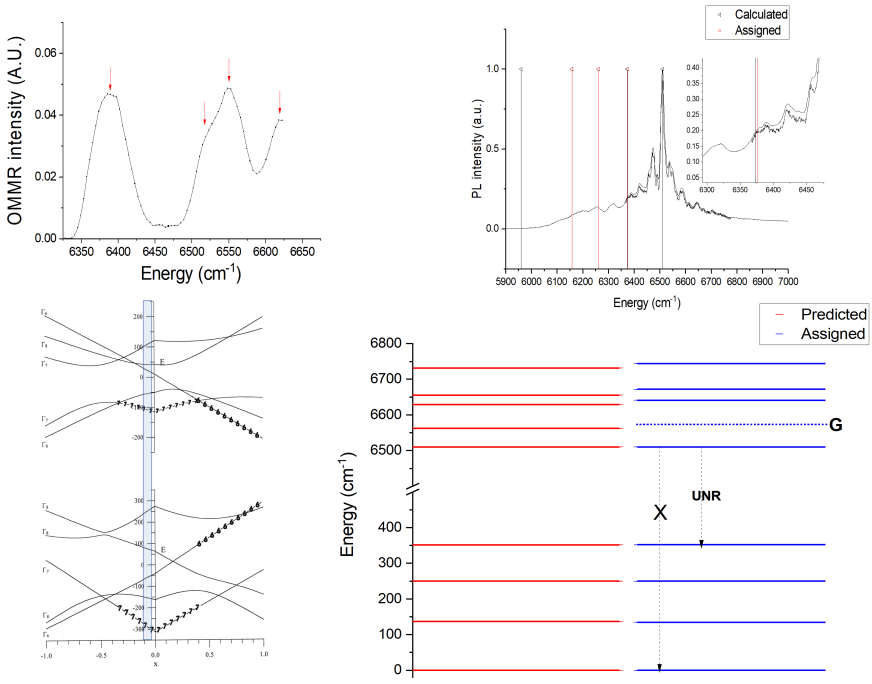

Figure 3.12: Procedure of OMMR & PL peak fit: Top left is the OMMR spectrum at 1173 G with the observed peaks, bottom left is the assumed range of x for the cubic fit, top right the PL spectrum with the selected and predicted peaks for the 15/2 split and bottom right shows the comparison between calculated and observed energies of the ground and first excited manifolds.

1173 G

The broad peaks identified at [103] for the 1173 G field are (without accounting for offset energy): 6390, 6520, 6550 and 6620 cm^{-1} which we label 1-4 from left to right in fig. 3.12. We notice that the 13/2 splitting of $\Gamma_7 \rightarrow \Gamma_6$, $\Gamma_6 \rightarrow \Gamma_8$, $\Gamma_8 \rightarrow \Gamma_7$ for small $x < 0$ (highlighted as blue region in fig. 3.12) resembles the difference between peaks 1-3, 3-4, 4-5 of the OMMR spectrum. In section 3.2.2 it was shown that the value of x should be consistent between 15/2 and 13/2. Therefore, by assuming 6510 cm^{-1} as the ground level (that wouldn't be present in PL based on selection rules), some PL transitions that could correspond to the 15/2 manifold were estimated. Combining the PL and OMMR splittings a set of cubic CFPs were fitted; the results were in very good agreement with $\left(\chi^2 = 0.02\right)$. The predicted complete set of energy levels was then obtained and compared to the observed levels. The results were in line with theoretical prediction with the lowest energy peak outside the resolution of the detector, and the highest energy peak being

forbidden. The line marked as 'G' for 'guessed' in the 13/2 manifold is missing in the OMMR spectrum. To confirm our assignment, we included it in the 13/2 splitting and recomputed the 15/2 level now only based on the 13/2 OMMR+guessed spectra; the results were consistent. Since the mechanism of OMMR is not fully understood, it is possible that the missing peak is due to a forbidden magnetic dipole transition. It is also possible that the assignment to a cubic centre based on the above methodology is incorrect since we once more highlight the ambiguity of cubic peak assignment despite previous notions; furthermore, there have been no prior reports of an EPR active cubic centre, making this assignment unlikely. Therefore further investigation and repeated measurements would be required if one wanted to establish a more robust interpretation. Regardless, the remaining unassigned PL lines confirm our initial assumption that the Er centers under investigation occupy multiple symmetry sites. Previous measurements of angular dependence of the Er-related electron spin resonance (ESR) lines in Er implanted Si have identified a number of different Er-O ESR centers: three monoclinic centers labelled OEr-1, OEr-1' and OEr-3, and three trigonal centers labelled OEr-2, OEr-2' and OEr-4 [55], [85], [113].

3.3 Chapter summary

This chapter presented results of the site structure of an Er:Si sample (B3a) through crystal field splitting simulations and PL spectra correlation. Section 3.1 highlighted the ambiguity around Er:Si centre formation, and section 3.2.1 introduced the SPECTRE software simulation package employed in this work. An investigation into the cubic symmetry site was performed in section 3.2.2. By invoking selection rules in section 3.2.2 and following the previously established tetrahedral energy level splitting, an improved PL peak identification relating to the cubic site was made for sample B3a. Section 3.2.2 further linked the outcomes of selection rules in cubic symmetry and noted their implications might not have been taken into consideration in the traditional cubic model for which the otherwise forbidden lowest $^4I_{13/2} \rightarrow^4 I_{15/2}$ emission is dominant in the spectrum. By using SPECTRE to reinforce this argument and proposing that Er:Si could in principle occupy multiple cubic symmetry sites both of tetrahedral and octahedral arrangement, the need for re-evaluation of the currently accepted cubic model was suggested. Section 3.2.3 compared other groups' published data on lower Er:Si symmetry sites. Existence of the well-defined Si:Er-1 centre in this work's sample B3a was ruled out, whilst simulated projections of the ground state based on new first excited level waveguide measurements led to a best fit for a centre of orthorhombic C_{2v} symmetry that could be shared amongst our samples. Finally, fig. 3.12 laid out basic principles of a recently developed technique namely 'Optically Modulated Magnetic Resonance'

(OMMR) and re-examined the possibility of the 1773 G OMMR spectrum to originate from a centre of cubic symmetry.

4.PHOTOLUMINESCENCE SPECTROSCOPY OF ER:SI

Erbium centre formation depends on sample preparation conditions, co-doping and processing parameters such as annealing temperatures and time. In this section, spectra comparison of samples grown with different dopant concentrations and post implantation processing recipes are examined in order to establish the optimal conditions for optically active centres and luminescence yields. Correlation between lattice damage from implantation is probed through Raman measurements.

4.1 Sample fabrication

Samples were prepared by implanting Er and O into phosphorous (P)-doped $< 100 > 500$ μm thick Si wafer, supplied by Topsil. The resistivity of the unimplanted wafer measured at (8000 ± 500) Ωcm corresponding to a P concentration of $(5.5 \pm 0.3 \times 10^{11})$ cm^{-3}. A Monte Carlo simulation software package namely Stopping and Range of Ions in Matter (SRIM) was used to estimate defect depth distribution and straggle after the Er and O ion implantation [114]. Implantation energies were chosen to produce flat erbium and oxygen profiles fig. 4.1. The samples were fabricated using a chain of 7 erbium and 10 oxygen implantation steps with a tilt angle of 7°off the ion beam to avoid channeling. Implantation was performed at 77 K at the Ion Beam Center of the University of Surrey using the 166Er ion isotope (zero nuclear spin).

For a singular sample, labelled CZ4, five erbium implantation steps were performed for an Er target concentration of 3×10^{18} cm^{-3}. No oxygen co-implantation took place. The wafer of this sample consisted of a 2" wide 325 μm thick, $< 100 >$ oriented CZ n-type silicon with resistivity values between 0.027-0.033 Ωcm due to antimony (Sb) impurities.

Samples were subjected to either a one, or two step post implantation thermal anneal treatment. For the first step, referred to as long anneal, samples were treated at 450°C for 30 minutes followed by 180 minutes at 620°C (labelled recipe A, standard). Exception to this is sample CZ4 which was annealed at 850°C for 30 minutes only (referred to as recipe B in table 4.1). Erbium and oxygen target concentrations for all samples are shown in table 4.1.

4.2 Experimental setup

Photoluminescence spectra used in chapters 3 and 4 were obtained using the setup illustrated in fig. 4.2. A Thorlabs L462P1400MM 462 nm multimode laser diode was placed in a TCLDM9 mount. Diode temperature and current control was achieved with the

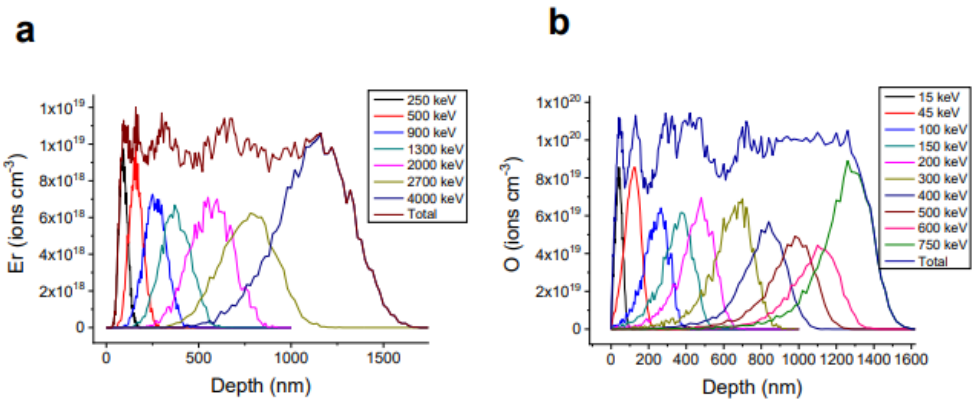

Figure 4.1: Simulated implant profile of (a) erbium and (b) oxygen with peak concentration of 10^{19} cm^{-3} and 10^{20} cm^{-3} respectively. Figure reproduced with permission from Supplementary information in [103].

Sample name	Erbium concentration (cm^{-3})	Oxygen concentration (cm^{-3})	Long anneal	RA temperature (°C)	RA duration (s)
A1	1×10^{19}	1×10^{20}	NO	850	30 s
A2	1×10^{19}	1×10^{20}	NO	900	30 s
A3	1×10^{19}	5×10^{20}	NO	950	30 s
B0	1×10^{19}	1×10^{20}	YES	NO	N/A
B1	1×10^{19}	1×10^{20}	YES	750	30 s
B2	1×10^{19}	1×10^{20}	YES	800	30 s
B3a	1×10^{19}	1×10^{20}	YES	850	30 s
B4a	1×10^{19}	1×10^{20}	YES	900	30 s
B5a	1×10^{19}	1×10^{20}	YES	950	30 s
B3b	1×10^{19}	1×10^{20}	YES	850	50 s
B4b	1×10^{19}	1×10^{20}	YES	900	50 s
B5b	1×10^{19}	1×10^{20}	YES	950	50 s
B4c	1×10^{19}	1×10^{20}	YES	900	20 s
B5c	1×10^{19}	1×10^{20}	YES	950	20 s
C1	1×10^{18}	1×10^{19}	YES	850	50 s
C2	1×10^{18}	5×10^{19}	YES	850	20 s
C3	1×10^{18}	1×10^{20}	YES	850	20 s
CZ4	3×10^{18}	N/A	YES, B	NO	NO

Table 4.1: Implantation and annealing details for the samples investigated in this thesis. The B in the long anneal recipe of CZ4 corresponds to recipe B mentioned in the text.

use of Thorlabs TED200C temperature controller and Thorlabs LDC210C laser diode controller respectively. The laser diode controller was set as the current source and the laser's output was modulated with a TTi TG210 2MHz function generator. The function generator's square wave output acted as a reference signal for the Stanford Research Systems SRS830 Lock-in amplifier (LIA).

The sample was positioned inside an Oxford Instruments MicrostatHe-R sample-in-vacuum cryostat finger. The vacuum system consisted of two separate lines; a turbo-molecular pump backed by an Edwards nXDS10i scroll pump dedicated to evacuating the sample vacuum chamber, and another turbomolocular pump accompanied by a rotary pump to ensure constant thermal insulation of the continuous flow liquid nitrogen (LN) transfer line. Cryogenic flow was determined through a needle valve, whilst further adjustments could be made to the LN return line pressure. Chamber temperature was regulated between 65 K - 300 K with a Mercury iTC Oxford Instruments controller.

The optical setup consisted of a co-linear excitation and collection part. Excitation was guided through a DMLP650L longpass dichroic mirror with 650 nm cut-on wavelength placed at a 45°angle. Laser light was then focused on the sample via a Mitutoyo MY10X-823 10x plan apochromat NIR objective, with 31 mm working distance, f=200 and 0.26 NA. Fluorescence was collected through the same objective and dichroic and focused with a Thorlabs LA1433-C lens onto the entrance slit of a Bentham TMc300 monochromator. An FEL850 850 nm cut-on wavelength longpass filter was placed in front of the entrance slit. The monochromator included two gratings, and in this experiment the T306R1u6 grating was used, with blaze angle at 1550 nm. The exit beam from the monochromator was detected by a thermoelectrically cooled Hamamatsu NIR PMT H10330C unit with an InGaAsP photocathode (PMT). The PMT output was connected to the LIA signal input.

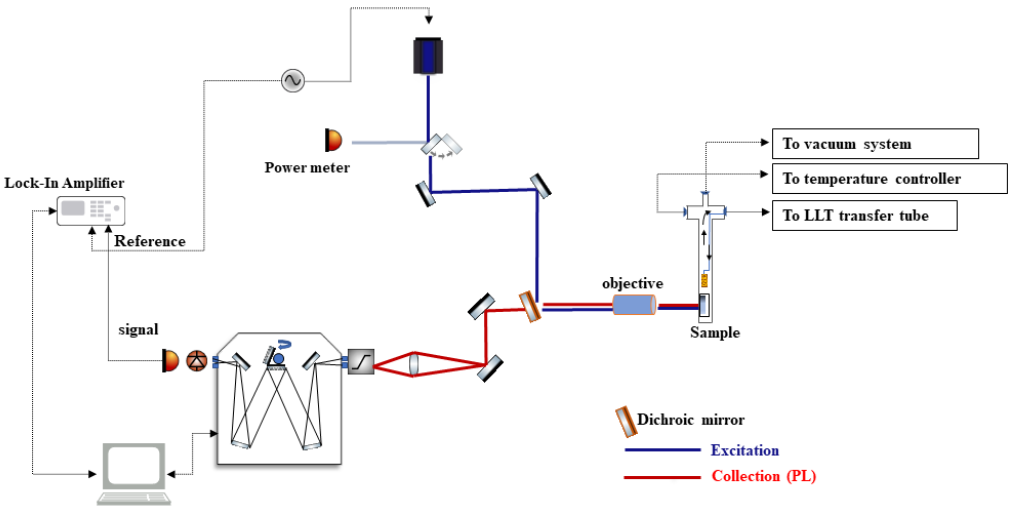

Figure 4.2: Schematic diagram of the PL setup employed in these measurements. The excitation path is denoted with blue and the collection path with red. Modulated light is guided through the dichroic mirror and focused onto the cryostat-mounted sample using the NIR objective. The flip-up lens mount after the laser beam exit allowed for near-field power measurements using the power meter. Luminescence is collected through the NIR objective, guided via the dichroic and other mirrors and is focused on the monochromator's entrance using a lens. An additional longpass filter is placed at the entrance to minimise any potential leakage of reflected laser light from the dichroic mirror. The PMT detector (symbolised using both diode and detector symbols) is placed after the exit. See text in section 4.2 for more details.

4.2.1 System automation

Devices were interfaced by myself using LabVIEW environment. The monochromator was controlled using Dynamic Link Library (DLL) commands, whilst the LIA followed RS232 commands and had a pre-existing instrument library available from which sub-codes (sub-vis) were selected and adapted accordingly to create the required sequence. An abridged flow diagram of the code process is shown in fig. 4.3.

To begin with, the instruments were initialise and grating, time constant (τ_c) and filter values were set. A settling multiplier x was introduced so that prior to measurement reading the LIA had a waiting time of x$*\tau_c$. An averaging number was additionally created corresponding to the readings taken for each wavelength. These readings were inter-programmatically averaged with the mean and standard deviation value saved in arrays and exported for each step/wavelength position. The averaging method ensured as small as possible noise interference with the output, excluding the systematic noise introduced from the PMT dark current. Sequencing of events was achieved using LabVIEW's state machine architecture.

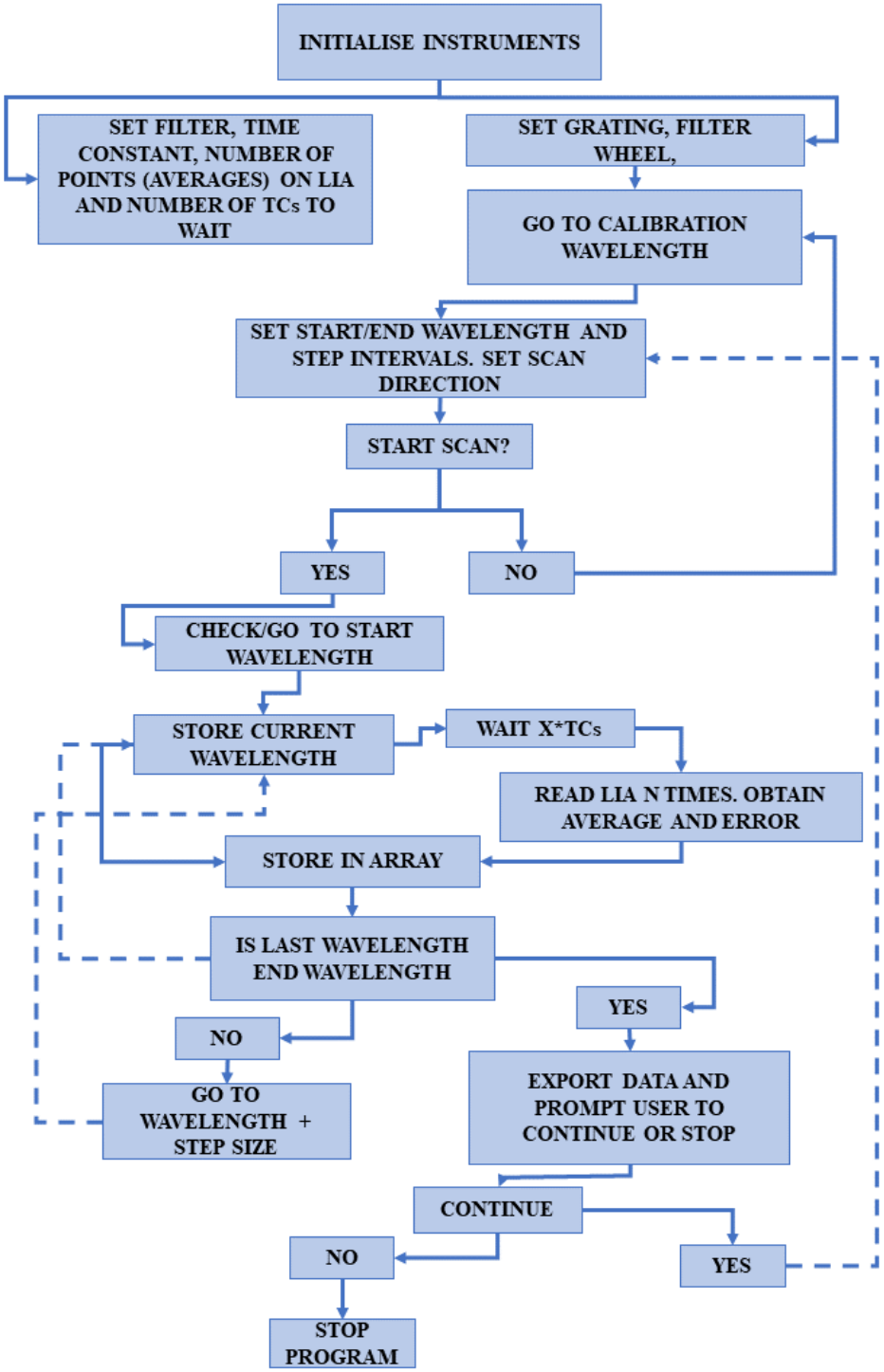

Figure 4.3: Simplified flow chart of the code process created to obtain PL spectra.

4.2.2 Monochromator calibration

The monochromator's grating position was calibrated against a standard mercury (Hg) vapour discharge lamp to ensure accurate reading of transition energies during our experiments. Slit widths were decreased significantly to allow correct peak centre observation of the ultra-narrow Hg emission lines shown in fig. 4.4(a). Observed transitions were checked against the expected emission lines of mercury [115]. One of these lines located at ≈1529.6 nm was of particular interest due to its proximity to the erbium main emission region and was selected to confirm repeatability of measurement output. Six scans were performed encompassing that emission, with three of them moving from low to high wavelength (forward scan) and the other 3 moving from high to low wavelength (backwards scan). As shown in fig. 4.4(b) all scans are in excellent agreement, confirming the reliability of the setup and the correct implementation of monochromator's directionality in the interfacing code. These results are particularly important in the context of peak selection in the crystal field splitting analysis presented in chapter 3. The presented spectra in this thesis are corrected following fig. 4.4(c).

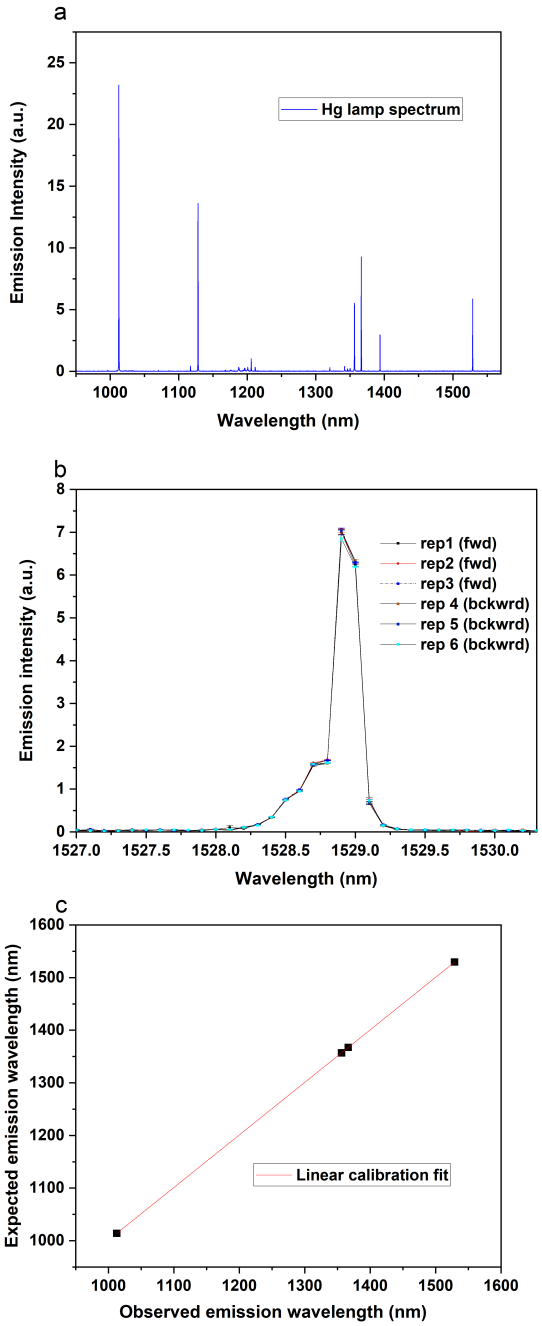

Figure 4.4: Monochromator calibration procedure using a mercury (Hg) lamp. All wavelengths presented in this figure are uncalibrated. In (a), as-obtained Hg emission spectrum. (b) shows the repeatability test for a selected emission line and (c) shows the final calibration equation.

4.2.3 Beam profile

The excitation beam diameter at the sample position was measured using the knife-edge method [116], [117]. Following [116] and assuming a Gaussian beam profile, the total

power detected behind the knife as the knife edge is moved perpendicularly across the beam is given by:

$$\phi(x) = \phi_0 \left[0.5 + 9.5\text{erf}\left(\frac{\sqrt{2}x}{\omega} \right) \right] \tag{4.2.1}$$

where x stands for the relative position of the knife edge with respect to the beam centre, ϕ_0 is the beam radius at $1/e^2$ irradiance. The $1/e$ beam diameter can then be obtained by:

$$D_e = \sqrt{2}\omega \tag{4.2.2}$$

and the full width at half maximum (FWHM) is:

$$\text{FWHM} = \sqrt{2ln(2)}\omega \tag{4.2.3}$$

Measurements were performed with a knife edge mounted on a post on a 0.02 mm precision translation stage. The blade was positioned at the focal point of the microscope objective where the sample would otherwise be located. A Thorlabs PM16-405 power meter was placed in the beam path behind the blade. Background measurements were performed by fully obstructing the beam and measuring the average power. All readings were background corrected. Figure 4.5 presents the beam width measurement for 462 nm excitation source used in this chapter. The same methodology is applied for the beam profile measurement in chapter 7.

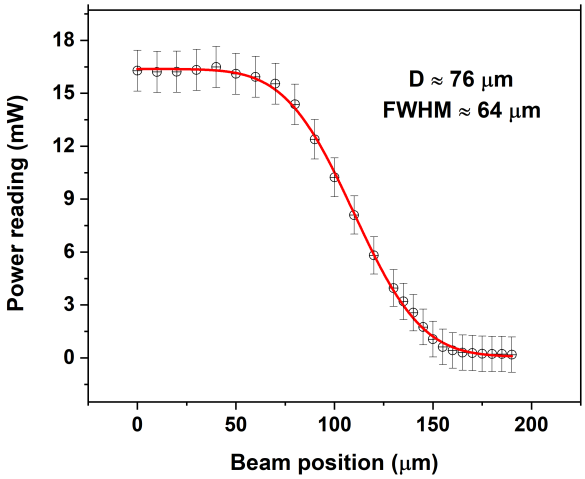

Figure 4.5: Measurements of the beam diameter at focus waist of the sample for the PL 462 nm excitation using the knife-edge method. Red lines are fits to equation eq. (4.2.1). The sample was located approximately 40 cm away of the laser source. A collimating lens was used immediately after the diode laser exit and only the most intense part of the beam that resembled a top-hat profile was selected using a zero aperture iris diaphragm. The selected beam did not diverge significantly throughout the beam path.

4.3 Results and Discussion

4.3.1 Raman spectroscopy

Main principles of Raman spectroscopy

Raman spectroscopy is a spectroscopic analytical technique which utilises scattered light in order to measure the vibrational energy modes (phonons) of a sample. Light scattering by a molecule results in the photon's electromagnetic field inducing a polarisation of the molecular electron cloud around the nuclei. The energy transferred by the photon to the molecule leads to the creation of a short-lived state, called the virtual state. This state is unstable and the photon is almost immediately re-emitted as scattered light. The energy of the virtual states is determined by the frequency $v_0 = 1/\lambda_0$ of the light source used. For most scattering events, the energy of the molecule is preserved upon its interaction with a photon therefore the wavelength of the scattered photon is identical to that of the incident photon. This is a dominant process referred to as Rayleigh or elastic scattering. Raman scattering constitutes a much rarer event (at a rate of ≈1 in 10 million photons) and occurs where nuclear motion is induced during the scattering process leading to energy transfer between (either from or to) the incident photon and the molecule. This process is referred to as inelastic and the energy of the scattered photon differs from that of the incident photon by one vibrational unit (see eq. (4.3.1)) [118]. Figure 4.6 depicts the processes taking place for one vibration.

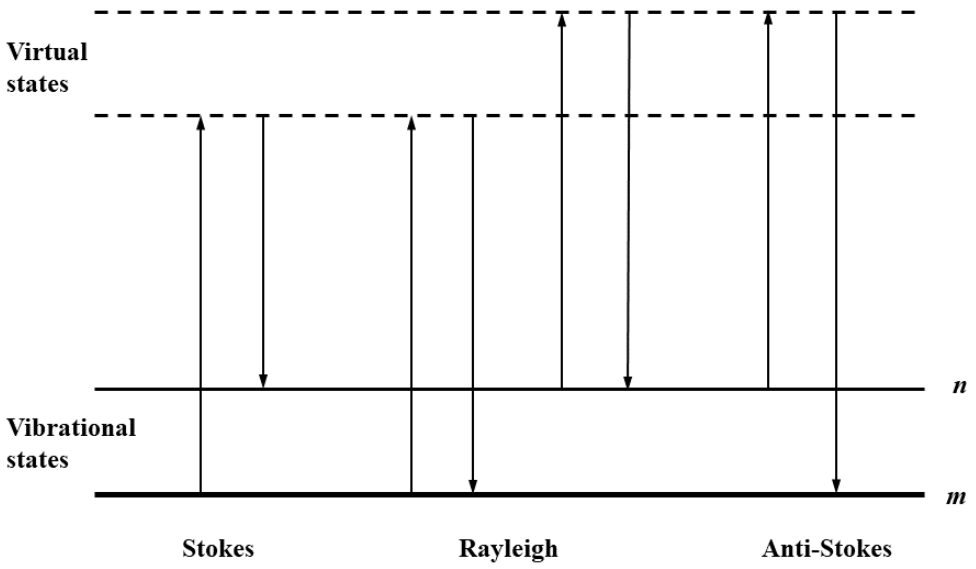

Figure 4.6: Schematic diagram of the Rayleigh and Raman scattering processes. State m corresponds to the lowest energy vibrational state and n is a state of increasing energy.

At room temperature, most (but not all) molecules lie in the lowest energy vibrational level m. During Rayleigh scattering there is no energy change and light returns to the same energy state. During Raman scattering from the lowest vibrational state m, the molecule absorbs energy and is promoted to a higher energy excited vibrational state n. This is named Stokes scattering. The reverse (Raman scattering from thermally occupied excited state n to the ground state m) is called anti-Stokes scattering and involves transfer of energy to the scattered phonon. At room temperature, the Boltzmann distribution dictates minimum occupancy of molecules in the excited vibrational state and therefore measurements primarily observe Stokes scattering [118]. Raman scattering is located at:

$$\Delta_v \ (\mathrm{cm}^{-1}) = (v_0 \pm v_m) = \left(\frac{1}{\lambda_0 \ (\mathrm{nm})} \pm \frac{1}{\lambda_m \ (\mathrm{nm})} \right) \times \frac{10^7 \ \mathrm{nm}}{\mathrm{cm}} \tag{4.3.1}$$

where v_m, λ_m are the vibrational frequency and wavelength of a molecule respectively and v_0,λ_0 are the incident light beam frequency and wavelength. The $-$ and $+$ correspond to Stokes and anti-Stokes lines.

Nevertheless, not all vibrational and rotational transitions are Raman active. Following Chapter 1 (pp. 13-30) of [119], the electric strength of an electromagnetic wave such as a laser fluctuates with time so that: $E = E_0 \cos 2\pi v_0 t$. Upon sample illumination, it induces an electric dipole P according to $P = \alpha E$ where a is a proportionality constant called polarizability. For a molecule vibrating with frequency v_m one can express the nuclear displacement q as $q = q_0 \cos 2\pi v_m t$. For vibrations with small amplitudes, the polarizability becomes a linear function of q taking the form:

$$\alpha = \alpha_0 + \left(\frac{\partial x}{\partial q} \right)_0 q_0 \tag{4.3.2}$$

where α_0 refers to the polarizability at equilibrium and $\left(\frac{\partial x}{\partial q}\right)_0$ is the rate of change of α with respect to q at equilibrium. To be Raman-active, the rate of change of polarizability (α) with the vibration must not be zero (see eq.1-39 in [119]). One can see that the electric dipole P and polarizability α are linked. In real molecules, both P and E are vectors consisting of three components in the x, y and z directions, leading to polarizability taking a tensor form (see eq.1-47 in [119]). As a result, the selection rules applied to determine whereas a vibration is Raman-active depend on the space symmetry elements. In solid state, group theory decomposition is used to derive these rules (see Chapters 1.14, 1.15, 1.18 in [119]).

Raman spectroscopy in silicon

Silicon has diamond structure O_h^7. For its crystalline form (c-Si), selection rules concerning the first-order Raman scattering dictate that only the optical phonons located

at the centre of the Brillouin zone are Raman active. In c-Si this constitutes of a triply degenerate first-order optical phonon at the centre of the Brillouin zone at 519 cm^{-1}. Much weaker second-order transverse acoustic and optical modes can appear at ≈305 cm^{-1} and 975 cm^{-1} respectively [120]. In this work, the effect of annealing parameters on the crystallinity of silicon was investigated through Raman spectroscopy.

This distinction is made possible by considering the differences between crystalline and amorphous materials. Amorphous materials, whilst sharing the same chemical composition with their crystalline equivalent, lack order in their spacial arrangement and have a wider array of bond angles, bond lengths and bond energies as well as dangling bonds depending upon their nearest neighbour bond interaction. This variation produces a distribution of states of slightly differing vibrational energies (phonons). Additionally, amorphisation leads to disruption of long-range translational symmetry in the crystal lattice. Consequently, the selection rules that otherwise hold true in crystalline materials relax for their amorphous equivalents. For silicon, this leads to all phonons from the Brillouin zone centre to the edge being sampled, and Raman scattering being detected over a wide region which in turn manifests as peak broadening on the spectrum [121].

Raman spectroscopy measurements

Samples were illuminated with a 488 nm laser set at 70 mW at source corresponding to 5.6 mW at sample via the use of a neutral density (ND) filter. They were tested with an Olympus MPLN 50x objective and a Syncerity detector equipped with a high resolution 1800 $grmm^{-1}$ grating with acquisition time of 2 seconds and 5 accumulations. Data were collected for 3 different spots across the samples to examine the potential variation in crystallinity over the surface of the deposited silicon. Raman measurements were conducted by Andrij Zadoroshnyj at the University of Manchester. Analysis was performed by myself. Data were plotted and curve-fitted using Lorentzian profile [122]. No significant deviation amongst the 3 selected spots was found, suggesting a uniform implantation layer post thermal annealing.

The unimplanted silicon wafer revealed a Raman peak at (520.34±0.02) cm^{-1} with full width at half maximum (FWHM) (3.2±0.1) cm^{-1}. This is in agreement with typical Raman spectra of Si substrates in the absence of strain [123], [124]. On the contrary, the as-implanted with Erbium and Oxygen sample includes a very broad peak centered at approximately 460 cm^{-1} in addition to a narrower peak at ≈506 cm^{-1}, as shown in fig. 4.7. Following from section 4.3.1, the broad peak is indicative of amorphisation caused by implantation damage since the less orderly amorphous silicon has a distribution of possible bond arrangements and relaxation of selection requirements occurs. The narrow peak suggests some residual crystallinity, and the peak centre shift could arise from

tensile stress introducing different phonon density of states (see also section 4.3.1) [125], [126].

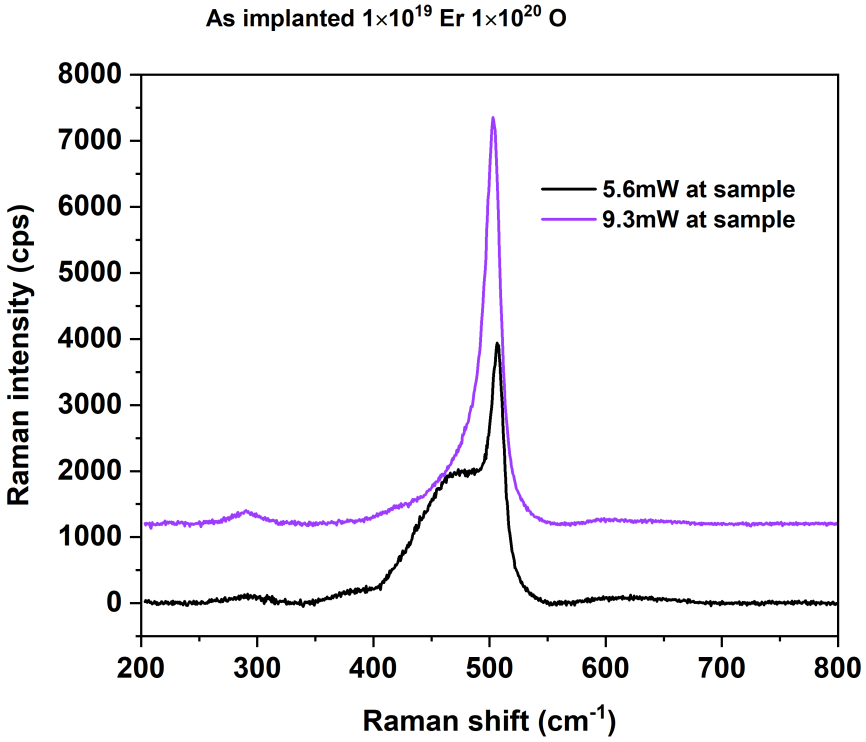

Figure 4.7: Raman spectra of the as-implanted sample at different incident laser power.

The ratio of the two peaks quantifies the relative amounts of amorphous and crystalline silicon. This ratio appears to be dependent to the incident to the sample laser power. It is possible that under sufficient excitation power amorphous silicon converts to its crystalline form. Previous work has observed partial recrystallisation above 4 mW but this threshold could vary for different silicon substrates [127].

Samples following a single rapid anneal show considerable recrystallisation yet amorphisation is still visible compared to the unimplanted sample in fig. 4.8. It is shown that whilst the broad peak remains identical for all samples, the narrow Raman peak shifts closer to the c-Si centre with increasing temperature, suggesting the potential reduction of surface stress as bonds re-achieve uniformity.

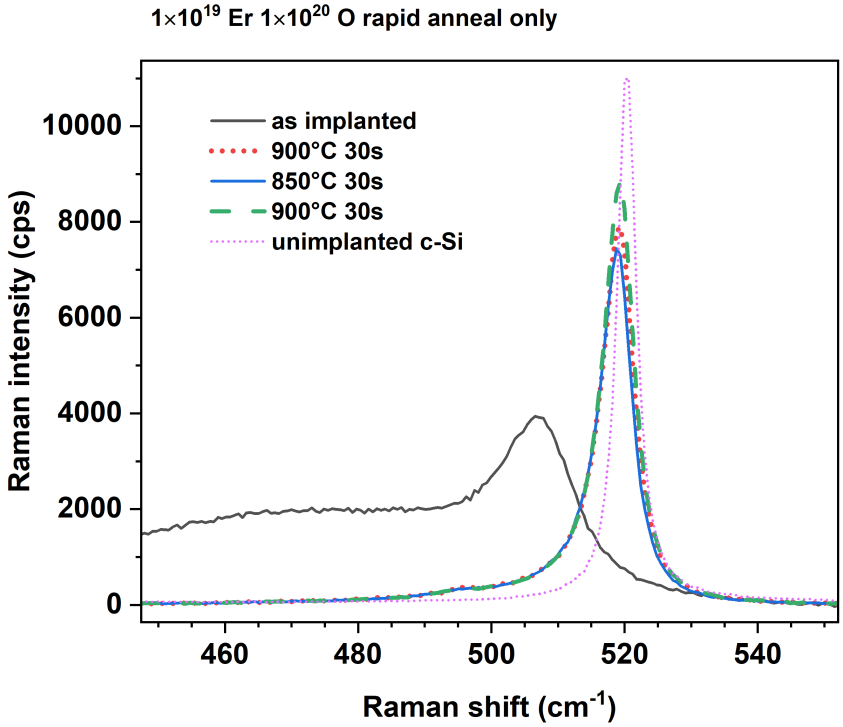

Figure 4.8: Raman spectra for samples following a single rapid anneal treatment. The y axis units refer to counts per second.

A two-step post implantation anneal including a longer 450 °C 30 min followed by 620 °C for 180 min thermal treatment prior to rapidly annealing is successful in recovering most of silicon's crystallinity as seen in fig. 4.9. In particular, $T_{RA} \geq 850$ °C produces the closest to c-Si spectra. This is further confirmed in fig. 4.10(a) where there is clear matching of fitted areas for the above-mentioned samples to that of the unimplanted sample. Interestingly, annealing for 50 s at elevated temperatures seems to increase the average peak area compared to its 30 s equivalent; however the changes are quite subtle and the results lie close to the c-Si value within uncertainty.

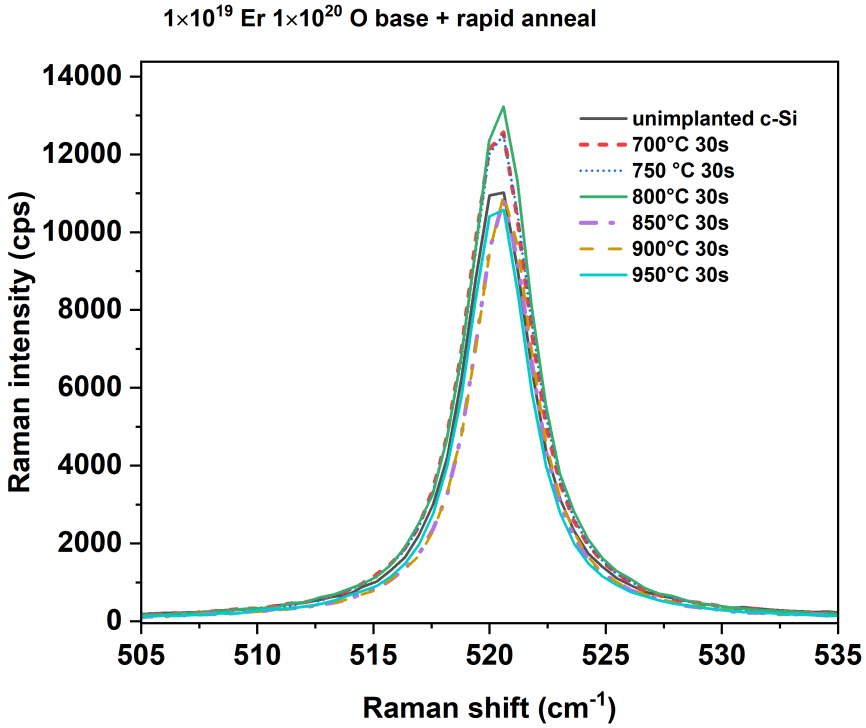

Figure 4.9: Raman spectra for samples following a two-step anneal treatment, with t_{RA}=30 s.

In conclusion, the two-step annealing process is more successful in removing implantation damage than a single rapid anneal treatment. Samples following the two-step treatment with rapid anneal temperature T_{RA}=850 °C appear to be fully recrystallised. The following section discusses the effect of post-implantation processing on the Er:Si luminescence.

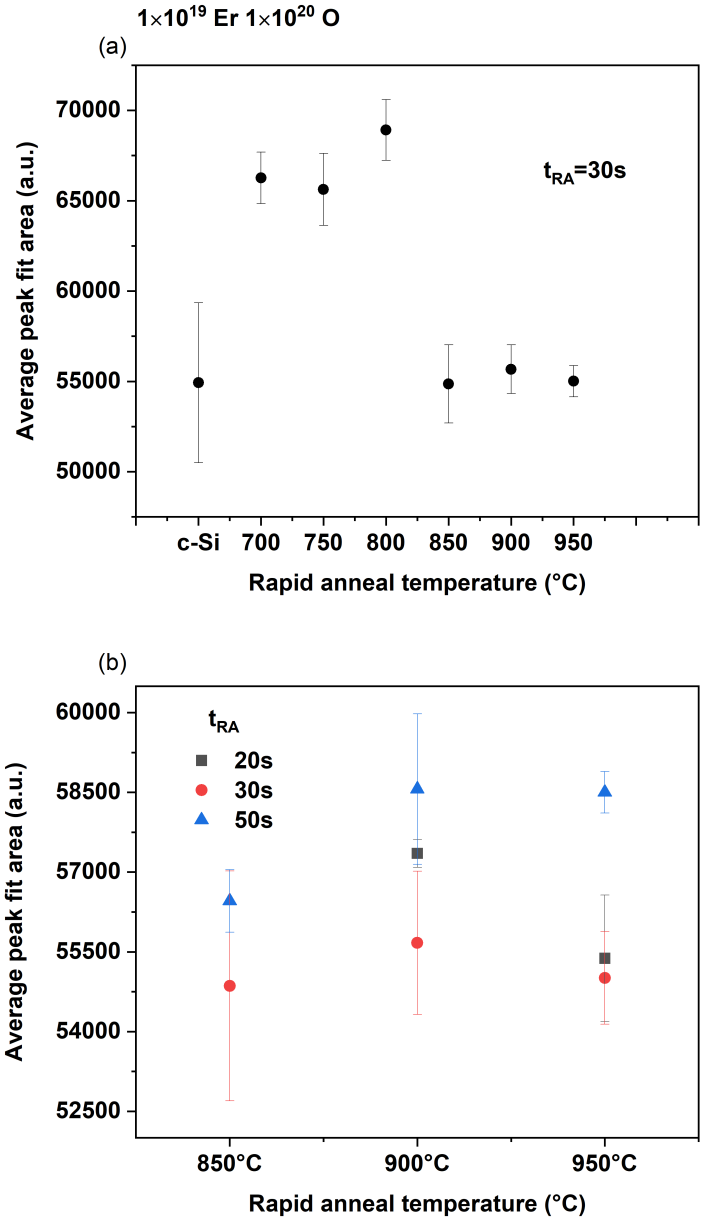

Figure 4.10: Lorentzian fit areas for various samples following a two step anneal treatment for various temperatures lasting 30 s (a) and (b) for different time duration at some of these temperatures.

4.3.2 Effect of single step rapid anneal temperature on Er:Si luminescence

Photoluminescence spectra of samples having undertaken a singular post-implantation rapid anneal treatment (labelled A series in table 4.1) are presented in fig. 4.11. The 'as grown' label refers to the as implanted sample that has not undertaken any thermal annealing treatment.

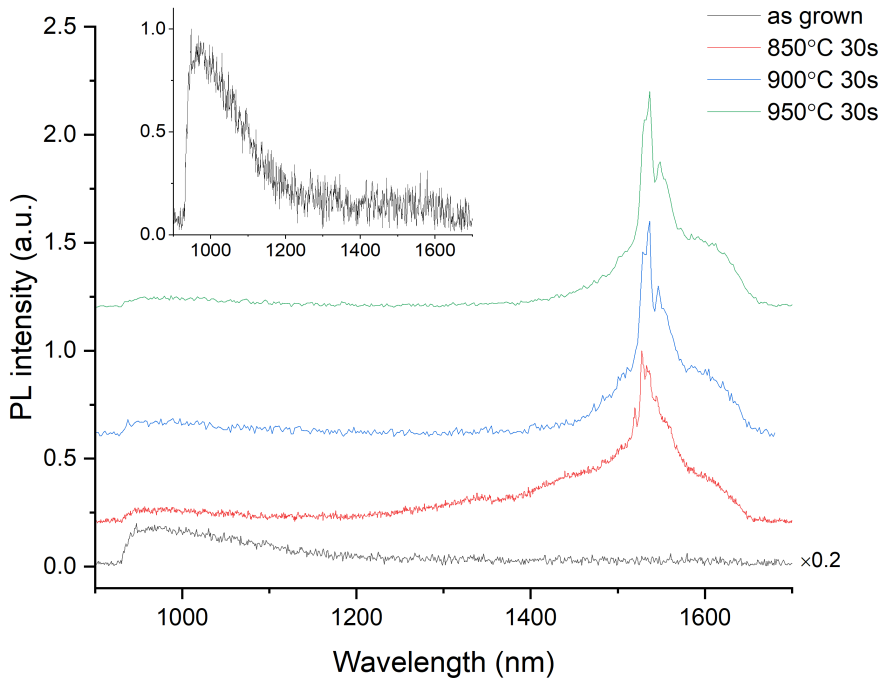

Figure 4.11: Photoluminescence spectra for samples following single step rapid anneal (RA) treatment. The as-grown label refers to the as implanted sample without thermal treatment and is magnified at inset for clarity. Inset has the same axes as main graph but PL intensity is normalised to the intrinsic silicon emission for features comparison (see main text). Spectra were taken at 77 K.

All samples show emission lines in the characteristic erbium luminescence region. These emission lines are superimposed upon some broad features. For the sample annealed at 850 °C, two broad features are indicated; one across 1250-1450 nm and another at 1450-1600 nm. Annealing at higher temperatures extinguishes the 1250-1450 nm peak, whilst the 1450-1600 nm one remains. This second feature could extend beyond 1600 nm yet such is unclear due to the non-linear response and decreased sensitivity of the PMT detector (see section 4.2) in the region. The visible dip at $\approx$ 1300 nm is attributed

to atmospheric water absorption arising from the high humidity in the lab. The small rise at 950 nm is due to the detector sensitivity, whilst the origin of the asymmetric peak around 980 nm remains unclear. It is possible that this peak relates to amorphous silicon emission. Whilst visible, this feature does not contribute more then 10% of the maximum observed erbium emission at ≈1536 nm and seems to decrease linearly with higher rapid annealing temperatures as shown in fig. 4.12. There is no significant silicon band-edge luminescence at 1010 nm. Therefore for these concentrations it appears that even a single step rapid anneal process is sufficient to suppress silicon emission in favour of the erbium dopant.

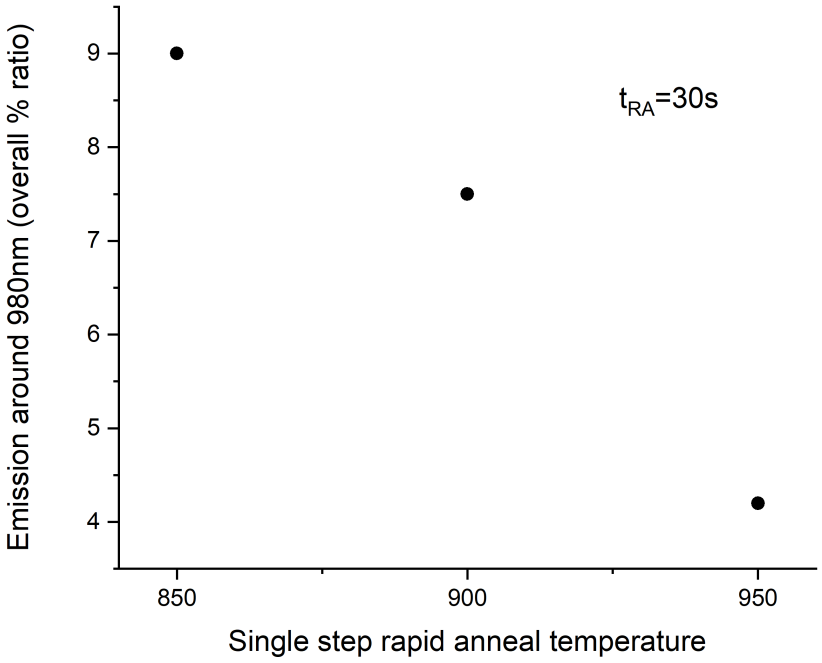

Figure 4.12: Intensity dependence of the 980 nm emission feature on the single step rapid anneal temperature. The equivalent overall spectrum is shown in fig. 4.11. For sample details refer to table 4.1. 100% (100 on the scale) corresponds to the as-grown sample.

Figure 4.13 presents a comparison for the main erbium related emissions amongst the three samples. The main peaks are alphabetically labelled, with all transition emission centres tabulated in table 4.2. It is evident that the most prominent peak for rapid annealing temperatures above 850 °C is the 1536.6 nm (labelled E) whereas at 850 °C (sample A1) the same peak is almost indistinguishable. Similarly, the 1519 nm (peak A) is absent at elevated T_{RA} whilst the 1544 nm (peak F) coexists with the 1547 nm (peak G) as part of a broader emission for T_{RA} = 900 °C (sample A2). Ultimately, annealing

at 950 °C (sample A3) eliminates peak F in favour of a singular peak G. Likewise, the transition at 1528 nm (peak B) disappears giving way to a previously unseen 1529 nm emission (peak C) for $T_{RA} > 850$ °C. Finally, peak D (1533 nm) potentially co-exists on all samples, yet is only clear for A1. Notably, there are no strong emissions for sample A1 for wavelengths above 1550 nm. In contrast, samples A2 and A3 present various less intense peaks. There is also improvement in the signal-to-noise ratio, with A3 showing more defined, narrower lines. It is suggested that for this sample series, annealing at

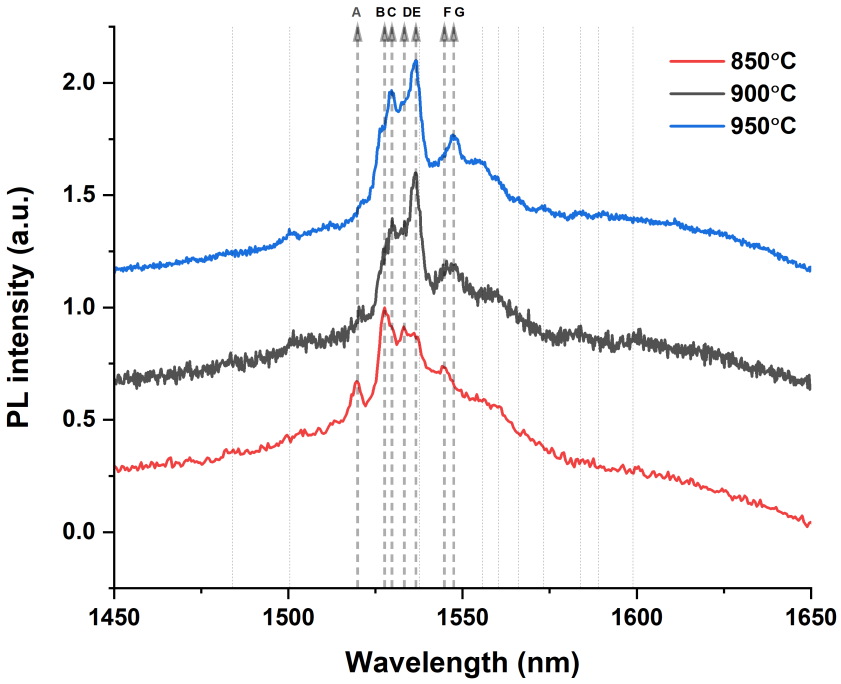

Figure 4.13: Erbium transitions comparison for the 1×10^{19} Er and 1×10^{20} O (cm^{-3}) 30 seconds rapid anneal only treatment series. The bold alphabetically labelled dashed lines indicate main emissions. All emissions are tabulated in table 4.2. This spectrum is the higher resolution version ($\approx$ 1.6 nm) of fig. 4.11 taken at 77 K.

temperatures above 850 °C introduces a different erbium centre, shown on the spectra as a shift of the main emission lines. The presence of a multitude of higher wavelength (lower energy) emissions unseen for A1 imply this centre could be of lower than cubic symmetry. The inclusion in a broader peak of a number of transitions present both for A1 and A3 in sample A2's spectra denote this sample could contain both centres in some proportion. However further increase of T_{RA} replaces the low temperature centre completely as seen for sample A3.

Peak label	Wavelength (nm)		
	850 °C	900 °C	950 °C
	1482	*1483.3*	*1481*
		1501	*1501*
	1513		*1512*
A	1519.6	*1520*	*1521*
			1526.6
B	1527.6		
C		1529	1529.6
D	1533		*1532.8*
E	1536.6	1536.4	1536.6
		1537.8	
F	1544		
G		1546.8	1547.2
			1555.6
		1558.2	
	1560		*1560*
	1567		*1566*
			1573.5
		1583.7	1583.7
			1590
	1600	1599.9	
		1619.3	

Table 4.2: Transitions for the 1×10^{19} Er and 1×10^{20} O (cm^{-3}) 30 seconds rapid anneal only treatment series (series A in table 4.1). Numbers in italic correspond to transitions that are weak. Peak labels correspond to the dashed lines labelling in fig. 4.13.

Broad background formation

Careful observation of the as-grown sample (seen as inset in fig. 4.11) shows that it displays some similarity with samples A1-A3 with respect to broad background feature formation. Two small wide peaks can be detected between 1200-1400 nm and 1400-1650 nm with $\approx$ 20% relative to maximum intensity (although not clearly distinguishable from the graph). Similar broad background can be found in cathodoluminescence (CL) reports for Er_2O_3 powder in the infrared region. The same group showed similarities in the visible CL spectra of c-Si:Er following 950 °C anneal in oxygen atmosphere for 1 h and the erbium oxide confirming that the interaction of Er with oxygen is important in the luminescence mechanism [128]. Comparable background in the 1400-1700 nm region has been further observed in erbium doped amorphous silicon oxycarbide thin films [129] as well as hydrogenated amorphous silicon suboxide films [130]–[133]. It is thus possible that the broad features arise from remaining amorphisation of the silicon matrix or from erbium oxide resulting from erbium clustering, as expected at high implantation doses. If the feature was a result of amorphisation, it is logical to think that better recrystallisation of the matrix would remove it. This is indeed true for the 1250-1400 nm region. We thus propose that this peak is a result of imperfect recrystallisation, and for single step-rapid annealing a minimum temperature of 900 °C is required to eliminate it. Such is in agreement with the Raman results in section 4.3.1.

To further investigate the origin of the 1400-1650 nm broad emission, spectra were compared to the photoluminescence of a CZ- silicon sample co-implanted with Er and oxygen following a different annealing recipe, labelled CZ4 in table 4.1. This sample underwent a singular long anneal at 850 °C for 30 minutes. Photoluminescence spectra for CZ4 at 77 K are shown in fig. 4.14 This sample exhibits a strong silicon-band edge related emission at $\approx$ 1130 nm. This emission is dominant, and there appears to be no luminescence arising from well-defined erbium centres. On the contrary, a broad feature spanning 1400-1650 nm is visible. It is therefore reasonable to attribute this broad emission to amorphous erbium in silicon. The strong similarity of this feature to the broad feature seen in samples A1-A3 suggests they have the same origin. We thus ascribe the 1400-1650 nm peak to amorphous erbium in silicon. Finally, the obvious spectral differences between fig. 4.13 and fig. 4.14 highlight the crucial role of both silicon matrix as well as processing parameters in achieving well-incorporated optically active erbium luminescence. Next, the effect of different erbium to oxygen concentration ratios in the PL spectra is examined for samples following identical post-implantation thermal treatment.

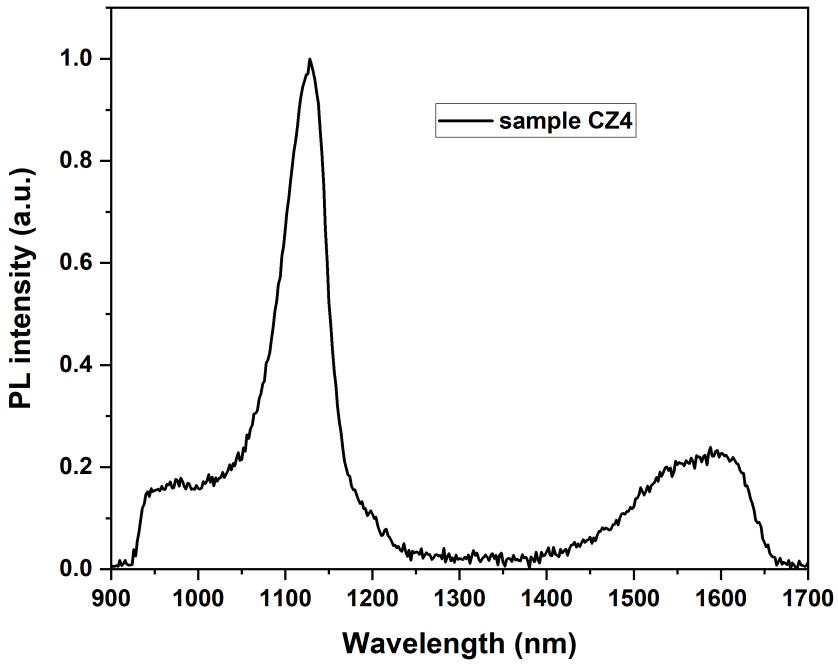

Figure 4.14: Photoluminescence spectra at 77 K for sample CZ4 annealed at 850 °C for 30 minutes.

4.3.3 Effect of Er:O implantation ratio on photoluminescence

Figure 4.15 presents the PL spectra of three samples with various Er:O concentrations taken at 77 K. Sample preparation and processing details are listed in table 4.3. Due to being less intense, these sample spectra were obtained with a 2.7 nm resolution.

Sample name	Er conc/tion (cm^{-3})	O conc/tion (cm^{-3})	Long anneal 650°C	RA temperature (°C)	RA duration (s)
C1	1×10^{18}	1×10^{19}	YES	850	30 s
C2	1×10^{18}	5×10^{19}	YES	850	30 s
C3	1×10^{18}	1×10^{20}	YES	850	30 s

Table 4.3: Implantation and annealing details for the sample series with various Er:O concentration ratio.

For sample C3 silicon band edge luminescence peak at 1121 nm can be discerned. The small peak at 1200 nm matches with the reported emission of a Si phonon replica [134]. Band edge silicon luminescence can also be seen for C2 but is completely absent from C1. This is in agreement with the higher erbium concentration series in section 4.3.2

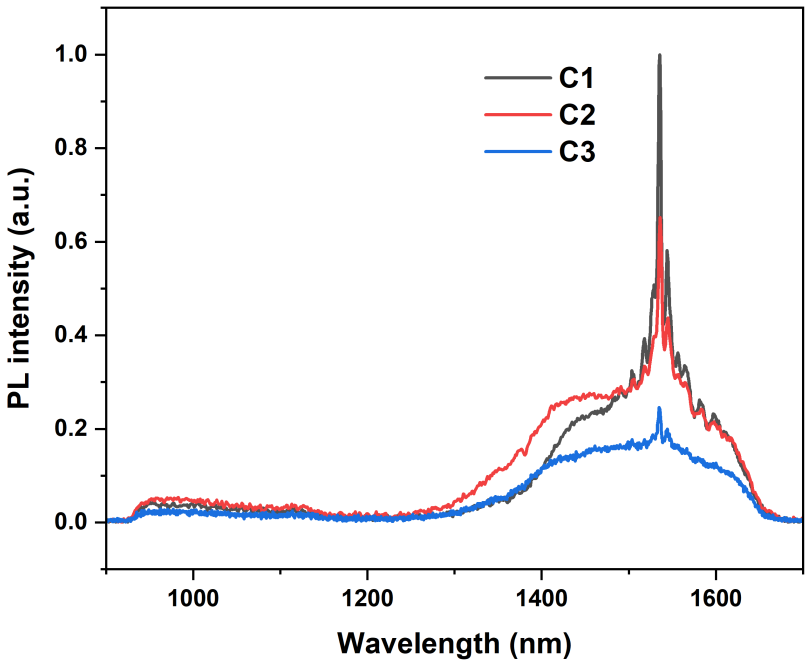

Figure 4.15: PL spectra of samples for various Er:O concentration ratios. All spectra are normalised with respect to background noise values for clarity upon comparing background emission. Measurements were performed at 77 K with a 2.7 nm resolution. Sample details are listed in table 4.3. Briefly, the Er:O ratio is 1:10, 1:50 and 1:100 for C1,C2 and C3 respectively.

and suggests that the Silicon emission is optimally suppressed for 1:10 Er:O concentration irrespective of the erbium dosage. Increased oxygen concentration appears to notably quench the relative erbium luminescence compared to the pronounced broad background emission. Since all samples have undergone the same post-implantation annealing process, the possibility this difference is a result of variation in damage induced amorphisation is low. It is proposed that this erbium luminescence quenching arises from lowering the percentage of optically active erbium centres. The role of oxygen in the erbium PL is well-accepted, however there is no unanimous preferential Er:O concentration ratio with previous work reporting ratios in the range of 1-10 [135]–[139]. This has yet to change with more recent reports indicating an optimum O:Er concentration ratio of 1 [140] and 2.5 [141]. It appears that this ratio is sample preparation and host matrix dependant, necessitating investigation for each sample batch. For the samples in this work, maximum erbium luminescence is achieved at 1:10 Er:O concentration ratio, above which there is oxygen saturation. The unpaired oxygen atoms could provide efficient non-radiative recombination routes through formation of precipitates and defects

[137].

A higher resolution scan across the region of erbium emission is shown in fig. 4.16 and suggests that despite the differences in broad feature characteristics, the erbium centres formed appear to be mostly shared. Sample C1 (Er:O = 1:10) presents striking similarity

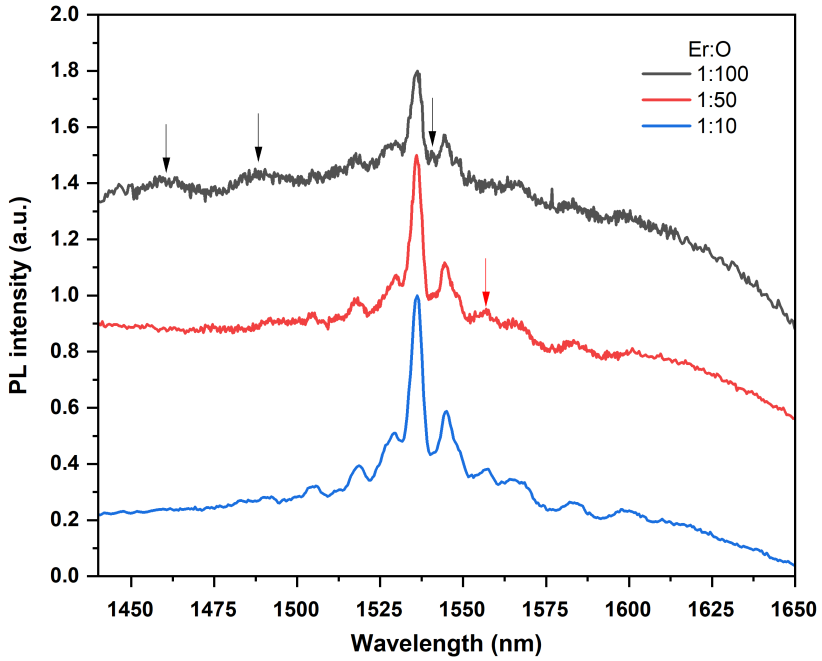

Figure 4.16: Zoomed-in plot of the different Er:O concentration ratio samples. Samples are normalised with respect to their maximum for ease of display. Measurements were taken at 65 K with 1.6 nm resolution. The arrows indicate features that are not shared amongst all samples (see text).

to the C2 (1:50) spectrum. Exception to this could be the seemingly more pronounced 'bump' from the amorphous feature centered at 1430 nm; however it is proposed that this is the same amongst the two samples and only appears different due to an enhanced erbium luminescence from C1. A narrow peak with FWHM$\leq$1 nm is seen at 1540 nm for C1 but could not be resolved for C2 and C3 (1:100). Finally, the 1557 nm transition is common for lower oxygen concentration but does not clearly manifest for C3, although the signal to noise ratio does not allow for clarity in the region. Similarly, a small bump can be seen for C1 at 1640 nm yet is hard to discern elsewhere. Common peaks across all samples (in nm) include 1505, 1518.6, 1529, 1536, 1544, 1548, 1566, 1583, 1600.

Hot line investigation

If some of the above mentioned transitions were hot lines they would follow a characteristic temperature dependence; the PL intensity ratio $I_{\mathrm{HL}}/(I_0 + I_{\mathrm{HL}})$ - where I_0 and I_{HL} are the respective main and satellite line intensities - is expected to increase at higher temperature with an activation energy equal to the energy distance between the two emission lines. Figure 4.17 shows temperature dependent spectra for the intra-4f transitions region.

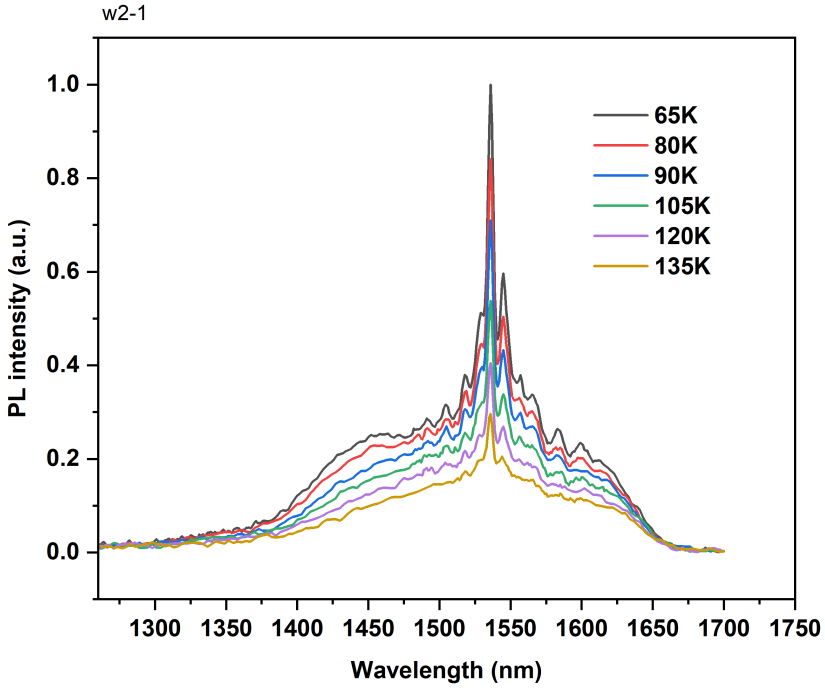

Figure 4.17: Temperature dependence for a selected region for sample C1 with 1:10 Er:O concentration ratio and two-step annealing with T_{RA}=850 °C for 30 sec. Data were normalised to the maximum at 65 K.

Pairs of emission lines from fig. 4.17 were selected based on their observed energy splitting and their temperature dependence was plotted. The results are presented in fig. 4.18. The first pair (a) originates from a state lying ≈ 30 cm^{-1} above the lowest excited state. Possible positions of additional transitions with shared energy splitting are shown in fig. 4.19. This splitting matches the reported shift of 28.8 cm^{-1} in [82] for the Er-01 centre. However out of the remaining suggested transitions from the same centre, only one more with predicted splitting 34.7 cm^{-1} at ≈1544 nm is seen in fig. 4.19 with a third at 1564 nm deviating by 8.2 cm^{-1} from the reported by them 1566 nm emission.

The same group attributes two further satellite line shifted by 74.5 cm^{-1} and 109

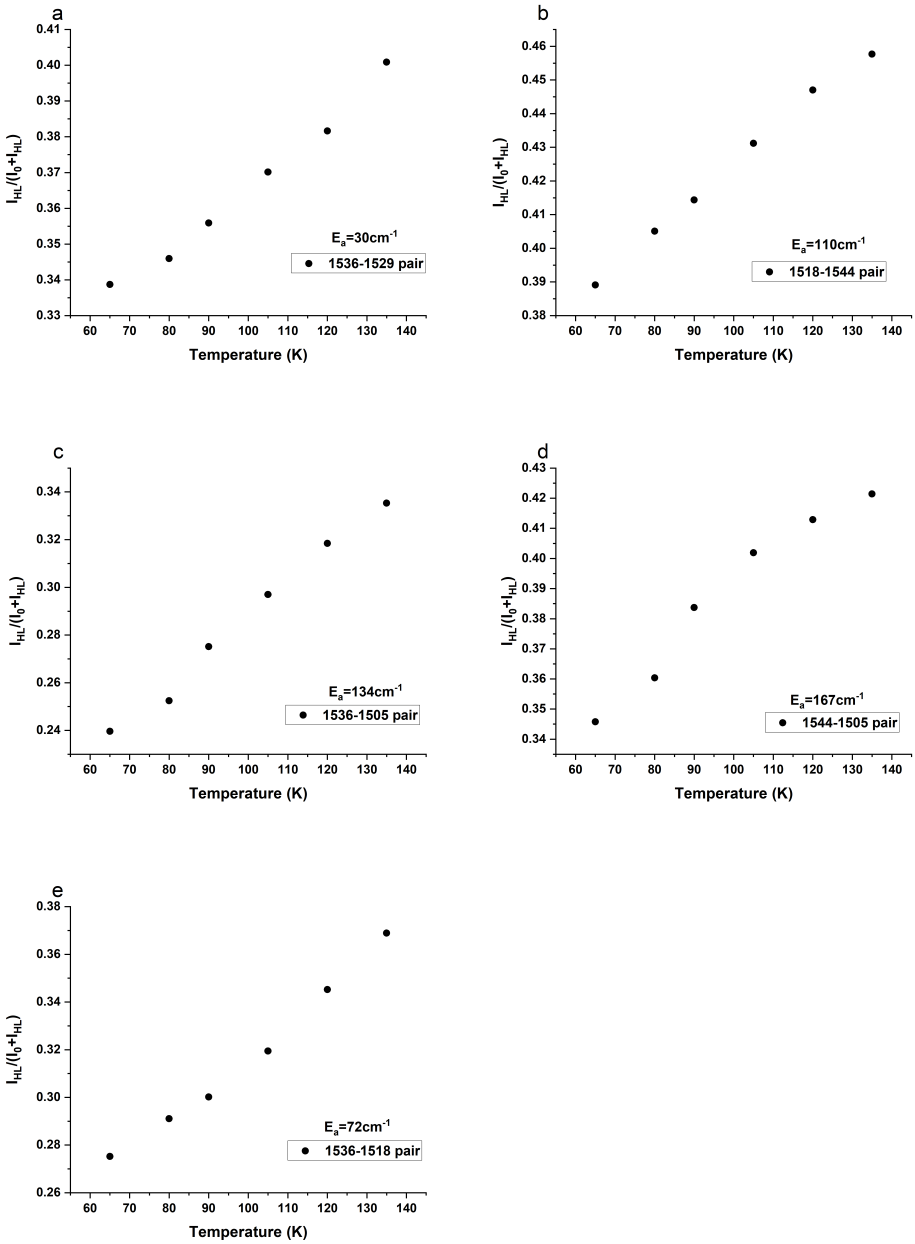

Figure 4.18: Temperature dependence ratios of the selected pairs of primary and respective hot line emissions for sample C1. Bottom right values in each graph indicate each pair and their affiliated energy splitting.

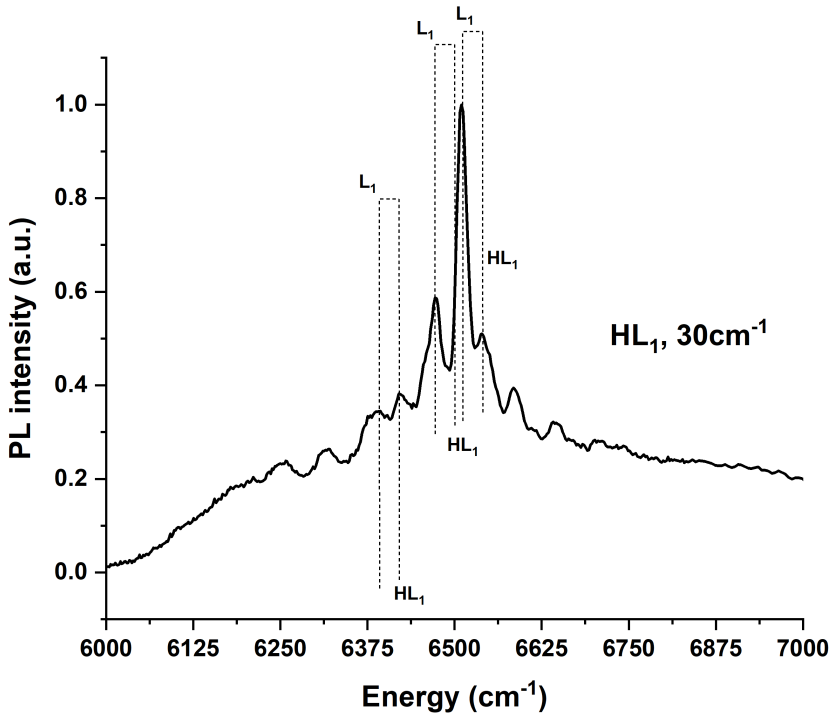

Figure 4.19: Possible primary transitions and hot lines for HL_1 pair from fig. 4.18(a).

cm^{-1} to the cubic centre transitions [82]. This scenario is depicted on pairs (b) and (e) in fig. 4.18. Possible peaks following this predicted splitting are shown in fig. 4.20.

For the case of (e), section 3.2.2 has indicated the improbability of observing the central 1536 nm emission from a cubic centre for x≈0.35, as was selected in the [82] study. As a result, hot line assignment of the 1536 nm - 1519 nm pair based of satisfying temperature ratio might be erroneous. Moreover, for that value of x the predicted splitting of the 13/2 manifold does not match their assigned energy diagram. Since the remaining hot lines overlap with primary emissions, it is difficult to confirm the intensity relationship and therefore we propose this 73 cm^{-1} level should be discounted. It is more plausible for the 1518 nm peak to be a hot line of the 1544 nm emission, such that scenario (b) holds true. This case would cover the (1538-1512) nm pair as well, yet this remains to be confirmed due to lack of spectral resolution. Similarly, the (1599-1567) nm intensity ratio is erratic.

Moving on to fig. 4.18(c), (d) there exist two possible ways of accounting for the 1505 nm emission as a hot line either originating from a level shifted by 134 cm^{-1} or another level shifted by 167 cm^{-1}. Here it is tentatively assigned as a hot line of the 1536 nm.

Lastly, another explanation for some of the peaks involves phonon replica lines arising from simultaneous emission of one or more phonons alongside an optical transition (here,

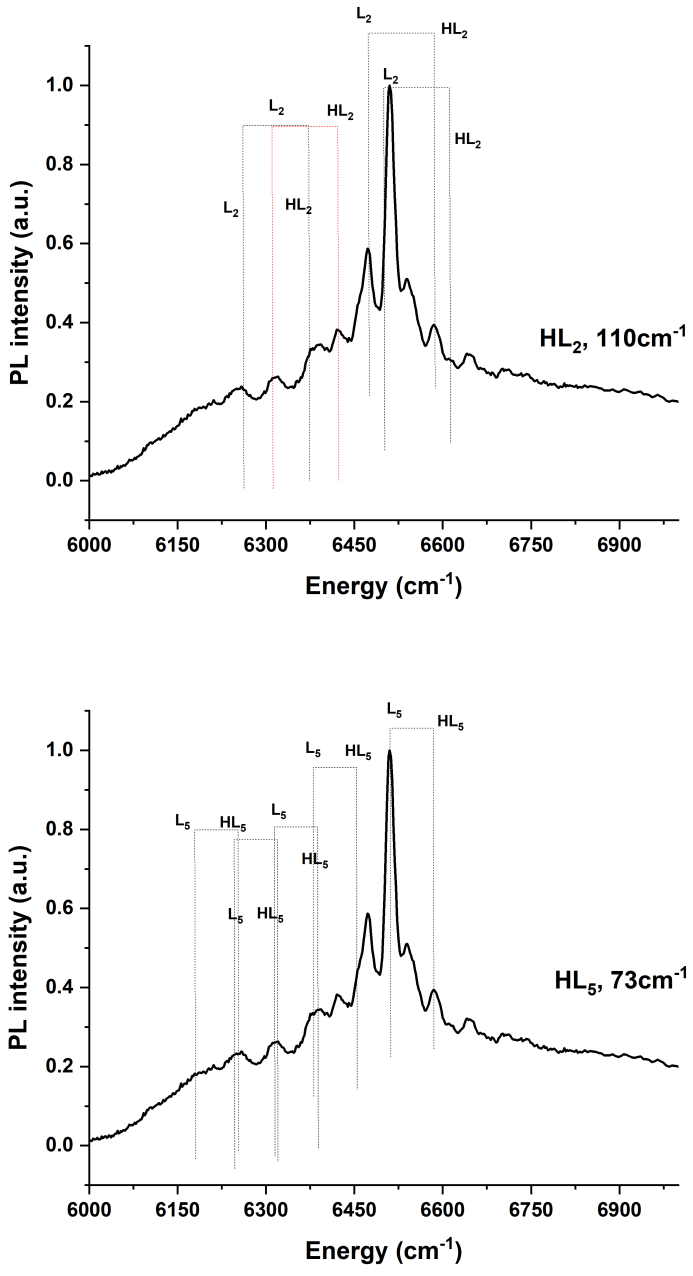

Figure 4.20: Possible transitions matching the splitting from fig. 4.18 (b) and (e). The red dot denotes constant pair ratio.

the 1536 nm emission) leading to less energy being available for the photon. The reverse process is referred to as anti-Stokes lines, where the phonon is absorbed the photon shifts higher in energy. Previously, the 1518 nm emission was ascribed as an anti-Stokes line, with 1555 nm being a phonon replica of the ≈1536 nm transition [104]. This was disputed by [82], who argued that if a local phonon was involved all crystal field states would interact with it having equal coupling strength. Further very low temperature investigation would be required to provide clearer answers. Next, section 4.3.4 investigates the effect of post-implantation annealing treatment for samples sharing erbium and oxygen doping details.

4.3.4 Effect of post-implantation annealing

The samples in this section (labelled B series in table 4.1) underwent a two step-annealing process, including a longer primary anneal as well as rapid anneal treatment. Sample details are shown in table 4.4:

Sample name	Er conc/tion (cm^{-3})	O conc/tion (cm^{-3})	Long anneal	RA temperature (°C)	RA duration (s)
B0	1×10^{19}	1×10^{20}	YES	NO	n/a
B1	1×10^{19}	1×10^{20}	YES	750	30 s
B2	1×10^{19}	5×10^{20}	YES	800	30 s
B3a	1×10^{19}	1×10^{20}	YES	850	30 s
B4a	1×10^{19}	1×10^{20}	YES	900	30 s
B5a	1×10^{19}	1×10^{20}	YES	950	30 s
B3b	1×10^{19}	1×10^{20}	YES	850	50 s
B4b	1×10^{19}	1×10^{20}	YES	900	50 s
B5b	1×10^{19}	1×10^{20}	YES	950	50 s
B4c	1×10^{19}	1×10^{20}	YES	900	20 s
B5c	1×10^{19}	1×10^{20}	YES	950	20 s

Table 4.4: Implantation and annealing details for the 1×10^{19} Er and 1×10^{20} O (cm^{-3}) concentration series treated under various annealing conditions.

The samples have been grouped for different RA temperature and duration, with B0 not following a rapid anneal step. All spectra presented were taken at LN temperatures (65-77 K), with similar excitation densities unless otherwise stated.

Effect of rapid annealing temperature

Figure 4.21 presents the PL spectra for B series samples rapidly annealed for 30 seconds under various temperatures. Spectra were normalised to each set's maximum for clarity. For sample B0 lacking RA treatment we see the base annealing recipe is sufficient for the

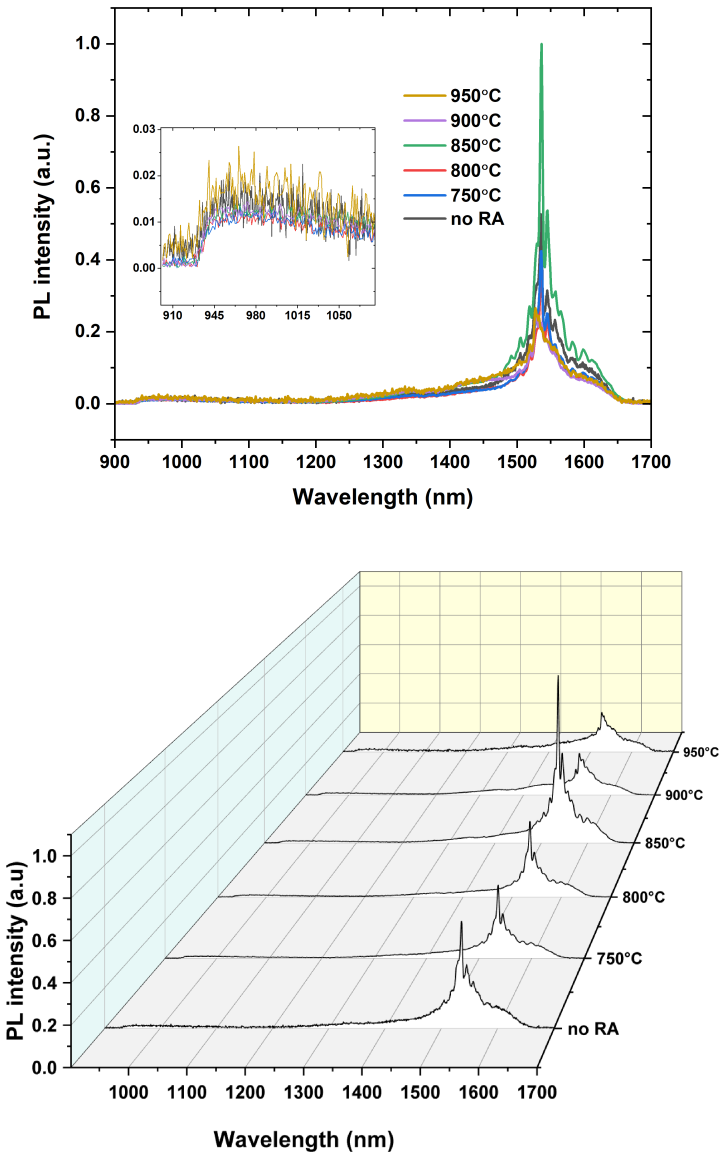

Figure 4.21: Line (top) and waterfall (bottom) plots of the PL spectra taken at 65 K for the B sample series. Spectra are normalised with respect to the sample series' maximum emission.

formation of optically active erbium centres. The broad background feature detected in series A and C examined in section 4.3.2 and section 4.3.3 is also evident here however to a lesser extend. This is to be expected following results in section 4.3.1 since the silicon

matrix in the B series shows much better re-crystallisation compared to the single-anneal only A series. Interestingly, increasing the rapid anneal temperature up to and including 850 °C coincides with enhanced erbium centre luminescence, whilst higher temperatures lead to quenching as shown in fig. 4.22. Near band edge (NBE) silicon luminescence is fully suppressed for all samples, and the feature around 980 nm is only weakly visible. In order to compare the well-defined erbium centres contribution in the overall sample

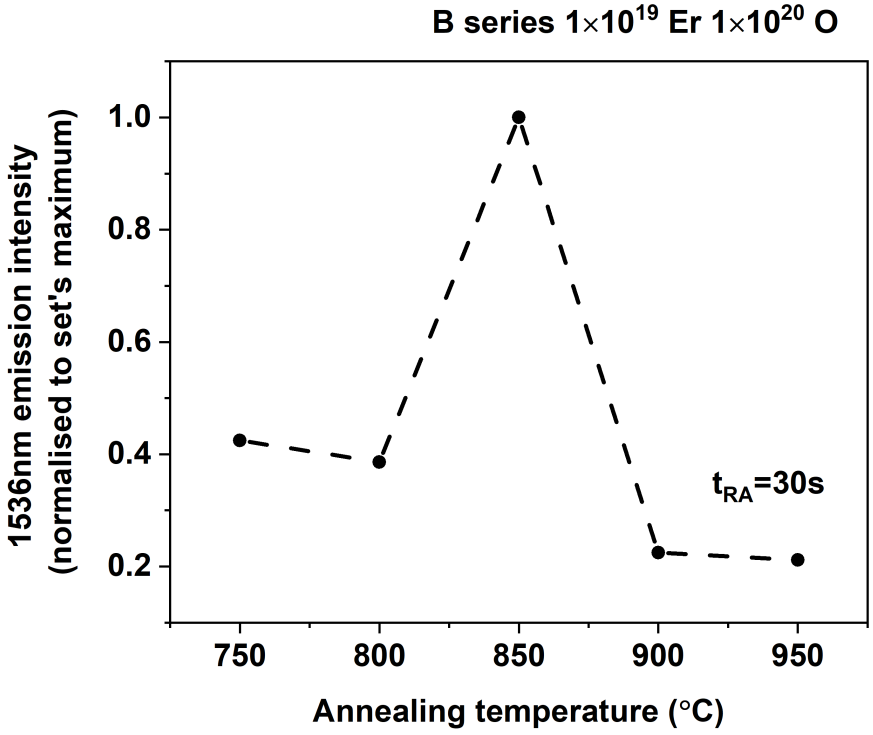

Figure 4.22: 1536 nm emission intensity comparison amongst selected B series samples annealed for 30 s at various temperatures (shown in x axis). Data has been normalised with respect to the set's maximum emission.

luminescence, the broad feature between 1250-1700 nm was assumed to have a Gaussian form centered at 1536 nm. The erbium centre 1536 nm emission shown in fig. 4.22 was then obtained by subtracting the manually estimated using cross-hairs intensity value of the broad feature's centre from the total emission intensity at that wavelength. Further, percentage values with respect to maximum emission intensity for the broad feature's centre as well as the 980 nm feature were obtained. Figure 4.23 shows a matching trend for the 980 nm and the broad feature's intensity ratios as a function of rapid anneal temperature.

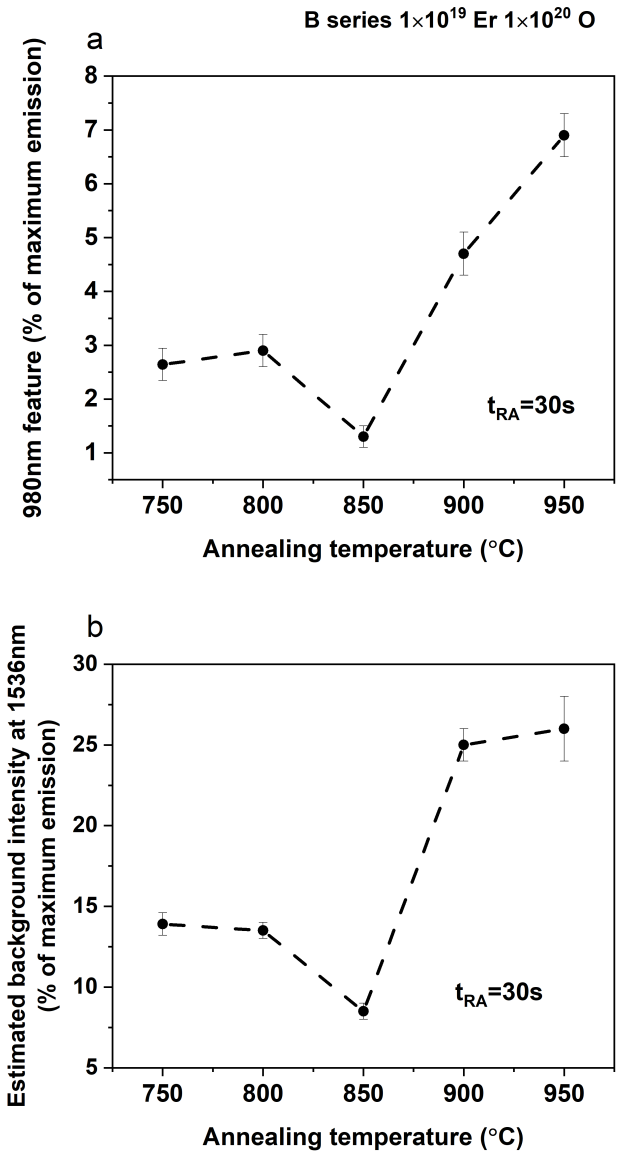

Figure 4.23: Percentage ratio of emission from the 980 nm feature (a) and the 1536 nm centre (b) of the estimated broad 'background' feature with respect to maximum sample emission.

Further examination of fig. 4.21 suggests an inverse trend in annealing temperature dependence between the total (integrated amongst all wavelengths) PL intensity and the 1536 nm erbium centre intensity. It is clear that for $T_{RA} \leq 850$ °C the PL is primarily a result of the 1536 nm erbium centre's luminescence; this ratio abruptly decreases for higher anneal temperatures. Moreover, by comparing fig. 4.23(b), fig. 4.24 and fig. 4.22 one can see that the estimated amorphous erbium in silicon emission is within the same range for 750 °C & 800 °C anneal yet rapidly drops at $T_{RA} \leq 850$ °C in contrast to total PL and 1536 nm intensities which double. Therefore 850 °C is the optimal temperature

in optimising erbium PL yield. The non-rapidly annealed sample (not pictured) follows the same behaviour as T_{RA}=750 °C in all cases.

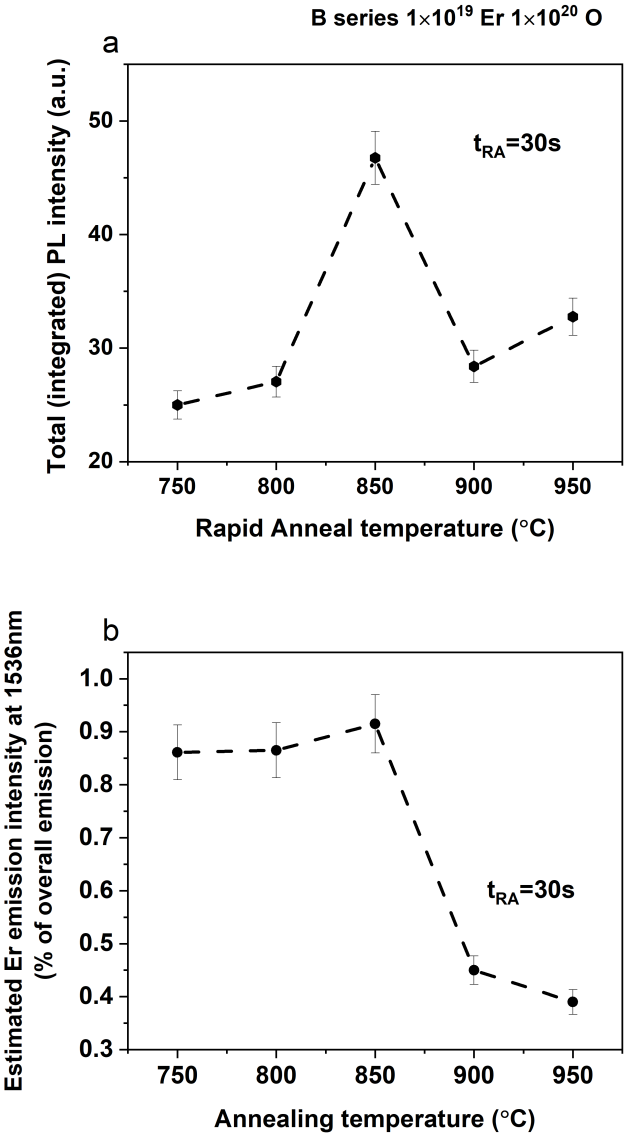

Figure 4.24: Photoluminescence yield comparison for B sample series rapidly annealed at various temperatures.

Previous investigations on annealing temperature dependence for similar Er:Si implantation details had proposed an optimal T_{RA}=900 °C for 30 s [136], whilst others found highest PL yields were produced for T_{RA}=950 °C [142]. Recent work in Er-Si-O films found an optimum T_{RA}=1100 °C and ascribed the decrease in luminescence to the dissociation of Er-O radiative centres [143]. To examine how this hypothesis fits our observations, albeit for a different optimal temperature, high resolution spectroscopy was

performed (see section 4.3.4 below).

Spectral evolution

Photoluminescence was collected at liquid nitrogen temperatures using the setup described in section 4.2 for a 0.2 mm monochromator slit width corresponding to a 1 nm resolution. The resulting spectra are presented in fig. 4.25.

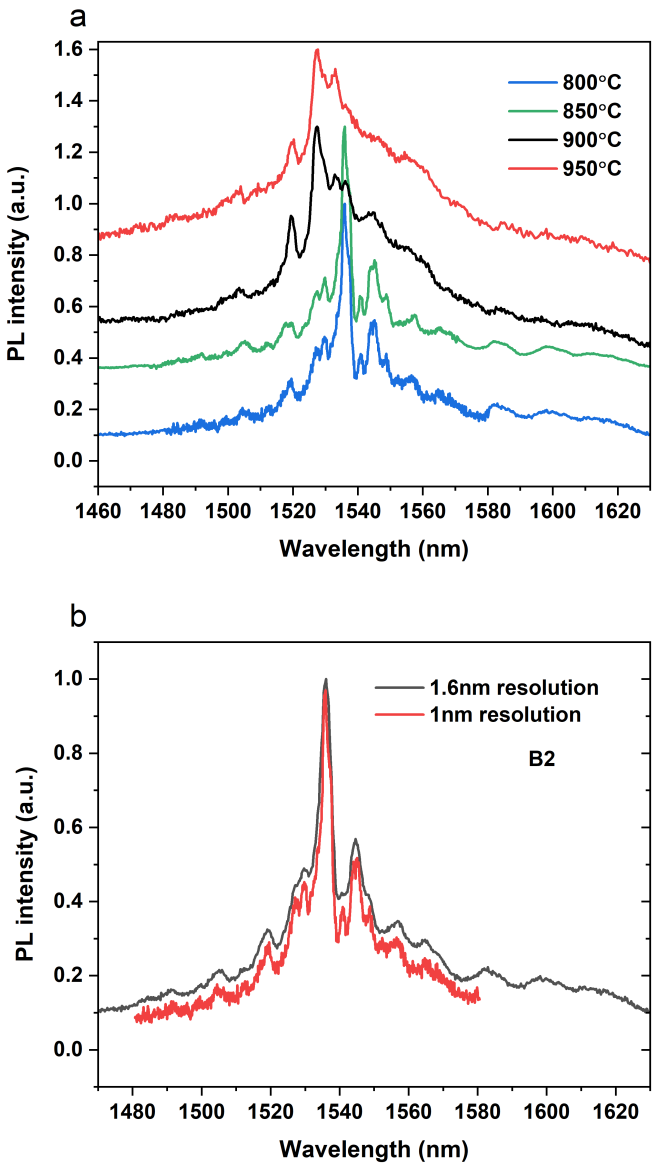

Figure 4.25: Comparative high resolution spectra for selected B series samples (a). In (b), a 1.67 nm resolution versus a sub-1 nm resolution spectrum for B2. Sample details are listed in table 4.4.

The need for such high resolution is shown with a comparative 1.67 nm resolution

spectrum in fig. 4.25(b); it is clear that many peaks have sub-1 nm linewidths and thus spectral characteristics can be lost at higher slit widths. This narrow peak width also suggests the successful incorporation of Er and O in a good quality single crystal. Notably, samples annealed at 800 °C and 850 °C present nearly identical spectra; there is a multitude of narrow peaks located around a central transition of approximately 5 nm linewidth, incorporating the main 1536 nm peak as well as a 1533 nm and ≈1538 nm emissions. At 900 °C, the main 1536 nm peak rapidly diminishes in intensity with neighbouring lower energy peaks broadening significantly or disappearing alltogether (i.e. 1538 nm emission). Any further RA temperature increase leads to merging of remaining peak characteristics and disappearance of features above 1580 nm. Curiously, at higher rapid anneal temperature the primary 1536 nm emission is absent, and the 1527.4 nm emission with intensity ratio 1/3 compared to the 1536 nm transition at lower annealing temperatures becomes dominant. Additionally, the peak centres that are shared between this B sample series appear at slightly lower wavelength (≈0.7 nm lower but with equal energy splitting amongst them) for the samples annealed at higher temperature (≥900 °C). This deviation amongst samples is not unusual as previously mentioned in section 3.2.2 (see i.e. [104]). In addition, the centre difference is within the uncertainty of the performed measurements (1 nm resolution spectra taken at 0.2 nm steps at 2 sec per step dwelling time). Finally, it could be that following higher annealing temperature there is an energy level shift (stretching or compressing) within silicon slightly affecting the crystal field interaction with erbium.

The results of fig. 4.25 are indicative of annealing temperature dependent erbium centre formation. One explanation could be due to the solubility limit of Er in Si. Generally, the solubility increases with temperature however in the case of Er:Si there is a solubility limit of $\approx 10^{18}$ cm^{-3} at 900 °C [144], [145]. Above 900 °C, an abundance of oxygen leads to the creation of Er-O clusters and loss of crystallinity due to erbium atom segregation. Segregation can be accelerated through the generation of ErSi platelets [146]. Moreover, at higher annealing temperatures there is the possibility of back-diffusion of some erbium atoms towards the silicon surface as the a-Si/c-Si interface changes.

Effect of rapid annealing time

Figure 4.26 displays lower resolution spectra for samples rapidly annealed under the same temperature but for different time duration. Due to the 20 sec and 50 sec annealed sample spectra being obtained prior to setup optimisation, lower resolution (≈2.4 nm) spectra from the 30 sec RA sample line were used.

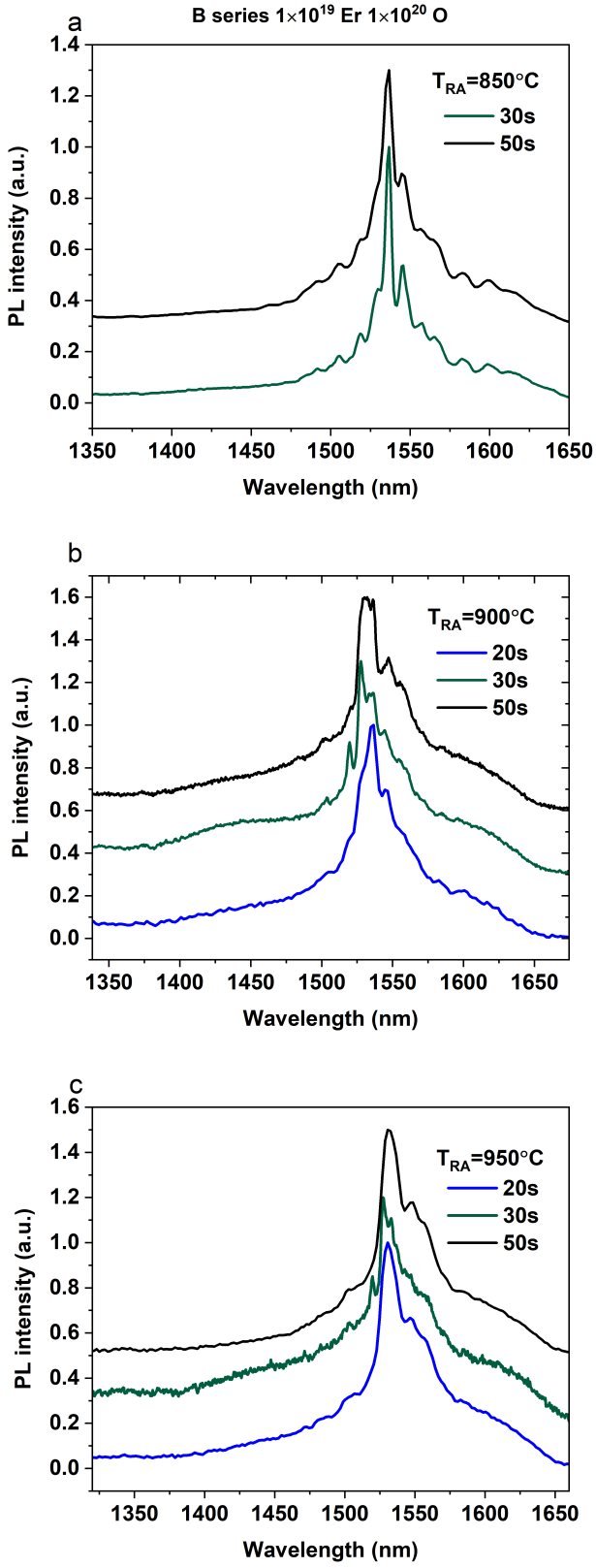

Figure 4.26: Comparative spectra for some B series samples sharing rapid anneal temperature but varying the anneal duration. Sample details can be found in table 4.4.

For samples annealed at 850 °C there are no notable differences in the number, location, and/or intensity ratio of observed transitions. The slightly broader emissions could be from the resolution discrepancy. Similarly, samples annealed at 950 °C have mostly shared characteristics with the exception of the broad background feature at 1350-1500 nm which seems amplified for the 30 sec anneal. At that temperature there is no variation of the 1536 nm peak intensity which is absent in all spectra. It is possible that this high of an annealing temperature does not favour the formation of the 1536 nm centre or, in the case of 1536 nm belonging both in a cubic and axial symmetry sites, it might imply a change in local environment prohibiting the observation of this transition. Comparably, the 900 °C anneal leads to a variation in intensity ratio between peaks, yet the 1536 nm emission is dominant for this temperature. The following section 4.4 investigates the temperature dependence of the PL of Er:Si in order to obtain information on erbium de-excitation dynamics.

4.4 Temperature dependence of photoluminescence

As discussed in section 2.6, doping silicon with erbium to increase the luminescence with the aim of developing efficient silicon-based light emitting materials has been considered as one of the most attractive approaches. Nonetheless, strong PL thermal quenching results in extremely low efficiency at room temperature (RT). Recently, processing methods such as deep cooling treatment of Er/O co-doped c-Si have been found to decrease the effect of thermal quenching by two orders of magnitude [141]. It is thought that this deep cooling process aids in avoiding erbium ion precipitation into Er-O-Si nanocrystals, a process that often occurs during standard rapid thermal annealing (RTA). Very recently the same group reported that co-doping fluorine (F) ions with erbium ions further suppresses the thermal quenching effect regardless of thermal annealing recipe [147]. They attributed this result to the fluorine ions passivating the surface states between erbium nanocrystals and Si lattice. Here, temperature dependent PL measurements will be used to determine the effect of processing conditions of Er:Si in the de-excitation dynamics of erbium.

4.4.1 Methodology

Photoluminescence emission spectra were collected for a series of temperatures from 65 K until 300 K. Measurements were performed at 0.5 mm monochromator slit width corresponding to 2.7 nm resolution. This was chosen as a compromise to obtain signal for as wide a temperature range as possible, whilst preserving some spectral characteristics. A side-effect of this decision was the merging of the less resolved peaks and the inaccurate depiction of transition intensities as a result. This point will be further examined in the result analysis.

Measurements were performed from colder to warmer temperatures with the same setup described in section 4.2. Preliminary measurements (not shown) indicated that there was no notable deviation between incremental or decremental temperature scans. The sample chamber was pumped to high vacuum and allowed to reach a stable LN ($\approx$68 K) temperature for 30 min. The liquid nitrogen flow was adjusted to minimise chamber temperature fluctuations. After obtaining the sample spectrum, the temperature was increased and a further waiting time of 6 min was established between measurements. Due to the anomalous temperature dependence in the samples, more of which will be shown in section 4.4.3, smaller temperature intervals were selected for the temperature region of $\approx 175 - 200$ K.

4.4.2 Results

Previously, the existence of a broad background feature (BBF) spanning across ≈1250-1700 nm in all samples was identified, and this feature associated with potential defect states of erbium in amorphous silicon (refer to section 4.3.2). Temperature dependence of this feature should be examined alongside the dependence of better defined centres, since they do not have to follow the same quenching behaviour. To begin with, the effect of Er:O concentration is examined. This choice is due to C1 spectrum presenting strong erbium emission with similar centres to sample B3a with larger erbium concentration but equal Er:O ratio (see relevant PL spectra in figs. 4.15 and 4.16 for sample C1 and figs. 4.21 and 4.25 for sample B3a). However, the higher oxygen concentration C3 sample is dominated by the BFF emission whilst in B3a this is greatly suppressed.

Er:O concentration PL temperature dependence

The temperature dependence spectrum for sample C1 is shown in fig. 4.27.

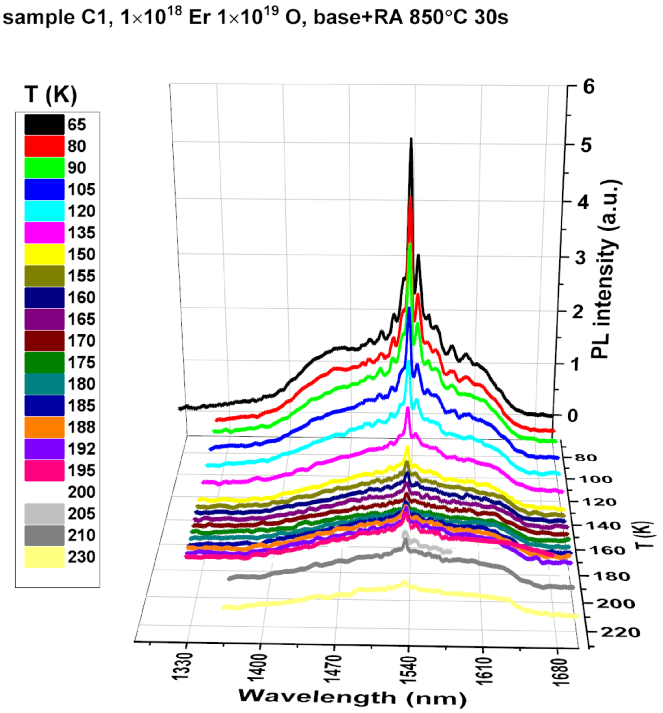

Figure 4.27: Temperature dependence for sample C1.

It is clear that the peak emission centres do not vary with temperature, confirming they originate from defined erbium sites. This is important, since dislocations in silicon can be quite efficient luminescent centres and their wavelength depends on their local

structure and associated strain field [148]–[150]. Silicon has an intense dislocation related luminescent line namely D1 with a broad emission band close to 1550 nm however this rapidly quenches in addition to shifting to longer wavelengths with increasing temperature. In contrast, owing to the $4f$ shielding the Er^{3+} $^4I_{13/2} \rightarrow ^4 I_{15/2}$ transition is insensitive to temperature [3], [151].

Between temperatures of 65 K - 120 K and whilst the narrower emission lines decrease in intensity at a small rate, the pronounced shoulder between 1400 nm-1470 nm appears to thermally quench completely. This feature -which is an addition to the BBF generally seen on all our samples but with different proportions- only appears in selective spectra. Its origin is unclear. Following our previous reasoning, it is possible it belongs to a dislocation or a silicide. Its rapid quenching implies a different de-excitation mechanism, and its overall contribution to the sample's behaviour can be deemed insignificant.

Coming back to this section's initial aim in examining the behaviour of the BBF, the BBF's centre is assigned to be around the 1536 nm region. An emission estimate for each temperature can then be obtained through manual cross hair selection, the results shown in fig. 4.28.

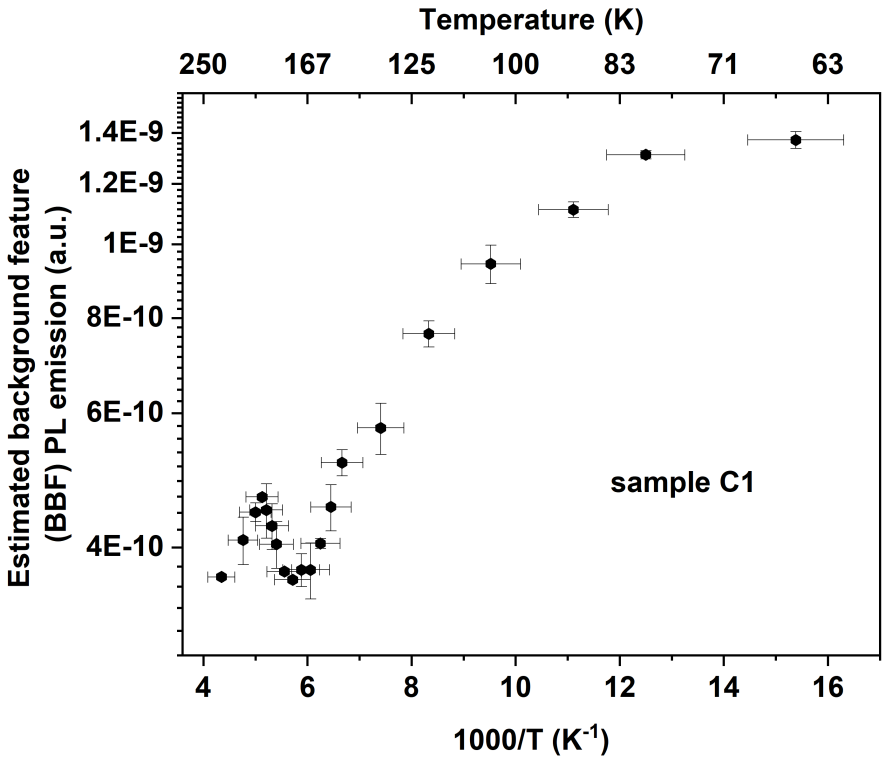

Figure 4.28: Estimated temperature dependence of the BBF for sample C1. Values plotted are the average of 3 estimates. The error bars were calculated as a standard 10% of the estimated value to avoid underestimating the error of the manual peak selection by using just the standard deviation as uncertainty.

Secondly, the maximum 1536 nm emission value is compared to its estimated background subtracted equivalent, shown in fig. 4.29.

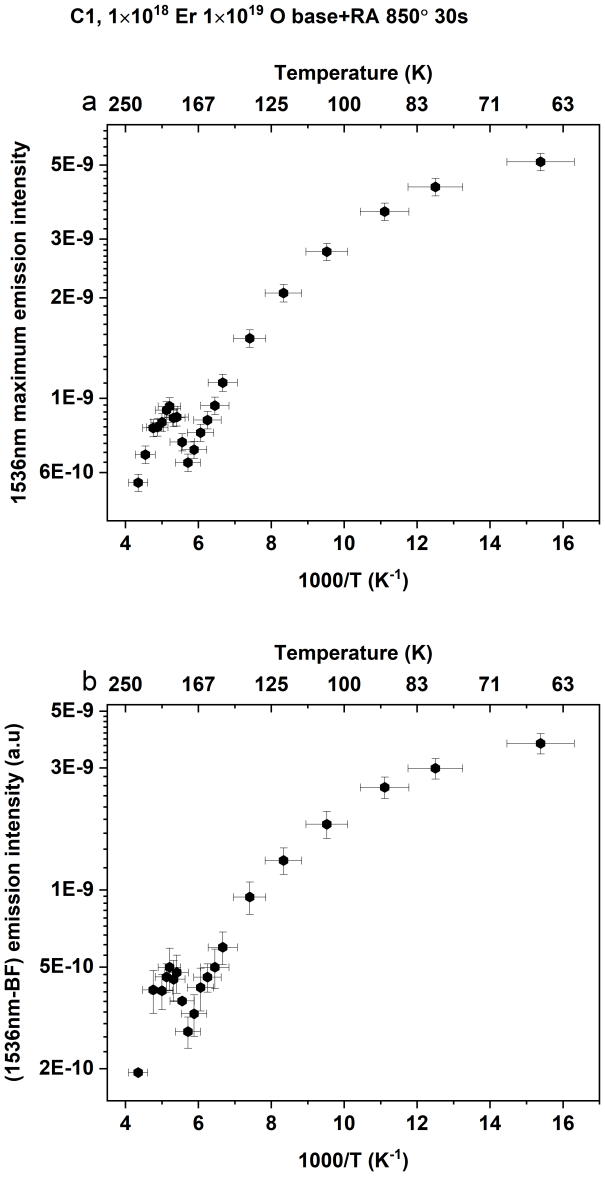

Figure 4.29: Comparison between (a) the maximum 1536 nm peak emission intensity and (b) the same peak's intensity with the fig. 4.28 subtracted for sample C1. Error bars are obtained by adding the fixed 10% uncertainty from fig. 4.28 to the standard deviation of the 1536 nm peak location amongst 3 consecutive spectra.

Since neither of the presented temperature behaviours follows the established Er:Si thermal quenching model of monotonic temperature decrease, and to confirm if this is an isolated incident affiliated with a possible erroneous calculation of the background, sample C3 is examined in a similar manner. Figure 4.30 shows clearly that in this sample

the BBF emission dominates, with the 1536 nm central peak area contributing less than 1% of the remaining BBF area.

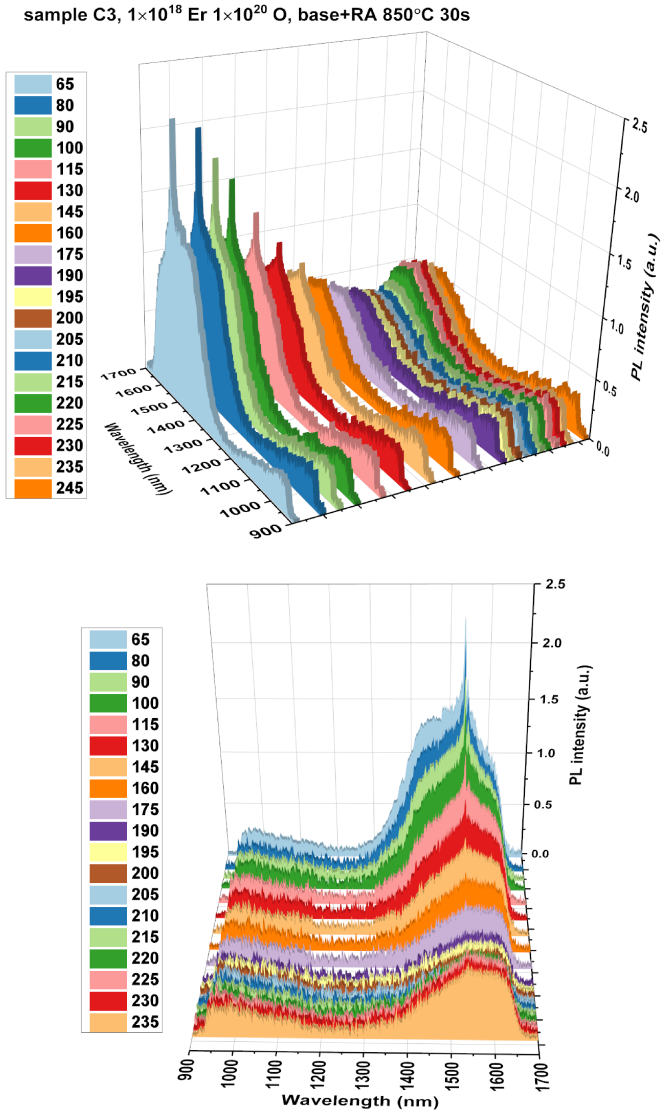

Figure 4.30: 3D plot of sample's C3 emission spectra for various temperatures. The visible noise is due to low signal and high PMT amplification.

For this high oxygen concentration rapid PL quenching is seen, with the erbium centre's emission being undetectable above ≈160 K. It is therefore reasonable to attribute the overall PL behaviour for remaining temperatures in this sample to the BBF. Consequently, the anomalous thermal quenching behaviour seen after 220 K relates to that BBF affirming our earlier observation that both the BBF and the erbium centre adopt similarly deviant from standard behaviour. The observed PL quenching from these samples shall be referred to as negative thermal quenching (NQ), and will be detailed later

in section 4.4.3.

Continuing, for sample C3 complete spectra were taken across 900-1700 nm and so comparison of the main BBF to the 980 nm feature could be made. This is visualised in fig. 4.31. The sample behaviour is notably different, with the 980 nm feature seemingly

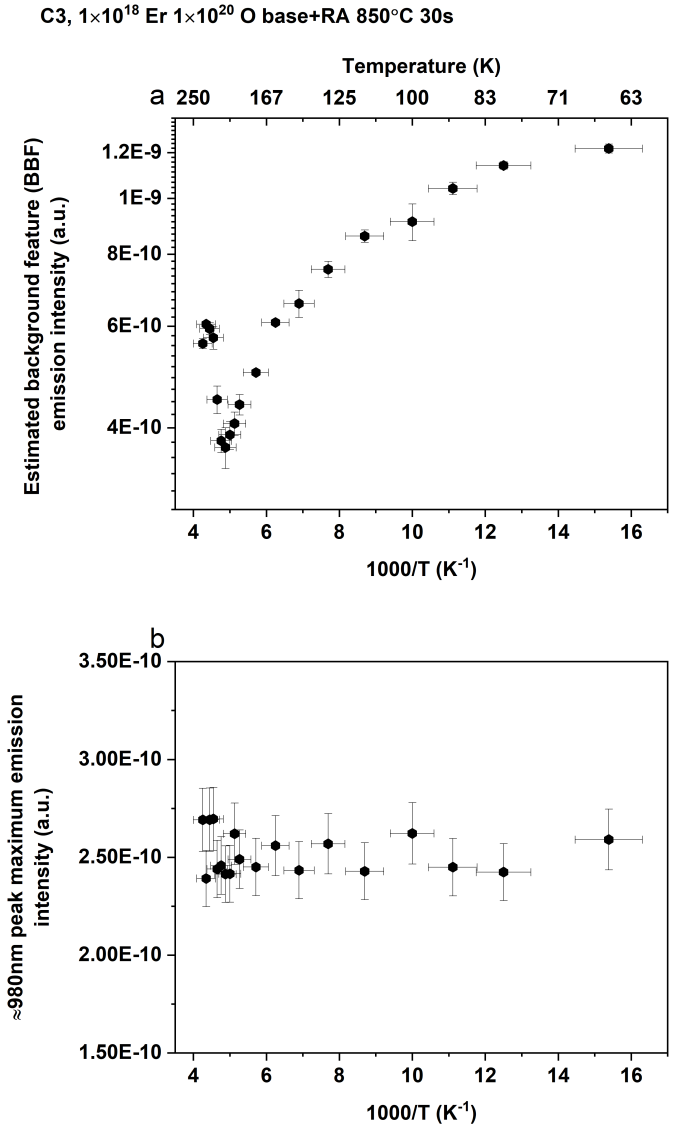

Figure 4.31: Temperature dependence of (a) estimated background feature (BFF) and (b) the 980 nm feature for sample C3.

having a constant value across all temperatures. To further explore these trends, the effect of rapid annealing temperature on the PL temperature dependence is examined.

PL temperature dependence on annealing conditions

Section 4.3 showed that the B series samples favour the formation of optically active erbium centres over the C series. Despite this, the negative quenching behaviour persists for higher optically active erbium samples of the B series. Temperature dependence of the PL intensity of sample B1 is presented in fig. 4.32. The total area (integrated over

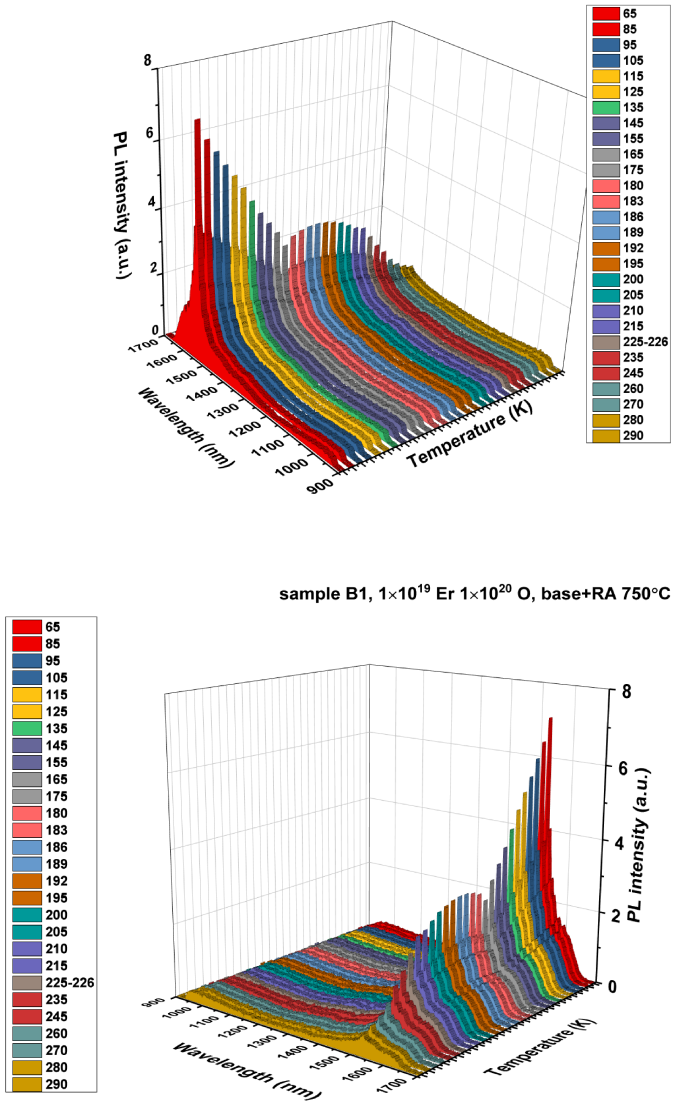

Figure 4.32: Temperature dependence for sample B1. Note the different rate of change between PL decrease and the start of PL increase compared to figs. 4.27 and 4.30. Sample details are shown on the graph and can also be found in table 4.4.

all wavelengths) and the area under the primary peak centered at 1536 nm incorporating transitions between 1533-1540 nm behave similarly, as shown in fig. 4.33(a). In contrast,

the broad emission around 980 nm until 1250 nm does not seem to follow a specific pattern (fig. 4.33(b)). Rather, it remains constant throughout all temperatures, and appears to be minimally increasing at higher temperatures. This agrees with the different Er:O ratio C series PL quenching observations and casts some doubts on the earlier suggestion of assigning both this, and the BBF to the same origin.

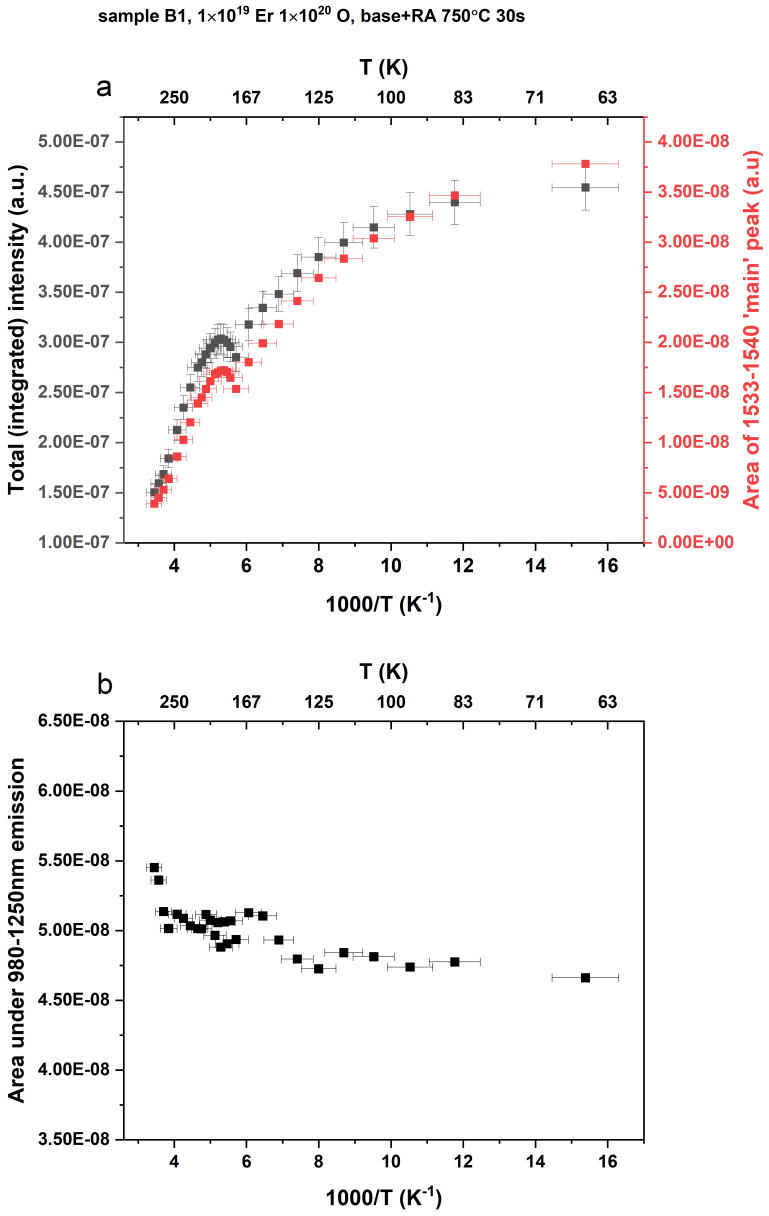

Figure 4.33: (a) Comparison between total area and area of the 'primary' 1533-1540 nm peak for sample B1. In (b), the 980 nm broad feature temperature dependence. The area of the primary emission was obtained by integrating using Gaussian peak fit with FWHM = 7 nm centered at 1536 nm.

There was difficulty in identifying correctly the BBF's emission intensity in this sam-

ple due to the larger erbium centre PL contribution. An earlier (see section 4.4.2) assumption on the similar behaviour of the BBF and total intensity is henceforth adopted, and it is proposed that under this assumption the erbium emissions can be examined without necessarily having to subtract the background. Figure 4.34 shows the uncorrected for background peak centres for various erbium centre transitions. Data have been normalised for each peak set for its equivalent intensity at 65 K. The total (integrated on all wavelengths) emission area is also included for comparison. All transitions follow a negative quenching (NQ) trend and, with the exception of 1529 nm, 1536 nm and 1544 nm, this trend resembles the one by the total emission area. Sample B2 with

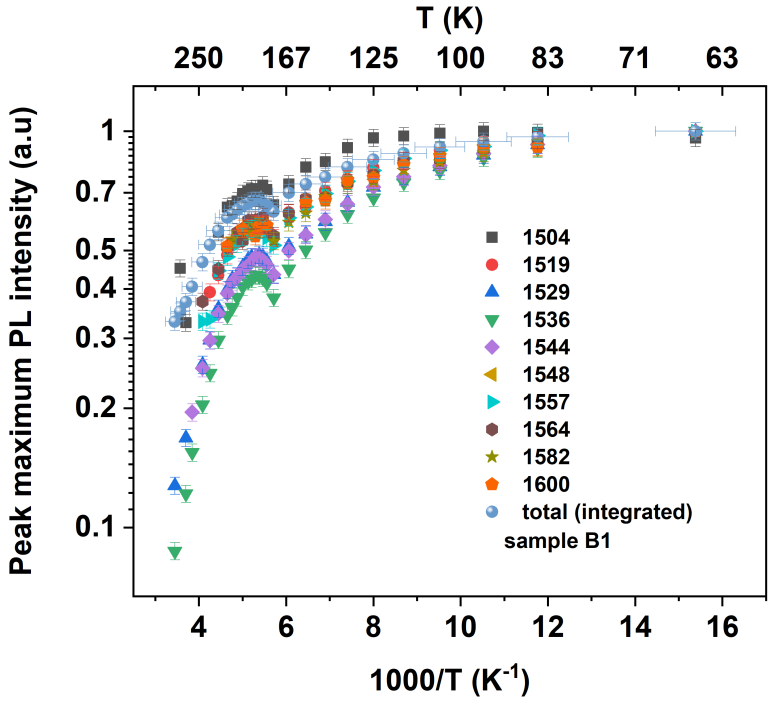

Figure 4.34: Temperature quenching behaviour of selected erbium centre transitions for sample B1. Temperature uncertainties are the same across spectra and are only included for one set for clarity.

T_{RA}=800 °C displays NQ behaviour as well as seen in fig. 4.35.

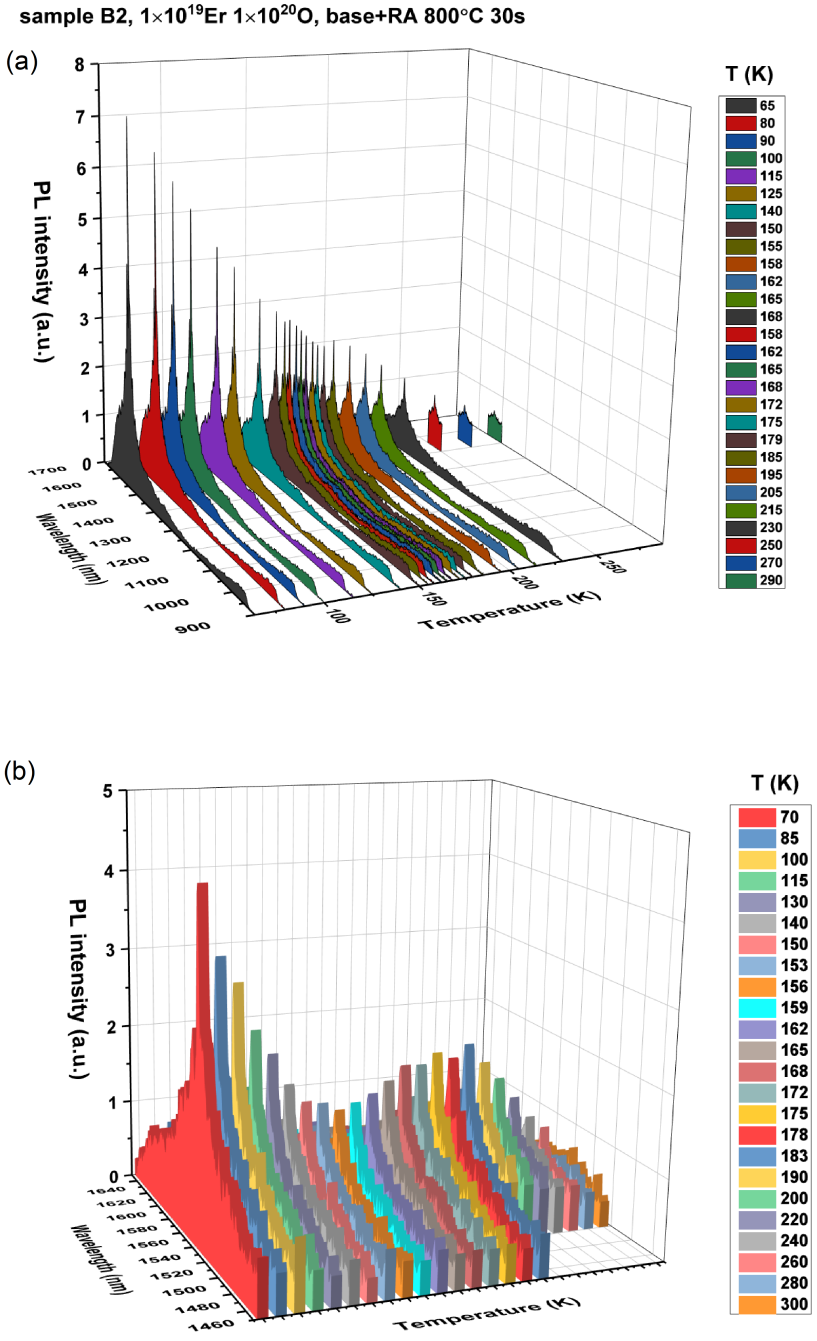

Figure 4.35: Temperature quenching behaviour for sample B2 (a) during a detailed spectra measurement one day and (b) quicker spectra after repositioning the sample.

For this sample the signal to noise ratio was lower and some peaks appeared convoluted at higher temperatures, or quenched faster making their distinction harder. Since comparison amongst samples was done by keeping all experimental parameters constant, instead of decreasing the resolution to obtain higher signal focus was given on the clearly

identifiable peaks across all temperatures. For B2, these are pictured in fig. 4.36.

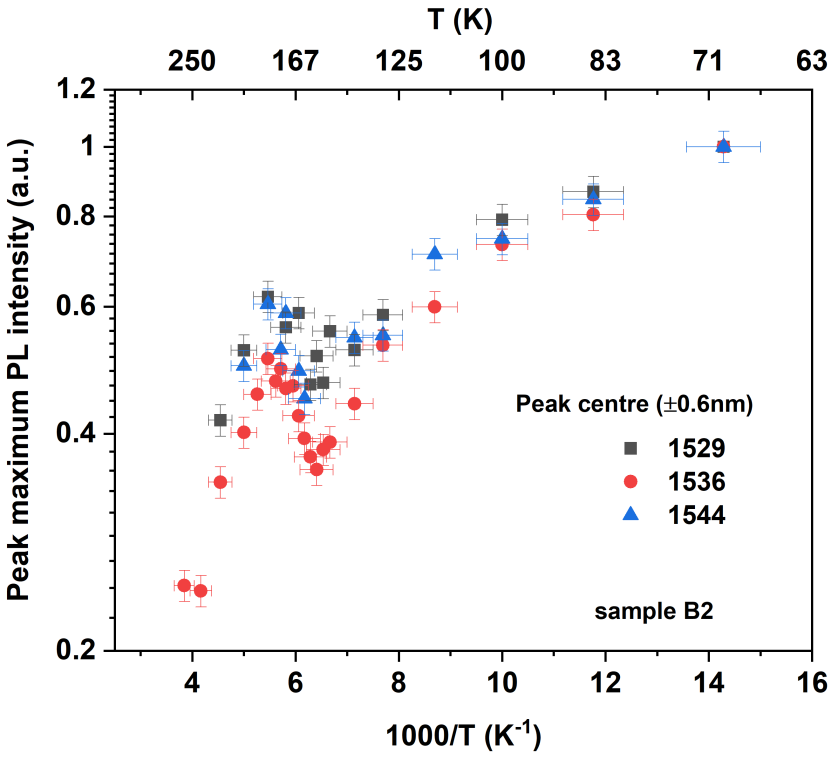

Figure 4.36: Temperature quenching behaviour of the three identifiable peak centres for sample B2.

The NQ trend continues for samples B4a and B5a in figs. 4.37 to 4.39. For these samples however, the 1536 nm emission is buried; for B4a it becomes indistinguishable after 150 K whereas for B5a it is absent alltogether. Instead, a previously integrated to a larger peak area 1533 nm emission is present for all temperatures. This confirms the findings of section 4.3 that there is preferential erbium centre formation for different annealing conditions and that higher annealing temperatures disadvantage the 1536 nm centre.

Notably, the tail (>1600 nm) of the emission at high temperatures (> 200 K) has a different shape than the one seen for C3 in fig. 4.30. In the former, it appeared as if the BBF emission extends further in the infrared and our detector's limit causes an artificial sharp drop at the cut-off limit. For B5a, this does not seem to be the case. Nonetheless, the same B5a sample shows noticeable skewness for low temperatures towards 1700 nm. It is possible that the BBF characteristics are in fact the same, yet for samples with higher erbium PL yield there is a 'transformation' of the BBF feature due to the overlaying erbium emission in a similar manner to the C2 and C3 spectra in section 4.3.3. The observation of atypical thermal quenching raises questions on the

nature of de-excitation of Er:Si in this work's samples. To this end, introduction of the negative thermal quenching model and comparison with our sample behaviour follows in section 4.4.3 and section 4.4.3.

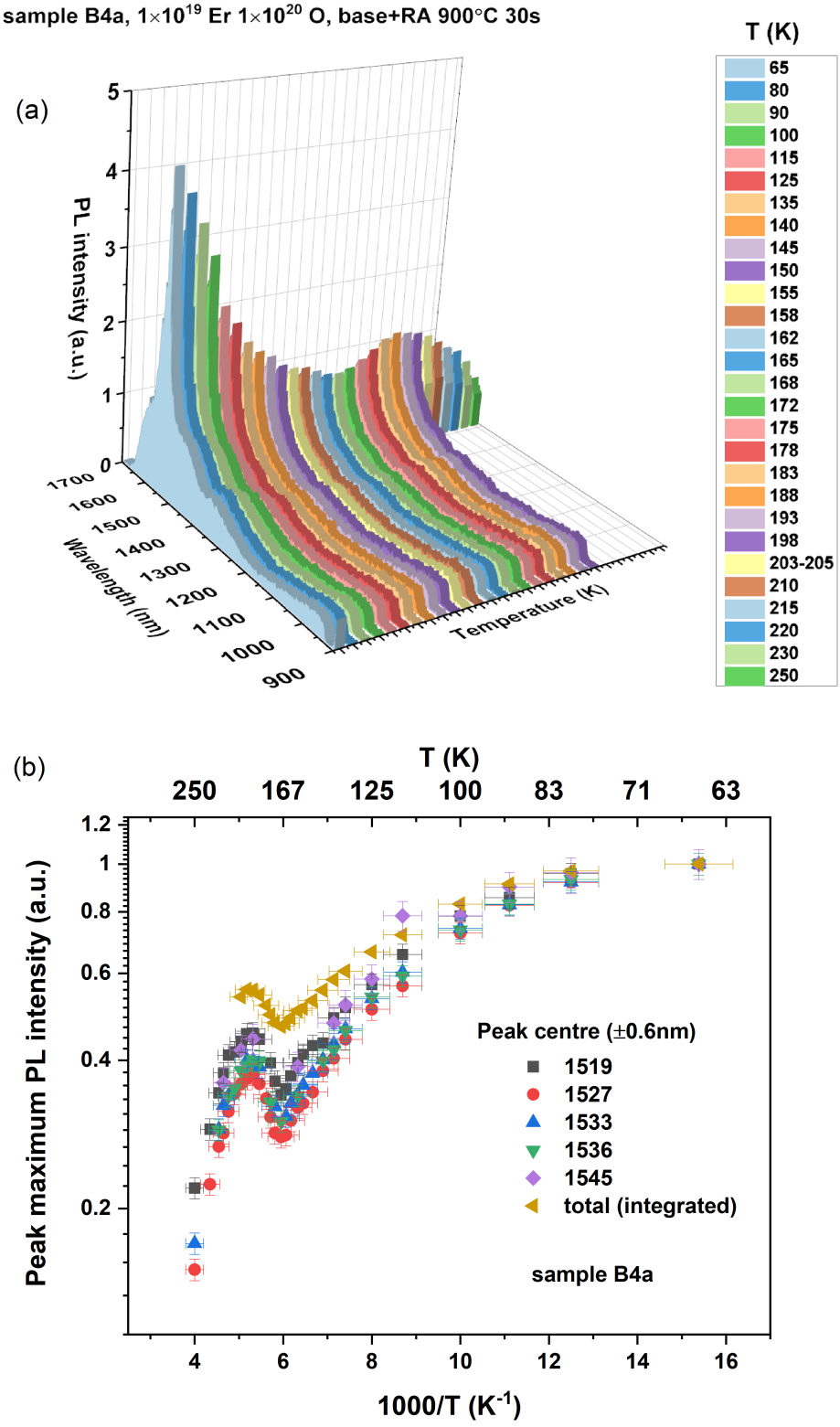

Figure 4.37: 3D depiction of the emission spectrum for sample B4a across different temperatures (a). In (b) selected peaks temperature dependence. One can see that compared to sample B1, both B2 and B4a's luminescence quenches rapidly at ≈ 200 K resulting in lack of room temperature emission.

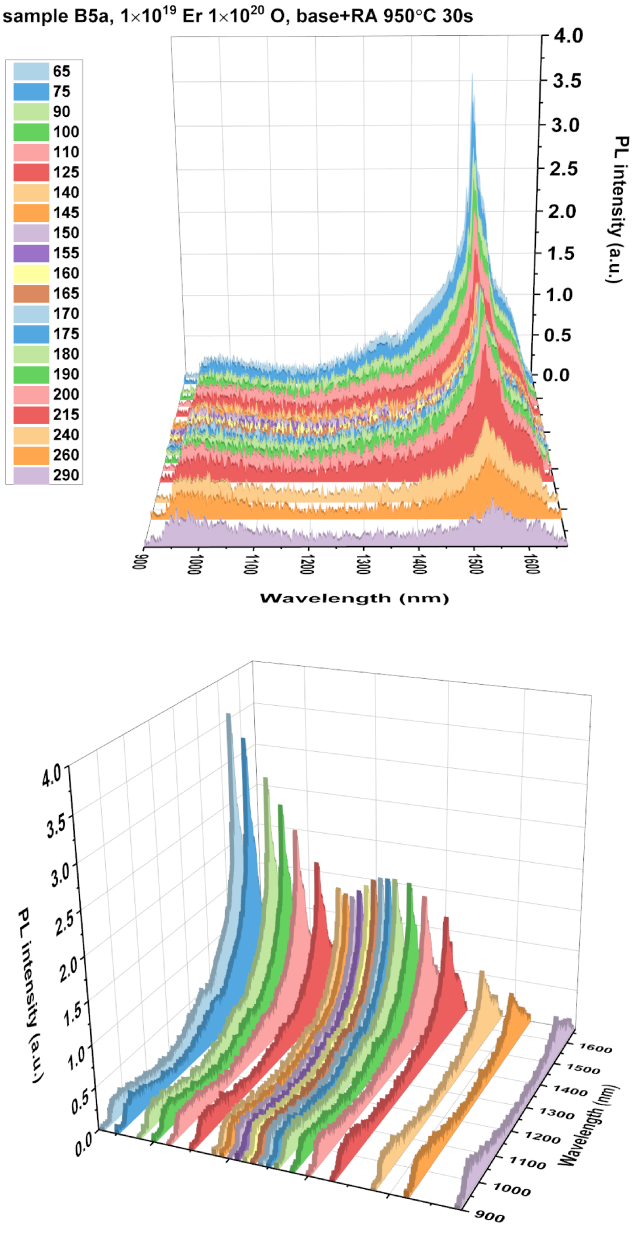

Figure 4.38: Temperature dependant spectra for sample B5a. The spectral noise is due to low signal to noise ratio since this sample had reduced luminescence intensity under the same measurement conditions (see section 4.3.4).

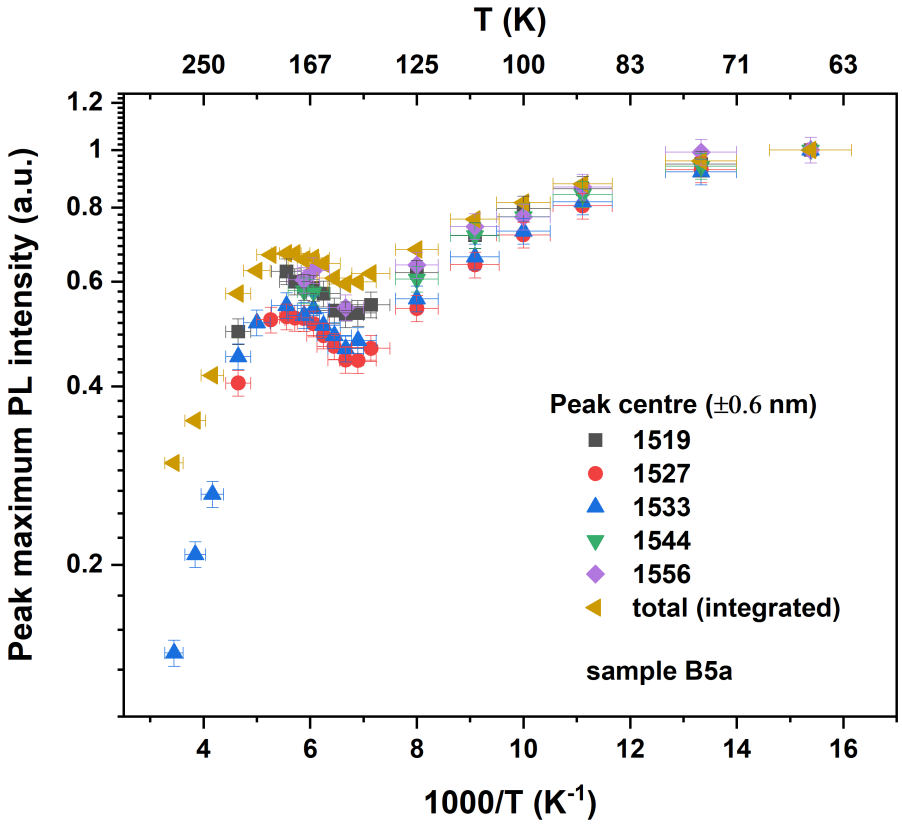

Figure 4.39: Thermal quenching behaviour for selected peaks in sample B5a. Similarly to sample B2, only peaks with well-defined temperature quenching character are selected; i.e. those that are convoluted or with low signal to noise ratio are omitted.

4.4.3 Negative Thermal Quenching

Negative PL Quenching model

The analytical formula for the temperature dependence of the photoluminescence (PL) for samples presenting with negative quenching was derived by Shibata in [152]. In their model they consider a multilevel system between the initial and final states contributing to PL emission. These in-between states are referred to as middle states and are denoted by B_k (where k=1-w). The initial and final states are labelled A and G respectively.

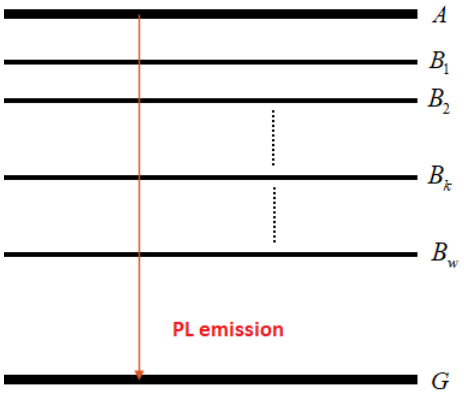

Figure 4.40: Energy level diagram of proposed NQ model. Figure recreated from [152].

The PL intensity is thought to be proportional to the number of electrons and holes in eigenstates A and G namely A(t,T) and G(t,T) respectively. This number is time and temperature dependent. Similar considerations hold for middle state B_k. The time evolution of the function A(t,T) comprises of four components including electron relaxation to A from higher energy levels, contributions from A to other electronic states and contribution by the thermal excitation of electrons to eigenstate A from some of the middle states. If we assume the activation energy E_q to be the energy difference between A and B_q, the negative quenching behaviour is explained as thermalisation of the middle state B_q leading to added contribution of thermal excitation of electrons to eigenstate A. Mathematically, the resulting PL intensity as a function of temperature, I(T), is described by:

$$I(T) = I(0)\frac{\left\{1 + \sum_{q=1}^{w} D_q \exp\{-E_q/k_\beta T\}\right\}}{\left\{1 + \sum_{j=1}^{m} C_j \exp\{-E_j/k_\beta T\}\right\}} \tag{4.4.1}$$

where E_q is the activation energy of the middle state, E_j is the activation energy for the j-th nonradiative transition mechanism contributions, k_β is Boltzman's constant and C_j, D_q some proportionality factors.

Fitted results using NQ model

Our temperature dependent PL was fitted using eq. (4.4.1) for one middle state B_q. Specifically:

$$I(T) = I(0)\frac{\{1 + D_1 \exp\{-E_a/k_\beta T\}\}}{\{1 + C_1 \exp\{-E_{BT}/k_\beta T\} + C_2 \exp\{-E_{AQ}/k_\beta T\}\}} \tag{4.4.2}$$

Here, the nonradiative processes are backtransfer (E_{BT}) and Auger quenching E_{AQ}, as described in section 2.6.4. Fitted curves are presented below, with red lines representing fits to eq. (4.4.2).

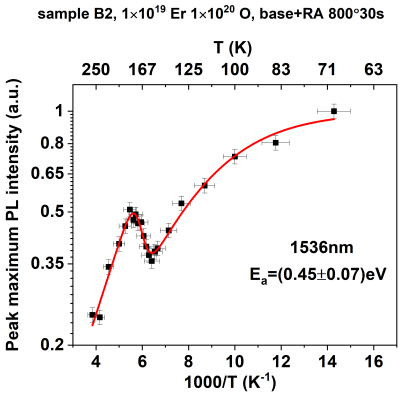

Figure 4.41: NQ fiting model for sample B2.

There is excellent agreement between the model in eq. (4.4.2) and the observed photoluminescence response for all the samples, suggesting that the negative thermal quenching mechanism could be shared between them. In turn, such implies the existence of a middle state B_q with activation energy E_a responsible for the anomalous quenching behaviour. To the best of my knowledge, this state has not been reported for other erbium implanted silicon samples or in fact erbium doped solids, despite PL investigations of samples of similar preparation conditions [56], [85]. The primary difference is the dopant implantation temperature (at 77 K) and the minimal concentration of phosphorus on our samples, leading to higher resistivity. Recent investigations have used intrinsic FZ silicon co-implanted with oxygen and erbium yet have also reported the well-established positive thermal quenching trend [147]. However, their implant chain only went to 200 keV compared to our 4 MeV. It is important at this point to underline the distinction between this middle state, and the otherwise well-accepted intermediate state playing a role in Er:Si excitation process. As discussed in section 2.6.3 the current model of optical excitation relies on the formation of an Er-related donor centre. Excitation of the erbium core is achieved through an Auger process where an electron-hole pair recombines nonradiatively at the donor state resulting in energy transfer to the Er $4f$ shell. Existence

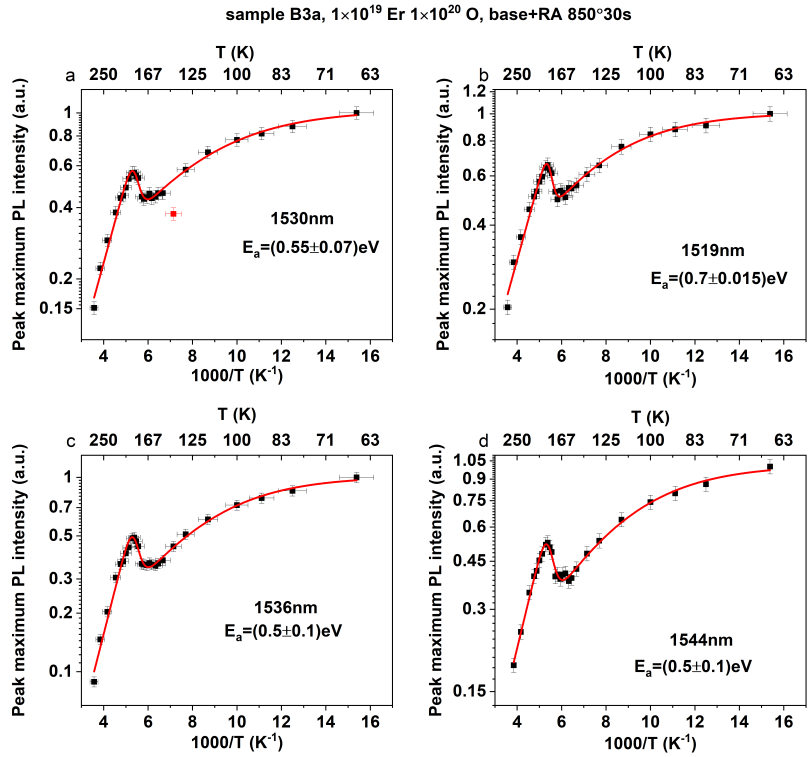

Figure 4.42: NQ fitting model for selected peaks of sample B3a. The singular red point on (a) was excluded from calculation.

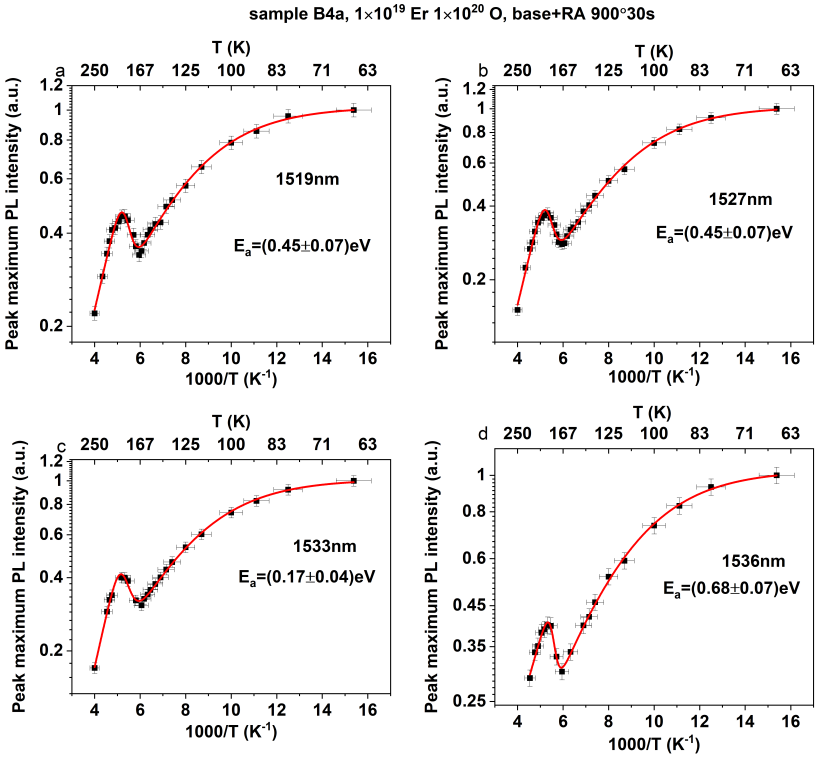

Figure 4.43: NQ fitting model for selected peaks of sample B4a.

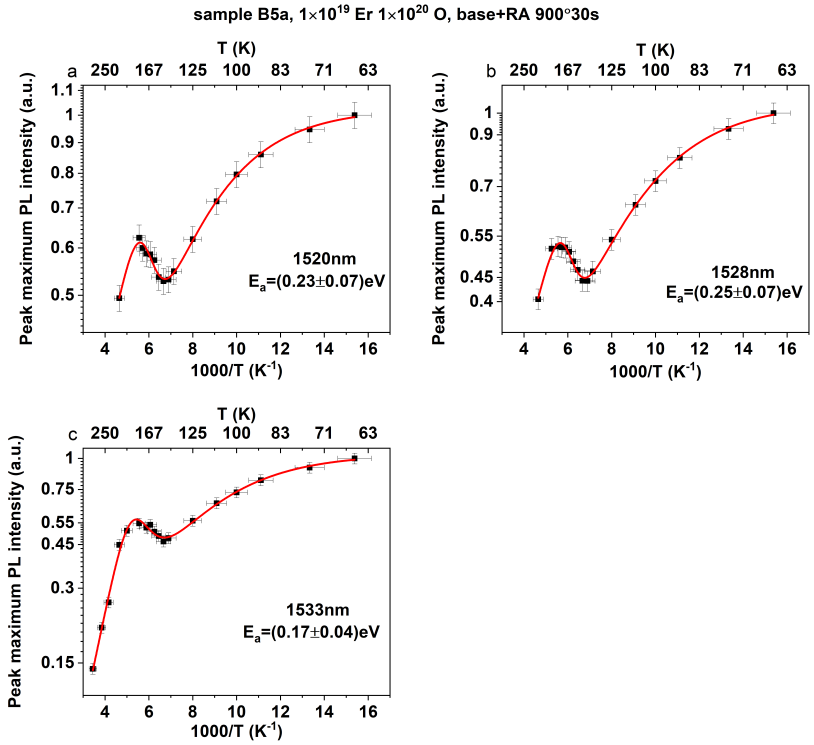

Figure 4.44: NQ fitting model for sample B5a. The annealing temperature is mislabelled and should read 950 °C for 30 s.

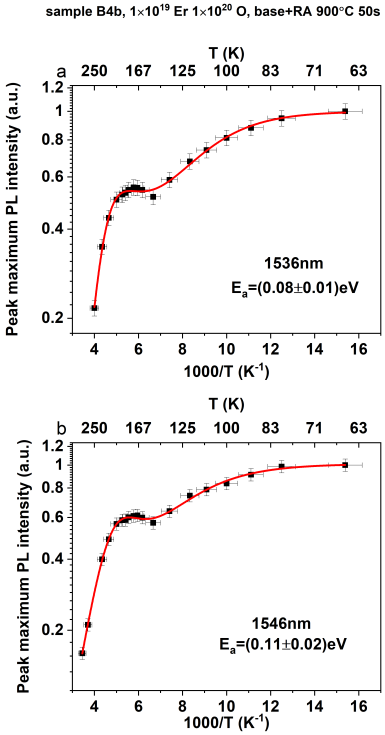

Figure 4.45: NQ fitting model for sample B4b.

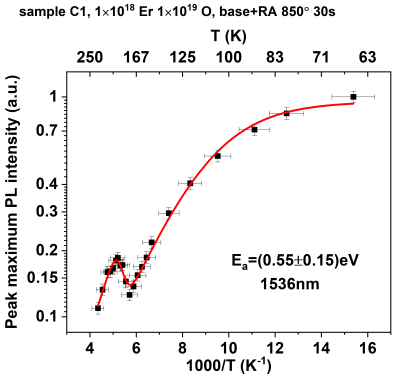

Figure 4.46: NQ fitting model for sample C1 with different Er:O concentration ratio than the rest.

of an Er-related intermediate state responsible for the energy transfer to the Er core has been stated theoretically in [66] and experimentally deduced by observation of a time delay seen between the termination of an excitation pulse and the start of Er PL decay [153]. Time-resolved photoluminescence following direct band-gap illumination and application of a THz pulse from a free-electron laser (FEL) has led to the direct observation of the dissociation of the intermediate state by the FEL pulse both for the primary 1.54 μm Er^{3+} emission [70] as well as broad features such as the 1400 nm peak linked to implantation damage [154]. This intermediate state plays a significant role in energy transfer dynamics, and its location within the forbidden gap of silicon is paramount in understanding both the chain leading to erbium luminescence as well as the processes that contribute to PL quenching. Recall that in section 2.6.4, the backtransfer mechanism responsible for high temperature PL reduction was a thermally activated process linked to the recreation of a bound exciton at the intermediate state starting from the excited erbium ion. These known competing processes are still present in eq. (4.4.2) with activation energies given by E_{BT} (backtransfer) and E_{AQ} (Auger quenching). The new defect state with E_{a} is not related to the intermediate state above. Instead, this middle state's energy levels form between the ground and first excited states of erbium, in our Er:Si equivalent of fig. 4.40. In this case, activation of this middle state with E_{a} leads to contribution of electrons from this state to the Er^{3+} first excited state. The higher excited state population manifests as an increase in photoluminescence upon erbium's radiative relaxation to the ground Er^{3+} state. At elevated temperatures exceeding ≈150 K the backtransfer de-excitation process also takes places adding to the already existing competing nonradiative pathways (such as Auger de-excitation). As a result of this added quenching process, the middle state's contribution to enhanced luminescence is reduced and becomes negligible above 200 K when backtransfers turns into the dominant

de-excitation process. This is seen as an abrupt PL decrease.

The activation energy of the proposed middle state is rather unclear. This is primarily for two reasons. Firstly, the script created for the fitting process has all the parameters correlated, leading to rather large uncertainties. Secondly, as mentioned at the start of section 4.4.1, there had to be a compromise between the selected resolution and the narrow width requirement. As a result, for a larger number of narrow peaks, the lower resolution leads to an integrated intensity skewing the maximum of the main peak. A solution would be to perform a multiple peak fit on each spectrum; however this requires precise knowledge of centre formation and location of any background features unless assumptions on the average emission linewidths are made. This concept was briefly tested for sample B1 where both broad background and multiple narrower erbium lines are visible. The output is shown in fig. 4.47.

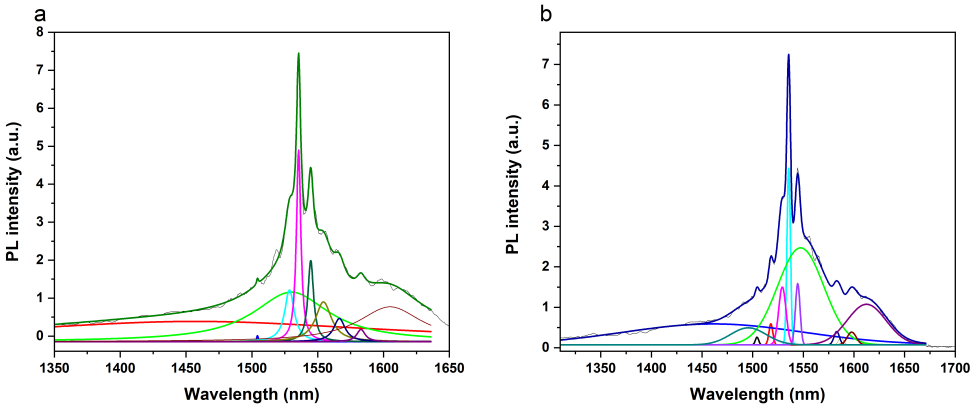

Figure 4.47: Peak fit comparison for sample B1. The light green peak in both (a) and (b) represents the selected broad background feature (BBF).

In both cases, 3 broader peaks were generated: the one between 1580-1650 nm (light brown on (a) and purple on (b) was deliberately placed to account for the artificial shoulder in the spectrum as a result of the detector limit. The light green peak is assigned to the BBF feature. Comparison amongst the two plots makes evident that the total number of peaks that were input in the spectrum's de-convolution, as well as their set FWHM and central transition location affects the shape, area and location of the BBF peak estimate. In turn, this has an effect on the maximum intensity of the rest of the fitted peaks. Therefore, whilst the general trends are still valid, the exact location of the middle state within the silicon bandgap can not be ascertained. To establish this general trend, the activation energies of peaks belonging to the same resolution group were plotted in fig. 4.48.

Interestingly, both the 1527-1529 nm emissions and the 1519 nm emission display very similar characteristics. The behaviour is reminiscent of the total luminescence intensity

trend observed in fig. 4.24. It could be that the middle state has formed a continuous energy band allowing interaction with all possible erbium centres. The alternative is a an energy state localised to a particular erbium environment. The fact that the BBF attributed to amorphous erbium in silicon experiences negative thermal quenching could indicate that this middle state is continuous. This is because the broad feature emission spans across 200 nm, forming an energy band throughout the sample space. A localised middle state would not interact with the whole of the energy band; in that case NQ quenching would not be expected for all wavelengths. Another general trend that the temperature dependence spectra show is good luminescence retention across high temperature region. Further investigation into the quenching behaviour by comparing the backtransfer and Auger quenching activation energies in the samples could allow deeper understanding on the non-radiative pathways present in these devices.

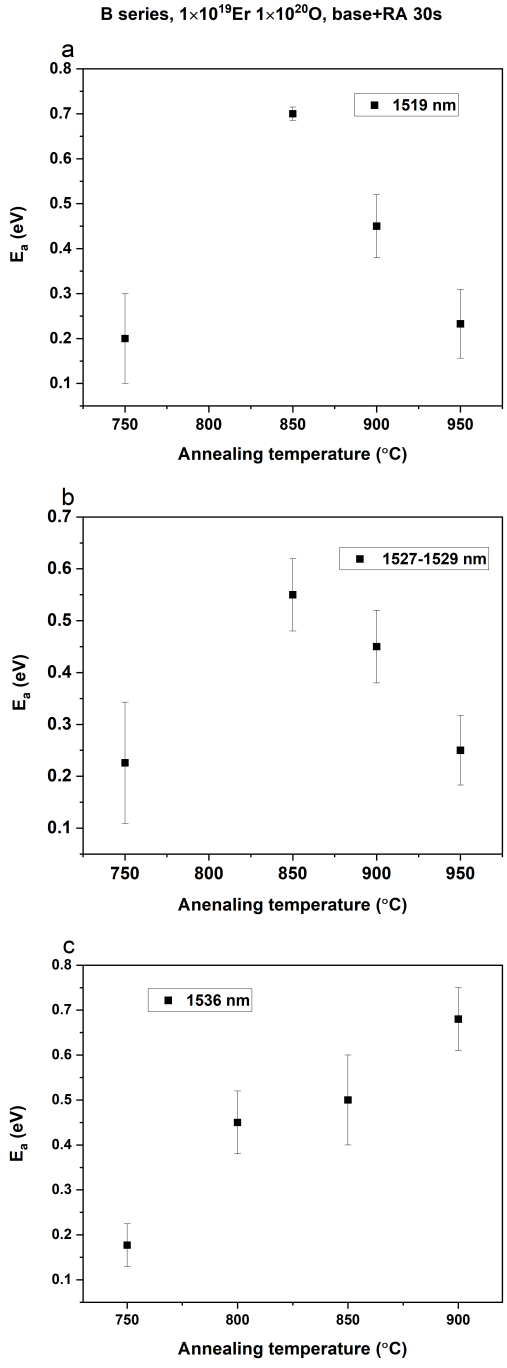

Figure 4.48: Estimated from peak maxima activation energies for (a) the 1519 nm (b) 1527-1529 nm and (c) 1536 nm emission lines.

4.5 Chapter summary

In this chapter, the effects of erbium and oxygen doping concentration ratio as well as post-implantation sample thermal processing on the erbium PL were investigated. Raman spectroscopy measurements in section 4.3.1 showed that recrystallisation of the silicon matrix occurred at temperatures ≥850 °C for samples following a two-step thermal anneal treatment. Section 4.3.2 demonstrated that a single-step rapid anneal treatment for 30 seconds was sufficient to optically activate erbium but lingering implantation defect damage limited the PL yield. For these samples temperatures in excess of $T_{RA} > 900$ °C were needed to form the erbium centre with primary emission at 1536 nm. In contrast, section 4.3.4 showed that for samples following a two-step annealing process this erbium centre was formed at low temperatures and rapidly dissipated at $T_{RA} > 850$ °C. The optimal temperature for maximum PL yield was found to be 850 °C for a 30 s anneal time coinciding with this 1536 nm centre formation (see section 4.3.4). Section 4.3.2 indicated the existence of an amorphous erbium background at 1400 - 1650 nm region for all samples. This was referred to as the broad background feature (BBF). In section 4.3.3, the most beneficial to PL Er:O concentration ratio was found to be 1:10, with further oxygen incorporation leading to luminescence quenching due to excess oxygen clustering. Temperature dependent photoluminescence measurements were performed in section 4.4. Section 4.4.2 found that for different Er:O concentrations but identical annealing processing parameters the PL quenching mechanism of the well-defined erbium centres and the BBF was shared. This was further confirmed in section 4.4.2 for samples whose rapid anneal was undertaken at different temperatures. All samples presented previously unreported anomalous temperature dependent PL behaviour compared to the commonly seen positive quenching model. This deviating behaviour was compared to a negative thermal quenching (NQ) model in section 4.4.3. The model was in agreement with this work's results, and the existence of a middle state between erbium's ground and upper excited states was proposed in section 4.4.3. The negative PL temperature behaviour was attributed to enhanced erbium emission as a result of thermalisation of the middle state which leads to thermal excitation of electrons in erbium's first excited state. The interaction between the proposed state and erbium and the ratio of competing excitation and de-excitation processes was responsible for the overall PL quenching behaviour. The following lifetime chapter aims to elucidate some of these energy transfer dynamics in this erbium system.

5.LIFETIME MEASUREMENTS

5.1 Methodology

5.1.1 Instrumentation

Previous attempts at measuring the lifetime of one of our samples (B3a) indicated a potential $1/e$ decay time less than the 1 μs response of the Thorlabs LDC210C laser diode controller used at the time [155]. As a result, integrated from all wavelengths lifetime measurements were performed using a similar set-up to the one described in section 4.2, with several differences with regards to excitation source and collection leg instrumentation.

The excitation source was an OSRAM PLT5 450B metal can TO56 laser diode with typical wavelength $\lambda_{\text{peak}} = 450$ nm, spectral bandwidth $\Delta\lambda \approx 1$ nm and high modulation frequency. Light output was TE polarised with a ratio of 100:1. A picoLAS LDS-VRM 005 seed driver was employed, allowing analog real time modulation up to 1 GHz with a rise time of < 1 ns. The diode head was directly soldered onto the driver for optimal performance. Due to temperature dependence of the peak diode wavelength, a simple heat-sink casing was machined. The heat-sink's temperature was periodically externally monitored using a thermocouple. Beam collimation was controlled via a lens mounted on an XYZ stage. A Thandar TS30215 30V-2A precision DC power supply was used to power the driver. It was noted that due the laser driver's factory settings, upon powering it a bias current around 28-30 mA would always flow through the laser diode. Since this particular diode had a very small threshold current, it remained in the "on" state even with no external current input. However, there was no sample response at such low excitation power so this state is denoted onwards as the "off" state.

Analog modulation was achieved via a Stanford DG-535 Digital Delay/Pulse Generator. The driver's response to the input signal was monitored through the driver's current output. To check the performance of the laser diode, a beam-splitter was inserted into the beam path with a portion of light directed towards a Thorlabs DET36A silicon detector. Output cables were connected on a RS-PRO RSDS1204CFL 200 MHz bench oscilloscope, triggered by the pulse generator's $\overline{AB}$ output. This channel has the same characteristics as the input fed to the laser driver (denoted as AB), but with inverted voltage. All cable connections were 50 Ω terminated, using as short cabling as possible.

Laser driver response was found to be almost identical to the pulse generator's trigger output. Typical driver propagation delays of 10 ns from input to start of current flow

were stated in the manual, however such delays were not observed on the oscilloscope. This counterbalance is attributed to delays caused due to cabling length and variation in instruments' response. This effect, however, ensured that triggering time matched the event start time during our experiment. Unfortunately, the rise and subsequent fall time of the silicon detector limited the quantification of the diode's response. We could only verify that the diode's fall time response was less than 10 ns and that the rising edge start time was the same as the current output start time.

The collection part of the experiment involved removal of the monochromator in order to maximise obtainable signal and minimise spectral deviations and time delays caused by the instrument's optics. Integrated luminescence was collected with the Photomultiplier Tube (PMT), the same detector used in section 4.2. Due to the signal's low amplitude, an attempt to maximise its intensity was performed through the use of a resistor box between the PMT and a Tektronix MDO3022 mixed domain oscilloscope on a 1 MΩ input. Signal from a test Si:Er sample was collected for various resistor values, however it was observed that the 1/e decay time did not plateau, indicating the RC constant superceded the 'true' lifetime unless the signal was terminated at 50 Ω. It was thus necessary to directly connect the PMT current output to the oscilloscope's 50 Ω termination input.

5.1.2 Data collection and analysis

Measurements were performed using a 3 μs excitation pulse with a repetition rate of 131 Hz. These values were found to produce a stable waveform whilst allowing enough relaxation time between measurements to enable detection of longer decay components, if present. The driving pulse amplitude of 0.17 V resulted in a diode current of corresponding power $P = 65$ mW at near field. The PMT voltage was set to its maximum of 880 V. The oscilloscope's resolution limit was set to its minimum 1 mV per division. During the driving pulse's leading edge transition time, overshooting was seen followed by slight undershooting during fall time (fig. 5.1). This fluctuations mirrored occasionally on the diode driver's output.

In contrast to the relatively clean 'off' levels of the generated pulse, the recovered lifetime signal can be difficult to distinguish as seen in fig. 5.2. The background signal level variation when there is no illumination (pulse off) can be attributed primarily to the dark current generated by the PMT at high amplification voltage bias. In addition, whilst every effort had been made to minimise any scattered/room light reaching the detector, it was noted that on occasion there would be fluctuations at the amplitude of the noise levels throughout the measurements. Furthermore, due to the AC nature of the retrieved signal and despite care to use as short cabling as possible, the signal's edge would on occasion resemble an under-damped sinusoidal waveform. This cable ringing

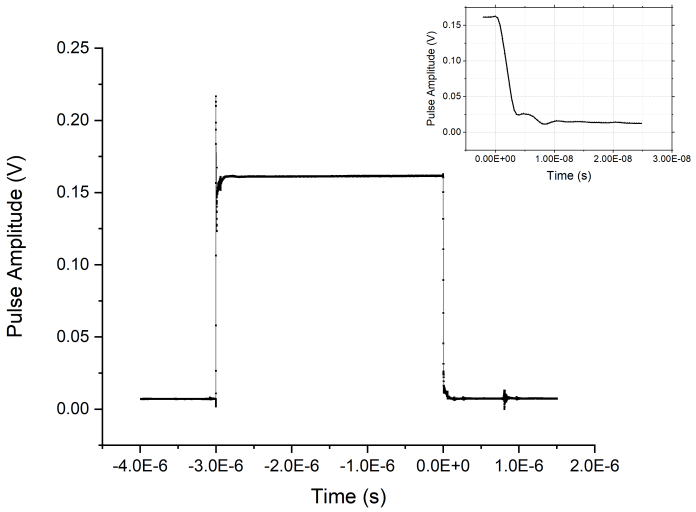

Figure 5.1: Pulse generator signal output. The inset depicts the pulse slightly before it switches off, followed by ringing at the tail end.

was particularly visible in samples with low signal-to-noise ratio. To account for the above and in order to ensure consistency in the methodology used across the samples several methods of analysing data were developed and listed below.

To begin with, each oscilloscope trace saved was the product of 512 instrument averages (the maximum number available) collected over 100.000 data points. The time scale resolution (Δt interval) was 4×10^{-10} s. Because of limited instrument averages, ten (10) of these traces were obtained for each sample per temperature. Both pulse and signal outputs were saved. Collected datasets were collated and averaged. Next, the pulse switching off time stamp would be identified as the time value corresponding to the last high voltage pulse amplitude point prior to clear pulse voltage drop. The need to identify this switch-off time,denoted as t_{start}, arises from the digital oscilloscope assigning t=0 s to the time coinciding with the trigger stamp that has been manually placed on the screen. As a result, the start of the decay might not be shown in the dataset as t=0 s. To correct this, signal values following t_{start} were selected for analysis and their respective time values were shifted by an amount equal to t_{start}. Figure 5.3 visualises this process. We note that t_{start} kept its value across all datasets.

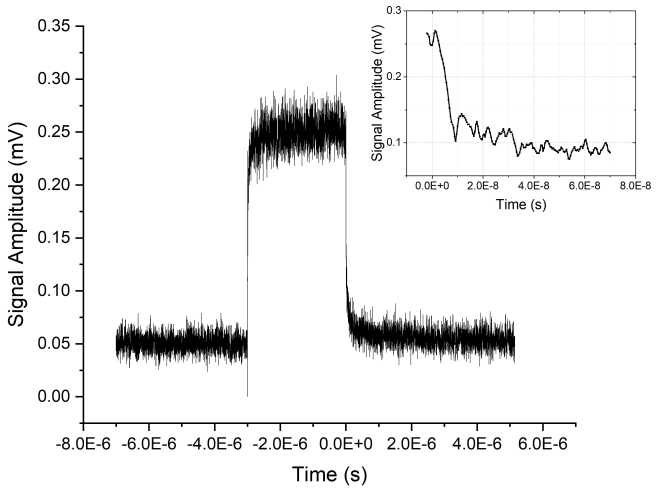

Figure 5.2: PMT signal output, converted to voltage as displayed on the oscilloscope (reduced time interval selected for clarity). In the inset, magnified region showing the signal decay starting at time t=0 s.

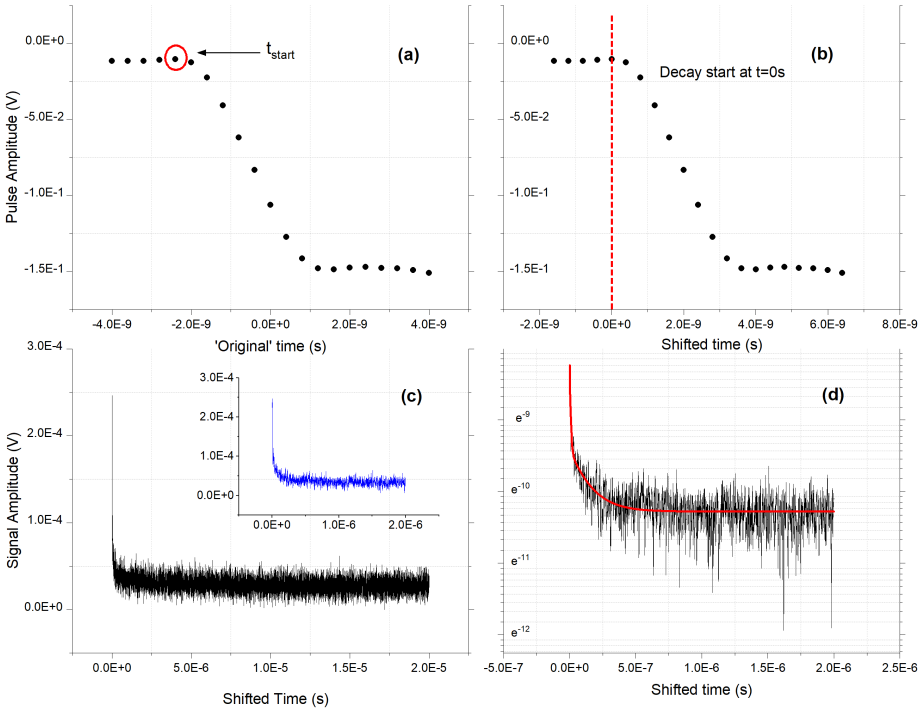

Figure 5.3: Fitting methodology progression: (a) depicts selected raw data close to pulse tail and the pulse decay starting point denoted as t_{start}, (b) shows the shifted by t_{start} time data so that the decay start now corresponds to t=0 s, (c) includes the sample decay data for $t \geq t_{\text{start}}$, shifted by t_{start} as well. The inset contains selected data range to be fitted. (d) fitting result as described in section section 5.1.3.

5.1.3 Fitting process

Figure 5.4(a) presents a typical sample decay. It is evident that the decay is multi-exponential and consists of at least two, potentially three components. Curve fitting for various time ranges was executed using bi-exponential as well as 3-part exponential decay fitting algorithms of the form:

$$I(t) = y_0 + a_1 \exp\left(-\frac{t}{\tau_1}\right) + a_2 \exp\left(-\frac{t}{\tau_2}\right), \tag{5.1.1}$$

$$I(t) = y_0 + a_1 \exp\left(-\frac{t}{\tau_1}\right) + a_2 \exp\left(-\frac{t}{\tau_2}\right) + a_3 \exp\left(-\frac{t}{\tau_3}\right) \tag{5.1.2}$$

where τ_1, τ_2 and τ_3 are the characteristic lifetimes with respective amplitude coefficients a_1, a_2 and a_3.

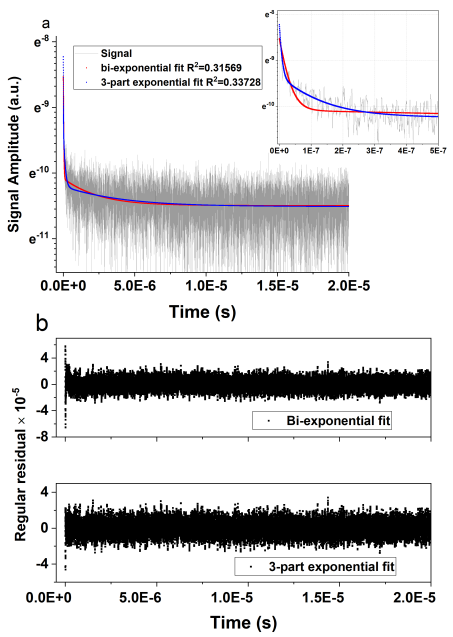

Figure 5.4: (a)Fitting example of a typical decay trace using 2 and 3 part exponential decays. inset presents zoomed area of interest. (b) shows regular residual of fits.

Fits were performed using the Levenberg-Marquardt iteration algorithm. Figure 5.4 shows a comparison between a bi-exponential and a 3-part exponential fit alongside their respective residuals; the coloured scattered points represent the fitted Y data generated by the algorithm. Clearly, commonly employed tools such as the R^2 value are not enough to provide sufficient information regarding the better fit. However, visualisation of the residual and observation of fit deviation from the signal's fast and intermediate components of interest suggests the 3-part exponential decay as the most suitable (see fig. 5.4(b)).

Extracted decay parameter values were tabulated, plotted, and smoothed using the adjacent averaging method. Each smoothed data point was computed from data points within a moving window. If $\{f_i|i = 1, 2, ...N\}$ are the input data points and $\{g_i|i = 1, 2, ...N\}$ the output data points, each g_i is computed from $\{f_m|i - \text{floor}(\text{npts}/2) < m < i + \text{floor}(\text{npts}/2)\}$ where npts is the selected points in window and floor is the floor function. Here, window size included 7 data points. Smoothing was only performed as a guide to the eye due to the very low signal amplitude. The window size was selected to incorporate data points belonging in the same temperature groups, as will be discussed further below. Where

decay trace data smoothing was required for comparison reasons, a misrepresentation of the fast component was seen. To avoid such the smoothed outcome's first 100 data points were replaced with the original dataset's values. This method is used during some graph plotting in further sections and provided virtually identical fits to the as-obtained data.

5.2 Temperature dependence of emission lifetime

All samples present similar decay characteristics, containing a fast nanosecond component followed by an intermediate component with lifetime in the tens to hundreds of nanoseconds and ending with a more elusive to fit microsecond lifetime component at the tail end of the signal. Figure 5.5 presents a summary of the 3 lifetime components across some samples. To the left (a), as-extracted from the fitting data for a couple of representative samples. To the right, smoothed data using the adjacent averaging algorithm mentioned in section 5.1.3. The as-obtained lifetimes with affiliated fitting algorithm error bars for all samples can be found in Appendix A. Smoothed data curves have been added a guide to the eye only.

The close range between the fast and intermediate components makes identification harder due to the parameters describing the decay in the fitting algorithm being highly correlated. A high-signal to noise ratio is thus required to confidently recover the multiple decay times and respective amplitudes. Nonetheless, the lifetime range remains valid. In fig. 5.5 the fast component, namely τ_1, appears to have fairly uniform response amongst this series. For the non-rapidly annealed sample (non RA), as well as those annealed (T_{RA}) for 30 sec at 900 °C and 750 °C, region I displays lifetime retention. Samples annealed at 800 °C, 850 °C and 950 °C show a slight reduction in lifetime as temperature increases. Interestingly, region II presents an increase in extracted lifetime values; after reaching a maximum, the trend reverses and the lifetime starts to decrease. Different samples appear to have different lifetime rates of change within that region, and the peak maximum is not achieved for a set temperature (T_{peak}). Rather, we observe the existence of primarily 2 separate T_{peak}; 162-165 K, 178-181 K. The high temperature region III is accompanied by lifetime quenching.

The intermediate τ_2 component behaves in a similar manner for regions I and II. The 850 °C, 900 °C and non-RA samples are almost identical in region I with very small lifetime reductions, while the 800 °C shows good retention. On the contrary, samples 750 °C and 950 °C decrease more rapidly. A larger discrepancy with lifetime values and annealing temperatures than the one seen for τ_1 is observed; whilst τ_1 values were fairly similar, ranging from 4 to 6 ns with the exception of the 850 °C nearing 8 ns at 80 K, there is a market 5-fold increase in τ_2 for T_{RA}=950 °C. Peak maximum is attained in

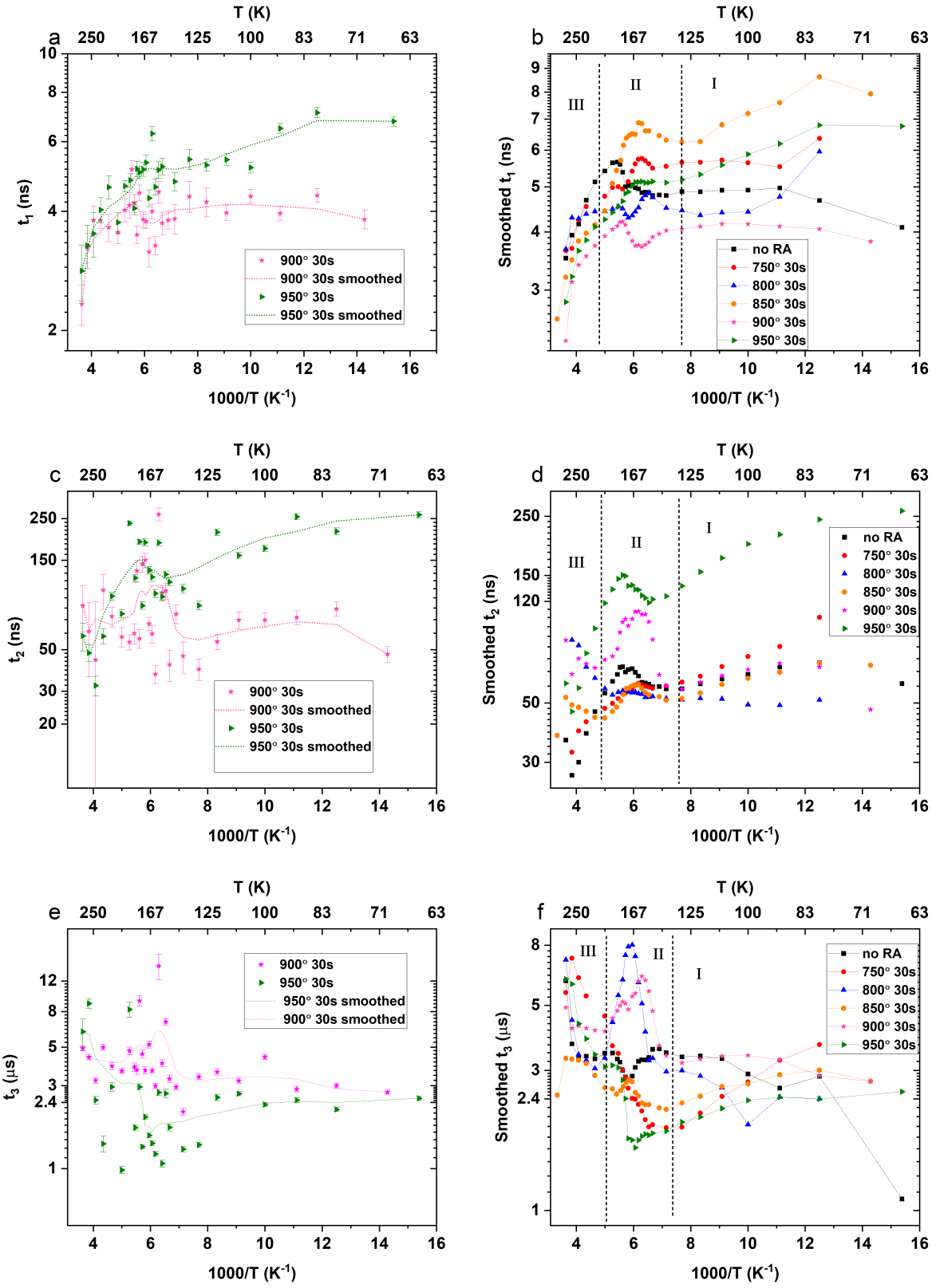

Figure 5.5: Decay trace (a) for sample B4a and B5a. Here, the y axis t_1, t_2, t_3 correspond to τ_1, τ_2 and τ_3. In (b), smoothed data using the adjacent averaging algorithm from section 5.1.3 for B sample series (see table 4.1 for sample details). Temperature regions I, II and III are indicated in the graphs using dotted lines. Region I refers to temperatures between 65 K and 140 K, region II includes 140 K to 200 K and region III follows from 200 K to room temperature (RT). The uncertainties pictured arise from the fitting algorithm and might not be representative of the total errors involved. Thus, the values presented are best fitting algorithm estimates. All sample decay traces are found in Appendix A.

region 2 for the same temperature ranges as τ_1. Region III on the other hand, suggests the existence of two different trends; annealing at 800 °C, 850 °C and 900 °C appears to cause a lifetime increase at high temperatures in contrast to the rest of the series whose lifetime decreases.

Equivalent increase in lifetime for high temperatures is seen for the slow τ_3 component, however this time this behaviour is all-sample inclusive. Region I suggests the existence of groups of slightly decreasing lifetime, alongside some samples with rising lifetime at those temperatures. Finally, region II follows τ_1 and τ_2's trend, with peak maxima at the same locations. Exception to this is a 153-159 K additional peak for T_{RA}=950 °C and (potentially) the sample not following RA. Identification and interpretation of τ_3 comes with higher uncertainties due to the larger data scatter present.

The smoothed amplitudes of the decay traces are seen in fig. 5.6. The same three distinct temperature regions are identified. The fast a_1 PL component follows the lifetime trend across all temperatures. In contrast, a_2 displays uniform behaviour including high temperature luminescence quenching as opposed to its τ_2 counterpart. Finally, a_3 does not show a singular trend compared to τ_3 for measured low temperatures, yet suggests certain similarities for region II. Region III shows overall lifetime increase but various PL responses depending on selected sample.

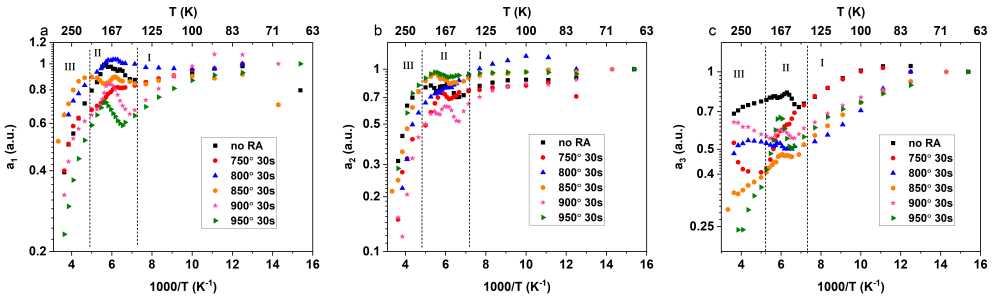

Figure 5.6: Extracted smoothed (using the averaging method described in section 5.1.3) decay amplitudes coefficients for fast (a), intermediate (b) and slow (c) components. Values have been normalised to 65 or 80 K for comparison. As extracted data can be found in the Appendix.

Longer high temperature anneal results in notable increase of the intermediate τ_2 component, as seen in fig. 5.7. No change occurs however for T_{anneal}=850 °C (not shown).

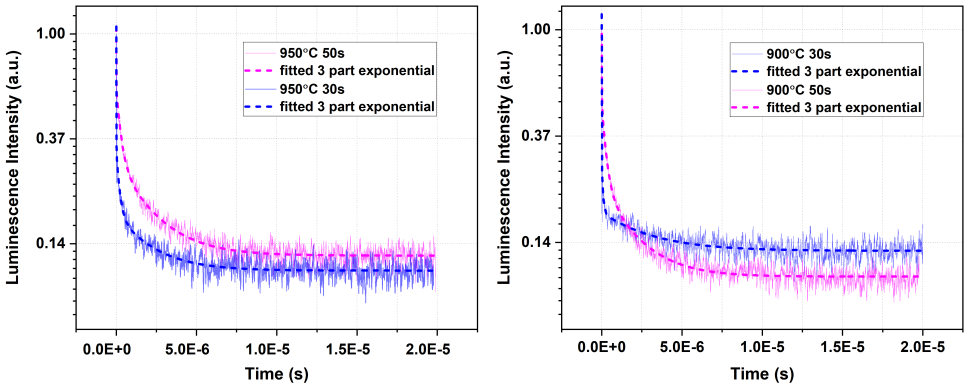

Figure 5.7: Time-dependent photoluminescence intensity for B series 1×10^{19}Er and 1×10^{20}0 (cm^{-3}) samples annealed under the same temperature but different time duration. Sample details are found in table 4.1. Data in decay traces have been smoothed for clarity when plotting multiple datasets whilst keeping the short lifetime data intact, as described at the end of section 5.1.3.

In a similar manner, altering the Er:O ratio or implant concentration affects the luminescence lifetime as pictured in fig. 5.8. For a fixed concentration, increasing the oxygen amount tenfold leads to a decrease of τ_2. Identical Er:O ratio does not equate to matching decay traces, with τ_2 being concentration dependent.

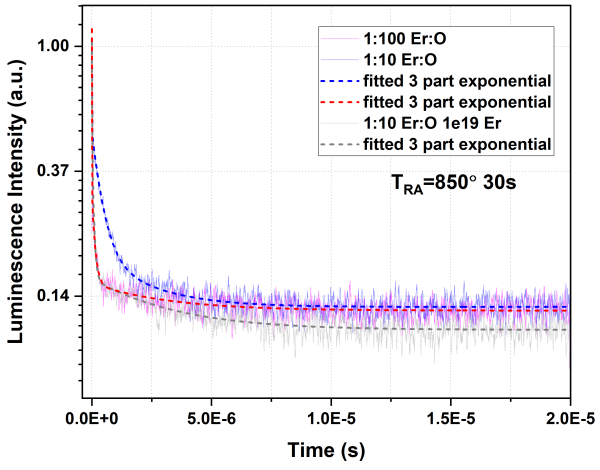

Figure 5.8: Decay traces for different Er:O concentration ratios under identical annealing conditions (samples C1, C2 and C3 in table 4.1). Data in decay traces have been smoothed for clarity when plotting multiple datasets whilst keeping the short lifetime data intact, as described at the end of section 5.1.3.

5.3 Lifetime pattern discussion

The presence of three separate decay times τ_i in the integrated luminescence traces implies the existence of multiple erbium sites in crystalline silicon which agrees with the steady-state PL spectra insection 4.3. We therefore ascribe the individual τ_i to Er^{3+} ions located in three different (crystalline) environments respectively. The observed effective lifetime is thus going to be representative of the mean lifetime of all the transitions affiliated with that centre. As discussed in section 2.6, the erbium intra $4f$-shell transitions are forbidden for a free ion and only partially allowed after incorporation in a host matrix. This leads to very long radiative lifetimes, commonly in the millisecond range. Table 5.1 lists several erbium related decay times for various hosts. The last three rows present other silicon related lifetimes arising from dislocations or defects. Our observation of an ultra fast decay is therefore of major significance and suggests the involvement of a competing non-radiative decay channel which to the best of our knowledge has not been reported for erbium doped systems. The section below elaborates on the nature of this non-radiative pathway.

System/host	Lifetime	Reference
Er:c-Si	$<$ 5 ns	this work
Er:Cs_2NaYF_6	≈100 ms	[156]
Er:SiO_2	9.5-22 ms	[157]–[159]
Er:c-Si	2 ms	[71]
Er:Si	0.31 ms	[64]
Er:Si	1 ms	[71]
Si:Er:O	200 μs	[160]
Er:$Y_3Al_5O_{12}$	7.7 ms	[161]
Er:Y_2SiO_3	8 ms	[161]
Er:SRN	0.34-4 ms	[162]
a-SiC:Er	0.6 ms	[163]
Er clusters silica glass fibre	3-10 μs	[164]
Si nanoclusters	2 μs-500 μs	[165]–[168]
O precipitates in Si	1-100 μs	[169]
Si defect D lines	ns-200 μ s	[170]

Table 5.1: Experimentally measured erbium luminescence decay times for various erbium systems. The last three rows show other Si related lifetimes such as precipitate, clusters and dislocations that could be relevant when observing all mid-IR wavelength decays.

Middle defect state model

In a semiconductor host the effective lifetime could be reduced by non-radiative processes or by a change in the local environment of the Er^{3+} ion affecting the probability of the $^4I_{13/2} \rightarrow {}^4I_{15/2}$ emission. Previously studied nonradiative pathways include the formation of optically inactive clusters and silicides at high doping concentrations for both implanted and MBE grown samples [52], [53]. As a result there is a possibility that any of the decay components could be attributed to such precipitates, with previous work obtaining lifetimes in the low microseconds region as indicated in table 5.1. Nevertheless, universal observation of this nanosecond component suggests it is independent of sample annealing conditions or Er:O concentration levels, and is rather a result of the erbium and oxygen interaction in the intrinsic silicon matrix.

In addition, measurements of the temperature dependence of erbium luminescence in section 4.4 agree with the existence of a proposed middle state as seen in section 4.4.3. This observation is in good agreement with the luminescence amplitude behaviour extracted from the decay fits, particularly for the fast and intermediate components exhibiting negative thermal quenching trend. The slowest microsecond component is difficult to distinguish due to its amplitude commonly being an order of magnitude lower than the fast component. Proof-of concept NQ model fitting using eq. (4.4.2) has been performed

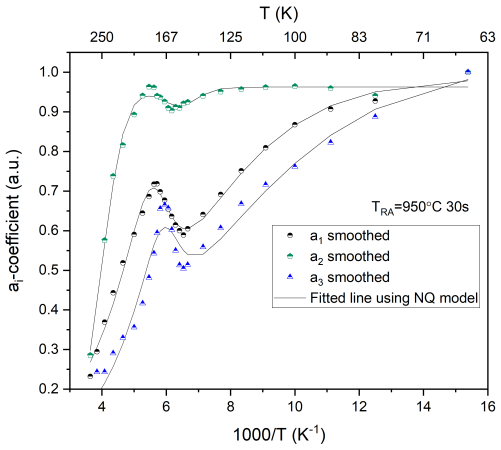

Figure 5.9: Smoothed decay coefficients for B series sample B5a annealed at 950 °C for 30 s. The solid lines are fits to the negative quenching (NQ) model.

on the averaged data points for one sample in fig. 5.9. Whilst the smoothed/averaged data graph is a guide to the eye, it is expected that clearer fitting of the raw data would yield an equally good fit following sufficiently improved signal magnitude. It is therefore proposed that the middle state responsible for the PL negative thermal quenching is the same middle state responsible for the anomalous lifetime behaviour. In this model, the

defect state introduces an energy state situated between the ground and first excited erbium states and has an affiliated activation energy E_a. Since erbium readily complexes with oxygen, it is possible this middle state is an Er-O related state. We propose that the interaction between the optically active erbium centre and the nonradiative defect state is responsible for the luminescence behaviour.

A possible representation of this state is shown in fig. 5.10. The excitation steps involve the conventional exciton trap centre E_T. As mentioned in section 2.6 this trap level is thought to be located $\approx$ 150 meV below the conduction band. The new defect state, marked Er-O defect state on the diagram, is placed between the $^4I_{13/2}$ and $^4I_{15/2}$ levels, with exact position depending on its activation energy E_a. Values for E_a and E_{BT}

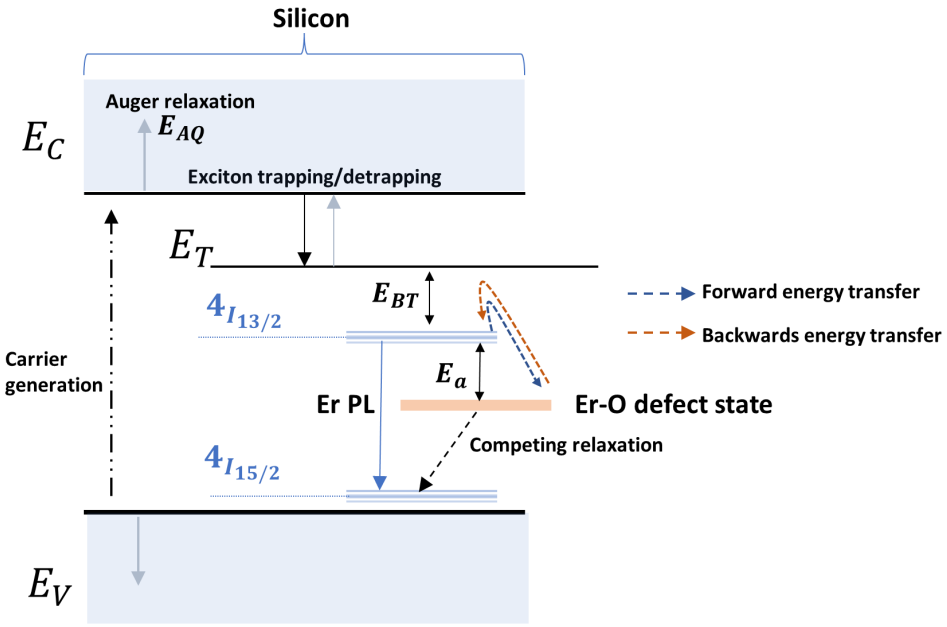

Figure 5.10: Possible energy band diagram including the proposed new Er-O defect state located between the $^4I_{13/2}$ and $^4I_{15/2}$.

can be obtained by fitting to eq. (4.4.2). Previously reported backtransfer energies have placed the $^4I_{15/2}$ manifold just above the valence band (VB) [3]. In this work, fitted values from the negative thermal quenching equation eq. (4.4.2) in section 4.4.3 have indicated variation in activation energy, whilst E_{BT} averaged around 40 meV. This would place the $^4I_{15/2}$ slightly higher above the VB compared to the standard model. In this model, in addition to the common non-radiative pathways of Er:Si, energy transfer from the excited $^4I_{13/2}$ to the Er-O defect state which offers a competing relaxation pathway is included. This is marked as 'forward energy transfer'. At elevated temperatures there is contribution by the thermal excitation of electrons to the $^4I_{13/2}$ state by the middle Er-

O defect state, marked as 'backward energy transfer'. This dynamic system interaction leads to variation in luminescence intensity and the reduction of observed erbium lifetime.

Existence of this middle state could also explain the differences in quenching rates reported in this work. Previous studies have indicated intensity quenching by nearly two orders of magnitude between 77 K to 200 K [171]. Here, the intensity at 300 K appears to be 20% of its 77 K value. For high temperature regions in particular (above 200 K), the backtransfer process which leads to reduced Er^{3+} excited state population competes with 'backwards' energy transfer originating from thermal population of the middle state. If the backtransfer process strongly dominates, then both intensity and lifetime quench. If $^4I_{13/2}$ population through the middle state can dominate, this might manifest as an increase in both luminescence intensity and lifetime. The balance of these processes gives rise to in-between scenarios as well.

Implications on quantum efficiency

Transition of an excited ion can occur either radiatively accompanied by photon emission or non-radiatively through multi-phonon decay. It is known that for a number of first-order quenching pathways W_{qi} the rate of non radiative decay W_q can be defined as [172]:

$$W_q = \sum W_{qi} \tag{5.3.1}$$

The sum of radiative and non-radiative decay rates, W, is:

$$W = W_r + W_q \tag{5.3.2}$$

where $W_r = 1/\tau_r$ is the radiative rate and τ_r, τ are the intrinsic and observed lifetime respectively. The probability that an excited ion will emit, namely the internal quantum efficiency η is:

$$\eta = W_r \tau \tag{5.3.3}$$

with temperature dependence:

$$\eta(T) = \frac{\tau(T)}{\tau_r(T)} \tag{5.3.4}$$

Taking τ_r to be 1 ms for all temperatures after [173] we can see how $\tau_q(T)$ and $\eta(T)$ for would take the same form as the lifetime component values. In fact, for an extracted lifetime value of 7 ns, it is clear that $\eta = 7 \times 10^{-6}$ and $\tau_q \approx$7 ns. This very result validates the assumption of the radiative decay time being constant, since the observed lifetime is scales of magnitude faster leading to a quenching rate of the same range as the obtained τ. The emission efficiency will also follow the form of τ across temperatures. Detection of such low quantum efficiency is testament to the sensitivity of our setup.

5.4 Amplitude Average lifetime

Due to the existence of multiple centres, calculation of the average lifetime was performed. The amplitude average lifetime is a statistical comparative tool representing the lifetime a fluorophore would have if its fluorescence was equal to the steady-state fluorescence of the fluorophore with several lifetimes, in our case the fluorescence of the different population species [174]. In integral form, the average lifetime can be expressed as [175]:

$$\tau_{av} = \frac{\int_{t=0}^{t=t_{lim}} tI(t)\,dt}{\int_{t=0}^{t=t_{lim}} I(t)\,dt} \tag{5.4.1}$$

, where the amplitude fraction $I(t)$ acts as a weight factor for the calculation of this average and t_{lim} is the time when the detection limit is reached. Due to the small signal to noise ratio of our data, no direct integration was possible since $t \times I(t)$ would become very erratic. As a result, the following tactic was employed.

A 3-part exponential decay was fitted with the offset fixed as $y_0 = 0$. The fitted Y values were then normalised from $[0, 1]$ representing $I(t)$ allowing calculation of $tI(t)$. Integration of the areas with $t_{lim} = 2 \times 10^{-5}$ s was performed. Visual representation of this procedure can be seen in fig. 5.11.

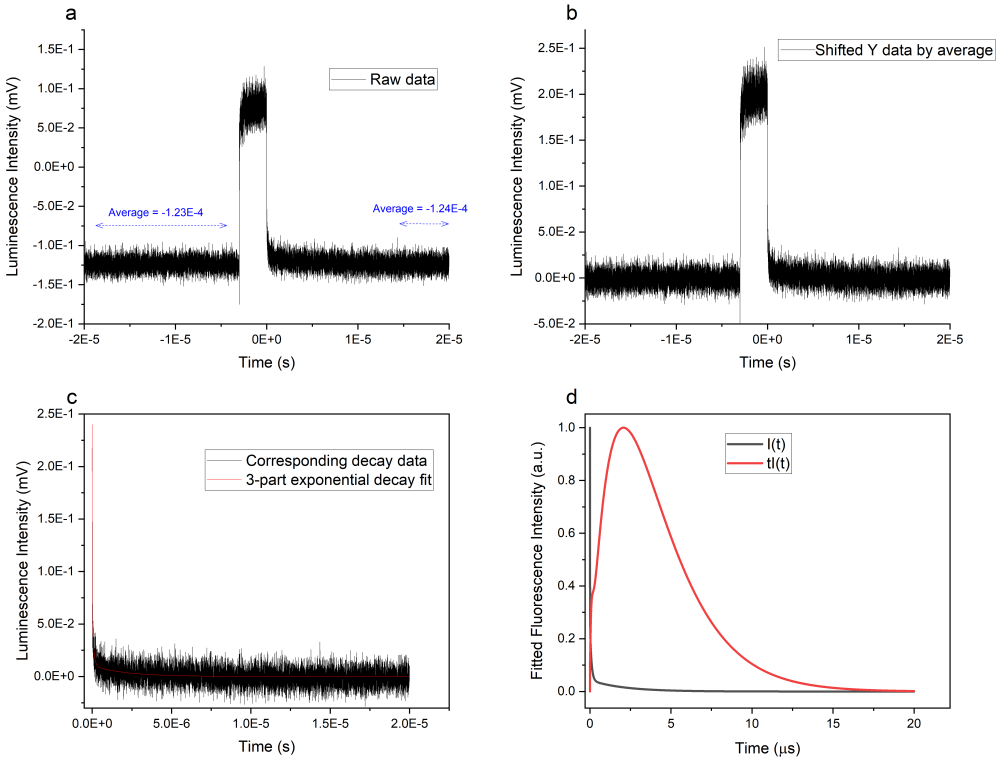

Figure 5.11: Procedure for lifetime averaging: Raw signal output (a) followed by average shifted luminescence values (b). Extracted fitted 3 part exponential decay (c) and its affiliated $I \times t$ (d). All values on (d) are normalised for clarity.

Figure 5.12(a) shows the evolution of average lifetime and integrated intensity (obtained as the area under the PL) for the 1×10^{19} Er and 1×10^{20} O (cm^{-3}) B sample series (see sample details at table 4.1). All values correspond to decay curves obtained at 80 K. The calculated τ_{av} exhibits a significant increase as the annealing temperature varies from 750 °C to 850 °C, followed by a mild drop for samples annealed at 900 °C and a steep decrease for T_{RA}=950 °C. Figure 5.12(b) shows the total intensity for the same samples, obtained as the area under the luminescence signal. This trend is in excellent agreement with the independent PL measurements shown in fig. 4.24 in section 4.3.4. We suggest that variation in τ_{av} could be attributed to differences in concentration and energy gap location of various defects in our samples.

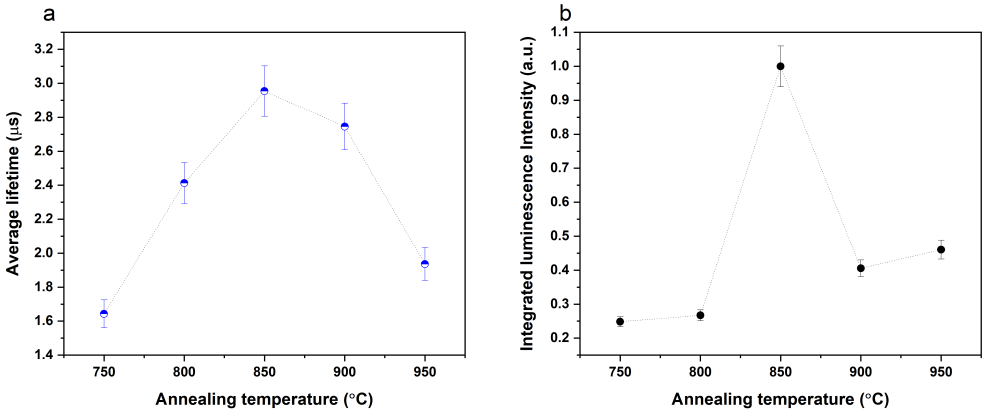

Figure 5.12: Average lifetime (a) and total intensity (b) comparison for the 2-step annealed B series 1×10^{19} Er and 1×10^{20} O (cm^{-3}) concentration at 80 K. Temperatures denote the rapid anneal (RA) temperature. All samples underwent a 30 seconds RA treatment. For sample names refer to table 4.1.

As previously mentioned, formation of Er-related defect centres in Si:Er,O is greatly dependent on the sample's annealing temperature [82]. Since Er defects in Si:Er, O have been directly linked to the Er^{3+} ions excitation mechanism [3], we could infer from fig. 5.12(a) that annealing at 850 °C leads to optimal formation ratio of those Er defects that positively contribute to excitation efficiency by successfully capturing free-excitons (and consequently transfer their energy to erbium ions via an impurity Auger process), whilst reducing antagonising defect complexes that enhance non-radiative decay. As a result, the probability of Er intra-4f shell radiative relaxation increases, which mirrors in the behaviour of τ_{av}. This observation would be in agreement with other groups' findings regarding the existance of an optimal temperature leading to the passivation of deeper defects in part responsible for non-radiative recombination [82].

However, whilst removal of deeper level defects supposedly occurs at higher rates at temperatures exceeding $T \approx$800 °C, we observe a reduction, rather than an increase of

τ_{av} above 850 °C. This drop could be explained as Er-defect complexes start to decrease due to increasing competition between their generation and dissociation, lowering their concentrations. Since this concentration includes both 'beneficial' to excitation defects, as well as less desirable defects we postulate that the dissociation ratio of $\frac{\text{beneficial complexes}}{\text{antagonising complexes}}$ shifts in favour of the denominator.

Furthermore, photoluminescence measurements in section 4.3 and crystal field splitting chapter 3 showed the existence of at least two Er centres of (possible) cubic and lower than cubic symmetry. These centres were superimposed upon a broad background feature (BBF) which was attributed to erbium in amorphous silicon environment (see section 4.3.2). For samples following a two-step annealing process, this BBF was suppressed in favour of erbium emission from well-defined centres. The two identified centres were present in different proportions for annealing temperatures up to 850 °C, with the 850 °C sample presenting the most intense luminescence. Further anneal temperature increase at 900 °C resulted in a dramatic shift in the spectrum, indicative of a change in the ratio between the two centres. It is proposed that the average lifetime depicts this proportionality of the two distinct erbium sites. Formation of the strongly luminescent optically active lower symmetry site increases for T_{RA} ≤850 °C reaching a maximum at 850 °C after which it dissociates. The reduction in optically active centres lowers the radiative rate and hence the average lifetime. Figure 5.13 presents the average lifetime variation for sample groups under the same rapid anneal temperature yet different anneal duration.

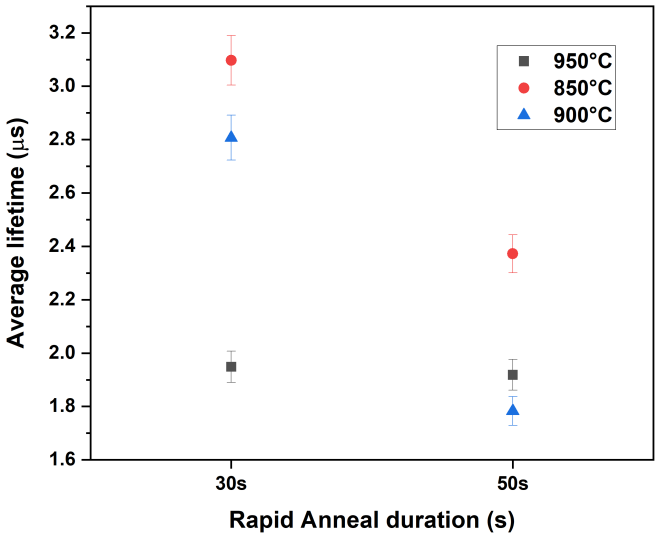

Figure 5.13: Average lifetime variation for the B sample series (1×10^{19} Er and 1×10^{20} O (cm^{-3}) annealed at the same RA temperature for different duration.

It is evident that following a longer rapid anneal leads to a significant drop in average lifetime with the exception of the sample annealed at 950 °C where the decrease is not noticeable. Additionally, the 50 s anneal series displays a smaller relative lifetime reduction for temperatures above 850 °C, and very slight lifetime deviation between 900 °C and 950 °C. This is interesting since photoluminescence spectra in section 4.3.4 have indicated a longer anneal does not significantly alter the erbium centre formation. However, the same measurements presented higher luminescence emission intensity for samples annealed at 30 seconds, compared to their 50 seconds equivalent. An increase in optically active erbium centres would consequently lead to an increase in excited Er^{3+} ions enhancing the radiative rate and thus showing a higher average lifetime.

Figure 5.14 shows the average lifetime for samples of different Er:O concentration ratios following the same base annealing recipes, and a rapid anneal (RA) of T_{RA}=850 °C for 30 s (C series in table 4.1). Most notably, the increase in lifetime for similar oxygen but higher erbium concentrations (between the 1×10^{18} Er and 1×10^{20} O (cm^{-3}) (sample C3) and the 1×10^{19} Er and 1×10^{20} O (cm^{-3}) (sample B3a)) indicates no Er $\rightarrow$ Er cross-relaxation taking place and thus eliminates the potential of the observed lifetime being a result of clustering.

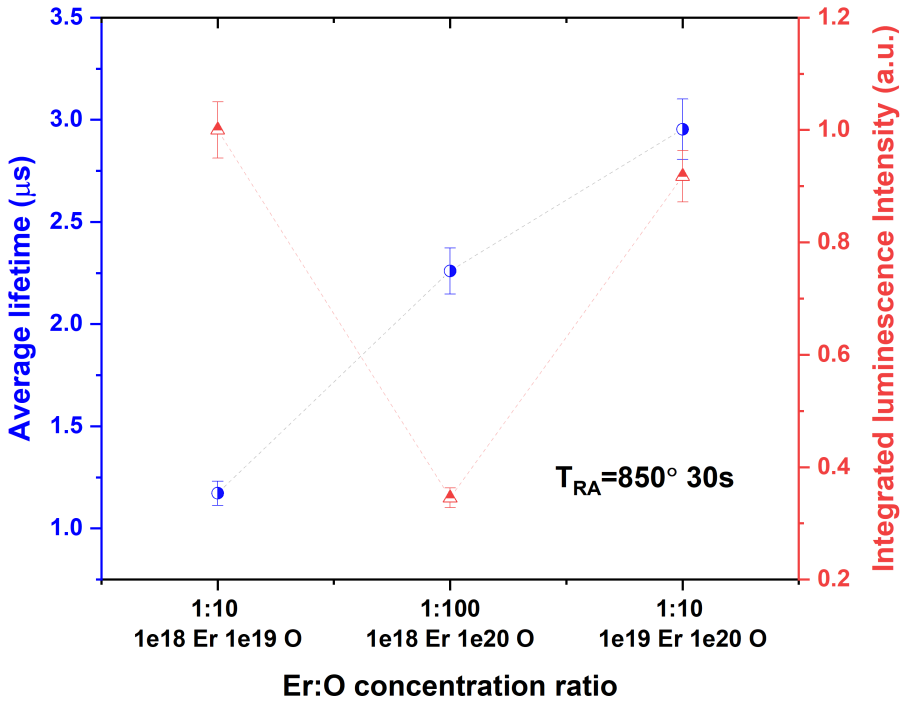

Figure 5.14: Average lifetime (blue) and integrated luminescence intensity (red) for different Er:O concentrations (C series in table 4.1) prepared under the same annealing recipe.

Surprisingly, there is an over two-fold increase in τ_{av} for a respective ten-fold increase in oxygen concentration which is antithesised by a steep reduction in emission intensity. It is proposed that this is due to the erbium in amorphous silicon broad emission (BBF). This requires the assignment of the third slower microsecond lifetime component to BBF related transitions. Figure 4.15 in section 4.3.3 showed that at high oxygen concentrations (sample C3) the BBF dominates on top of a weaker lower symmetry centre emission. The same low symmetry site is present for lower oxygen concentration (sample C1) yet the background is reduced significantly. The value of the average lifetime is therefore skewed in favour of the longest component for high oxygen concentration due to limited competition from the shorter radiative decay erbium centres. If assignment of the slow component to the erbium in amorphous silicon is correct, the significant reduction from the expected 1 ms lifetime seen would imply that the proposed middle state is in fact a continuous state, rather than a localised to well-defined erbium sites state. This qualitatively agrees with previous observation in section 4.4.3.

Finally, for similar 1:10 Er:O ratio characterised by a larger Er implantation dose, an increase in both lifetime and intensity can be seen. This is unexpected, for up-to-date it was assumed that similar Er:O ratios produced comparable results. It might be helpful to recall that earlier DLTS studies showed that the depth distribution profile of the defects agree with that of the erbium implant [82]. Therefore it is suggested that the total areal dose of Er and O is significant to the formation of different Er sites in silicon, since the varied implantation depth affects the formation depth and amount of radiation damage, with whom the Er ions can interact to form Er-related complexes. It is proposed that categorising samples solely based on their Er:O ratios as done before is insufficient. This underscores once again how important the role of damage impurities is, and how sensitive the samples are under different processing conditions.

5.5 Continuous lifetime distribution

Up until now, data were analysed by adopting a model of 3 discrete decay times assuming 3 different erbium environments. However, we have seen that it is difficult to fully resolve closely spaced lifetimes, in addition to having no confirmation on the exact number of erbium defect complex configurations. As a result, a discrete distribution of decay times can be expected reflecting the distribution of erbium conformations. In this case, the intensity model can be analyzed using the continuous lifetime distribution model, where the a_i values are replaced by distribution functions a_τ. Each component with lifetime τ is represented as:

$$I(\tau, t) = a(\tau) \exp(-t/\tau) \tag{5.5.1}$$

The total decay, governed by the sum of individual decays weighted by amplitudes, is then:

$$I(t) = \int_{\tau=0}^{\infty} a(\tau)\ \exp\{(-t/\tau)\}d\tau \tag{5.5.2}$$

where $\int a(\tau)d\tau = 1$ [175]. For discrete distributions:

$$I(t) = \sum_i a_i \exp(-t/\tau_i) \tag{5.5.3}$$

Equation (5.5.3) was implemented in MATLAB using the code provided in [176] with minor modifications to account for offset. The lifetime values τ_i were spaced logarithmically between two specified lifetimes. The amount of τ_i values was also defined. Here, the specified lifetime range was between 1 ns and 15 μs based on lifetime measurements in previous sections. For a test sample, the repeatability and limitations of the algorithm were tested by varying the number of τ_i values between $90 - 140$. The test results are presented in fig. 5.15.

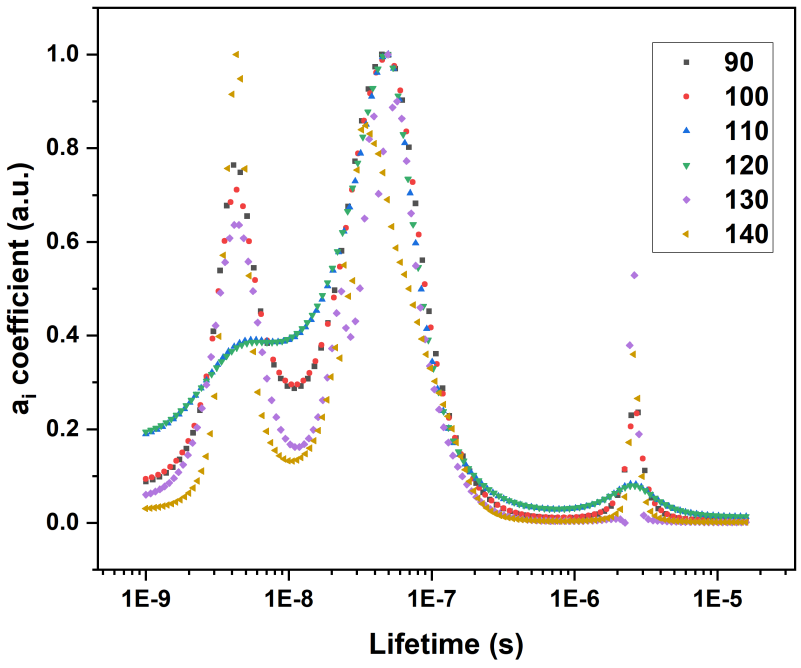

Figure 5.15: Semilogarithmic plot of continuous lifetime distribution for a test samples. Specificed lifetime range was kept constant while varying number of lifetime values τ_i.

For all values selected the algorithm identifies unambiguously three lifetime distributions. Discrepancies are observed with respect to the relative intensities and full width half maxima (FWHM) of the distributions, yet the centre of gravity remains the same

up until $\tau_i = 130$ where slight shifting can be seen. This change was assumed to be due to overparametrisation of the model that decreases reliability. To avoid inconsistencies in fitting amongst our samples but still have enough points to resolve across potentially closely spaced lifetime distributions, 120 τ_i values were used. Additionally, fitting was performed both on as-obtained averaged data sets at 80 K, as well as smoothed data. Smoothing was achieved by using the adjacent averages algorithm and a smoothing range of 100 values. To avoid under-representation of the fast component observed, the first 100 data points of the smoothed output were replaced with original data. Generally, no deviation was found between as-obtained and smoothed data. However for some samples a dependency was seen between the decay fitting offset and the relative amplitude of the a_i coefficient as well as the number of obtained distributions as pictured in fig. 5.16.

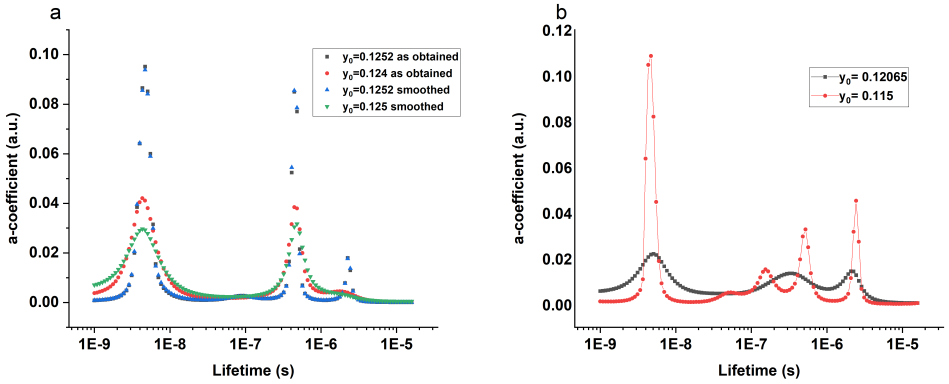

Figure 5.16: Offset dependency of a sample for both as-obtained as well as smoothed data (a). In (b), lifetime distribution peak number offset dependency.

Consequently, the discussion below will focus on the distribution number and peak centre, with only qualitative intensity observations. In fig. 5.17 recovered lifetime distributions are compared for the 1×10^{19} Er and 1×10^{20} O (cm^{-3}) two-step annealed sample series (B series in table 4.1). The distributions correspond to data sets at 80 K. All peaks are normalised with respect to their maximum value.

All samples contain at least 3 distribution lifetimes, centered at the nanosecond, tenths of nanoseconds and microsecond regime respectively. For the sample not having undertaken rapid anneal as the final step, four peaks can be discerned. Annealing at 750 °C shows 3 identifiable peaks, but their width suggests multi-species distribution. Further increasing the annealing temperature to 800 °C reduces the width. For T_{RA}=850 °C we observe 2 closely spaced fast distribution components, followed by a narrower intermediate and long lifetime component. Next, 3 narrow distributions are present for 900 °C anneal whereas the FWHM widens for all peaks on the 950 °C treated sample. Higher temperature anneal overall appears to diminish the contribution of intermediate

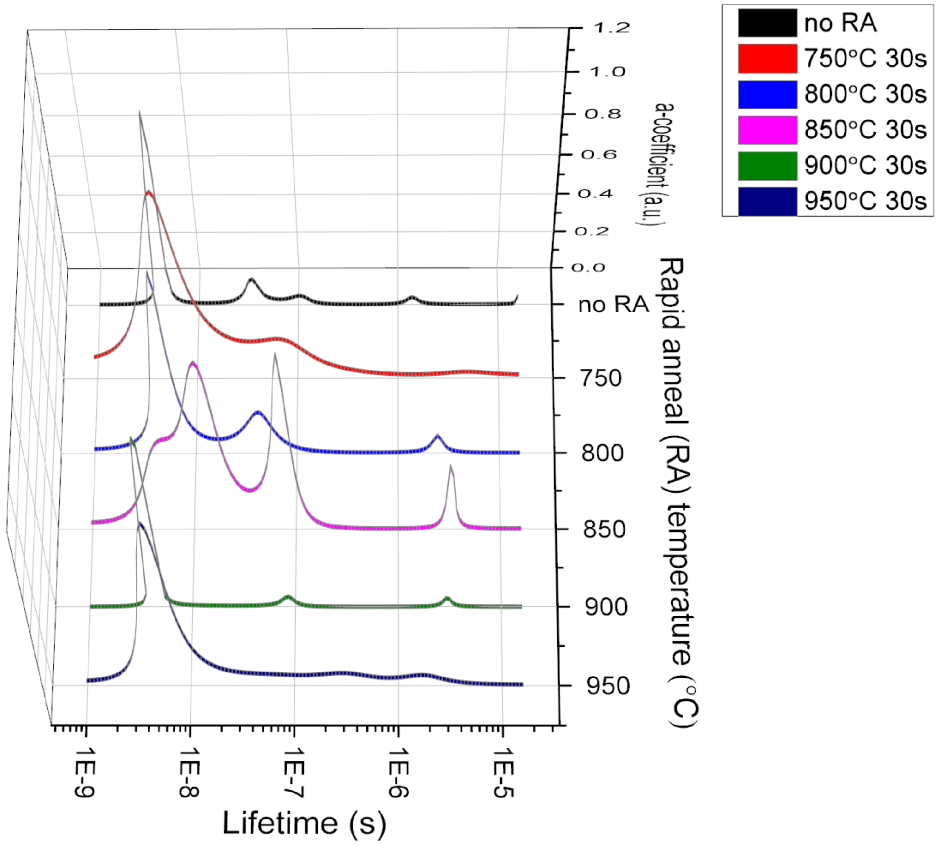

Figure 5.17: Modelled lifetime distribution for 1×10^{19} Er 1×10^{20} O (cm^{-3}) concentration series following a two-step anneal with different temperatures rapid anneal (B series in table 4.1).

and slow components.

For longer rapid anneal duration at temperatures above 850 °C, fig. 5.18 shows the introduction of more peaks. Peak centre location and FWHM are also affected. Using the smoothed data points for all datasets provided identical results, with the exception of the sample annealed at 950 °C for 50 s, where the model produced 4 distributions instead of 3. It was found that very small changes to the offset of the decay reverted the output to 3 wider distributions similarly to the un-smoothed dataset.
Altering the concentration of Er or the ratio of Er:O also results in visible changes in the lifetime distribution spectrum as shown in fig. 5.19.

To compare all the distribution spectra amongst each other as well as contrast them to our earlier model, numerical values for peak centres from the modelled distribution were tabulated alongside the extracted 3-part exponential parameters. These results can be found in the Appendix and provide an insight into the validity of our selected decay

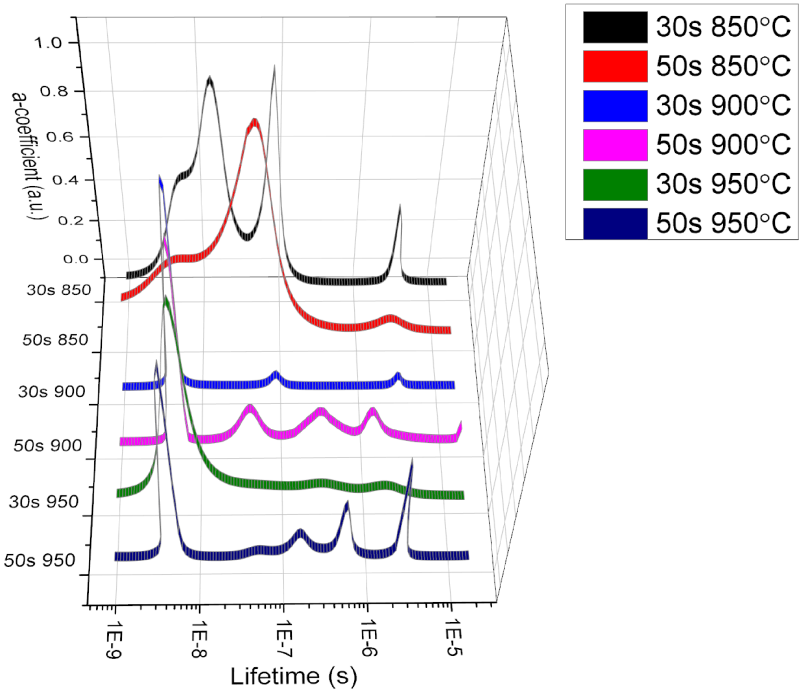

Figure 5.18: Comparative graph of lifetime distribution for groups of samples annealed at the same temperature for different time duration. Sample names can be found in table 4.1.

representation function in previous sections. Some of them are in excellent agreement. Others, whilst in the same numerical range present slight differences; a few indicate that the previously adopted model might be an oversimplification.

Excellent agreement of distribution values with our extracted fitting parameters is achieved for the 1×10^{19} Er and 1×10^{20} O (cm^{-3}) series (B series) annealed at 800 °C, 850 °C and 900 °C; an exception being the short component output of the 850 °C. In this case, it is seen that the lifetime distribution average of the narrow spaced components provides the same value with the fitting algorithm. Results for the 1:100 Er:O ratio sample (sample C3) are also in very good agreement with the fitting model, the slight variation in the longest component potentially being attributed to its very small overall contribution and its large FWHM. The same could be said for the 1:10 1×10^{18} Er (cm^{-3}) sample (sample C1), where peak 3 and 4 (from left to right) on our distribution are similar to fitted parameters. Yet, the fitting algorithm does not seem to account for the 2^{nd} peak. Moreover, deviation is observed on the values of the fastest distribution component. Likewise, samples annealed for 50 s, the sample annealed at 750 °C for 30 s and the sample without final rapid anneal present limited numerical agreement while remaining in the same range. It is possible that these samples

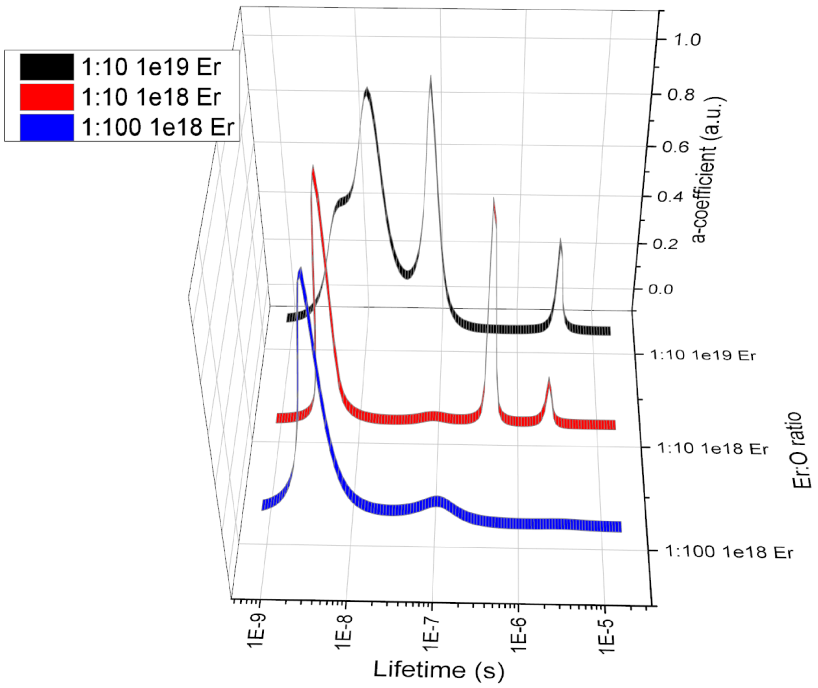

Figure 5.19: Lifetime distribution for different Er:O ratio samples annealed with T_{RA}=850 °C for 30 s.

required a different decay model approach. However, as one can see in fig. 5.20 it is quite difficult to discern between the fitting of our selected 3-part exponential decay model and the continuous lifetime distribution fitting results. This is true for both samples whose outcomes with both methods are in excellent agreement (fig. 5.20(a)) as well as samples whose results differ (fig. 5.20(b)). The latter sample was deliberately chosen since it also produced offset dependent variation in the amount of distribution peaks observed (see fig. 5.20(b)). Whilst both selected offsets were plausible given the amount of noise present in the original data (not shown), the fitting outcomes were almost indistinguishable. Thus, we conclude that considering the experimental limitations, the 3 part exponential fitting model was a good overall assumption.

Finally, it is interesting to note that for the B series samples annealed at 850 °C for 50 s, 900 °C for 30 s, 950 °C for 50 s, 850 °C for 30 s and the C series 1×10^{18} Er (cm^{-3}) for both 1:10 and 1:100 Er:0 share the same fast component centre of gravity of approximately 5 ns. Similarly, the 1×10^{19} Er (cm^{-3}) line samples annealed at 750 °C, 800 °C and 950 °C for 30 s have common fast component peak centres at 5 ns. This grouping can be expanded to include peak 2 for samples annealed at 950 °C for 30 s, peak 3 for 900 °C for 50 s as well as longer components for 1:10, 1:100 Er:0 with 1×10^{18}

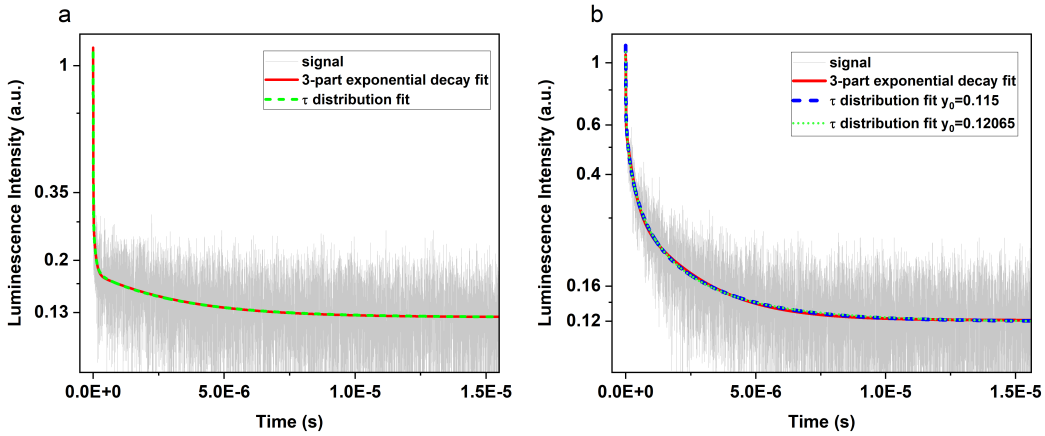

Figure 5.20: Comparison between the selected 3-part exponential decay fit and lifetime distribution output fits. On (a), 1:10 Er:O 1×10^{19} Er (cm^{-3}) sample annealed at 900 °C for 30 s whose outputs were in excellent agreement. On (b), sample annealed at 950 °C for 50 s whose outputs showed differences. Fits for 2 different distribution offsets resulting in peak number variation are also present for comparison.

Er (cm^{-3}), 1×10^{19} Er (cm^{-3}) samples annealed at 850 °C for 30 s, 800 °C for 30 s and 950 °C for 50 s.

We suggest that this trend is evidence of formation of similar Er^{3+} sites amongst the grouped samples, with each site having lifetime distributions centered at τ_i. This would confirm the validity of our earlier assumption at allocating the fitted lifetime components to different erbium ion classes as well as our postulating that some lifetime centres might be identifiable through cross-examination of photoluminescence spectra. On the same note however we confirm the difficulty faced in extracting the precise relationship between lifetime and amplitude despite the method used. Lastly, variation of peak centres amongst samples agrees with our previous suggestion that formation of different Er defect complexes is strongly dependent on processing conditions and affects (amongst others) the observed lifetime behaviour.

5.6 Chapter summary

This chapter investigated the luminescence lifetime of Er:Si samples. In section 5.1.2, luminescence from all centres was collected and analysed using a three part exponential decay model. Extracted results included a fast (≈5 ns) as well as an intermediate (≈50-100 ns) and slow (≈2 μs) component for all samples irrespective of processing conditions. The individual components with associated lifetime τ_i were ascribed to Er^{3+} ions located in three different environments. The derived lifetime values would represent the mean lifetime of all transitions affiliated with that centre. Section 5.3 discussed the

unlikeliness of occurrence of such an unreported ultrafast radiative lifetime in an erbium related solid system and suggested the involvement of a previously unseen non-radiative quenching pathway. Linking the findings with earlier observations it was proposed that the same defect state assumed to exist in section 4.4.3 is responsible for the decreased emission lifetime due to interaction and energy transfer between the middle state and the optically active erbium ions. This model was explained in section 5.3 with the universal appearance of the nanosecond lifetime component potentially implying that this defect state is continuous. Implications of this state's formation on the observed lifetime and quantum efficiency were discussed in section 5.3. To directly compare samples, calculations of average lifetime were performed in section 5.4. The maximum average lifetime was found for sample B3a with 30 s rapid anneal treatment at 850 °C. The average lifetime was linked to the ratio of the two distinct erbium sites and variations in optically active erbium centres in the samples. Notably, for different Er:O concentration ratios it was found that higher erbium concentration does not quench the lifetime confirming that the nanosecond component is not a result of ion-ion interaction or precipitates. Finally, section 5.5 employed a continuous lifetime distribution model whose output validated the 3-part exponential decay model selection.

6.ELECTRICAL CHARACTERISATION OF ER:SI

6.1 Thermopower measurements

6.1.1 Seebeck effect

The Seebeck effect, also known as thermopower, is a method allowing the identification of the majority carrier type of a material. Its operation principle relies on the conversion of a temperature difference into a potential difference, thus driving an electrical current in a conductor or semiconductor [177]. Named after Thomas Johann Seebeck who formulated it in 1821 this effect arises from thermal energy of electronic carriers [178]. Briefly, a temperature gradient across the device leads to an increase of the hot end's carrier thermal energy and consequently average velocity compared to the cold end. Diffusion of the thermally excited (charged) carriers towards the cold end results in the generation of a thermoelectric voltage. The direction of the voltage difference enables the determination of the majority carrier type. In time, as the energy stored in the carrier generated electric field balances the thermal energy, further diffusion is prevented. Equation (6.1.1) defines the Seebeck constant S, where ΔV and ΔT are the potential difference and temperature difference respectively between a set of two points on the sample.

$$S = -\frac{\Delta V}{\Delta T} = -\frac{V_{\text{left}} - V_{\text{right}}}{T_{\text{left}} - T_{\text{right}}} \tag{6.1.1}$$

Experimental setup

Our heating source consisted of a cylindrical heated element with a conical end upon which the sample's 'hot end' rested. The other end of the sample -labelled 'cold end'- was placed on the edge of a probe station's chuck. The probe station included manipulators on XYZ stage for positioning adjustments. Tungsten probe tips of 0.5 mm radius were mounted on the end of the manipulators' arms. A Keithley 236 source meter was utilised for the voltage readout. Its triaxial connectors allowed for the use of shielded triax cabling, therefore minimising external electrical noise that could affect our very small thermopower signal. For temperature readout, two Omega 5SRTC-TT-K-40-36 precision fine wire thermocouples were placed next to the individual probe tips to ensure temperature difference was determined at the same point with the electrical measurement, as illustrated in fig. 6.1. Temperature values were displayed on a computer after interfacing the thermocouples to a temperature controller unit (see section 6.1.1 below).

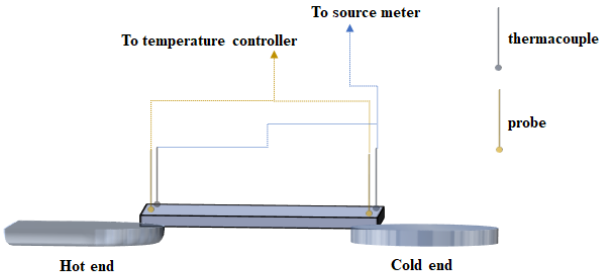

Figure 6.1: Simple illustration of Seebeck experiment setup sample positioning.

Measurement automation

The heating source had an associated power supply with internal PID control that could not be modified. There was a minimum power output leading to a temperature of approximately 160°C at the heating element's core for the lowest setting. The small sample size contributed to fast heat diffusion across the sample, but overall the measurements presented below focus on relatively large temperature difference. Due to the large temperature fluctuations resulting in a range of ΔT for a set heating source temperature, collection of multiple sets of voltage and corresponding thermocouple readings was deemed preferential, in order to reduce measurement error. To this end, LabVIEW (Laboratory Virtual Instrument Engineering Workbench) was used to interface across our devices. A Pico Technology USB TC-O8 temperature logger was used to record the thermocouple readings and store the values in an array. Correspondingly, the Keithley voltage output was stored in a separate array. A total number of 120 readings was taken with 1 second settling time between each voltage-temperature pair, in order to account for the thermocouple's time constant. A flow diagram of this process is indicated in fig. 6.2.

Upon testing the system at zero temperature difference (at room temperature), a small generated voltage was detected. At first, it was thought that it might be due to localised temperature differences from air currents in the room. To examine this, the thermocouples were calibrated against each other with hot and iced water. This was followed by logging the 'hot' and 'cold' sample end temperatures for two minutes. A small temperature oscillation was indeed present however the temperature difference was negligible. It was speculated that this voltage could be a result of probe contact with the sample, or an instrument error. Since the value did not remain constant across our samples, it was recorded at the start of each run and treated as an offset during data analysis.

A visual representation of setup automation testing is seen in fig. 6.3. Here, we

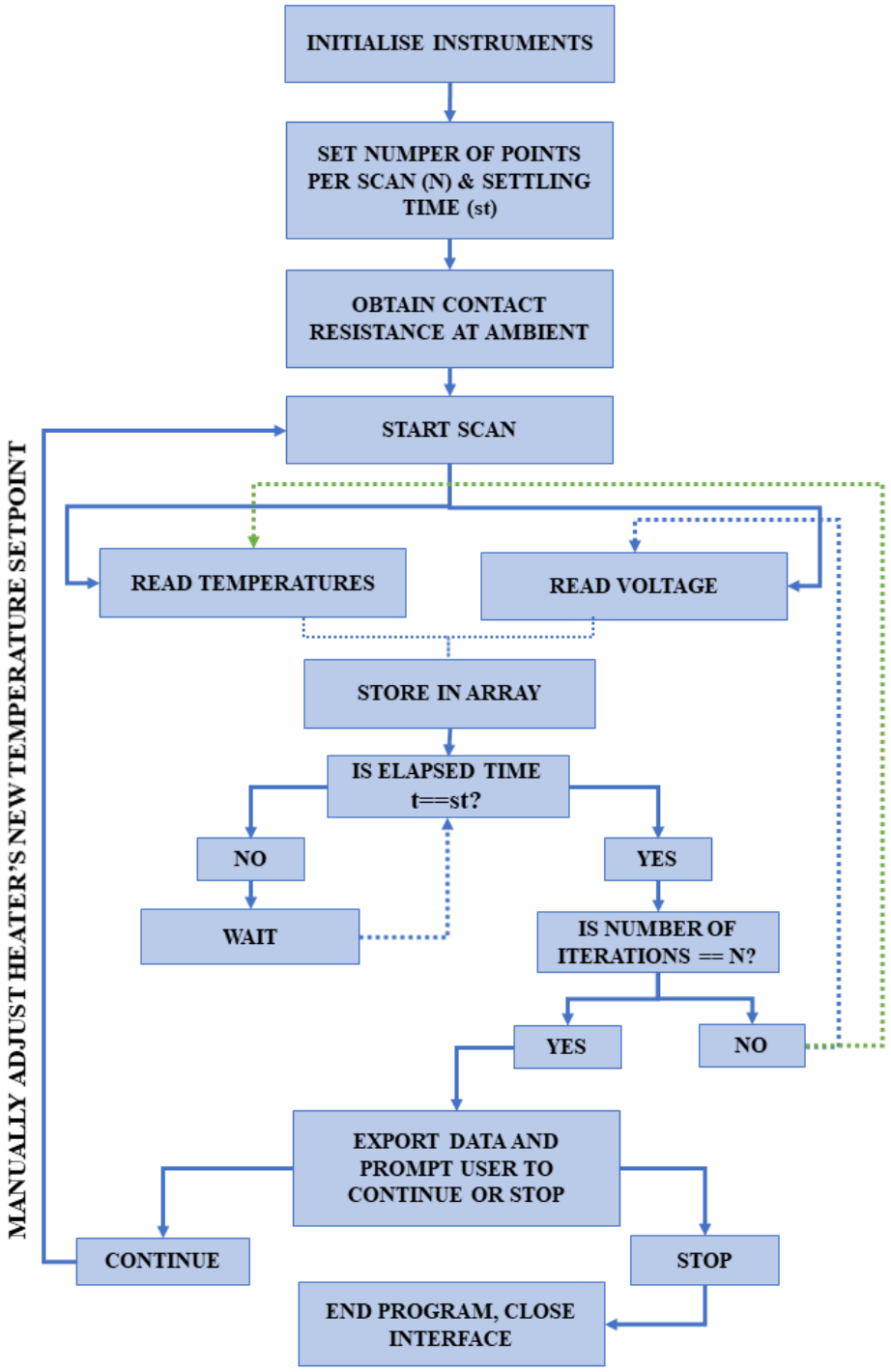

Figure 6.2: Simple flow chart of the programming process for Seebeck measurements.

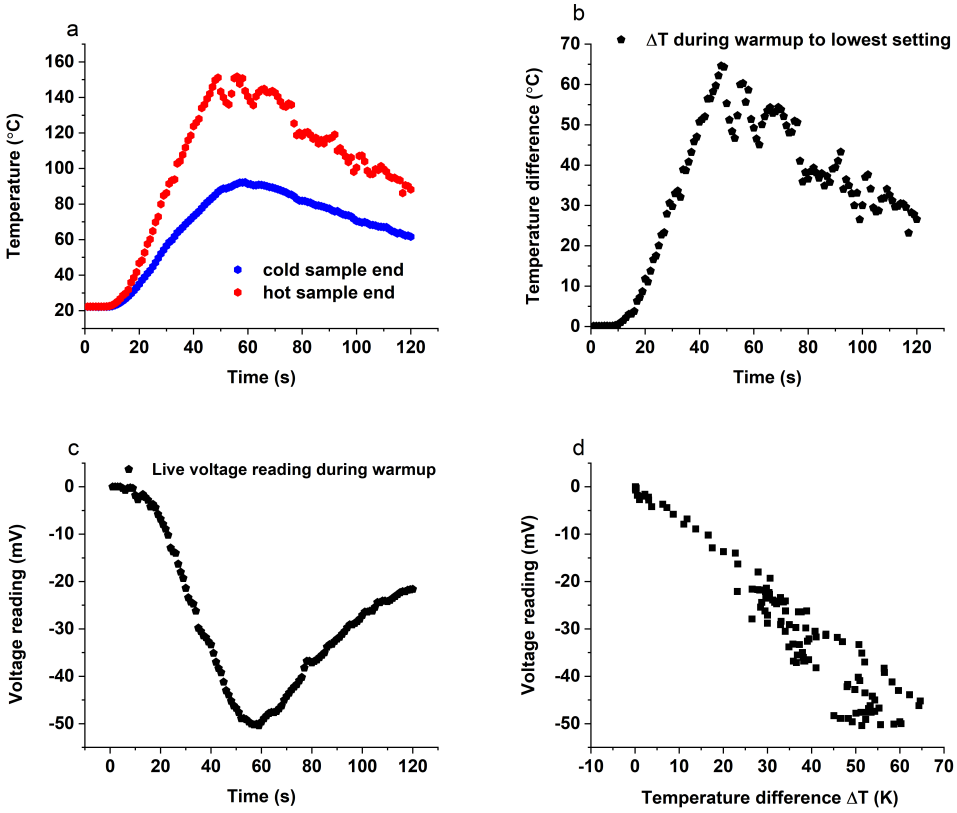

Figure 6.3: Real time data collection plots for sample B2 from room temperature until the lowest heater setting point. In (a), thermocouple outputs during the run, (b) the associated temperature difference (c) the obtained voltage as a function of time and (d) the obtained voltage as a function of temperature difference.

tested the real time responsivity of our system from room temperature, to the lowest power setting of our heat source. The gradual increase of the sample's cold end is seen in fig. 6.3(a); it is also evident that the cold end temperature fluctuates minimally, whilst oscillations in hot end temperature match the heat source's PID control power output variation overshooting or undershooting its set value. This oscillation reflects in the temperature difference ΔT ((b) in same figure), as well as the voltage-ΔT plot on (d). To this end, for every set heater output there was a waiting time of 2 minutes to stabilise the temperature as much as possible. Afterwards, 120 data points were collected with a rate of 1 point per second, to ensure thermocouple reading has settled. Measurements were taken for both increasing and decreasing heater power output. From the exported data sets, the contact potential was offset from the voltage readouts and the temperature difference for each point was obtained. Average values were then calculated alongside their respective standard deviation. Whilst the inclusion of a large data set could allow for the use of standard error, it was thought that standard deviation was more representative

of the 'true' error accounting for the heater's fluctuating output.

6.2 Results

Seebeck coefficient results are presented in fig. 6.4. The negative coefficient value in-

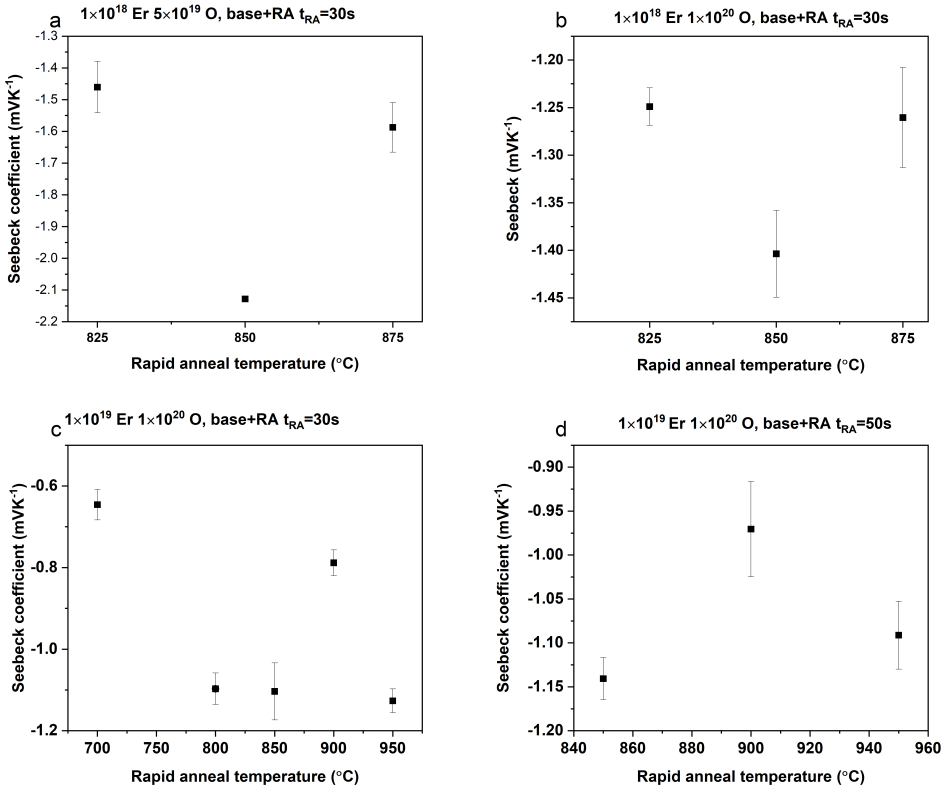

Figure 6.4: Seebeck coefficient for various Er:Si samples annealed at different temperatures. All presented samples followed a two-step rapid anneal treatment (recipe A in table 4.1 and rapid anneal.)

dicates the samples are primarily n-type. This is to be expected, since as mentioned in section 2.6.2 the erbium readily complexes with near interstitial oxygen atoms, the resulting Er-O species acting as a donor. Since electrical active centres are not necessarily optically active, there is limited information that can be extracted. It is shown in fig. 6.4(a),(b) that for shared erbium but higher oxygen concentration the Seebeck coefficient trendline is the same. Similarly in fig. 6.4(c),(d), for the B sample series (see table 4.1) the Seebeck coefficient attains a maximum at 900 °C. To complement the thermopower measurements, the resistivity of the samples was examined. Resistivity (ρ) measurements were taken by Mr. Andrew Smith using a four point probe setup. The results for some selected samples are presented in fig. 6.5. These samples were selected since they were the only line amongst our devices with enough temperature parameter

variation (here the annealing temperature) to have a basis for comparison (recall that there are only 3 different Er:O concentration samples and only sets of two for the different rapid anneal time duration samples). The resistivity follows a fairly constant relationship

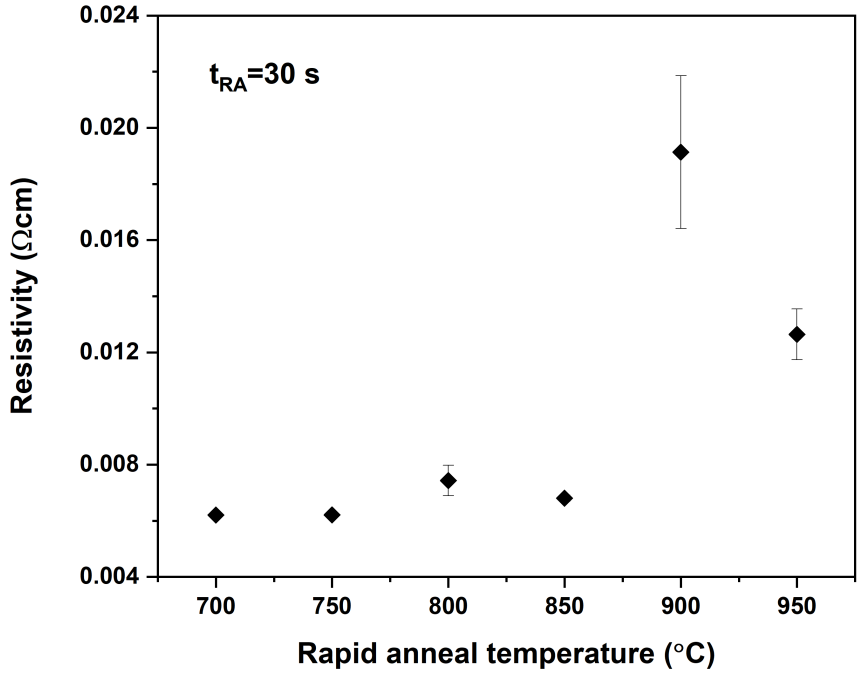

Figure 6.5: Resistivity measurements for the B sample series 1×10^{19} Er and 1×10^{19} O (cm^{-3}) following a two step anneal treatment with 30 seconds rapid anneal duration. See table 4.1 for sample details.

for lower rapid anneal temperatures with a mild increase for T_{RA}=800 °C. At 900 °C, there is an abrupt increase followed by a slight decrease at 950 °C. Since the resistivity is inversely related to conductivity, these results could connect to carrier concentration and mobility. It is possible that the crystal field structure can affect the carrier distribution in the crystal lattice and thus influence the material resistivity. This argument could relate to photoluminescence measurements in section 4.3 where a sudden shift in the ratio of the two observed erbium sites was seen at T_{RA}=900 °C. Further investigation would be required in order to establish a link between electrically active and optically active centres.

6.3 Chapter summary

This short chapter addresses electrical measurements of Er:Si. Information of the carrier type was provided through successful built and automation of a thermopower measure-

ments setup. The samples were found to be n-type in agreement with literature. Four point probe measurements showed the resistivity range is shared amongst all samples. For the 2 step annealed B sample series, a maximum resistivity is attained at 900 °C. This temperature coincides with the apparent change of preferential erbium site symmetry formation; therefore it is possible that carrier distribution and resistivity are affected as a result of different crystal field environments. The relationship between electrically and optically active centres remains to be established.

7.PHOTON ECHO SPECTROSCOPY OF ER:YSO

This chapter aims to discuss the development of a two pulse photon echo setup for optical coherence measurements. In particular, erbium doped crystals were of interest due to the Er^{3+} transition falling in the 1.5 μm spectral range where fused silica fibres have a window of minimum loss. Proof-of-concept measurements are presented for Er^{3+}:Y_2SiO_5, and the material's potential usefulness for quantum memory applications is briefly discussed.

7.1 Crystal structure of Er^{3+}:Y_2SiO_5

7.1.1 Energy levels of Er^{3+}

As discussed in section 2.1, trivalent erbium (Er^{3+}) has a $^4f^{11}$ electron configuration. This odd-electron configuration plays a direct role in the formation of Er^{3+} energy levels. For the free ion, angular momenta J and M_j are good quantum numbers and the energy levels are $(2J+1)$ - fold degenerate giving rise to multiplets labeled by J. Incorporation of the ion into a crystal results in reduced crystal field symmetry and distortion of the $4f$ waveforms, partially or fully lifting the $(2J+1)$ fold M_J degeneracy. For ions with an odd number of electrons, Kramers theorem dictates that all levels have degeneracy that can only be fully lifted by a magnetic field [179]. As a result, in the absence of a magnetic field, the crystal field can only partially lift the degeneracy to a maximum of $J+1/2$ electronic doublets of state $|M_J| = J, J-1, J-2...., 1/2$, depending on the ion's site symmetry. The $^4I_{15/2}$ ground multiplet can therefore split into 8 Kramers doublets, whilst the $^4I_{13/2}$ multiplet can split into 7. At cryogenic temperatures, only the lowest energy doublet of the ground state will be populated and so the system can be thought of as having an effective spin $S = 1/2$. For the even isotopes which lack nuclear spin, the states are not split any further past the degenerate doublets. There are several stable isotopes of erbium, however ^{167}Er is the only one with a non-zero nuclear spin ($I = 7/2$). The interaction with the electron spin lifts the degeneracy of the spin 1/2 doublet even without a magnetic field, resulting in 16 hyperfine substates arising from the possible state combinations of I and S, shown in fig. 7.1. Transition frequencies between these states vary from nearly 0 to 5 GHz, and change in an applied magnetic field.

Transitions between the $^4I_{15/2} \rightarrow^4 I_{13/2}$ lowest energy doublets (namely Z_1 and Y_1 respectively) are around the 1.5 μm spectral region, namely the telecom C-band, where optical fibre transmission losses are at a minimum, and is therefore of interest to technological applications. These Z_1, Y_1 levels will serve as the ground and excited state

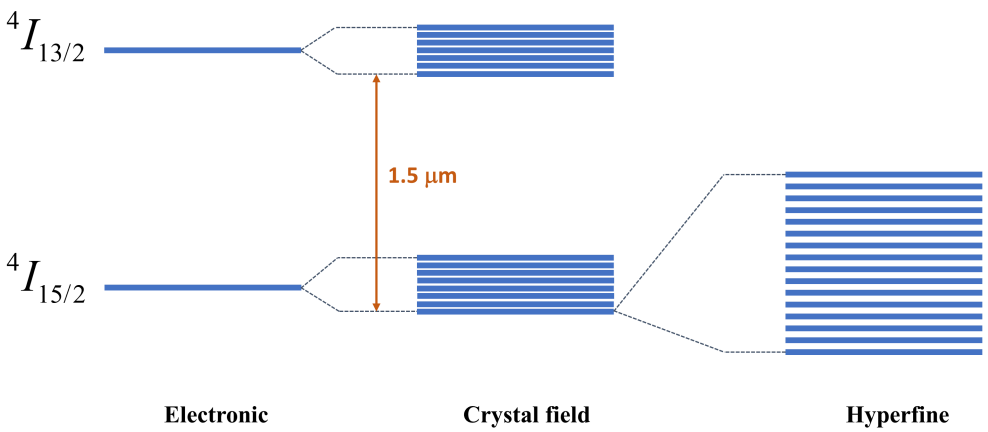

Figure 7.1: Energy level structure of $^{167}Er^{3+}$ in a crystal host.The crystal field splits the electronic states into doublets, and the lowest energy doublet is split into 16 hyperfine levels by the nuclear spin.

of the two level atom for coherent transients. Magnetic dipole transitions between these states are allowed with selection rules $\Delta J = 0, \pm 1$ and $\Delta M_J = 0, \pm 1$.

7.1.2 Yttrium Orthosilicate as the host crystal

Yttrium orthosilicate (Y_2SiO_5) is a well known host material for use with rare-earth dopants. Its potential to achieve ultraslow optical dephasing at low temperatures is due to the low magnetic moments of its consituent elements (-0.137 mu_N for ^{89}Y), or small abundance of magnetic isotopes (4.7% for ^{29}Si and 0.04% for ^{17}O) [180]. This is because one of the primary sources of dephasing or "noise" in a rare-earth doped crystal is caused by the fluctuating magnetic field at the rare-earth dopant arising from spins in the host crystal. As a result, by minimizing the magnetic moments in the host lattice dephasing due to this 'noise' can be dramatically reduced [181].

The crystal structure of Y_2SiO_5 shown in fig. 7.2 is monoclinic with space group C_{2h}^6 and so has two-fold rotational symmetry along its C_2 axis. The lattice constants are given as: a=1.041 nm, b=0.6721 nm, c=1249 nm and $\beta = 102°39'$. The C_2 space-group symmetry axis corresponds to the crystallographic b axis, while the crystallographic a and c axes are located in the mirror plane that is perpendicular to b [182]. It is quite common in work involving Y_2SiO_5 to follow the convention by Li et al. and specify the sample orientation by labelling the optical extinction axes $D1$ and $D2$ which are perpendicular to each other and in the same plane as a and c [185]. The relationship between the two axes sets is found using Laue x-ray diffraction and is of important since clockwise and anticlockwise rotations about the C_2 axis are not equivalent [186] (see below). The

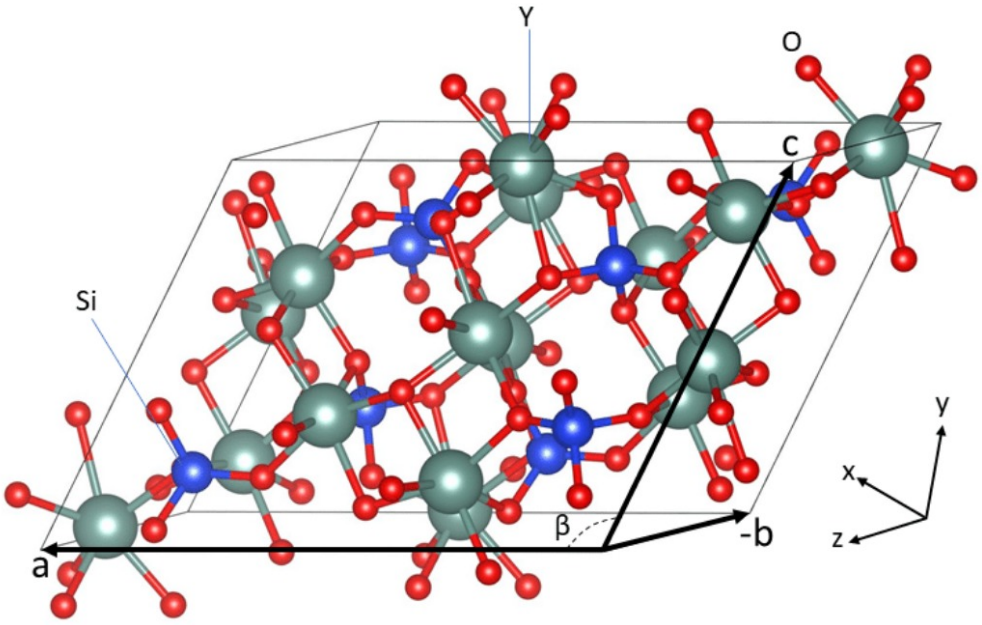

Figure 7.2: Schematic representation of a Y_2SiO_5 unit cell consisting of 64 atoms and with the commonly used (B2/b, 15) crystal structure. Several space groups exist for this material; group selection can change depending on researcher (i.e. [183] used the I2/a group). The unit cell is comprised of basic molecules of Y, Si, and O shown as gray, blue and red spheres respectively. Lattice parameters are denoted as a, b, and c. Image reproduced under Creative Commons free licence from [184].

orientation of the sample with respect to this set of axes is shown in fig. 7.3. Each unit cell is made up of eight Y_2SiO_5 molecules, and there are two substitutional sites Y_1 and Y_2 occupied by yttrium atoms. Both sites have a triclinic point-group symmetry C_1 and are distinguished by their coordinate numbers of six and seven respectively, referring to the number of bonds each site has to surrounding oxygen atoms [187].

Trivalent erbium (Er^{3+}) ions substitute for Y host ions without charge compensation at one of those two crystallographycally inequivalent sites, referred to as site 1 and site 2 [183]. Due to Y_1 and Y_2 having different crystal structure, transition frequencies differ between the two sites. Furthermore, for a RE^{3+} ion substituting at one of these sites there are additional subclasses of ions due to the C_{2h} space-group symmetry of the unit cell. As a result, each site can also exist in four different orientations, related by the C_2 rotation and inversion. Two of theses sites are related by inversion symmetry; for these sites, application of a magnetic field will not result in different spectra as the two inversions are magnetically equivalent (meaning that their interaction upon application of a magnetic field in an arbitrary direction is identical) [188]. However, sites related by the rotational symmetry of π multiplicity (rotation of the C_2 axis) have distinguishable

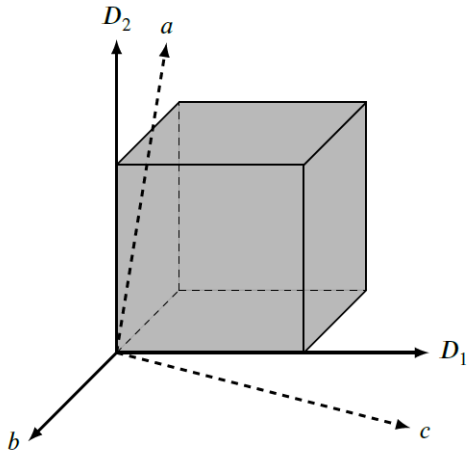

Figure 7.3: The crystallographic axes of the space group C_{2h}^6 for monoclinic Y_2SiO_5. Image re-used from [187] under Creative Commons 3 attribution license.

interactions with an external magnetic field, and will result in different spectra unless the magnetic field is applied along the b axis, or in the $D_1 - D_2$ plane [186]. Theses interactions will be of context in section 7.5.2.

7.2 Theoretical Concepts and Approximations

This section follows the formalism of [37] and [189]. Relevant chapters and page numbers will be referred to in text.

A two-level atom can be treated in the same way as a spin-on-half particle in a magnetic field. The basic dynamical equations derived from Schrodinger's equation governing the evolution of two-level atom variables are practically the same as those appropriate to spins. As a result, the spin vector formalism of Bloch, developed for magnetic resonance, applies to optical resonance problems too.

7.2.1 Optical Bloch vector model

The optical Bloch equations are the equations of motion for the optical Bloch vector, derived from population matrix treatment for an ensemble of harmonically excited two-level systems [189]. The model is based on electric-dipole analogues of relations governing spin-precession in magnetic resonance, where the electric dipole has an associated "pseudospin" vector $\mathbf{s}(t)$ (see Chapter 2, pp. 40-46 in [37]). The model's main results originate from relations derived by semi-classical radiation theory of two-level atoms, including the conservation law associated with the expectation values that leads to $\mathbf{s}(t)$ being a unity vector. As a result, the pseudospin can be visualised as tracing out an orbit on a unit sphere with a known torque acting on it. For an observer in the rotating frame, an appropriate rotation matrix is introduced for $\mathbf{s}$ by defining a nearly stationary pseudospin vector ρ in the rotating frame with components u, v and w obeying equations of motion such that:

$$\dot{u} = -(\omega_0 - \omega)u, \tag{7.2.1}$$

$$\dot{v} = +(\omega_0 - \omega)u + \kappa\mathscr{E}w, \tag{7.2.2}$$

$$\dot{w} = -\kappa\mathscr{E}v \tag{7.2.3}$$

where ω_0 is the transition frequency, ω the laser frequency and κ is defined so that $\frac{\hbar\kappa}{2} \equiv d$ with $\hbar$ being Planck's constant and d the magnitude of the dipole matrix element.

Component w, referred to as inversion, measures population inversion between ground and excited state while u and $-v$ produce the in-phase and in-quadrature polarization components with respect to the field E when multiplied by the ground-excited dipole matrix element. Visualisation of the optical Bloch equations in fig. 7.4 show vector $\rho \equiv (u, v, w)$ precessing in a cone about an effective field Ω following $\frac{d}{dt}\rho = \Omega \times \rho$ where Ω is the effective field with $\Omega = (\kappa E_0, 0, \Omega^{'} - \omega_0)$. Note that the strength of the

interaction between molecules and magnetic field κE_0 and the detuning of the field from resonance $\Omega^{'} - \omega_0$ lie on the I-III plane respectively. So in thermal equilibrium, κE_0, u, v are zero so ρ is zero too and ends up pointing towards the -III axis. When an optical field E_0 is present, however, ρ begins moving in a cone about Ω introducing polarization components u and v resulting in population difference w. This representation fits a system absorbing or emitting radiation and will act as the basis model to describe the photon echo phenomenon encountered later on.

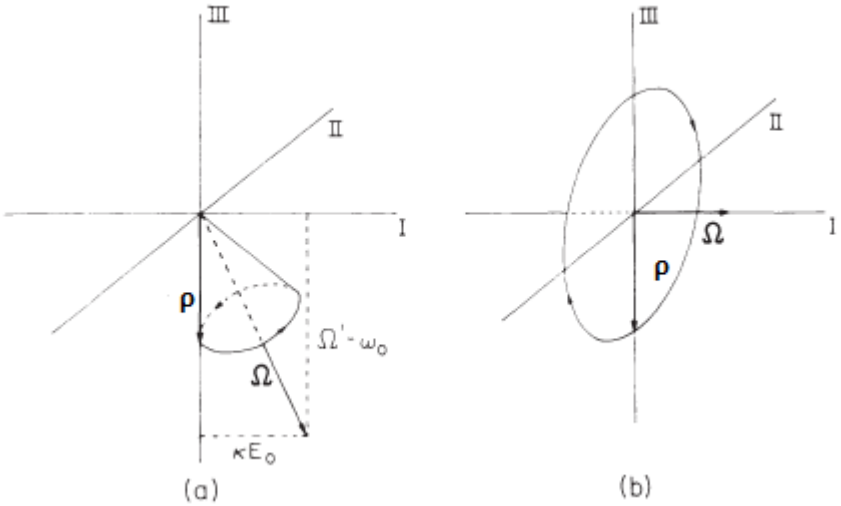

Figure 7.4: The vector model of a transition. (a) the driving vector Ω causes ρ to precess in a cone about Ω. (b) at exact resonance the cone of precession flattens into a circle in the II-III plane. Image modified from figure 3-4 in [189].

7.2.2 π pulses

The Bloch equations 7.2.1-3 can be used to determine the rate of energy absorption at optical frequencies for a two-level atom with an associated Bloch vector. The simplest solution is referred to as a Rabi solution and applies to atoms exactly at resonance with the laser field (pp. 53-56 in [37]).

Let $\theta(t)$ be a dimensionless quantity defined by:

$$\theta(t) = \int_{-\infty}^{t} \kappa \mathscr{E}(t^{'})\, dt^{'} \tag{7.2.4}$$

where $\mathscr{E}$ is the amplitude of a driving field $E = \mathscr{E}[e^{i\omega t} + \text{c.c}]$ and κ as defined in previous section. Thus, 7.2.1 becomes:

$$u(t;0) = u_0, \tag{7.2.5}$$

$$v(t;0) = w_0 sin\theta(t) + v_0 cos\theta(t), \tag{7.2.6}$$

$$w(t;0) = -v_0 sin\theta(t) + w_0 cos\theta(t) \tag{7.2.7}$$

where $u_0 = u(0;0)$ etc., and the zero in $u(t;0)$ and $w(t;0)$ refer to the detuning frequency $\Delta = \omega_0 - \omega$. Here, $\theta(t)$ can be viewed as the upward tipping angle of the vector $\boldsymbol{\rho}$ for an on-resonance atom. Integration of 7.2.4 for a steady value electric field $\mathscr{E}_0$ between t_1 and t_2 gives:

$$\theta = \kappa \mathscr{E}_0 (t_2 - t_1) = \Omega(0)(t_2 - t_1) \tag{7.2.8}$$

where $\Omega(0) = \kappa \mathscr{E}_0$ determines the rate at which transitions are coherently induced between two atomic levels and is referred to as the Rabi frequency. For an initially relaxed atom with $w_0 = -1$ and $u_0 = 0$ one can notice that after a time interval δt such that $\kappa \mathscr{E}_0 \delta t = \pi$, $w = +1$ resulting in the atom's state inversion from ground state to upper state. We saw that by definition a pulse envelope area can be represented as the net tipping angle θ [37]. As a result, resonant coherent radiation in the form of a square pulse with area of π, hereafter referred to as a π pulse, has the power to invert the atomic population.

7.2.3 Phenomenological decay constants

Because of interactions that can disturb the dipole oscillations off the resonant atom without disturbing its energy (such as phonon scattering in a solid), differences in decay rates between w, v and u have created the need for the introduction of some phenomenological decay times: A decay time T_1 is assigned to the inversion whilst dipole moment decay is noted as $T_2^{'}$. These are referred to as longitudinal and transverse homogenous lifetimes respectively. Finally it is worth observing that $T_2^{'}$ only describes moment lifetime effects due to incoherent interactions that affect homogenously all atoms, whereas inhomogenous lifetime effects (i.e. local strains in solids, see section 2.4) are described through T_2^*. The random distribution of resonant frequencies leads to a dephasing of the ensemble's individual dipole moments and a macroscopic polarisation damping regardless of the behaviour of $T_2^{'}$ and therefore total transverse decay time namely T_2 is defined as (pp. 60-61 in [37]): $\frac{1}{T_2} \equiv \frac{1}{T_2^{'}} + \frac{1}{T_2^*}$.

Incorporation of the decay constants in the nonlinear Bloch equations 7.2.1 gives:

$$\dot{u} = -\Delta v - \frac{u}{T_2'}, \tag{7.2.9}$$

$$\dot{v} = \Delta u - \frac{v}{T_2'} + \kappa \mathscr{E} w, \tag{7.2.10}$$

$$\dot{w} = -\kappa \mathscr{E} v - \frac{(w - w_{eq})}{T_1} \tag{7.2.11}$$

where w_{eq} is an equilibrium value towards which the inversion relaxes when $\mathscr{E} = 0$.

7.3 Photon echo

This section follows Chapter 9 (pp. 195-220) of [37].

In the absence of a driving field, inhomogenous broadening causes the macroscopic polarization density P (and therefore the dipole oscillations) of the sample to damp out at a rate $1/T_2^*$. This damping can be observable as Free Induction Decay (FID). If one wanted to recover the energy stored in the dephased moment in a coherent fashion (via coherent emission), they should aim for the interval between T_2^* and T_2' after which each individual dipole will have relaxed to its ground state. We know that individual dipole moments get out of phase with each other due to their oscillating at different frequencies, which would imply that observation of the original phased condition for two dipoles with frequencies differing by $\delta\omega$ is possible after a time interval $\delta t = 2\pi/\delta\omega$. However, due to the continuous distribution $g(\Delta)$ of detunings from a fixed frequency, observation of the original phased condition would be highly unlikely and could only occur for an interval $\delta t \to \infty$; but if one was to interfere with the oscillations reversing their dephasing after a time t, one would succeed in engineering their rephasing at the time $2t$. Successful application of this principle was demonstrated in nuclear spin echo in 1950 by E.L.Hahn [190]. Photon echoes are the optical/electric dipole analogue of the spin echo effect, and were first demonstrated in ruby in 1964 [191].

7.3.1 Two-Pulse Photon Echo

Our assumption includes that the atoms begin in their ground state, so that $u_0 = v_0 = 0$, $w = -1$. For a field envelops $\kappa \mathscr{E}_0 > 1/T_2^*$.

In a two-pulse photon echo experiment, two laser pulses separated by a time delay, τ excite the sample as shown in fig. 7.5. The first pulse known as a $\pi/2$ pulse creates a coherent superposition of the ground and excited states through $\theta = -\pi/2$ rotation of the ground state vector $(-\hat{\mathbf{Z}})$ to to vector $\hat{\mathbf{Y}}$. After the first pulse, this coherent superposition state has a macroscopic oscillating dipole moment, whose re-radiation is

the free induction decay. For an elapsed time interval t_{12}, this dipole moment quickly dephases across the $\hat{\mathbf{X}} - \hat{\mathbf{Y}}$ plane.

A π pulse is then applied to the ensemble, and the vector representing each ion rotates 180 ° about the $\hat{\mathbf{X}}$ axis, reversing the time evolution of the ensemble. Hence after another time period of length t_{12}, the ensemble vectors rephase to the $-\hat{\mathbf{Y}}$ vector. Coherent light emission follows, due to the non-zero net polarisation of the ensemble. As t_{12} is increased, a reduction in intensity of the echo reflects the decay of coherence during the time $2t_{12}$, a result of stochastic processes in the crystal. Measuring the photon echo intensity as a function of time delay t_{12} between the two pulses yields for ideal two-level systems a single exponential decay as $\exp\{-4t_{12}/T_2\}$, whose time constant allows determining the dephasing time T_2 [192]. The first photon echo in Er^{3+}:Y_2SiO_5 was measured by Macfarlarne [180].

In the presence of spectral diffusion, where the homogenous linewidth evolves on a timescale of the pulse sequence, observed echo decays are non-exponential and can be described by the Mims expression: $I(t) = I_0 \exp\left\{-\frac{4t_1}{T_M}\right\}^x$ first introduced in the context of electron spin echoes and later used in the analysis of photon echoes. The parameter, x, describes the deviation from a pure exponential, while T_M corresponds to T_2, in the specific case of $x = 1$. An effective homogenous linewidth can be extracted from the phase memory time, T_M as $\Gamma_{\text{hom}} = \frac{1}{\pi T_M}$

Please note that in the sections to follow, the pulse separation t_1 will be referred to as t_{12}. Here, t_1 is used only due to the notation adopted in [80], where fig. 7.5 was obtained from.

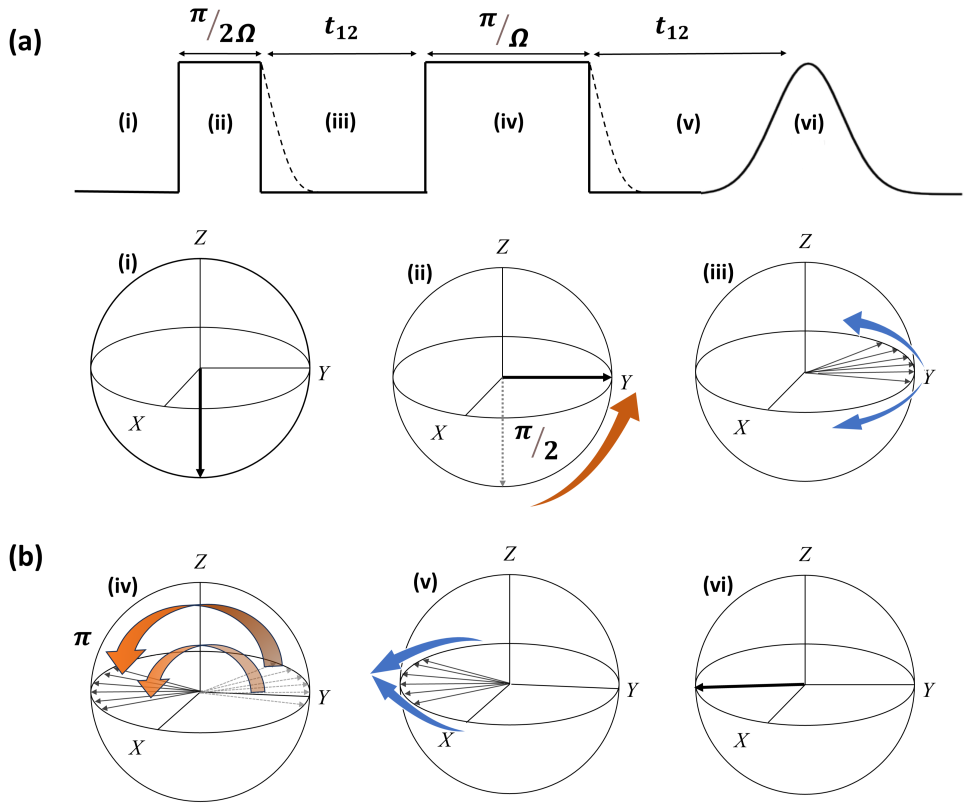

Figure 7.5: The stages of photon echo production: solid lines represent the applied light pulses, while dotted lines refer to the FID. In (a), dark lines represent the $\pi/2$ and π pulse light sequence (over stage (ii) and (iv) respectively), followed by photon echo emission in stage (vi). Dotted lines show the free induction decay (FID). Part (b) is a visual representation of the Bloch sphere evolution of the ensemble atoms. Part (i) shows the initial quantum state, part (ii) shows the application of the $\pi/2$ pulse with the resulting detuning (iii) followed by a π pulse in stage (iv). Rephasing (v) followed by coherent emission (vi) from the in phase ensemble ions concludes the sequence. Image re-created after [80].

7.4 Experimental set-up

A Thorlabs TLK-L1550R external cavity laser (ECL) kit in Littrow configuration was used as the light source for photon echo experiments. It consisted of a mounted Thorlabs Single-Angled-Facet (SAF) gain chip with center wavelength at 1550 nm, allowing for tuneability between 1530-1570 nm. Tuning adjustment was achieved by controlling the angle of incidence for light onto the external grating using a DC Servo Motor. The laser output was amplified to about 72 mW using an erbium doped fibre amplifier (EDFA). Control interfacing was achieved using Visual Basic and was performed by Dr. Michael J. Dowhyj. Wavelength calibration was done with the aid of a Thorlabs OSA 203B Optical Spectrum Analyzer (OSA). Motor position and OSA wavelength output were found to follow a linear relationship. Since there was no continuous access to the OSA, measurements were periodically recorded and the obtained gradient and intercept were saved in a text file which was programmatically called to recalibrate any drifting wavelength caused by motor missteps. Two Stanford digital delay/pulse generators (DG535) were used to create the pulse sequences used and acousto-optic modulators were employed for light frequency modulation. The Pulse Generating DG535 was internally triggered to set the frequency.

The DG535 pulse sequence is formed by setting relative time delays between the input channels as seen in fig. 7.6. In our case, the output AB formed the $\pi/2$ pulse whilst output CD formed the π pulse. All channels were set as variable outputs, with the exception of channel A whose TTL output acted as a trigger for the Lock-in amplifier. The AB and CD channels' output were used to digitally drive the RF power supply of the 'fast pulse AOM' ,whilst the T_0 output was connected to the 'envelope' AOM through its analog input. The function of the 'envelope' AOM was to improve the on/off contrast ratio. The 'envelope' AOM was externally triggered from the 'pulse' DG535. To account for rise time differences amongst the equipment, as well as to avoid signal 'clipping", 'rise' and 'fall' offsets were introduced programmatically. Pulse output was monitored using a Tektronix TBS 2000 series Digital Oscilloscope.

The beam was focused inside the crystal to a waist of (358±3.91) μm with ($1/e^2$diameter) spot (see section 4.2.3) at about 50% absorption (≈36 mW). A third acousto-optic modulator was used to 'gate' the echo by switching the echo signal from the transmitted beam. The echo was then detected by a Thorlabs InGaAs photodiode, and averaged with a Stanford Research SR830 Lock-In Amplifier. Upon completion of the first coherence scan, the pulse separation would increase by a given value (namely the stepping size) and the gate sweep would restart. The 2D set of data (Lock in output as a function of gate delay, for a particular pulse separation) could then be combined for all acquired

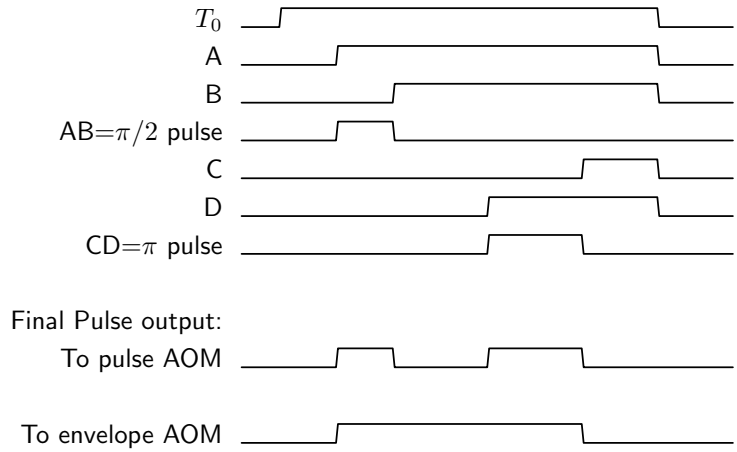

Figure 7.6: Pulse generation sequence using the DG535. Please note that the envelope AOM graphic does not incorporate the experimental rise and fall offset delays but rather depicts an ideal scenario.

t_{12} pulse separations, and a 3D plot would be built for better understanding of the echo's behaviour. Two-pulse echo decay curves were obtained for ions at both sites 1 and 2 (see section 7.1.2 and [183]) for several values of the external field B. All experiments were conducted in an Oxford Spectromag cryostat superconducting magnet system capable of producing magnetic fields up to 7 T. With minor exceptions, the sample was maintained at a temperature of 1.6 K. The crystal under investigation was purchased from Scientific Materials Corp. (growth number 2-430, $10 \times 10 \times 1$ mm^2) and had nominal Er^{3+}-dopant concentration of 0.02%. There was no known crystallographic information at the time of the experiments, so the crystal was placed with its front facet perpendicular to the propagation direction of light and the external magnetic field applied perpendicularly to the light propagation direction. The results presented have a typical pulse separation (t_{12}) of 800 ns, gate width of 200 ns, and are averaged 3 times over a time constant of 300 ms. The repetition rate is set to 48 kHz. A simple representation of the setup can be seen in fig. 7.7.

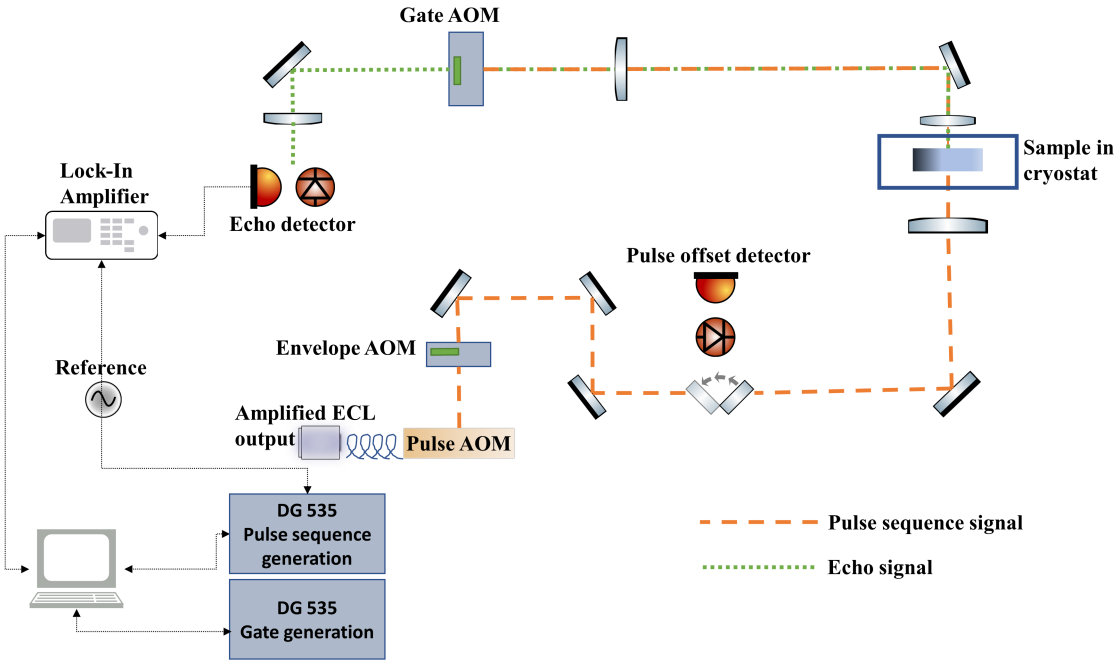

Figure 7.7: General setup for 2 pulse photon echo experiments. The RF drivers of the AOM have been removed for better visibility. Pulse and echo 'paths' are just a visual representation.

7.5 Results

7.5.1 Laser Instability

Before presenting further obtained results if feels noteworthy pointing out that the ECL kit had been factory assembled, however got misaligned during transport. Additionally, the spring that was pulling the grating arm into contact with the actuator was moved, and the laser had to be effectively recalibrated to the best of our ability following a provided manual. As a result, optimum coupling efficiency for the diffracted light back into the gain chip might not have been achieved. Lack of a scanning Fabry Perot (SFP) interferometer also resulted in numerous mode hops occurring during scans, an example of which is shown in fig. 7.8.

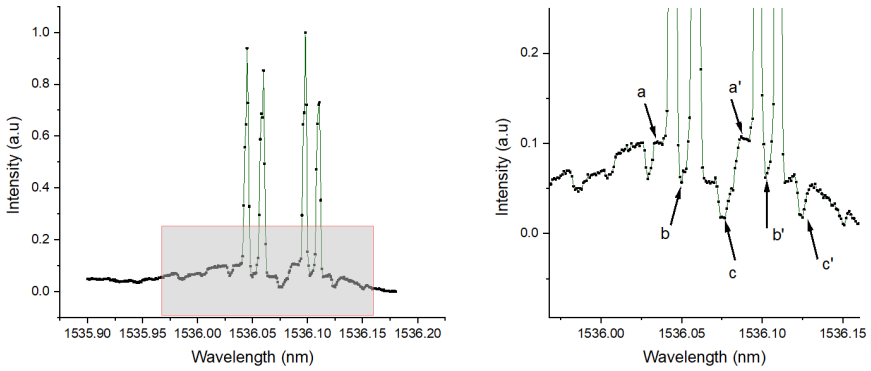

Figure 7.8: Typical representation of a mode hop during a spectroscopic sweep scan (see section 7.5.2). Full scan is presented on the left whilst the right is the zoomed section of the highlighted box. Features a, b, c and a',b',c' surrounding the visible peaks are mirrors of each other, representing the mode hop. As a result, wavelength allocation of features becomes complicated.

7.5.2 Low field Zeeman spectroscopy

Due to laser instability there was a need to locate the ever changing 'centre' of the peaks corresponding to transition energies of sites 1 and 2. As a result, the ability to scan across a wavelength range was added to the program utilising the same setup presented for the 2-pulse photon echo. Spectroscopic sweeps were performed following the same pulse sequence for photon echo but with fixed pulse separation and a wider gate located where the echo would be expected. Coherence measurements would then be performed

on each peak centre. Spectroscopic scans at 1.5 K with B=0 T (not shown) revealed the central emission lines at ≈1536.4 nm and ≈1538.6 nm for sites 1 and 2 respectively. Recall from fig. 7.1 that the crystal field splits the electronic states into 8 doublets for the $^4I_{15/2}$ (labelled Z1-Z8) and 7 doublets for the $^4I_{13/2}$. Operating at 1.5 K ensured that only the lowest crystal field level of the $^4I_{15/2}$ J multiplet (here labelled Z1) was initially populated. Therefore, the central emission lines corresponded to the Y1→Z1 transition. Application of a magnetic field lifts remaining degeneracy and each crystal field splits into two Zeeman sub-levels. During low magnetic field operation, Zeeman splitting was observed for fields up to 1 T. For higher magnetic fields and due to time constraints, only limited data were obtained. This is the first time to the best of our knowledge that the Zeeman effect has indirectly been observed using a photon echo sequence. Measurements were performed for B=10 mT up to B=100 mT in steps of 10 mT. A single measurement for B=200 mT is also included.

Site 2

Figure 7.9 shows a waterfall plot of the observed photon echo pulse driven Zeeman splitting for site 2. Each data plot was 'corrected' so that the 'central' observed line coincides

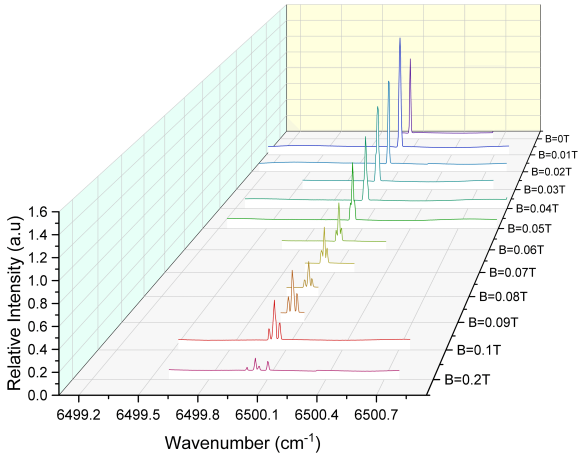

Figure 7.9: A waterfall graph representation of the magnetic field induced peak separation we attributed to Zeeman splitting for site 2.

with the zero field transition line. Immediately after the introduction of the magnetic field, a slight increase in intensity is seen, followed by a decreasing trend for increasing magnetic field values with the exception of 0.08 T. However, it is worth noting that this behaviour should only be treated as a hypothesis since the datasets were obtained across different days, and no direct comparison can be made with full accuracy. To minimise the uncertainty, the plotted datasets include results taken within 2 days of each other, and

with equal dwelling time between measurements to avoid skewing the output in favour of scans with larger integration time. Subplots have been magnified and arranged for better visibility in figure 7.10.

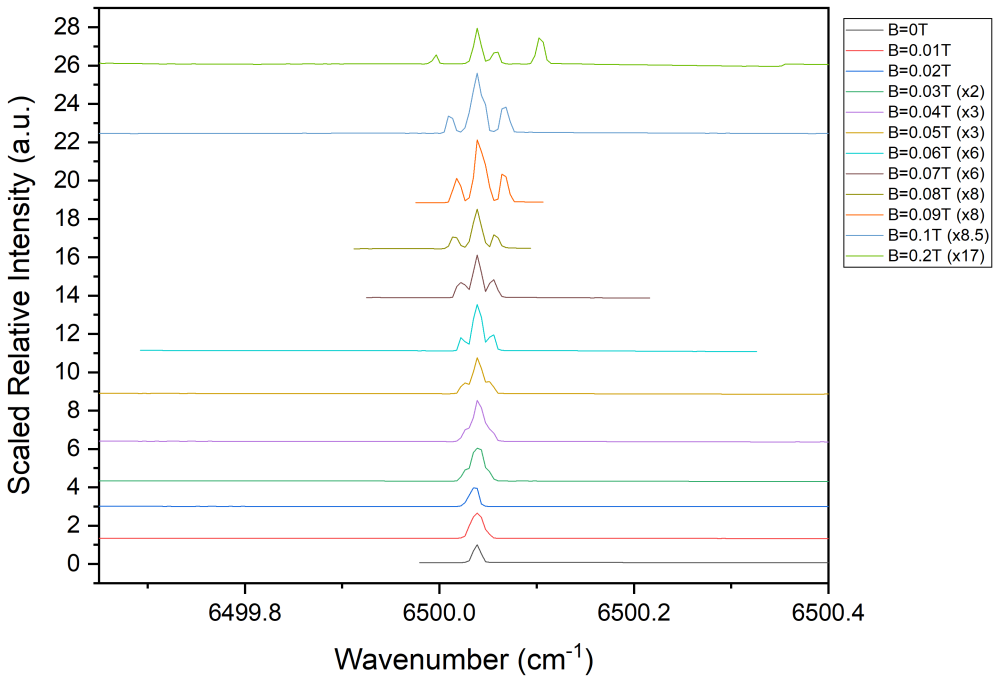

Figure 7.10: Stacked Zeeman spectra for site 2 as a function of the magnetic field.

Splitting can be observed as early as 0.03 T, with the lines clearly starting to separate at 0.06 T. The result for 0.2 T is of particular interest, since it implies that the 'central' line is splitting as well. Assignment of lines to exact Zeeman transitions proved to be complicated and is still a work in progress. Correct assignment of each peak is essential for the calculation of the g-factors for the ground and excited states for both crystallographic sites. There are four transitions between the ${}^4I_{15/2} : Z1$ and the ${}^4I_{13/2} : Y1$ levels for each site as denoted in figure 7.11. Letters g and e correspond to ground and excited state with g^+ and g^-, e^+ and e^- showing the Zeeman upper (+) and lower (-) components of each level. Possible optical transitions between the Zeeman-split levels are marked a, b, c and d. Knowing these transition energies (E_i, $i = a, b, c, d$) enables the calculation of ground (g_g) and excited (g_e) g-factors using [186]:

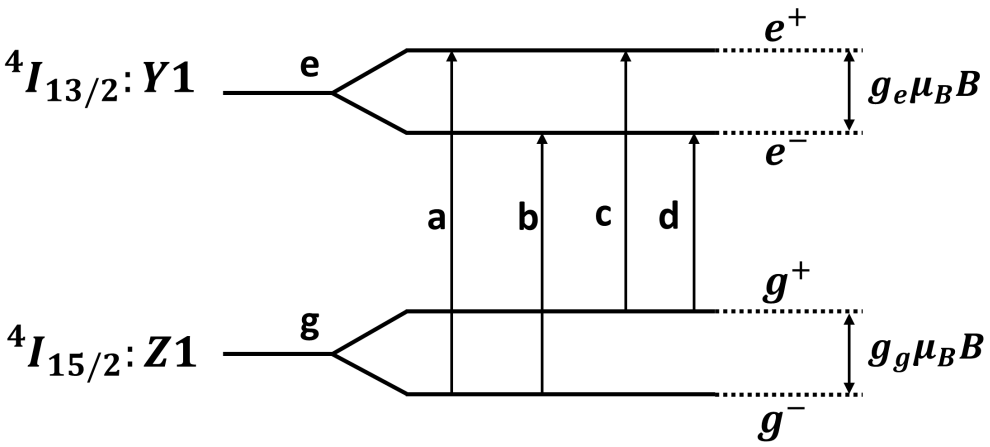

Figure 7.11: Transition labelling scheme for the lowest energy levels $^4I_{15/2} : Z1$ and $^4I_{13/2} : Y1$ with the Kramer's degeneracy being lifted by an external magnetic field.

$$g_g = \frac{E_a - E_c}{\mu_B B} = \frac{E_b - E_d}{\mu_B B} \tag{7.5.1}$$

$$\tag{7.5.2}$$

$$g_e = \frac{E_a - E_b}{\mu_B B} = \frac{E_c - E_d}{\mu_B B} \tag{7.5.3}$$

where μB is the Bohr magneton and B is the strength of the magnetic field. As a result the ground and excited state g value along a specific axis can be determined through field dependence measurements of a specific transition between two split Kramers doublets. Recall from section 7.1.2 that both crystallographic sites (site 1 and 2) have C_1 local symmetry. Each site consists of four differently oriented subclasses related by inversion and by C_2 rotation. The two subclasses related by inversion are magnetically equivalent, however those related by rotation interact differently with a magnetic field applied in an arbitrary direction and thus are magnetically inequivalent [188]. This inequivalence arises because of the different angles that the magnetic field makes with the two different sets of the local site axes. Therefore, generally the magnetic field being parallel to one local axis of symmetry for one ion does not imply that it will be parallel for the others leading to the crystallographic site breaking up into two magnetically inequivalent orientations [193]. Exception to this rule is when the magnetic field is applied along the b axis or in the $D_1 - D_2$ plane where all the subclasses of a given site become magnetically equivalent [194],[195]. As a result, for a general case there will be eight expected transitions for each site, four from each subclass.

For a given subclass, transitions a and d in fig. 7.11 are the highest and lowest energy transitions; a starts from the lower Zeeman component of the ground state g^- terminat-

ing on the upper component of the excited state e^+. On the other hand, transition d starts from g^+ and terminates in e^-. Inner transitions b and c are harder to identify since either can be higher in energy. Normally, their assignment requires further temperature dependent study in order to identify the depletion region of the upper Zeeman component of the ground state (g^+). In other words, g^+ suffers from depopulation with rising temperature due to the Boltzmann distribution of the population of the energy levels. Therefore, transitions c and d are expected to decrease in intensity with higher temperatures. Here, no temperature dependent measurements were performed. However, by using previously determined ground state g values (g_g) derived from EPR studies [195] and optical spectroscopy [186], the excited state g_g can be re-expressed in terms of a and d splitting as well as g_g (see eq. 4.3 in [187]). Rearranging eqs. (7.5.1) and (7.5.3) we obtain:

$$g_e = \frac{E_a - E_d}{\mu_B B} - g_g \tag{7.5.4}$$

(7.5.5)

$$g_e = \frac{E_c - E_b}{\mu_B B} + g_g \tag{7.5.6}$$

Since the value of the effective g factor is axis dependent, application of eq. (7.5.4) requires knowledge of the crystal orientation with respect to the crystallographic b axis. When both subclasses coexist, grouping transitions per class becomes more complex. One possible way would be to perform temperature dependent measurements and find if sets of emissions c and d diminish in intensity in a similar rate of enhancement of a set a and b with decreasing temperature.

Relating the above to fig. 7.10 we can make the following observations. The spectrum consists of four visible peaks with the central more dominant peak being in fact a convolution of at least two peaks. It is possible that both subclasses are present and that their associated a and d transitions (highest and lowest energy) are out of bounds. Comparing our spectral boundaries with previous investigations does not provide clear answers. For example, fig. 5.12 in [196] observed the energy difference between c and b lines to be $\approx$1 cm^{-1} whilst [193] (see their fig. 5.12) saw all 4 transitions within the same range. If the wavelength range scanned was indeed restrictive it is more likely that the four present lines in fig. 7.10 correspond to b_I, c_I and b_{II}, c_{II} where subscripts I and II denote the associated subclass. In principle it is possible to obtain a g_e value with these lines (see eq. (7.5.4)) however distinguishing the pairs correctly would require as discussed temperature dependent measurements and higher magnetic field studies to allow for clear line separation, which were not undertaken. If, on the other hand the magnetic field is aligned along b axis, or in the $D_1 - D_2$ plane and the two related by rotation classes become magnetically equivalent, identification is more feasible. Such accidental align-

ment is unlikely, however for demonstration purposes the following analysis is performed under the assumption that the 4 peaks in fig. 7.10 are a result of magnetic equivalence of the two subclasses. In that case, transitions a and d can readily be identified as the highest (rightmost) and lowest (leftmost) energy peaks respectively. Transitions b and c are convoluted at low magnetic fields; as a result, peak fitting was performed for the 0.2 T subplot and is shown in fig. 7.12. Subsequent peak fits ensued for lower magnetic field subplots using the peak widths obtained from the 0.2 T fit and keeping them fixed where possible. For ease of comparison, corresponding colours to peak numbering have been set.

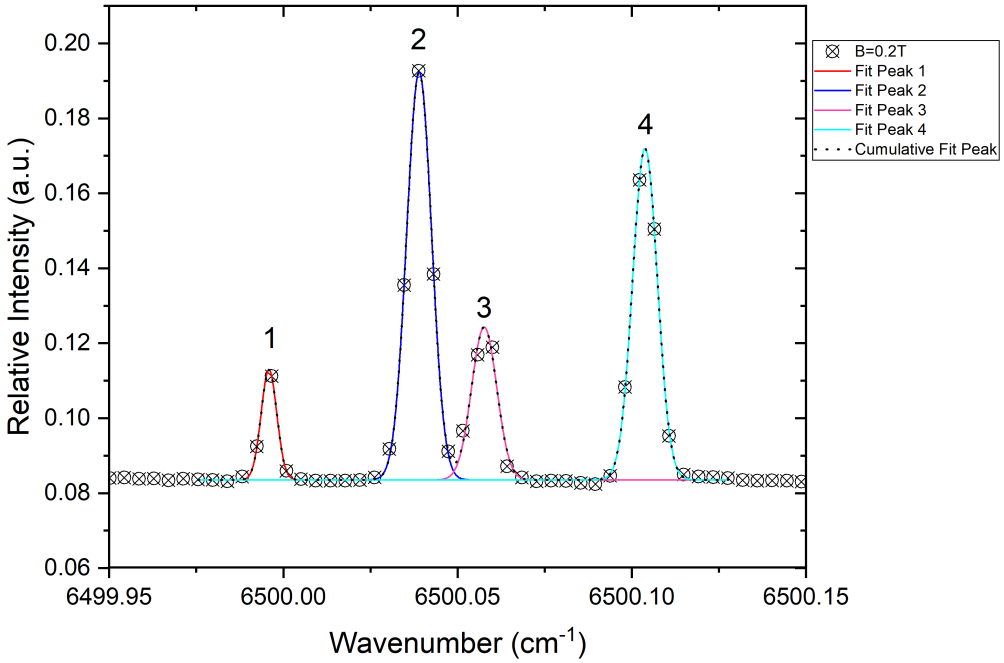

Figure 7.12: Peak fitting results for the 0.2 T subplot. The same numbering is used for the rest of the peak fits. Under the single subclass assumption, peak 1 would correspond to d and peak 4 to a line

.

The combined peak fitting results can be seen in fig. 7.13 and the corresponding peak centres for peaks 1 and 4 as a function of magnetic field is shown in fig. 7.14.

With respect to fig. 7.13, we should note that finding a peak by assigning a fixed width can be problematic, since there are many centres where that peak could be located, and the fitting algorithm would still be correct even if the result is physically wrong. In particular, peak 3 at lower magnetic fields has a potentially large centre error, and

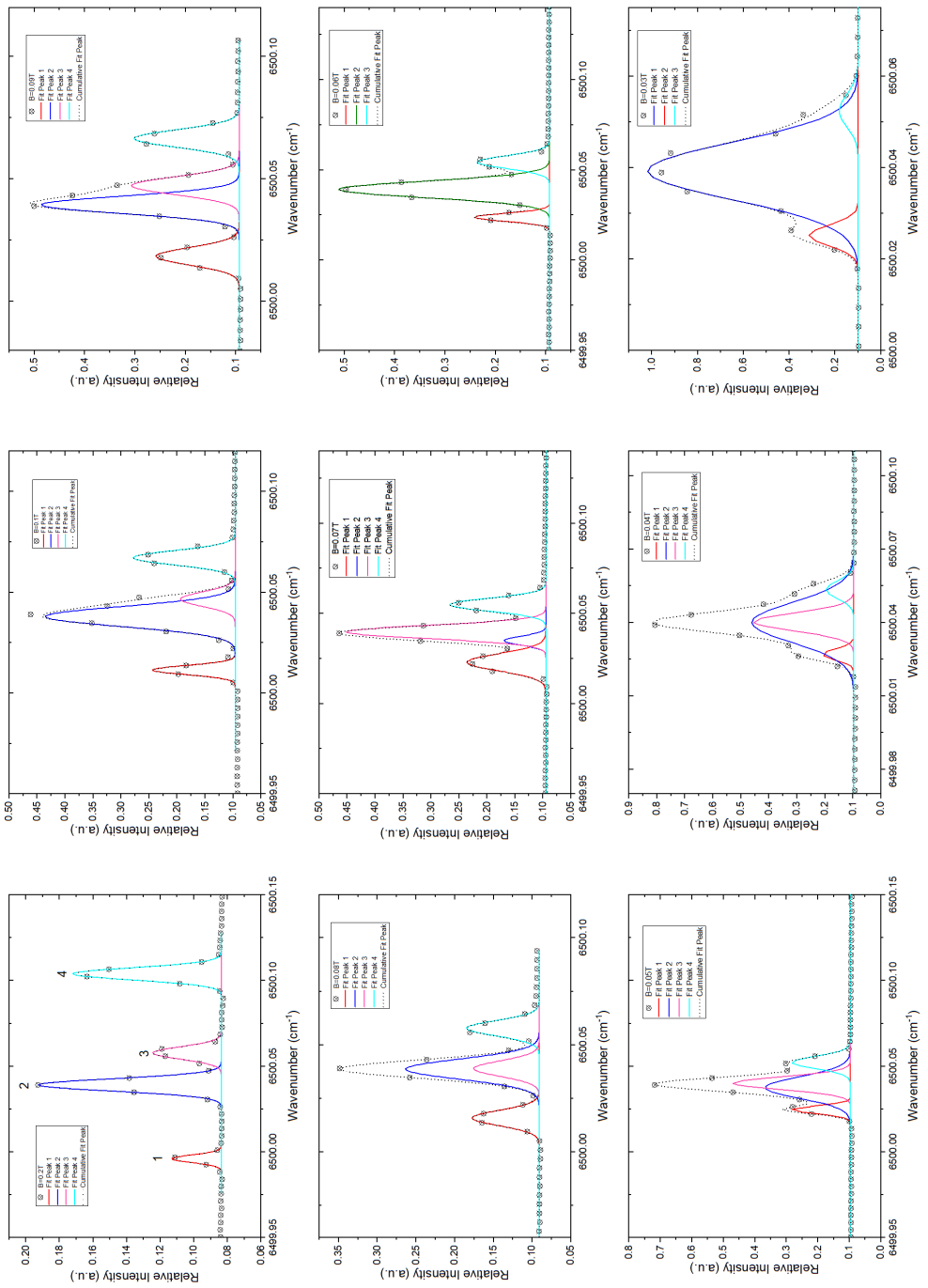

Figure 7.13: The resulted outputs of the peak fitting attempt keeping peak 1,3 and 4 constant. Peak 2 (blue) was allowed to obtain any value and was not taken into consideration in the magnetic field peak centre dependence. Deviations from fixed width occurred in some cases, see text.

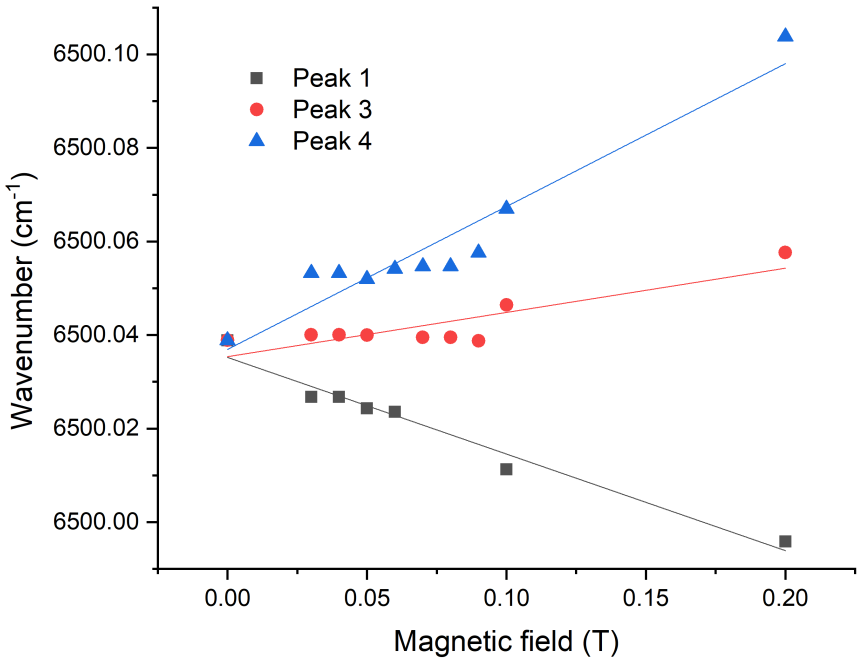

Figure 7.14: Linear fits for peaks fitted having peak widths being kept fixed. It is worth noting that the error bars on the peak centres are included but not representative of the true uncertainty, since they are only obtained through the fitting algorithm; a good fit would result in a small centre error regardless.

thus, should not be taken into consideration. Peaks 1 and 4 are promising, since their splitting is clear. However, only a number of fits are in agreement with our constant width assumption; for peak 1, 0.06 T-0.09 T graphs have different widths, and in fact keeping the width similar to the rest results in erroneous fitting. Nonetheless, if one were to combine all the 'good' fit outputs for peak 1, the result would still be linear. Such could imply that there are more lines buried within that centre, yet their transition probabilities change depending on the magnetic field strength. Similarly, for peak 4, we only now include points where the splitting is 'obvious', removing previous low field points. The resulting graph can be seen in fig. 7.15.

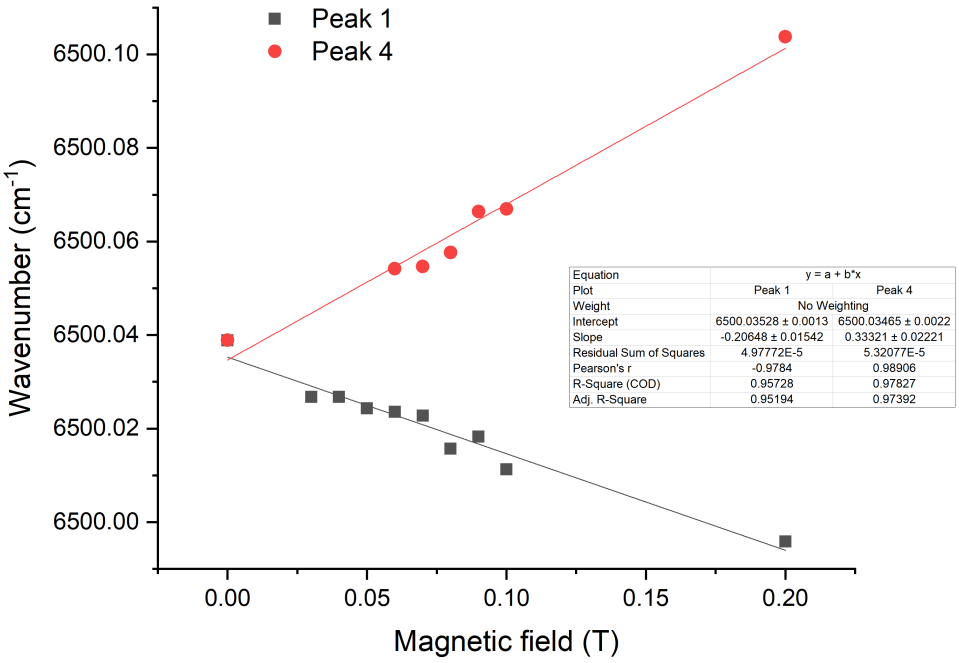

Figure 7.15: Linear fitting of peak 1 and peak 4's clearly visible transitions, with more relaxed rules with regards to peak widths. Peak 2 is excluded all-together in this attempt, and smaller magnetic field value outputs are removed due to their high uncertainty. Please note that error bars are present, but not visible. They are not representative of the true uncertainty, however, since they were only extracted from the peak fitting algorithm and thus do not include systematic errors.

The asymmetric nature of fig. 7.15 is not surprising if one considers the origin of the Zeeman effect. As discussed in section 2.2.6, the splitting of the Kramers' doublets can be described with the effective spin Hamiltonian:

$$H_Z = \mu_B \left(\vec{S} \cdot \vec{g} \cdot \vec{B} \right) \tag{7.5.7}$$

where $\vec{S}$ is the effective spin, $\vec{g}$ is the g tensor determined by the crystal field and site symmetry and $\vec{B}$ is the applied magnetic field. In principal axis representation (x,y,z) the g tensor can be described by components corresponding to the lengths of the 3 axes and the three angles that determine the axis orientation with respect to the crystallographic site. Therefore, crystal symmetry is important with high symmetry sites allowing for simplification of the g tensor through reduction of the number of individual g_x, g_y, g_z components [197]. On the contrary, the C1 symmetry of the Y_2SiO_5 does not allow for such simplification, leaving each crystal field with distinct value of g_x, g_y, g_z. This anisotropic nature of the g tensor manifests as asymmetry on the Zeeman energy split.

By performing a linear least squares fit for the Zeeman splitting observed in fig. 7.14 the effective splitting E_a-E_d was determined. If published values of g_g along the crystallographic b axis were used (≈ 9 for site 2 in [196]) calculation of the g factor from eq. (7.5.4) was unsuccessful since it led to negative values. It is therefore much more possible the sample was placed in an arbitrary orientation with respect to the magnetic field, leading to 8 lines from the 2 magnetically inequivalent subclasses and that further work with increased scanning spectral range should be undertaken for correct identification of the transitions.

Site 1

A typical spectrum for site 1 in a low magnetic field is presented below:

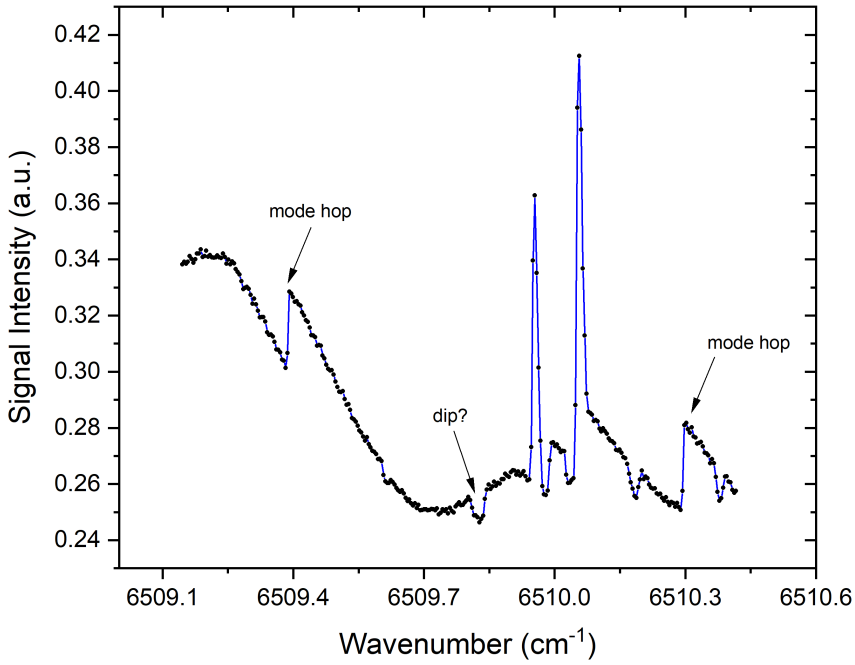

Figure 7.16: 0.1 T spectrum for site 1. Spectrum is uncorrected, and multiple mode hops are observed.

Due to the lack of a 'central' peak, a different approach was attempted for referencing. It was noted that for site 1 scanning region, a 'dip' of unknown origin yet of consistent appearance was present on the sweep spectra. The dip was first observed in the full absorbance spectrum that was taken to be used as a background spectrum seen in fig. 7.17. The bumps have been attributed to the EDFA's preferential absorption regions, whilst the almost cyclic spectrum behaviour upon zooming in [seen as the inset]

have not been fully explained. One possible reason could relate to the readjustment of the laser's external grating, which involved tweaking the mode hop micrometer and the position of the external grating with respect to the motor shaft that would move it upon sweeping. The cyclic behaviour could therefore be as a result of a mechanical spring oscillation that causes the grating to move almost back and forth during each step. Suc-

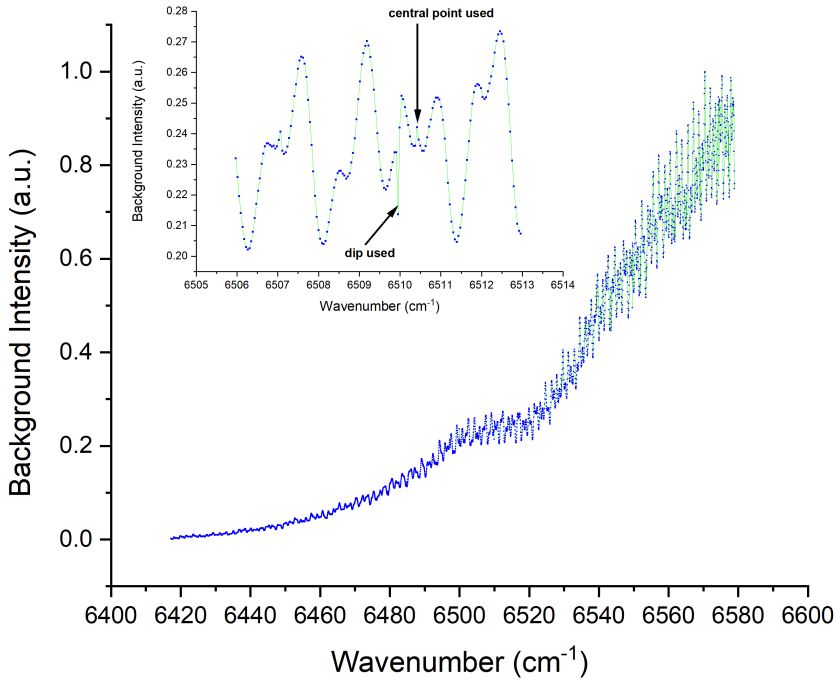

Figure 7.17: Background spectrum whilst sweeping across the ECL wavelength range.

cessful application of this referencing approach using the background was very limited, due to the fact that sweeps were restricted to the wavelength region of interest. As a result, mode hops that occurred during the scan varied from sweep to sweep, and each resulting graph would have to be manually corrected and shifted based on the number of mode hops before noting down the position of the 'reference dip'. This has yet to be attempted, and thus the following photon echo measurement results will refer to the peaks of site 1 simply as 'peak 1' and 'peak 2'.

7.5.3 Photon echo results

Photon echo Model development

The fitting model developed was a combination of expected output and observed results. The echo was expected to appear at a time $\sim 2 \times t_{12}$ for a square pulse input, with the echo having a Gaussian form. Previous investigations rely on an oscilloscope for echo observation, primarily through usage of a laser carrier which acts as a local oscillator being switched on just before the echo was due. The echo signal thus takes the form of a heterodyne beat on the optical detector prior to being mixed down, filtered and recorded on an oscilloscope [193][80]. In this project, however, we were effectively sweeping with our gate across the 'echo formation' time domain region, and recording the intensity of the signal as a function of gate delay position for a set pulse separation. Furthermore, the difference in rise and fall times amongst our different acousto-optic modulators created a constraint in the form of our minimum pulse separation. More precisely, whilst technically the fast pulse driven AOM was the one determining the system's response time and by extend the minimum pulse separation, it was the envelope AOM that practically set that limit. The envelope AOM had both slower rise and fall times compared to its pulse driven equivalent, and as a result had to be switched earlier (rising offset) and turned off at such a time to minimize the tail offset between it and the pulse end tail (falling offset). The longer tail was seen as an exponential decay at the start of the signal recording, followed by the echo. For shorter pulse separations, the signal was almost overlapping with the envelope tail almost getting clipped. As a result, a minimum pulse separation of 800 ns was decided. Figure 7.18 shows the raw output of different scans for increasing pulse separation. For ease of comparison, the combined datasets have been plotted together. Marked with arrows in (a) are the exponential decay residue from the envelope AOM's tail, followed by the echo. Figure 7.18(b-d) display a 3D plot of the dataset from different angles. As the pulse separation increases, the echo is expected to form at a later time and so it appears further from the envelope's tail. The arrows in bold indicate points where the echo deviates from 'pure' Gaussian output, and could be due to power fluctuation of the laser output. A fitting function script consisting of an exponential decay part and a Gaussian part was written in Origin. The function had the form:

$$y = \left(y_0 + A_1 e^{-x/t_1}\right) + \left(y_0 + \frac{A \exp\left(\frac{-4ln(2)(x-x_c)^2}{w^2}\right)}{w\sqrt{\frac{\pi}{4ln(2)}}}\right) - y_0 \tag{7.5.8}$$

where y_0 is the shared offset, A_1 and t_1 the exponential part's amplitude and decay constant respectively, x_c the centre of the Gaussian, A its area and w the peak's Full Width

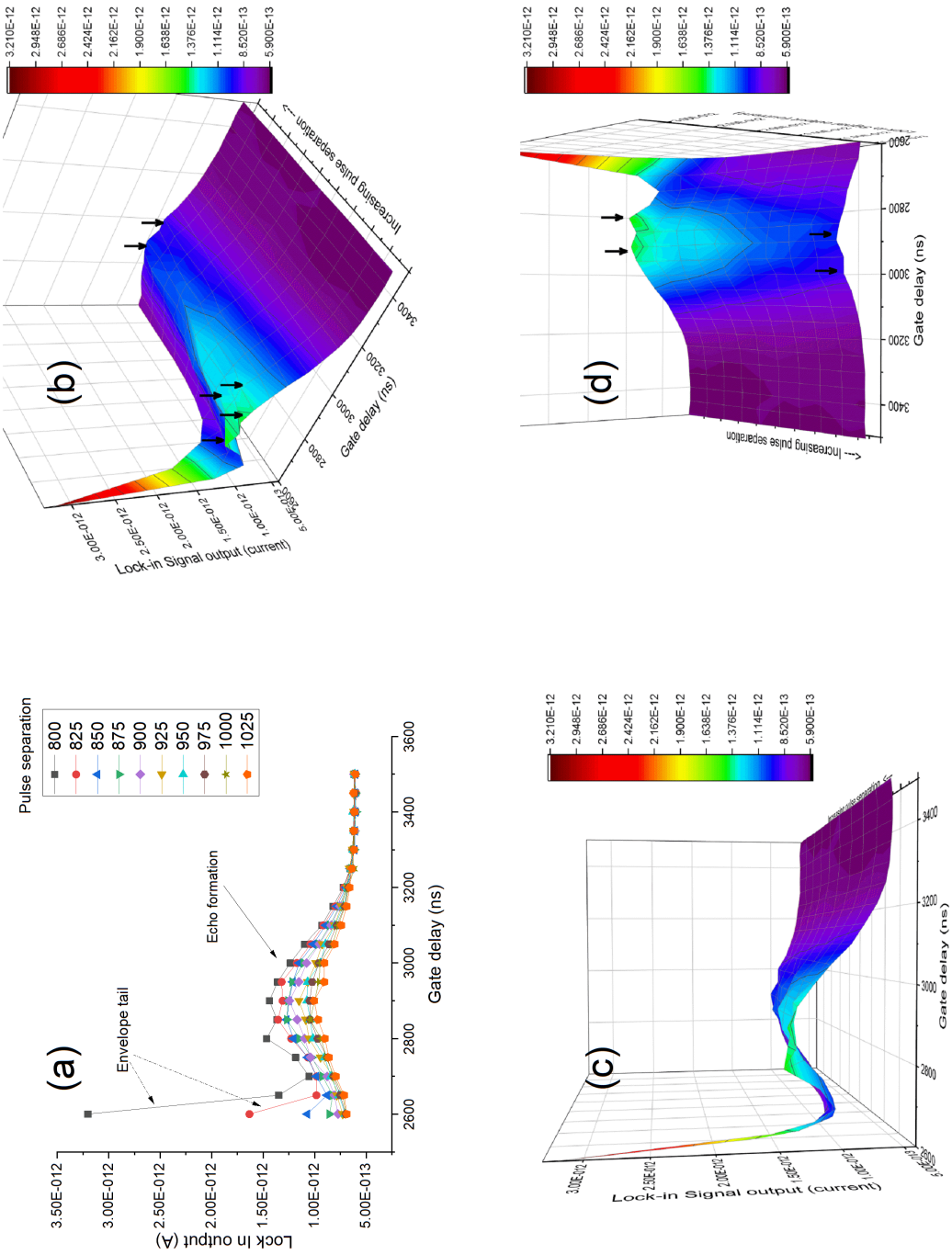

Figure 7.18: Photon echo results interpretation. In (a), stacked 2D raw output of the echo signal as a function of gate delay (gate being sweeped) for a set pulse separation. For shorter separations the envelope tail is seen as an exponential curve residual. For larger pulse separations, the contribution of the exponential becomes smaller. (B),(c) and (d) are 3D representations of cumulative data. Colour chart is mapped to signal intensity. The arrows point on deviations from 'pure' Gaussian output, and could be a result of laser power output fluctuating.

Half Maximum (FWHM). To check the validity of the model, a data set was selected and fitted with the function script, in addition to fitted separately to its individual parts (not shown). The value of the area under the Gaussian was extracted for each step with the echo decay behaviour visible through a plot of the changing integrating area as a function of pulse separation. The model was found to be suitable for datasets where the echo signal to background noise was relatively large. However, 'ringing' behaviour from the envelope AOM would interfere with the echo signal, causing the model to breakdown as seen in fig. 7.19. Inclusion of a sinc function to represent the ringing behaviour in the algorithm was attempted, yet its implementation was unsuccessful.

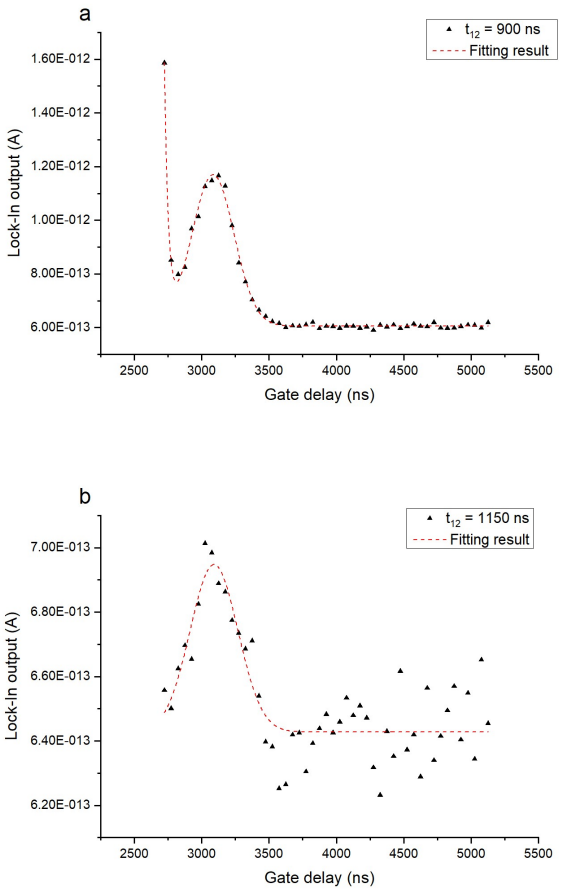

Figure 7.19: Fitting model comparison of two coherence spectra belonging to the same scan, but having different pulse separations. The interference caused by the envelope AOM ringing is visible on both sets, yet much more prominent on graph b. It is worth noting that graph b's echo signal output was also lying on the detection limit of our apparatus.

7.5.4 Coherence results

Preliminary coherence results for Peak 1 are presented in fig. 7.20.

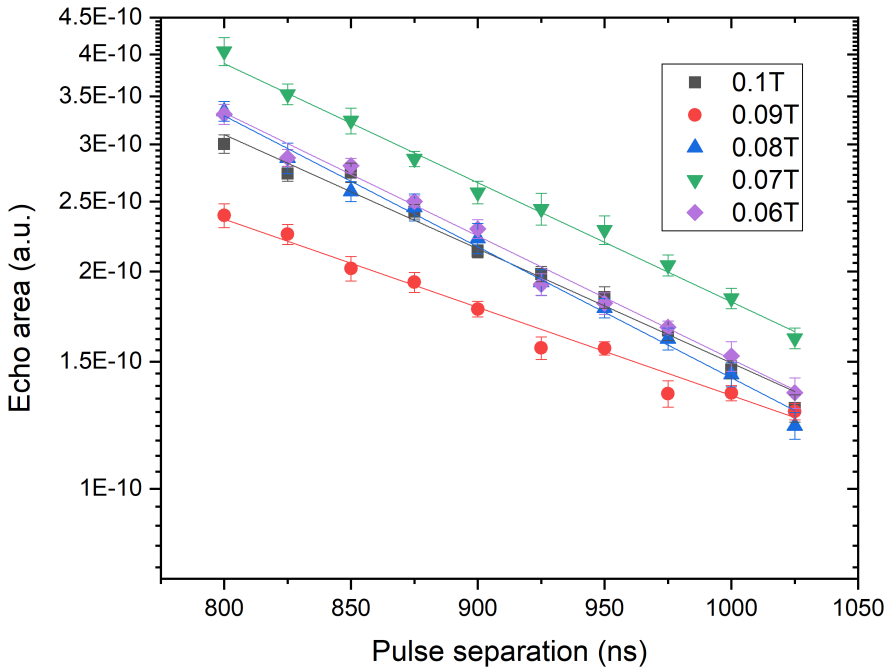

Figure 7.20: Two pulse photon echo decays for Er in site 1, peak 1 (transition unknown) for several values of the magnetic field. All decays have been fitted linearly.

We are expecting an exponential decrease in echo amplitude with increasing time delay. The decrease would be proportional to $\exp(-4t_{12}/T_2)$ describing the effect of decoherence during the t_{12} sections of the echo sequence due to the homogenous linewidth [198]. Graphs have thus been plotted on a logarithmic scale and linear fittings have been performed on all datasets. The extracted coherence times for peak 1 are shown in table 7.1.

Peak 1 T_2 (μs)	Peak 2 T_2 (μs)	Magnetic field B (T)
2.53 ± 0.24	1.4 ± 0.21	0.1
3.28 ± 0.3		0.09
2.2 ± 0.12		0.08
2.42 ± 0.14	1.08 ± 0.07	0.07
2.34 ± 0.17	1.03 ± 0.1	0.06

Table 7.1: Coherence times T_2 for peaks 1 and 2 of site 1.

For peak 2, there were only a few successful coherence measurements. A combined plot can be seen in fig. 7.21. Images (a) and (b) were both taken at 0.1 T magnetic field, however at different dates. In both cases deviation from linear behaviour occurs. For (a), the oscillatory-looking modulation behaviour of the echo could be attributed to Electron Spin Envelope Echo Modulation (ESEEM) observed for Er:YSO in Electron Spin Resonance (ESR) experiments [199], originating from the dipole-dipole coupling of the erbium electronic spin to the nearby nuclear spins of yttrium Y^{89} and oxygen [200]. There are not enough data to form an accurate hypothesis, but we could assume that the coherence time is expected to be even shorter in this case, since as mentioned in section 2.4 a larger $\Gamma_{Er-host}$ factor would increase the homogenous linewidth and the imposed maximum coherence limit due to it. However, the potential existence of ESEEM could indicate the ability of Er:YSO to act as a nuclear spin quantum memory upon optimization and given an adequate spin coherence time. For (b) not much can be inferred; however, it could be implied that peak 2 consists of different sub-peaks, and so the different outputs might correspond to different Zeeman transitions. Coherence times for peak 2 are plotted in table 7.1.

The shorter coherence times observed in this study could be attributed to numerous factors. Firstly, it has been suggested that maximising the splitting of each doubly degenerate crystal field level relative to the thermal energy, kT, causes the thermal population of the upper Zeeman level to 'freeze out', and thus reduce dephasing due to electron spin fluctuations of neighbouring Er^{3+} ions. However, our experiments were performed at very low magnetic fields, where the Zeeman doublets are quite close to each other and so the Γ_{Er-Er} is significant.

In addition, the importance of sample orientation was unknown to us at the time of the experiment and as a result no particular attention was given upon the sample's placement in the cryostat. Previous research has indicated that slow dephasing should be expected along the magnetic field direction that simultaneously maximises the g-values of ground and excited state for both crystallographic sites [193]. On the contrary, an arbitrary magnetic field orientation with low g-values for both sites would result in faster dephasing and large homogenous linewidth. It is plausible that our orientation was not (the most) favourable.

Finally, the case of non-exponential photon echo decays is worth mentioning. These ave been observed in literature, indicating the existence of spectral diffusion, mainly attributed to Er-Er spin flips and Y nuclear-spin fluctuations [201]–[203]. In these cases fitting of the Mims' equation as seen in section 7.3.1 is applied [38]. It is expected that when x=1, the phase memory time T_M is equal to the normal transverse dephasing time T_2. The parameter x takes values between 1 and 3, most commonly not exceeding 2.

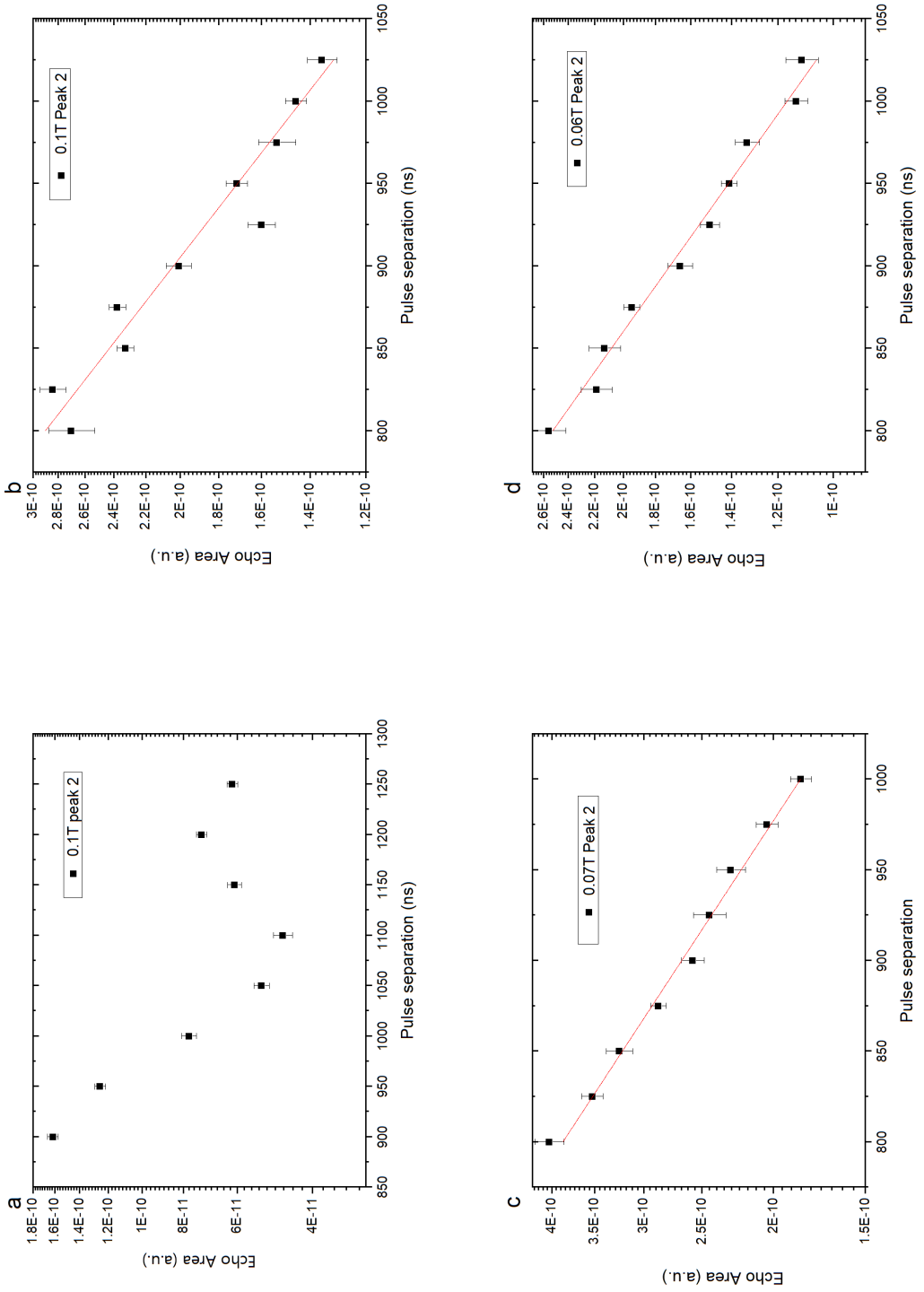

Figure 7.21: Two pulse photon echo decays for Er in site 1, peak 2 (transition unknown) for several values of the magnetic field. Graphs a and b correspond to the same magnetic field but were taken at different dates.

Attempts to fit the Mims' equation were performed, however due to the small region of data there were cases where it was unclear whereas application of Mims or a linear fit were appropriate. Figure 7.22 presents a comparison of a linear and a Mims fit on the same set of data for site 2, peak 1 at 0.1 T. Both fittings were successful, yet each produces a different output; linear fitting results in $T_2 = (0.95 \pm 0.13)$ μs whilst the Mims fitting for x=2.37 results in $T_M = (3.26 \pm 1.48)$ μs. The large error in the Mims fitting is due to the lack of data, and the algorithm trying to estimate the intercept.

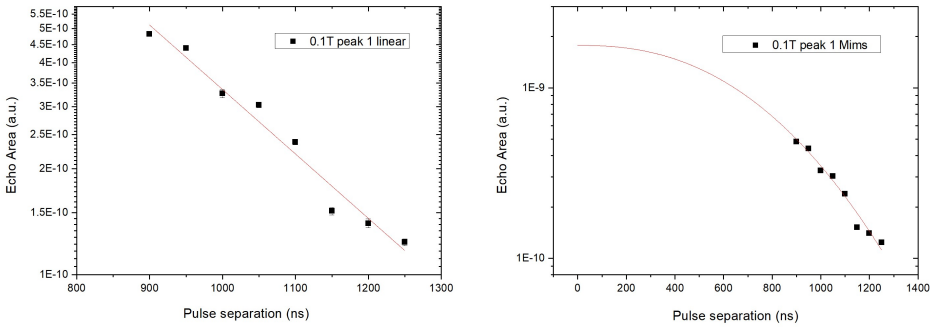

Figure 7.22: Site 2 peak 1 0.1 T spectrum. To the left, a linear fit, to the right a Mims equation fit.

Furthermore, there are limited two-pulse photon echo published data for the sample. There can not be a lot of information extracted with regards to the system dynamics by just the two-pulse photon echo system. A stimulated photon echo spectroscopy study would be required to investigate the diffusion mechanisms further.

7.6 Chapter Summary

This chapter successfully demonstrated proof-of concept optical coherence measurements using two pulse photon echo sequence. Section 7.1.2 introduced yttrium orthosilicate (Y_2SiO_5) as the host material and listed some relevant composition and crystallographic properties. Introduction of erbium in Y_2SiO_5 and the role of space group symmetry on the material interaction with an externally applied magnetic field were discussed. Next, section 7.2.1 reviewed the spin vector Bloch formalism and applied it to optical resonance through the semi-classical treatment of an electric dipole. The phenomenological decay constants relevant to dipoole moment dephasing were shown in section 7.2.3. The two-pulse photon echo sequence formation was described in section 7.3.1 alongside the relevant experimental setup. The need to locate the transition centres led to the introduction of spectroscopic sweeps using the photon echo sequence. Application of a magnetic field in section 7.5.2 led to the observation of Zeeman splitting of the lowest $^4I_{15/2}$:Z1, $^4I_{13/2}$:Y1

manifolds. Analysis suggested that the transitions observed for each site belonged to two magnetically inequivalent subclasses of Er:YSO and that further wider spectral sweeps are required to ensure correct assignment. Lastly, low magnetic field two-pulse photon echo spectroscopy was performed for the Zeeman split energy levels. For two unassigned transitions of site 1, optical coherence T_2 was found to be (2.5 $\pm$ 0.24) μs and (1.4 $\pm$ 0.21) μs at B=0.1 T.

8.CONCLUSION AND FUTURE WORK

The principal aim of this thesis was to examine the optical properties of erbium implanted silicon as a possible material for quantum technology platforms. The thesis was successful in spectroscopically addressing luminescence characteristics of the embedded rare earth whilst unearthing further questions on the nature of the erbium centres in silicon in general. To this end, various experimental setups were built and interfaced in-house and several characterisation methods were employed. Specifically, knowledge on erbium site symmetry is paramount in achieving qubit control and interaction in a two-level quantum bus. Whilst some information on crystal field interaction between erbium and silicon exists, there is no uniformity in findings with respect to centre consistency amongst samples grown under different fabrication and processing conditions. Chapter 3 re-evaluated the existing knowledge base on centre formation starting from the most studied and regularly reported for erbium implanted silicon cubic site. Crystal field (CF) simulations for one of our samples whilst using the well accepted ground state energy level CF splitting for this site suggested the centre's presence. By invoking selection rules on allowed transitions for cubic symmetry, the photoluminescence emission lines attributed to this site were found to be an improvement compared to a previous model for this sample. The outcomes of these selection rules brought to the surface a paradox regarding the allocation of the primary emission line as the otherwise forbidden $^4I_{13/2} \rightarrow {}^4I_{15/3}$ transition. Through previously unperformed computational simulations on the first excited state manifold crystal field splitting projected from the ground state manifold splitting, this work provided some clarity on parameters pertaining the location of crystal field levels. The results underlined the need for re-evaluation of the cubic Er:Si spectrum erbium, with suggestions on the potential co-existence of multiple cubic sites, or cubic assigned peaks being a part of a lower-symmetry site instead. Finally, through CF simulations of PL transitions identified in literature, the potential of an erbium site in orthorhombic symmetry was noted. This section would benefit from future PL measurements undertaken at very low cryogenic temperatures. This is because the origin multitude of peaks observed at 77 K, our system limitation, is not restricted to the lowest crystal field level of the upper excited state leading to numerous 'hot' lines being seen. Isolating the primary emissions at liquid helium temperatures would allow for a much clearer peak selection and easier comparison of shared centre formation amongst different samples.

Detailed studies on the optical activity of erbium centres in silicon followed in chapter 4. The relationship between processing conditions and maximum luminescence yield

was examined and a clear indication of annealing temperature dependence of erbium centre formation was observed. For a dual-step anneal for samples of 1×10^{19} Er and 1×10^{20} O (cm^{-3}), 850 °C for 30 seconds was found to be the optimal setting for the formation of the 1536 nm situated centre whose concentration appeared to decrease at elevated temperatures. A broad background feature (BBF) was also noted and attributed to erbium in amorphous silicon. De-excitation dynamics of Er:Si were probed through measurements of temperature dependent photoluminescence. For the first time for erbium in silicon, luminescence negative thermal quenching (NQ) was seen. Analysis indicated that erbium in crystalline and amorphous environments both followed this trend. This behaviour was successfully modelled by assuming a middle defect state whose energy level is located between erbium's $^4I_{13/2}$ and $^4I_{15/2}$ states. However, compromises on the spectral resolution arising from low emission signal led to difficulties in peak deconvolution; as a result, no quantitative measurements of the number and energy location of the defect states could be made through calculation of the state's activation energy. Nevertheless, the universal nature of the NQ effect which also took place by erbium in amorphous background suggests the formation of a continuous energy level in the sample. Further de-excitation comparison with the standard model identified similar nonradiative pathways including the backtransfer and Auger quenching processes. Nonetheless, overparametrisation of the fitting equation did not yield a usable output and the activation energy E_a could only be estimated with maximum $E_a \approx 0.6$ eV for the 1×10^{19} Er and 1×10^{20} O (cm^{-3}) sample annealed with T_{RA}=850 °C for 30 s. It would be beneficial in the future to perform Deep Transient Level Spectroscopy (DLTS) aiming to pinpoint the location of trap levels and compare with the currently accepted excitation mechanism. Findings would allow for value selection and/or restriction in the NQ model algorithm, therefore providing a better fit. Two-level photoluminescence spectroscopy could be of additional interest; there, direct information on the excitation pathways could be inferred.

The investigation of Er:Si decay dynamics continued in chapter 5 through temperature dependent lifetime measurements. There, two major previously unseen nanosecond radiative lifetime components (≈5 ns for the fastest at 65 K) were successfully recovered and assigned to two distinct classes of erbium in different crystalline environments. A smaller component within 5 μs range was attributed to erbium in amorphous environment. Findings were liked to earlier observations of NQ quenching and we postulated that the middle state responsible for the PL NQ was the same state responsible for the reduced effective lifetime, through interaction and energy transfer between the middle state and the optically active erbium ions. The validity of our previous speculation on the continuous nature of the defect state was underscored through universal appearance of the nanosecond lifetime component inclusive or samples where the amorphous background

was dominant. Average lifetime measurements eliminated clusterring or precipitates as the origin of lifetime quenching. Continuous lifetime distribution models were used as validation for the decay fitting scheme. These lifetime measurements would greatly benefit from the option to select the transition observed. Our lock-in amplifier limitations meant we could not perform frequency-resolved lifetime measurements. Therefore in the future, a faster instrument in conjunction with liquid helium temperatures and high spectral resolution could allow for the identification of individual peak centre emission lifetimes. This in turn could enable connection of sets of lifetimes to separate crystal site symmetry groups since all transitions belonging to the same centre would be governed by similar radiative lifetimes. A connection between crystal field interaction and Er:Si transfer properties could then be made.

Electrical characterisation on chapter 6 was successful in confirming the n-type nature of the material however did not provide any further input on the connection between optically and electrically active centres. Resistivity measurements found a maximum resistivity for samples undergoing rapid thermal annealing at 900 °C for 30 s. A previously detected apparent change of preferential erbium site symmetry at this temperature could imply that the carrier distribution and resistivity are affected by different crystal field environments. A more robust interpretation could be given following in-situ electrical characterisation with the sample mounted on a cryostat with electrical feedthrough. In particular, measurement comparison between illuminated and non illuminated samples would be useful by linking optically and electrically active centres. Scanning across a wavelength range for different temperatures, and linking spectral features and electrical values could further clear whether the proposed defect state is indeed continuous, or local.

Finally chapter 7 demonstrated the completion of a two pulse photon echo setup. Zeeman splitting was observed by using a photon echo sequence for the first time, for an arbitrarily oriented Er^{3+}:Y_2SiO_5 crystal. The Zeeman transitions were attributed to two magnetically inequivalent subclasses. Optical coherence measurements using two-pulse photon echo sequence were performed for low magnetic fields at 1.5 K with a representative T_2 value for an unassigned site 1 transition being $T_2 = (2.5 \pm 0.24)$ μs at B=0.1 T. Unfortunately, no crystallographic information accompanied the sample and therefore we have no means of identifying the primary axes. This makes knowledge of sample alignment in a magnetic field impossible. Future experiments should be designed using a well-characterised sample as reference, and utilising part of the laser beam as reference. Continuous collection of the beam's power output and wavelength (using an interferometer) for each step would take into account the instruments' response avoiding issues such as laser tuning. Of course preferably, a stable laser with narrow linewidth

should be used. Additionally, the photon echo experiment was interrupted due to laboratory closure during the COVID-19 pandemic. Experimental time constrains in utilising the magnet meant data collection did not resume; as a result, a lot of analysis remains incomplete.

REFERENCES

[1] L. Pavesi, "Will silicon be the photonic material of the third millenium?" *Journal of Physics: Condensed Matter*, vol. 15, no. 26, R1169, 2003.

[2] L. Pavesi and D. J. Lockwood, "Silicon fundamentals for photonics applications," in *Silicon Photonics*. Springer Berlin Heidelberg, 2004, pp. 1–50, ISBN: 978-3-540-39913-1. DOI: 10.1007/978-3-540-39913-1_1. [Online]. Available: https://doi.org/10.1007/978-3-540-39913-1_1.

[3] A. Kenyon, "Erbium in silicon," *Semiconductor Science and Technology*, vol. 20, no. 12, R65, 2005.

[4] M. Zia, C. Wan, Y. Zhang, and M. Bakir, "Electrical and photonic off-chip interconnection and system integration," in *Optical Interconnects for Data Centers*, Elsevier, 2017, pp. 265–286.

[5] K. Powell, L. Li, A. Shams-Ansari, J. Wang, D. Meng, N. Sinclair, J. Deng, M. Lončar, and X. Yi, "Integrated silicon carbide electro-optic modulator," *Nature Communications*, vol. 13, no. 1, p. 1851, 2022.

[6] N. Li, D. Vermeulen, Z. Su, E. S. Magden, M. Xin, N. Singh, A. Ruocco, J. Notaros, C. V. Poulton, E. Timurdogan, *et al.*, "Monolithically integrated erbium-doped tunable laser on a CMOS-compatible silicon photonics platform," *Optics Express*, vol. 26, no. 13, pp. 16 200–16 211, 2018.

[7] N. Li, M. Xin, Z. Su, E. S. Magden, N. Singh, J. Notaros, E. Timurdogan, P. Purnawirman, J. D. Bradley, and M. R. Watts, "A silicon photonic data link with a monolithic erbium-doped laser," *Scientific Reports*, vol. 10, no. 1, p. 1114, 2020.

[8] A. W. Fang, E. Lively, Y.-H. Kuo, D. Liang, and J. E. Bowers, "A distributed feedback silicon evanescent laser," *Optics express*, vol. 16, no. 7, pp. 4413–4419, 2008.

[9] S. Chen, W. Li, J. Wu, Q. Jiang, M. Tang, S. Shutts, S. N. Elliott, A. Sobiesierski, A. J. Seeds, I. Ross, *et al.*, "Electrically pumped continuous-wave III–V quantum dot lasers on silicon," *Nature Photonics*, vol. 10, no. 5, pp. 307–311, 2016.

[10] D. Loss and D. P. DiVincenzo, "Quantum computation with quantum dots," *Physical Review A*, vol. 57, no. 1, p. 120, 1998.

[11] D. P. DiVincenzo, "The physical implementation of quantum computation," *Fortschritte der Physik: Progress of Physics*, vol. 48, no. 9-11, pp. 771–783, 2000.

[12] A. Morello, J. J. Pla, F. A. Zwanenburg, K. W. Chan, K. Y. Tan, H. Huebl, M. Möttönen, C. D. Nugroho, C. Yang, J. A. Van Donkelaar, *et al.*, "Single-shot readout of an electron spin in silicon," *Nature*, vol. 467, no. 7316, pp. 687–691, 2010.

[13] M. Fuechsle, J. A. Miwa, S. Mahapatra, H. Ryu, S. Lee, O. Warschkow, L. C. Hollenberg, G. Klimeck, and M. Y. Simmons, "A single-atom transistor," *Nature nanotechnology*, vol. 7, no. 4, pp. 242–246, 2012.

[14] J. J. Pla, K. Y. Tan, J. P. Dehollain, W. H. Lim, J. J. Morton, D. N. Jamieson, A. S. Dzurak, and A. Morello, "A single-atom electron spin qubit in silicon," *Nature*, vol. 489, no. 7417, pp. 541–545, 2012.

[15] K. Saeedi, S. Simmons, J. Z. Salvail, P. Dluhy, H. Riemann, N. V. Abrosimov, P. Becker, H.-J. Pohl, J. J. Morton, and M. L. Thewalt, "Room-temperature quantum bit storage exceeding 39 minutes using ionized donors in silicon-28," *Science*, vol. 342, no. 6160, pp. 830–833, 2013.

[16] C. Yin, M. Rancic, G. G. de Boo, N. Stavrias, J. C. McCallum, M. J. Sellars, and S. Rogge, "Optical addressing of an individual erbium ion in silicon," *Nature*, vol. 497, no. 7447, pp. 91–94, 2013.

[17] M. Raha, S. Chen, C. M. Phenicie, S. Ourari, A. M. Dibos, and J. D. Thompson, "Optical quantum nondemolition measurement of a single rare earth ion qubit," *Nature communications*, vol. 11, no. 1, p. 1605, 2020.

[18] J. M. Langer, "Ionization energies of rare earth impurities in III-V and II-VI semiconductor compounds," in *Defects in Semiconductors 17*, ser. Materials Science Forum, vol. 143, Trans Tech Publications Ltd, Oct. 1993, pp. 721–724.

[19] C. Delerue and M. Lannoo, "Description of the trends for rare-earth impurities in semiconductors," *Physical review letters*, vol. 67, no. 21, p. 3006, 1991.

[20] R. Macfarlane and R. Shelby, "Coherent transient and holeburning spectroscopy of rare earth ions in solids," in *Modern Problems in Condensed Matter Sciences*, vol. 21, Elsevier, 1987, pp. 51–184.

[21] K. Stevens, "Matrix elements and operator equivalents connected with the magnetic properties of rare earth ions," *Proceedings of the Physical Society. Section A*, vol. 65, no. 3, p. 209, 1952.

[22] B. R. Judd, *Operator techniques in atomic spectroscopy*. Princeton University Press, 2014, vol. 35.

[23] B. G. Wybourne and L. Smentek, *Optical spectroscopy of lanthanides: magnetic and hyperfine interactions*. CRC press, 2007.

[24] M. Weissbluth, *Atoms and molecules*. Elsevier, 2012, pp. 385–412.

[25] W. Carnall, G. Goodman, K. Rajnak, and R. Rana, "A systematic analysis of the spectra of the lanthanides doped into single crystal LaF_3," *The Journal of chemical physics*, vol. 90, no. 7, pp. 3443–3457, 1989.

[26] R. Withnall and J. Silver, "Physics of light emission from rare earth-doped phosphors," in *Handbook of Visual Display Technology*. Berlin, Heidelberg: Springer Berlin Heidelberg, 2014, pp. 1019–1028.

[27] G. Liu and B. Jacquier, *Spectroscopic properties of rare earths in optical materials*. Springer Science & Business Media, 2006, vol. 83, p. 33.

[28] A. de Bettencourt-Dias, *Luminescence of lanthanide ions in coordination compounds and nanomaterials*. John Wiley & Sons, 2014, pp. 1–22.

[29] D. J. Griffiths and D. F. Schroeter, *Introduction to quantum mechanics*. Cambridge university press, 2018, pp. 121–133.

[30] V. Sastri, J. Perumareddi, V. R. Rao, G. Rayudu, and J.-C. Bunzli, *Modern aspects of rare earths and their complexes*. Elsevier, 2003, pp. 741–743.

[31] H. Rahman, "Optical intensities of trivalent erbium in various host lattices," *Journal of Physics C: Solid State Physics*, vol. 5, no. 3, p. 306, 1972.

[32] K. Saxena and G. Malli, "A tabulation of the 6-j symbols," *Canadian Journal of Physics*, vol. 47, no. 24, pp. 2811–2814, 1969.

[33] C. Nielson and G. F. Koster, *Spectroscopic Coefficients for the p^n, d^n, and f^n Configurations*. MIT press, 1963.

[34] J. Stark, "Beobachtungen über den effekt des elektrischen feldes auf spektrallinien. i. quereffekt," *Annalen der Physik*, vol. 348, no. 7, pp. 965–982, 1914.

[35] B. R. Judd, "Optical absorption intensities of rare-earth ions," *Physical review*, vol. 127, no. 3, p. 750, 1962.

[36] G. Ofelt, "Intensities of crystal spectra of rare-earth ions," *The journal of chemical physics*, vol. 37, no. 3, pp. 511–520, 1962.

[37] L. Allen and J. H. Eberly, *Optical resonance and two-level atoms*. Courier Corporation, 1987, vol. 28.

[38] W. Mims, "Phase memory in electron spin echoes, lattice relaxation effects in $CaWO_4$:Er, Ce, Mn," *Physical Review*, vol. 168, no. 2, p. 370, 1968.

[39] R. Orbach, "Spin-lattice relaxation in rare-earth salts," *Proceedings of the Royal Society of London. Series A. Mathematical and Physical Sciences*, vol. 264, no. 1319, pp. 458–484, 1961.

[40] G. Wang, R. Equall, R. Cone, M. Leask, K. Godfrey, and F. Wondre, "Optical dephasing mechanisms in $Tm^{3+} : Y_2Si_2O_7$," *Optics letters*, vol. 21, no. 11, pp. 818–820, 1996.

[41] T. L. Harris, "Erbium-based optical coherent transient correlator for the 1.5-micron communication bands," Ph.D. dissertation, Montana State University-Bozeman, College of Letters & Science, 2001.

[42] R. Cone, R. Equall, Y. Sun, R. Macfarlane, and R. Hutcheson, "Ultraslow dephasing and dephasing mechanisms in rare earth materials for optical data storage," *Laser Phys.*, vol. 5, pp. 573–575, 1995.

[43] C. Thiel, T. Böttger, and R. Cone, "Rare-earth-doped materials for applications in quantum information storage and signal processing," *Journal of luminescence*, vol. 131, no. 3, pp. 353–361, 2011.

[44] E. F. Schubert, "Phenomenology of deep levels," in *Doping in III-V Semiconductors*. Cambridge University Press, 1993, pp. 54–77. DOI: 10.1017/CBO9780511599828.005.

[45] B. A. Monemar, "Electronic structure and bound excitons for defects in semiconductors from optical spectroscopy," *Critical Reviews in Solid State and Material Sciences*, vol. 15, no. 2, pp. 111–115, 1988.

[46] E. F. Schubert, "Shallow impurities," in *Doping in III-V Semiconductors*. Cambridge University Press, 1993, pp. 6–53. DOI: 10.1017/CBO9780511599828.004.

[47] K. W. Böer and U. W. Pohl, "Deep-level centers," in *Semiconductor Physics*. Cham: Springer International Publishing, 2018, pp. 731–732, ISBN: 978-3-319-69150-3. DOI: 10.1007/978-3-319-69150-3_19. [Online]. Available: https://doi.org/10.1007/978-3-319-69150-3_19.

[48] D. Thao *et al.*, "Photoluminescence spectroscopy on erbium-doped and porous silicon," Ph.D. dissertation, Ph. D Thesis. University of Amsterdam. Amsterdam, 2000.

[49] A. Polman, "Erbium implanted thin film photonic materials," *Journal of applied physics*, vol. 82, no. 1, pp. 1–39, 1997.

[50] Y. Li, C. Tan, C. Xue, J. Zhang, H. Xu, P. Liu, and L. Wang, "Defect formation and annealing behavior of Si implanted by high-energy ^{166}Er ions," *Nuclear Instruments and Methods in Physics Research Section B: Beam Interactions with Materials and Atoms*, vol. 174, no. 1-2, pp. 137–142, 2001.

[51] W. Gillin, Z. Jingping, and B. Sealy, "Rutherford backscattering and secondary ion mass spectrometry studies of erbium implanted silicon," *Solid state communications*, vol. 77, no. 12, pp. 907–910, 1991.

[52] H. Efeoglu, J. Evans, T. Jackman, B. Hamilton, D. Houghton, J. Langer, A. Peaker, D. Perovic, I. Poole, N. Ravel, *et al.*, "Recombination processes in erbium-doped MBE silicon," *Semiconductor science and technology*, vol. 8, no. 2, p. 236, 1993.

[53] D. Eaglesham, J. Michel, E. Fitzgerald, D. Jacobson, J. Poate, J. Benton, A. Polman, Y.-H. Xie, and L. Kimerling, "Microstructure of Erbium-implanted Si," *Applied Physics Letters*, vol. 58, no. 24, pp. 2797–2799, 1991.

[54] P. Liu, J. Zhang, R. Wilson, G. Curello, S. Rao, and P. Hemment, "Effect of fluorine co-implantation on MeV erbium implanted silicon," *Applied physics letters*, vol. 66, no. 23, pp. 3158–3160, 1995.

[55] J. Carey, R. Barklie, J. Donegan, F. Priolo, G. Franzò, and S. Coffa, "EPR study of erbium-impurity complexes in silicon," *Journal of luminescence*, vol. 80, no. 1-4, pp. 297–301, 1998.

[56] F. Priolo, G. Franzò, S. Coffa, A. Polman, S. Libertino, R. Barklie, and D. Carey, "The erbium-impurity interaction and its effects on the 1.54 μm luminescence of Er^{3+} in crystalline silicon," *Journal of applied physics*, vol. 78, no. 6, pp. 3874–3882, 1995.

[57] J. Michel, J. Benton, R. Ferrante, D. Jacobson, D. Eaglesham, E. Fitzgerald, Y.-H. Xie, J. Poate, and L. Kimerling, "Impurity enhancement of the 1.54-μm Er^{3+} luminescence in silicon," *Journal of applied physics*, vol. 70, no. 5, pp. 2672–2678, 1991.

[58] M. Needels, M. Schlüter, and M. Lannoo, "Erbium point defects in silicon," *Physical Review B*, vol. 47, no. 23, p. 15 533, 1993.

[59] K. Thonke, K. Pressel, G. Bohnert, A. Stapor, J. Weber, M. Moser, A. Molassioti, A. Hangleiter, and F. Scholz, "On excitation and decay mechanisms of the Yb^{3+} luminescence in InP," *Semiconductor science and technology*, vol. 5, no. 11, p. 1124, 1990.

[60] K. Takahei, A. Taguchi, H. Nakagome, K. Uwai, and P. Whitney, "Intra-4 f-shell luminescence excitation and quenching mechanism of Yb in InP," *Journal of applied physics*, vol. 66, no. 10, pp. 4941–4945, 1989.

[61] P. S. Whitney, K. Uwai, H. Nakagome, and K. Takahei, "Electrical properties of ytterbium-doped InP grown by metalorganic chemical vapor deposition," *Applied physics letters*, vol. 53, no. 21, pp. 2074–2076, 1988.

[62] G. Davies, T. Gregorkiewicz, M. Z. Iqbal, M. Kleverman, E. Lightowlers, N. Vinh, and M. Zhu, "Optical properties of a silver-related defect in silicon," *Physical Review B*, vol. 67, no. 23, p. 235 111, 2003.

[63] N. Vinh, J. Phillips, G. Davies, and T. Gregorkiewicz, "Time-resolved free-electron laser spectroscopy of a copper isoelectronic center in silicon," *Physical Review B*, vol. 71, no. 8, p. 085 206, 2005.

[64] N. Q. Vinh, N. N. Ha, and T. Gregorkiewicz, "Photonic properties of Er-doped crystalline silicon," *Proceedings of the IEEE*, vol. 97, no. 7, pp. 1269–1283, 2009.

[65] A. Taguchi, K. Takahei, and Y. Horikoshi, "Multiphonon-assisted energy transfer between Yb 4f shell and InP host," *Journal of applied physics*, vol. 76, no. 11, pp. 7288–7295, 1994.

[66] I. Yassievich and L. Kimerling, "The mechanisms of electronic excitation of rare earth impurities in semiconductors," *Semiconductor science and technology*, vol. 8, no. 5, p. 718, 1993.

[67] S. Libertino, S. Coffa, G. Franzo, and F. Priolo, "The effects of oxygen and defects on the deep-level properties of Er in crystalline Si," *Journal of applied physics*, vol. 78, no. 6, pp. 3867–3873, 1995.

[68] V. Masterov and L. Gerchikov, "The possible mechanism of excitation of the f-f emission from Er-O clusters in Silicon," *MRS Online Proceedings Library (OPL)*, vol. 422, 1996.

[69] M. Bresler, O. Gusev, B. Zakharchenya, and I. Yassievich, "Exciton excitation mechanism for erbium ions in silicon," *Physics of the Solid State*, vol. 38, no. 5, pp. 813–817, 1996.

[70] I. Tsimperidis, T. Gregorkiewicz, H. T. Bekman, and C. Langerak, "Direct observation of the two-stage excitation mechanism of Er in Si," *Physical review letters*, vol. 81, no. 21, p. 4748, 1998.

[71] F. Priolo, G. Franzò, S. Coffa, and A. Carnera, "Excitation and nonradiative deexcitation processes of Er^{3+} in crystalline Si," *Physical Review B*, vol. 57, no. 8, p. 4443, 1998.

[72] O. Gusev, M. Bresler, P. Pak, I. Yassievich, M. Forcales, N. Vinh, and T. Gregorkiewicz, "Excitation cross section of erbium in semiconductor matrices under optical pumping," *Physical Review B*, vol. 64, no. 7, p. 075 302, 2001.

[73] B. Pawlak, N. Vinh, I. Yassievich, and T. Gregorkiewicz, "Influence of p- n junction formation at a Si/Si:Er interface on low-temperature excitation of Er3+ ions in crystalline silicon," *Physical Review B*, vol. 64, no. 13, p. 132 202, 2001.

[74] N. Vinh, H. Przybylińska, Z. Krasil'nik, and T. Gregorkiewicz, "Optical properties of a single type of optically active center in Si/Si:Er nanostructures," *Physical Review B*, vol. 70, no. 11, p. 115 332, 2004.

[75] A. Taguchi and K. Takahei, "Erbium in Si: Estimation of energy transfer rate and trap depth from temperature dependence of intra-4f-shell luminescence," *Journal of applied physics*, vol. 83, no. 5, pp. 2800–2805, 1998.

[76] A. Prokofiev, I. Yassievich, and T. Gregorkiewicz, "Theoretical modeling of thermally activated luminescence quenching processes in Si:Er," *Physical Review B*, vol. 72, no. 4, p. 045 214, 2005.

[77] A. Moskalenko, I. Yassievich, M. Forcales, M. Klik, and T. Gregorkiewicz, "Terahertz-assisted excitation of the 1.5 μm photoluminescence of "e"r in crystalline "s"i," *Physical Review B*, vol. 70, no. 15, p. 155 201, 2004.

[78] J. Palm, F. Gan, B. Zheng, J. Michel, and L. Kimerling, "Electroluminescence of erbium-doped silicon," *Physical Review B*, vol. 54, no. 24, p. 17 603, 1996.

[79] M. Forcales, T. Gregorkiewicz, and M. Bresler, "Auger deexcitation of Er^{3+} ions in crystalline Si optically induced by midinfrared illumination," *Physical Review B*, vol. 68, no. 3, p. 035 213, 2003.

[80] M. Rancic, "High resolution spectroscopy of erbium doped solids," Ph.D. dissertation, The Australian National University, 2017.

[81] Y. Tang, K. Heasman, W. Gillin, and B. Sealy, "Characteristics of rare-earth element erbium implanted in silicon," *Applied physics letters*, vol. 55, no. 5, pp. 432–433, 1989.

[82] H. Przybylinska, W. Jantsch, Y. Suprun-Belevitch, M. Stepikhova, L. Palmetshofer, G. Hendorfer, A. Kozanecki, R. Wilson, and B. Sealy, "Optically active erbium centers in silicon," *Physical Review B*, vol. 54, no. 4, p. 2532, 1996.

[83] D. Adler, D. Jacobson, D. Eaglesham, M. Marcus, J. Benton, J. Poate, and P. Citrin, "Local structure of 1.54-μm-luminescence Er^{3+} implanted in Si," *Applied physics letters*, vol. 61, no. 18, pp. 2181–2183, 1992.

[84] F. d'Acapito, S. Mobilio, S. Scalese, A. Terrasi, G. Franzò, and F. Priolo, "Structure of Er-O complexes in crystalline Si," *Physical Review B*, vol. 69, no. 15, p. 153 310, 2004.

[85] J. Carey, R. Barklie, J. Donegan, F. Priolo, G. Franzo, and S. Coffa, "Electron paramagnetic resonance and photoluminescence study of Er-impurity complexes in Si," *Physical Review B*, vol. 59, no. 4, p. 2773, 1999.

[86] M. Huang and X. Ren, "Evidence of oxygen-stabilized hexagonal interstitial erbium in silicon," *Physical Review B*, vol. 68, no. 3, p. 033 203, 2003.

[87] J. Wan, Y. Ling, Q. Sun, and X. Wang, "Role of codopant oxygen in erbium-doped silicon," *Physical Review B*, vol. 58, no. 16, p. 10 415, 1998.

[88] M. Hashimoto, A. Yanase, H. Harima, and H. Katayama-Yoshida, "Determination of the atomic configuration of Er–O complexes in silicon by the super-cell FLAPW method," *Physica B: Condensed Matter*, vol. 308, pp. 378–381, 2001.

[89] A. Raffa and P. Ballone, "Equilibrium structure of erbium-oxygen complexes in crystalline silicon," *Physical Review B*, vol. 65, no. 12, p. 121 309, 2002.

[90] D. Prezzi, T. Eberlein, R. Jones, J. Filhol, J. Coutinho, M. Shaw, and P. Briddon, "Electrical activity of Er and Er-O centers in silicon," *Physical Review B*, vol. 71, no. 24, p. 245 203, 2005.

[91] U. Wahl, A. Vantomme, J. De Wachter, R. Moons, G. Langouche, J. Marques, J. Correia, I. collaboration, *et al.*, "Direct evidence for tetrahedral interstitial Er in Si," *Physical review letters*, vol. 79, no. 11, p. 2069, 1997.

[92] S. Moloi, S. Omogiate, and M. Masekane, "Erbium implanted Silicon: Erbium lattice location, diffusion mechanisms and segregation," *SSRN (preprint)*,

[93] S. Pizzini, S. Binetti, D. Calcina, N. Morgante, and A. Cavallini, "Local structure of erbium–oxygen complexes in erbium-doped silicon and its correlation with the optical activity of erbium," *Materials Science and Engineering: B*, vol. 72, no. 2-3, pp. 173–176, 2000.

[94] N. Vinh, H. Przybylińska, Z. Krasil'nik, B. Andreev, and T. Gregorkiewicz, "Observation of Zeeman effect in photoluminescence of "E"r^{3+} ion imbedded in crystalline silicon," *Physica B: Condensed Matter*, vol. 308, pp. 340–343, 2001.

[95] N. Vinh, H. Przybylińska, Z. Krasil'nik, and T. Gregorkiewicz, "Microscopic structure of Er-related optically active centers in crystalline silicon," *Physical review letters*, vol. 90, no. 6, p. 066 401, 2003.

[96] A. Peaker, "Erbium in semiconductors: Where are we coming from; where are we going?" *MRS Online Proceedings Library (OPL)*, vol. 866, pp. V1–1, 2005.

[97] L. Weiss, A. Gritsch, B. Merkel, and A. Reiserer, "Erbium dopants in nanophotonic silicon waveguides," *Optica*, vol. 8, no. 1, pp. 40–41, 2021.

[98] A. Gritsch, L. Weiss, J. Früh, S. Rinner, and A. Reiserer, "Narrow optical transitions in erbium-implanted silicon waveguides," *Physical Review X*, vol. 12, no. 4, p. 041 009, 2022.

[99] H. Ennen, J. Schneider, G. Pomrenke, and A. Axmann, "1.54-μm luminescence of erbium-implanted III–V semiconductors and silicon," *Applied Physics Letters*, vol. 43, no. 10, pp. 943–945, 1983.

[100] A. Boothroyd, "SPECTRE, A Program for Calculating Spectroscopic Properties of Rare Earth Ions in Crystals," 1990.

[101] K. Lea, M. Leask, and W. Wolf, "The raising of angular momentum degeneracy of f-electron terms by cubic crystal fields," *Journal of Physics and Chemistry of Solids*, vol. 23, no. 10, pp. 1381–1405, 1962.

[102] S. Laachir, M. Moussetad, and R. Adhiri, "Crystal-field energy levels of trivalent Erbium ion in cubic symmetry," *Zeitschrift für Naturforschung A*, vol. 66, no. 6-7, pp. 457–460, 2011.

[103] M. A. Hughes, H. Li, N. Theodoropoulou, and J. D. Carey, "Optically modulated magnetic resonance of erbium implanted silicon," *Scientific reports*, vol. 9, no. 1, pp. 1–10, 2019. DOI: https://doi.org/10.1038/s41598-019-55246-z.

[104] I. de Maat-Gersdorf, T. Gregorkiewicz, C. Ammerlaan, and N. Sobolev, "Photoluminescence measurements on erbium-doped silicon," *Semiconductor science and technology*, vol. 10, no. 5, p. 666, 1995.

[105] G. F. Koster, J. O. Dimmock, R. G. Wheeler, and H. Statz, *Properties of the thirty-two point groups*. MIT press, 1963, vol. 24.

[106] J. Leech and D. Newman, "How to use groups," *Ltd., London, UK*, 1969.

[107] S. Y. Ren and J. D. Dow, "Crystal-field splitting of Er^{3+} in Si," *Journal of applied physics*, vol. 81, no. 4, pp. 1877–1882, 1997.

[108] I. de Maat-Gersdorf *et al.*, "Spectroscopic analysis of erbium-doped silicon and ytterbium-doped indium phosphide," Ph.D. dissertation, University of Amsterdam-UvA, 2001.

[109] M. Stepikhova, B. Andreev, V. Shmagin, Z. Krasil'Nik, V. Kuznetsov, V. Shengurov, S. Svetlov, W. Jantsch, L. Palmetshofer, and H. Ellmer, "Properties of optically active Si:Er and $Si_{1-x}Ge_x$ layers grown by the sublimation MBE method:[thin solid films 369 (2000) 320–323]," *Thin Solid Films*, vol. 381, no. 1, pp. 164–169, 2001.

[110] H. Przybylinska, N. Vinh, B. Andreev, Z. Krasil'nik, and T. Gregorkiewicz, "Microscopic structure of Er-related optically active centers in Si," *MRS Online Proceedings Library (OPL)*, vol. 770, 2003.

[111] C. Ammerlaan, "Spectroscopic characterisation of the erbium impurity in crystalline semiconductors," *Physica B: Condensed Matter*, vol. 308, pp. 387–390, 2001.

[112] B. Cavenett, "Optically detected magnetic resonance (ODMR) investigations of recombination processes in semiconductors," *Advances in Physics*, vol. 30, no. 4, pp. 475–538, 1981.

[113] J. Carey, J. Donegan, R. Barklie, F. Priolo, G. Franzo, and S. Coffa, "Electron paramagnetic resonance of erbium doped silicon," *Applied physics letters*, vol. 69, no. 25, pp. 3854–3856, 1996.

[114] J. F. Ziegler, M. D. Ziegler, and J. P. Biersack, "SRIM–the stopping and range of ions in matter," *Nuclear Instruments and Methods in Physics Research Section B: Beam Interactions with Materials and Atoms*, vol. 268, no. 11-12, pp. 1818–1823, 2010.

[115] W. E. Wallace, "Mass spectra," *NIST chemistry webbook, NIST standard reference database*, no. 69, p. 20 899, 2018.

[116] W. J. Marshall, "Two methods for measuring laser beam diameter," *Journal of Laser Applications*, vol. 22, no. 4, pp. 132–136, 2010.

[117] J. M. Khosrofian and B. A. Garetz, "Measurement of a Gaussian laser beam diameter through the direct inversion of knife-edge data," *Applied optics*, vol. 22, no. 21, pp. 3406–3410, 1983.

[118] E. Smith and G. Dent, *Modern Raman spectroscopy: a practical approach*. John Wiley & Sons, 2019, pp. 1–21. DOI: 10.1002/0470011831.ch1.

[119] J. R. Ferraro, *Introductory Raman spectroscopy*. Elsevier, 2003.

[120] P. A. Temple and C. Hathaway, "Multiphonon Raman spectrum of silicon," *Physical Review B*, vol. 7, no. 8, p. 3685, 1973.

[121] A. Zwick and R. Carles, "Multiple-order Raman scattering in crystalline and amorphous silicon," *Physical Review B*, vol. 48, no. 9, p. 6024, 1993.

[122] I. De Wolf, J. Vanhellemont, A. Romano-Rodrıguez, H. Norström, and H. Maes, "Micro-Raman study of stress distribution in local isolation structures and correlation with transmission electron microscopy," *Journal of Applied Physics*, vol. 71, no. 2, pp. 898–906, 1992.

[123] J. Parker Jr, D. Feldman, and M. Ashkin, "Raman scattering by silicon and germanium," *Physical Review*, vol. 155, no. 3, p. 712, 1967.

[124] D. A. Long, *The Raman effect: a unified treatment of the theory of Raman scattering by molecules*. Wiley Chichester, 2002, vol. 8.

[125] C.-Y. Peng, C.-F. Huang, Y.-C. Fu, Y.-H. Yang, C.-Y. Lai, S.-T. Chang, and C. Liu, "Comprehensive study of the Raman shifts of strained silicon and germanium," *Journal of Applied Physics*, vol. 105, no. 8, p. 083 537, 2009.

[126] R. Vink, G. Barkema, and W. van Der Weg, "Raman spectra and structure of amorphous Si," *Physical Review B*, vol. 63, no. 11, p. 115 210, 2001.

[127] T. Deschaines, J. Hodkiewicz, and P. Henson, "Characterization of amorphous and microcrystalline silicon using Raman spectroscopy," *Technical Note 51735*, 2009.

[128] E. Nogales, B. Méndez, J. Piqueras, R. Plugaru, A. Coraci, and J. Garcıa, "Visible luminescence of erbium oxide layers grown on crystalline and amorphous silicon," *Journal of Physics D: Applied Physics*, vol. 35, no. 4, p. 295, 2002.

[129] S. Gallis, M. Huang, H. Efstathiadis, E. Eisenbraun, A. E. Kaloyeros, E. E. Nyein, and U. Hommerich, "Photoluminescence in erbium doped amorphous silicon oxycarbide thin films," *Applied Physics Letters*, vol. 87, no. 9, p. 091 901, 2005.

[130] C.-Y. Chen, W.-D. Chen, S.-F. Song, Z.-J. Xu, X. Liao, G. Li, and K. Ding, "Study on Er^{3+} emission from the erbium-doped hydrogenated amorphous silicon suboxide film," *Journal of applied physics*, vol. 94, no. 9, pp. 5599–5604, 2003.

[131] C. Chen, W. Chen, S. Song, and C. Hsu, "Photoluminesfcence of Er-doped SiO_2 films containing Si nanocrystals and Er," *Journal of crystal growth*, vol. 253, no. 1-4, pp. 10–15, 2003.

[132] C. Chen, W. Chen, S. Song, Z. Xu, X. Liao, G.-H. Li, L. Bian, and K. Ding, "Correlation between Er^{3+} emission and Si clusters in Erbium-doped a-SiO_x:H films," *Physica E: Low-dimensional Systems and Nanostructures*, vol. 27, no. 1-2, pp. 21–25, 2005.

[133] C. Chang-Yong, C. Wei-De, L. Guo-Hua, S. Shu-Fang, D. Kun, and X. Zhen-Jia, "Role of amorphous silicon domains on Er^{3+} emission in the Er-doped hydrogenated amorphous silicon suboxide film," *Chinese Physics*, vol. 12, no. 4, p. 438, 2003.

[134] W. S. Yoo, K. Kang, G. Murai, and M. Yoshimoto, "Temperature dependence of photoluminescence spectra from crystalline silicon," *ECS Journal of Solid State Science and Technology*, vol. 4, no. 12, P456, 2015.

[135] R. Sauer, J. Weber, J. Stolz, E. Weber, K.-H. Küsters, and H. Alexander, "Dislocation-related photoluminescence in silicon," *Applied Physics A*, vol. 36, no. 1, pp. 1–13, 1985.

[136] S. Coffa, F. Priolo, G. Franzo, V. Bellani, A. Carnera, and C. Spinella, "Optical activation and excitation mechanisms of Er implanted in Si," *Physical Review B*, vol. 48, no. 16, p. 11 782, 1993.

[137] F. Priolo, S. Coffa, G. Franzo, C. Spinella, A. Carnera, and V. Bellani, "Electrical and optical characterization of Er-implanted Si: The role of impurities and defects," *Journal of applied physics*, vol. 74, no. 8, pp. 4936–4942, 1993.

[138] S. Scalese, G. Franzo, S. Mirabella, M. Re, A. Terrasi, F. Priolo, E. Rimini, C. Spinella, and A. Carnera, "Effect of O:Er concentration ratio on the structural, electrical, and optical properties of Si:Er:O layers grown by molecular beam epitaxy," *Journal of Applied Physics*, vol. 88, no. 7, pp. 4091–4096, 2000.

[139] G. Franzò, E. Napolitani, P. Cardile, S. Boninelli, A. Marino, and F. Priolo, "Erbium–oxygen interactions in crystalline silicon," *Semiconductor science and technology*, vol. 26, no. 5, p. 055 002, 2011.

[140] M. Lourenço, M. Milošević, A. Gorin, R. Gwilliam, and K. Homewood, "Super-enhancement of 1.54 μm emission from erbium codoped with oxygen in silicon-on-insulator," *Scientific Reports*, vol. 6, no. 1, pp. 1–6, 2016.

[141] P. Zhang, J. Hong, H. Wen, H. Wei, J. Liu, F. Yue, and Y. Dan, "Fluorescence optimization and ratiometric thermometry of near-infrared emission in erbium/oxygen-doped crystalline silicon," *Journal of Luminescence*, vol. 250, p. 119 035, 2022.

[142] J. Michel, L. Assali, M. Morse, and L. Kimerling, "Erbium in silicon," in *Semiconductors and Semimetals*, vol. 49, Elsevier, 1997, pp. 111–156.

[143] M. He, D. Yang, and D. Li, "Electroluminescence from metal–oxide–semiconductor devices based on erbium silicate nanocrystals and silicon nanocrystals co-embedded in silicon oxide thin films," *Journal of Materials Science: Materials in Electronics*, vol. 32, pp. 20 659–20 667, 2021.

[144] A. Polman, J. Custer, E. Snoeks, and G. Van den Hoven, "Incorporation of high concentrations of erbium in crystal silicon," *Applied physics letters*, vol. 62, no. 5, pp. 507–509, 1993.

[145] A. Polman, G. Van den Hoven, J. Custer, J. Shin, R. Serna, and P. Alkemade, "Erbium in crystal silicon: Optical activation, excitation, and concentration limits," *Journal of applied physics*, vol. 77, no. 3, pp. 1256–1262, 1995.

[146] X. Duan, J. Palm, B. Zheng, M. Morse, J. Michel, and L. Kimerling, "Defects in erbium/oxygen implanted silicon," *MRS Online Proceedings Library (OPL)*, vol. 442, 1996.

[147] X. Wang, J. He, S. Jin, H. Liu, H. Li, H. Wen, X. Zhao, R. Abedini-Nassab, G. Sha, F. Yue, *et al.*, "Fluorine-enhanced room temperature luminescence of Er-doped crystalline Silicon," *Advanced Photonics Research*, vol. 3, no. 12, p. 2 200 115, 2022.

[148] E. Fitzgerald, M. Currie, S. Samavedam, T. Langdo, G. Taraschi, V. Yang, C. Leitz, and M. Bulsara, "Dislocations in relaxed SiGe/Si heterostructures," *physica status solidi (a)*, vol. 171, no. 1, pp. 227–238, 1999.

[149] V. Higgs, E. Lightowlers, E. Fitzgerald, Y. Xie, and P. Silverman, "Characterization of compositionally graded Si_{1-x} Ge_x alloy layers by photoluminescence spectroscopy and by cathodoluminescence spectroscopy and imaging," *Journal of applied physics*, vol. 73, no. 4, pp. 1952–1956, 1993.

[150] A. Blumenau, R. Jones, S. Öberg, P. Briddon, and T. Frauenheim, "Dislocation related photoluminescence in silicon," *Physical Review Letters*, vol. 87, no. 18, p. 187 404, 2001.

[151] N. Sobolev, O. Gusev, E. Shek, V. Vdovin, T. Yugova, and A. Emel'yanov, "Photoluminescence and structural defects in erbium-implanted silicon annealed at high temperature," *Applied physics letters*, vol. 72, no. 25, pp. 3326–3328, 1998.

[152] H. Shibata, "Negative thermal quenching curves in photoluminescence of solids," *Japanese journal of applied physics*, vol. 37, no. 2R, p. 550, 1998.

[153] J. H. Shin, G. Van den Hoven, and A. Polman, "Direct experimental evidence for trap-state mediated excitation of Er^{3+} in silicon," *Applied physics letters*, vol. 67, no. 3, pp. 377–379, 1995.

[154] M. Forcales, I. Bradley, J.-P. Wells, and T. Gregorkiewicz, "Mid-infrared induced quenching of photoluminescence in Si:Er," *Materials Science and Engineering: B*, vol. 81, no. 1, pp. 80–82, 2001.

[155] M. A. Hughes, N. A. Panjwani, M. Urdampilleta, N. Theodoropoulou, I. Wisby, K. P. Homewood, B. Murdin, T. Lindström, and J. D. Carey, "Erbium implanted silicon for solid-state quantum technologies," *arXiv:2006.00225(preprint)*, 2020. DOI: https://doi.org/10.48550/arXiv.2006.00225.

[156] E. Snoeks, A. Lagendijk, and A. Polman, "Measuring and modifying the spontaneous emission rate of erbium near an interface," *Physical Review Letters*, vol. 74, no. 13, p. 2459, 1995.

[157] A. Karim, W.-X. Ni, A. Elfving, P. Å. Persson, and G. Hansson, "Characterization of Er/O-doped Si-"led"s with low thermal quenching," *MRS Online Proceedings Library (OPL)*, vol. 866, 2005.

[158] C. Creatore, L. C. Andreani, M. Miritello, R. Lo Savio, and F. Priolo, "Modification of erbium radiative lifetime in planar silicon slot waveguides," *Applied Physics Letters*, vol. 94, no. 10, p. 103 112, 2009.

[159] A. Vredenberg, N. Hunt, E. Schubert, D. Jacobson, J. Poate, and G. Zydzik, "Controlled atomic spontaneous emission from Er^{3+} in a transparent Si/SiO_2 microcavity," *Physical review letters*, vol. 71, no. 4, p. 517, 1993.

[160] H. Isshiki, M. De Dood, A. Polman, and T. Kimura, "Self-assembled infrared-luminescent Er–Si–O crystallites on silicon," *Applied physics letters*, vol. 85, no. 19, pp. 4343–4345, 2004.

[161] T. Schweizer, T. Jensen, E. Heumann, and G. Huber, "Spectroscopic properties and diode pumped 1.6 μm laser performance in Yb-codoped Er: $Y_3Al_5O_{12}$ and Er:Y_2Si_{O5}," *Optics communications*, vol. 118, no. 5-6, pp. 557–561, 1995.

[162] R. Li, S. Yerci, and L. Dal Negro, "Temperature dependence of the energy transfer from amorphous silicon nitride to "e"r ions," *Applied Physics Letters*, vol. 95, no. 4, pp. 41–111, 2009.

[163] S. Gallis, H. Efstathiadis, M. Huang, E. E. Nyein, U. Hommerich, and A. E. Kaloyeros, "Photoluminescence at 1540 nm from erbium-doped amorphous silicon carbide films," *Journal of materials research*, vol. 19, pp. 2389–2393, 2004.

[164] R. Quimby, W. Miniscalco, and B. Thompson, "Clustering in erbium-doped silica glass fibers analyzed using 980 nm excited-state absorption," *Journal of Applied Physics*, vol. 76, no. 8, pp. 4472–4478, 1994.

[165] A. Kenyon, M. Wojdak, I. Ahmad, W. Loh, and C. Oton, "Generalized rate-equation analysis of excitation exchange between silicon nanoclusters and erbium ions," *Physical Review B*, vol. 77, no. 3, p. 035 318, 2008.

[166] D. Tetelbaum, O. Gorshkov, A. Ershov, A. Kasatkin, V. Kamin, A. Mikhaylov, A. Belov, D. Gaponova, L. Pavesi, L. Ferraioli, *et al.*, "Influence of the nature of oxide matrix on the photoluminescence spectrum of ion-synthesized silicon nanostructures," *Thin Solid Films*, vol. 515, no. 1, pp. 333–337, 2006.

[167] M. Dovrat, Y. Goshen, J. Jedrzejewski, I. Balberg, and A. Sa'Ar, "Radiative versus nonradiative decay processes in silicon nanocrystals probed by time-resolved photoluminescence spectroscopy," *Physical Review B*, vol. 69, no. 15, p. 155 311, 2004.

[168] O. Guillois, N. Herlin-Boime, C. Reynaud, G. Ledoux, and F. Huisken, "Photoluminescence decay dynamics of noninteracting silicon nanocrystals," *Journal of Applied Physics*, vol. 95, no. 7, pp. 3677–3682, 2004.

[169] J. Murphy, K. Bothe, M. Olmo, V. Voronkov, and R. Falster, "The effect of oxide precipitates on minority carrier lifetime in p-type silicon," *Journal of Applied Physics*, vol. 110, no. 5, p. 053 713, 2011.

[170] H. Sugimoto, M. Inoue, M. Tajima, A. Ogura, and Y. Ohshita, "Analysis of intragrain defects in multicrystalline silicon wafers by photoluminescence mapping and spectroscopy," *Japanese journal of applied physics*, vol. 45, no. 7L, p. L641, 2006.

[171] S. Coffa, G. Franzo, F. Priolo, A. Polman, and R. Serna, "Temperature dependence and quenching processes of the intra-4f luminescence of Er in crystalline Si," *Physical Review B*, vol. 49, no. 23, p. 16 313, 1994.

[172] J. Demas, *Excited state lifetime measurements*. Elsevier, 2012, pp. 34–37.

[173] N. Hamelin, P. Kik, J. Suyver, K. Kikoin, A. Polman, A. Schönecker, and F. Saris, "Energy backtransfer and infrared photoresponse in erbium-doped silicon p–n diodes," *Journal of Applied Physics*, vol. 88, no. 9, pp. 5381–5387, 2000.

[174] A. Sillen and Y. Engelborghs, "The correct use of "average" fluorescence parameters," *Photochemistry and photobiology*, vol. 67, no. 5, pp. 475–486, 1998.

[175] J. R. Lakowicz, *Principles of fluorescence spectroscopy*. Springer, 2006, p. 99.

[176] M. A. Hughes, "Modified chalcogenide glasses for optical device applications," Ph.D. dissertation, University of Southampton, 2007.

[177] P. Paufler and S. Elliott, *Physics of amorphous materials*, 1984.

[178] T. J. Seebeck, *Magnetische polarisation der metalle und erze durch temperaturdifferenz*. W. Engelmann, 1895.

[179] H. Kramers, "General theory of paramagnetic rotation in crystals," in *Proc. Acad. Sci. Amsterdam*, vol. 33, 1930, p. 959.

[180] R. Macfarlane, T. Harris, Y. Sun, R. Cone, and R. Equall, "Measurement of photon echoes in Er:Y_2SiO_5 at 1.5 μm with a diode laser and an amplifier," *Optics letters*, vol. 22, no. 12, pp. 871–873, 1997.

[181] R. Yano, M. Mitsunaga, and N. Uesugi, "Ultralong optical dephasing time in Eu^{3+}:Y_2SiO_5," *Optics letters*, vol. 16, no. 23, pp. 1884–1886, 1991.

[182] B. Maksimov, V. Ilyukhin, K. YA, and N. Belov, "Crystal structure of yttrium oxyorthosilicate $Y_2O_3SiO_2$= Y_2SiO_5-dual function of yttrium," *SOVIET PHYSICS CRYSTALLOGRAPHY, USSR*, vol. 15, no. 5, p. 806, 1971.

[183] J. Doualan, C. Labbé, P. Le Boulanger, J. Margerie, R. Moncorgé, and H. Timonen, "Energy levels of the laser active Er^{3+} ion in each of the two crystallographic sites of yttrium orthosilicate," *Journal of Physics: Condensed Matter*, vol. 7, no. 26, p. 5111, 1995.

[184] A. Mirzai, A. Ahadi, S. Melin, and P. Olsson, "First-principle investigation of doping effects on mechanical and thermodynamic properties of Y_2SiO_5," *Mechanics of Materials*, vol. 154, p. 103 739, 2021. DOI: https://doi.org/10.1016/j.mechmat.2020.103739. [Online]. Available: https://www.sciencedirect.com/science/article/pii/S0167663620307614.

[185] C. Li, C. Wyon, and R. Moncorge, "Spectroscopic properties and fluorescence dynamics of Er^{3+} and Yb^{3+} in Y_2SiO_5," *IEEE journal of quantum electronics*, vol. 28, no. 4, pp. 1209–1221, 1992.

[186] Y. Sun, T. Böttger, C. Thiel, and R. Cone, "Magnetic g tensors for the $^4I_{15/2}$ and $^4I_{13/2}$ states of Er^{3+}:Y_2SiO_5," *Physical Review B*, vol. 77, no. 8, p. 085 124, 2008.

[187] S. Horvath, "High-resolution spectroscopy and novel crystal-field methods for rare-earth based quantum information processing," 2016.

[188] Y. Sun, G. Wang, R. Cone, R. Equall, and M. Leask, "Symmetry considerations regarding light propagation and light polarization for coherent interactions with ions in crystals," *Physical Review B*, vol. 62, no. 23, p. 15 443, 2000.

[189] J. Steinfeld, *Laser and coherence spectroscopy*. Springer Science & Business Media, 2013, pp. 226–238.

[190] E. L. Hahn, "Spin echoes," *Physical review*, vol. 80, no. 4, p. 580, 1950.

[191] N. Kurnit, I. Abella, and S. Hartmann, "Observation of a photon echo," *Physical Review Letters*, vol. 13, no. 19, p. 567, 1964.

[192] I. Abella, N. Kurnit, and S. Hartmann, "Photon echoes," *Physical review*, vol. 141, no. 1, p. 391, 1966.

[193] T. Bottger, "Laser frequency stabilization to spectral hole burning frequency references in erbium-doped crystals: Material and device optimization," Ph.D. dissertation, Montana State University-Bozeman, College of Letters & Science, 2002.

[194] I. Kurkin and K. Chernov, "EPR and spin-lattice relaxation of rare-earth activated centres in Y_2SiO_5 single crystals," *Physica B+ C*, vol. 101, no. 2, pp. 233–238, 1980.

[195] O. Guillot-Noël, P. Goldner, Y. Le Du, E. Baldit, P. Monnier, and K. Bencheikh, "Hyperfine interaction of Er^{3+} ions in Y_2SiO_5: An electron paramagnetic resonance spectroscopy study," *Physical Review B*, vol. 74, no. 21, p. 214 409, 2006.

[196] T. Bottger, Y. Sun, C. Thiel, and R. Cone, "Spectroscopy and dynamics of Er^{3+}:Y_2SiO_5 at 1.5 μ m," *PHYSICAL REVIEW B*, vol. 74, no. 7, 2006.

[197] J. A. Weil and J. R. Bolton, "Zeeman energy (g) anisotropy," in *Electron Paramagnetic Resonance*. John Wiley Sons, Ltd, 2006, ch. 4, pp. 85–117, ISBN: 9780470084984. DOI: https://doi.org/10.1002/9780470084984.ch4. [Online]. Available: https://onlinelibrary.wiley.com/doi/abs/10.1002/9780470084984.ch4.

[198] T. Böttger, C. Thiel, Y. Sun, and R. Cone, "Optical decoherence and spectral diffusion at 1.5 μ m in Er^{3+}:Y_2SiO_5 versus magnetic field, temperature, and Er^{3+} concentration," *Physical Review B*, vol. 73, no. 7, p. 075 101, 2006.

[199] S. Probst, H. Rotzinger, A. Ustinov, and P. Bushev, "Microwave multimode memory with an erbium spin ensemble," *Physical Review B*, vol. 92, no. 1, p. 014 421, 2015.

[200] O. Guillot-Noël, H. Vezin, P. Goldner, F. Beaudoux, J. Vincent, J. Lejay, and I. Lorgeré, "Direct observation of rare-earth-host interactions in Er:Y_2SiO_5," *Physical Review B*, vol. 76, no. 18, p. 180 408, 2007.

[201] R. Macfarlane and R. Shelby, "Sub-kilohertz optical linewidths of the $^7F_0 \longleftrightarrow {}^4D_0$ transition in Y_2O_3: Eu^{3+}," *Optics Communications*, vol. 39, no. 3, pp. 169–171, 1981.

[202] R. Macfarlane, R. Wannemacher, D. Boye, Y. Wang, and R. Meltzer, "Nonexponential photon echo decay of Er^{3+} in fluorides," *Journal of luminescence*, vol. 48, pp. 313–317, 1991.

[203] R. W. Equall, Y. Sun, R. Cone, and R. Macfarlane, "Ultraslow optical dephasing in Eu^{3+}:Y_2SiO_5," *Physical review letters*, vol. 72, no. 14, p. 2179, 1994.

APPENDIX

Lifetime data

Lifetime components and their respective amplitudes extracted from a three part exponential decay fit are shown below. The dotted lines represent the 7 point window smoothed average data, and are meant as a guide to the reader's eye. The error bars are indicative of the fitting error, not necessarily the total systematic error.

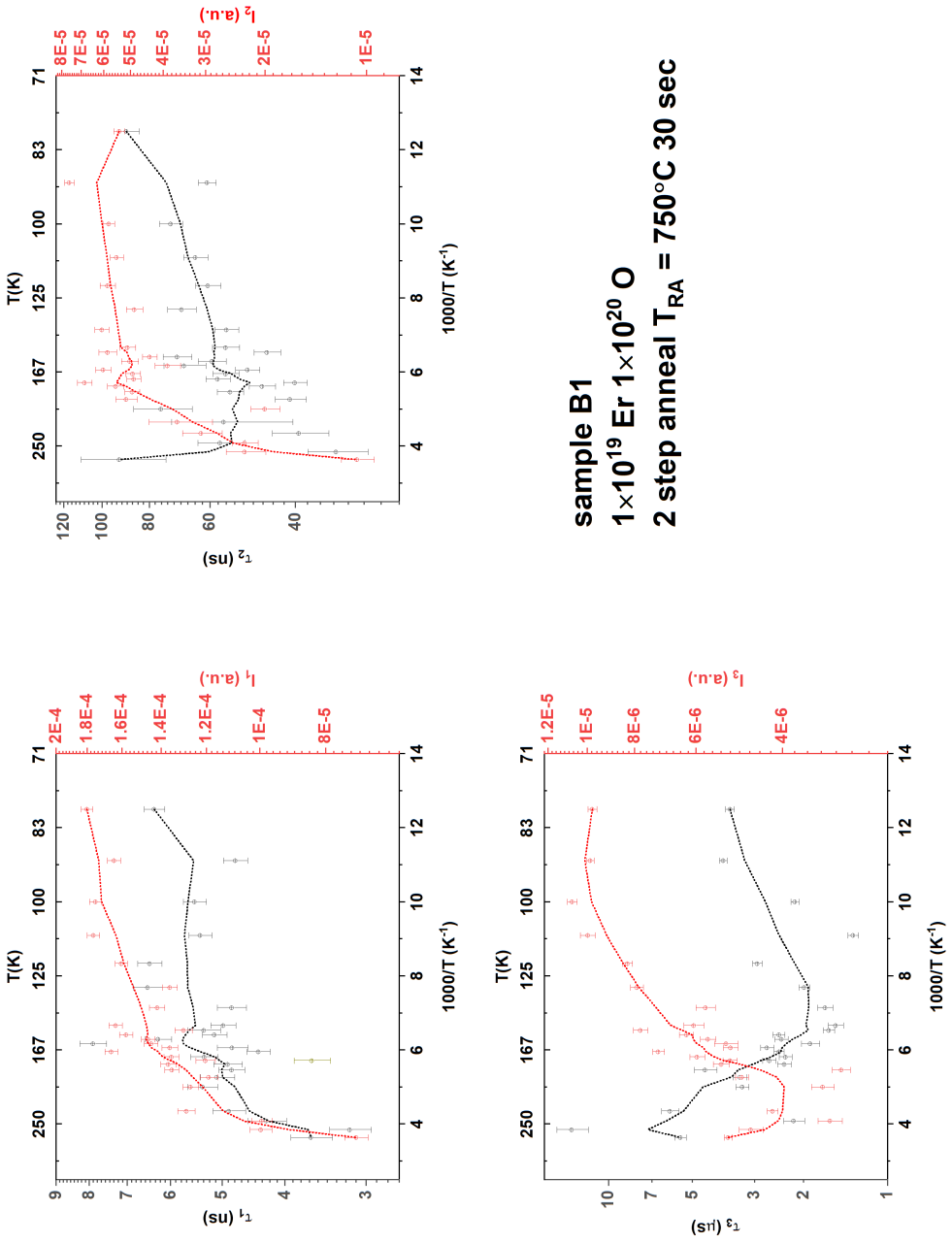

Figure 8.1: Extracted three-part exponential decay fit lifetime and amplitude components for sample B1

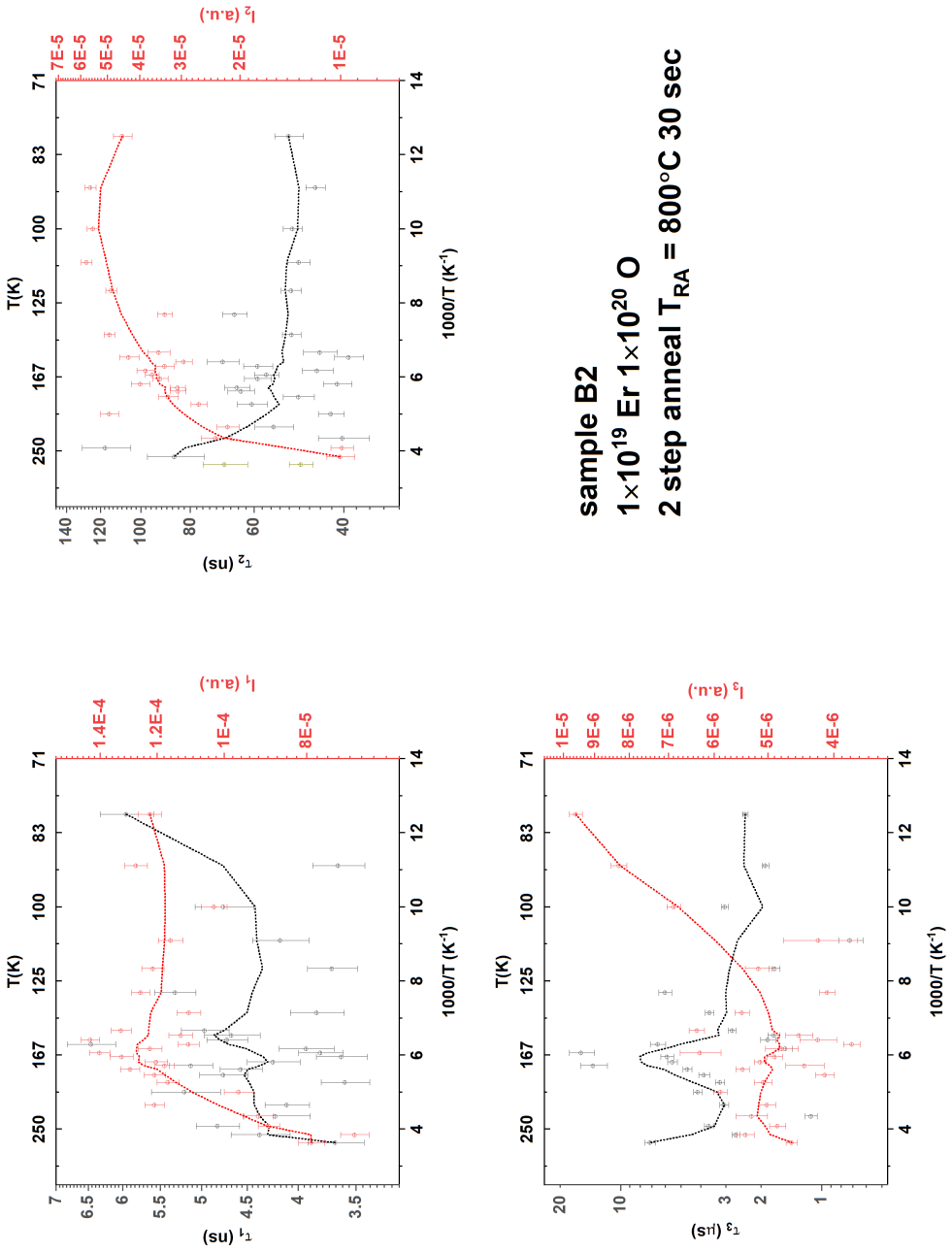

Figure 8.2: Extracted three-part exponential decay fit lifetime and amplitude components for sample B2

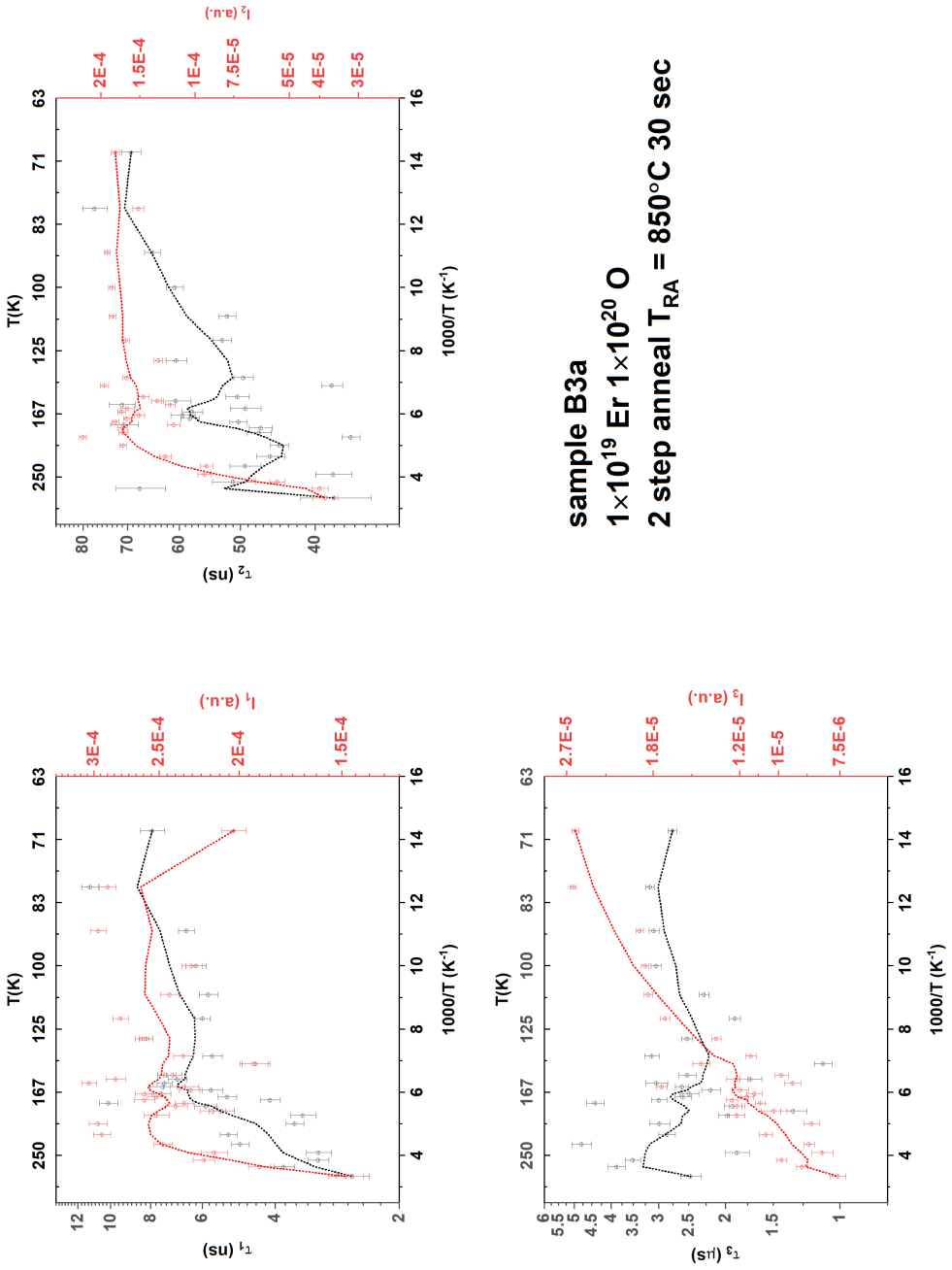

Figure 8.3: Extracted three-part exponential decay fit lifetime and amplitude components for sample B3a

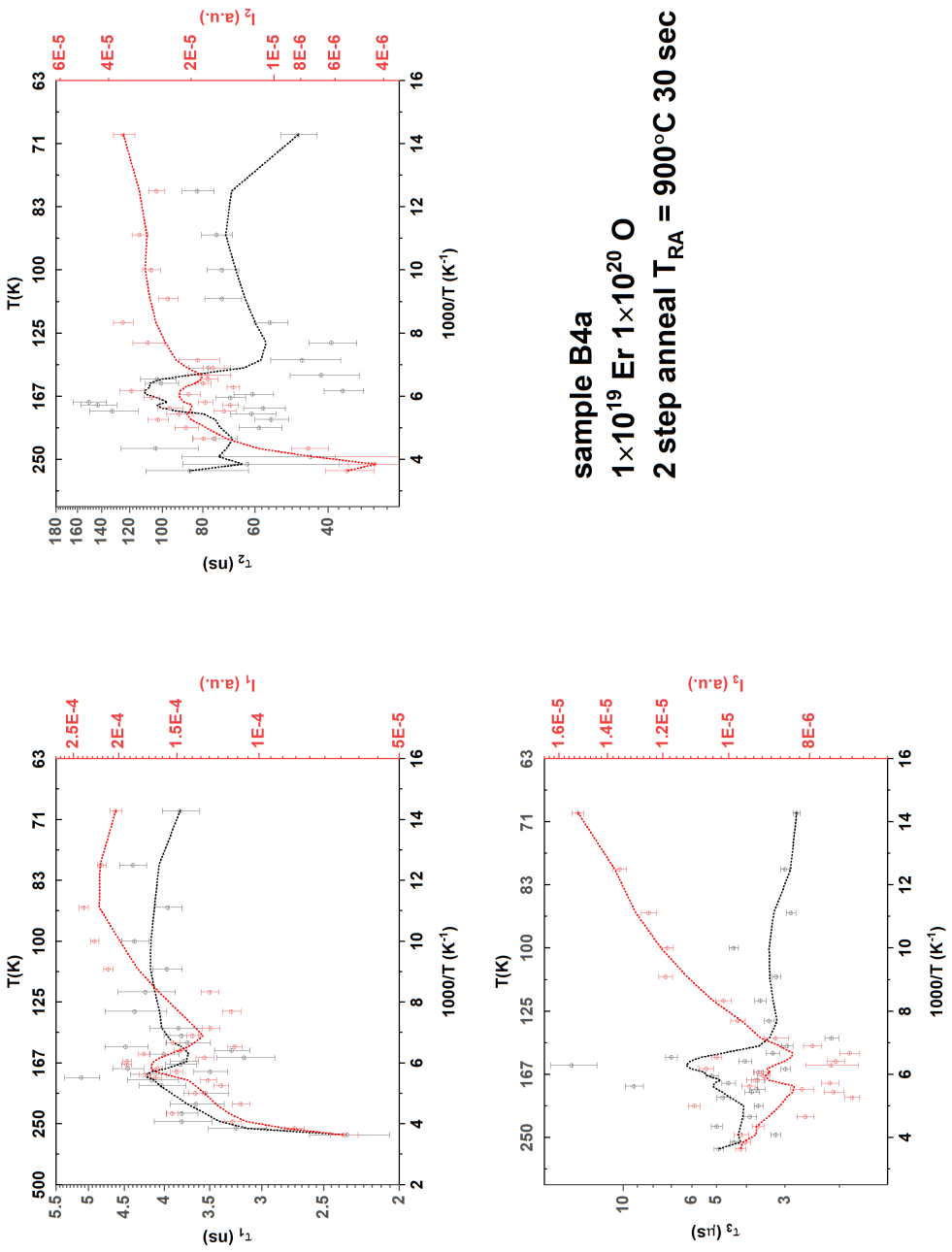

Figure 8.4: Extracted three-part exponential decay fit lifetime and amplitude components for sample B4a

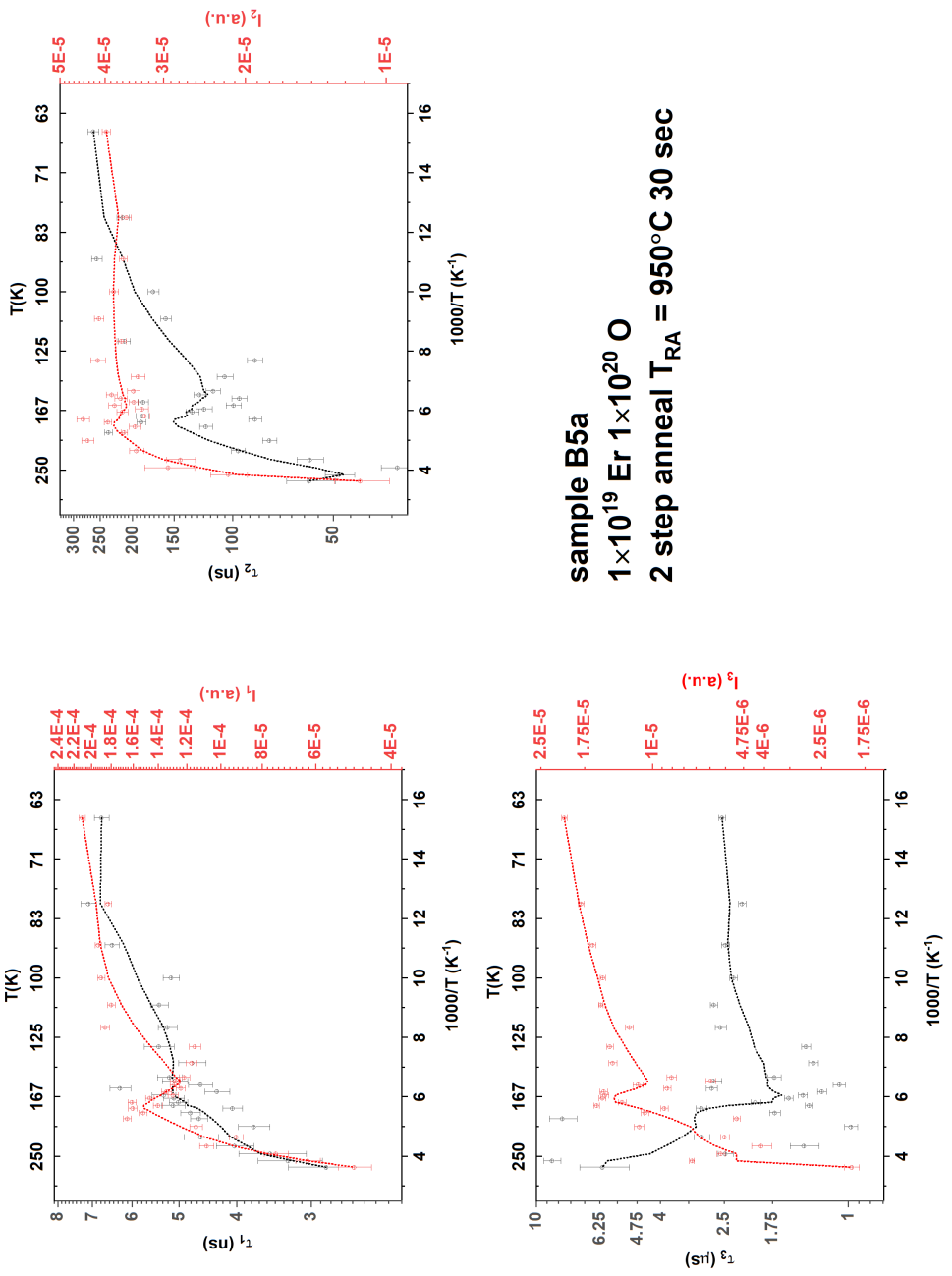

Figure 8.5: Extracted three-part exponential decay fit lifetime and amplitude components for sample B5a

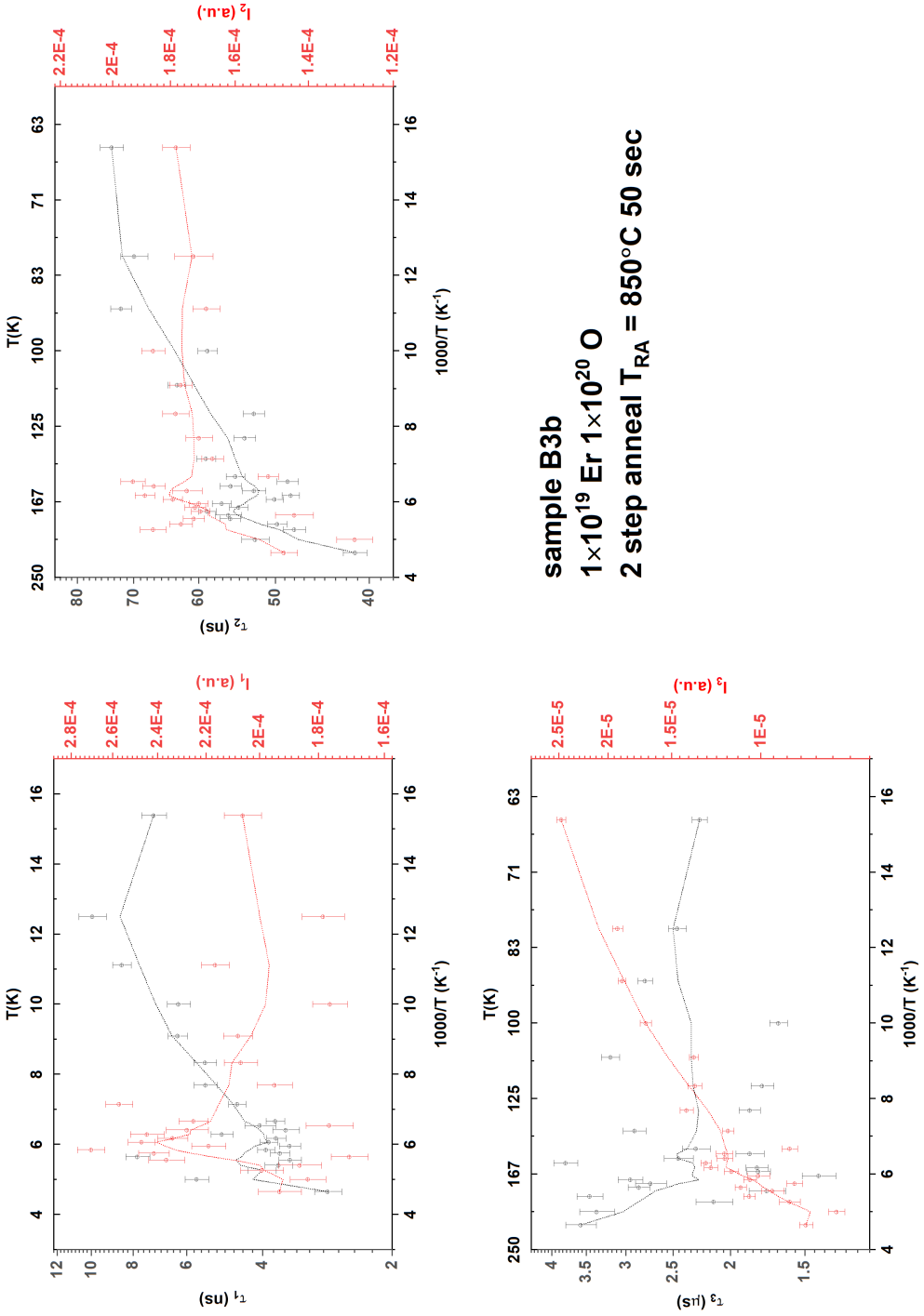

Figure 8.6: Extracted three-part exponential decay fit lifetime and amplitude components for sample B3b

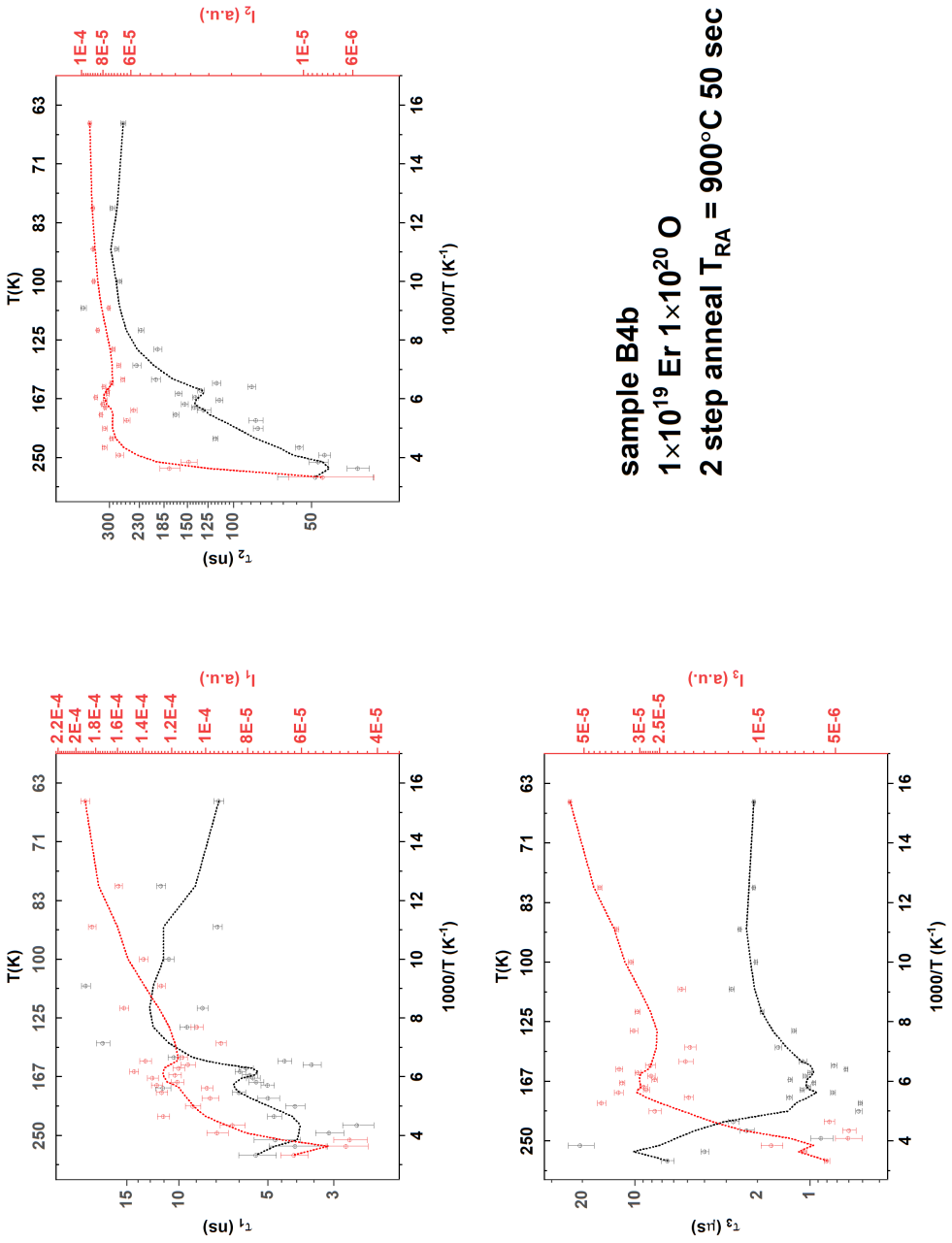

Figure 8.7: Extracted three-part exponential decay fit lifetime and amplitude components for sample B4b

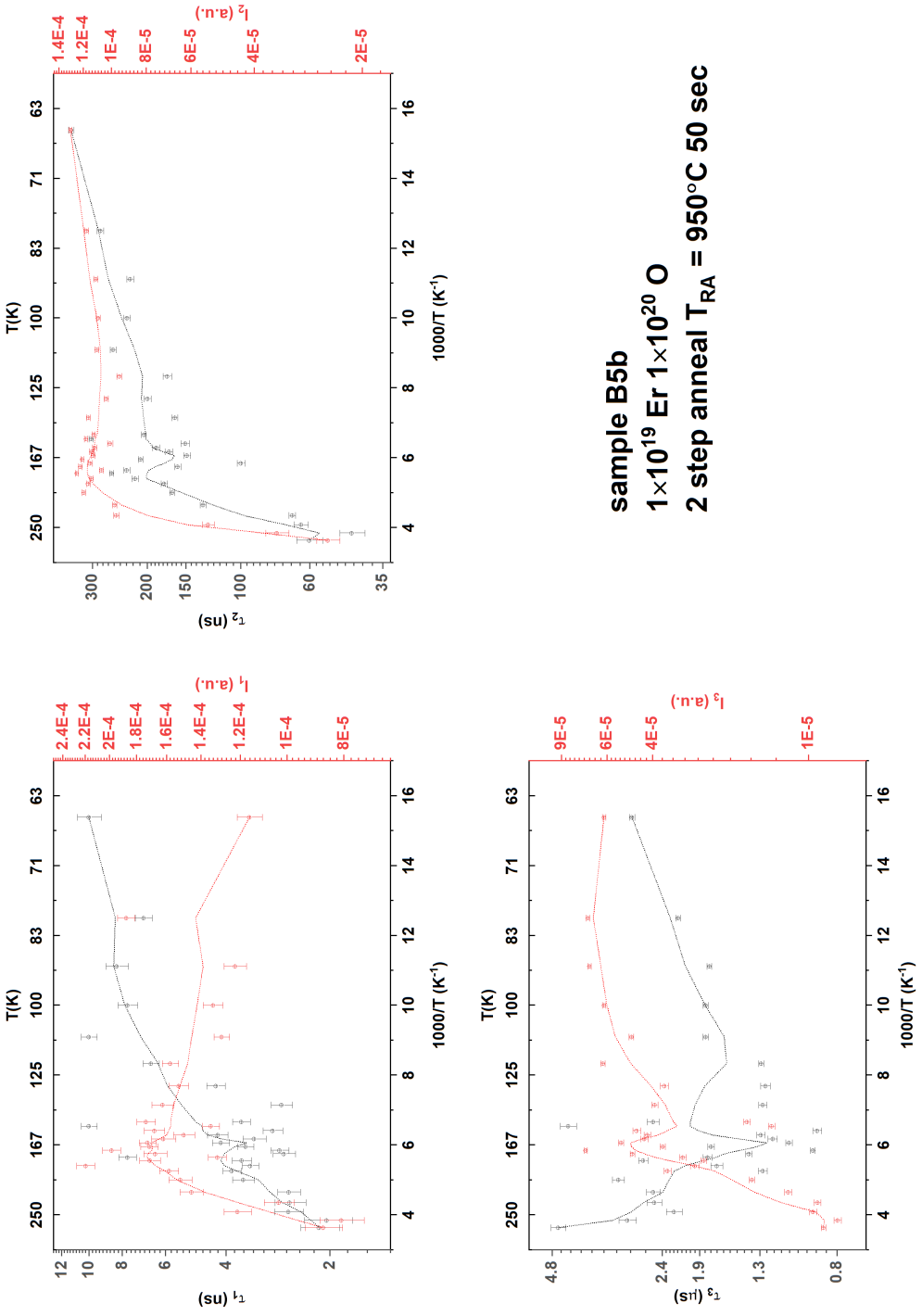

Figure 8.8: Extracted three-part exponential decay fit lifetime and amplitude components for sample B5b

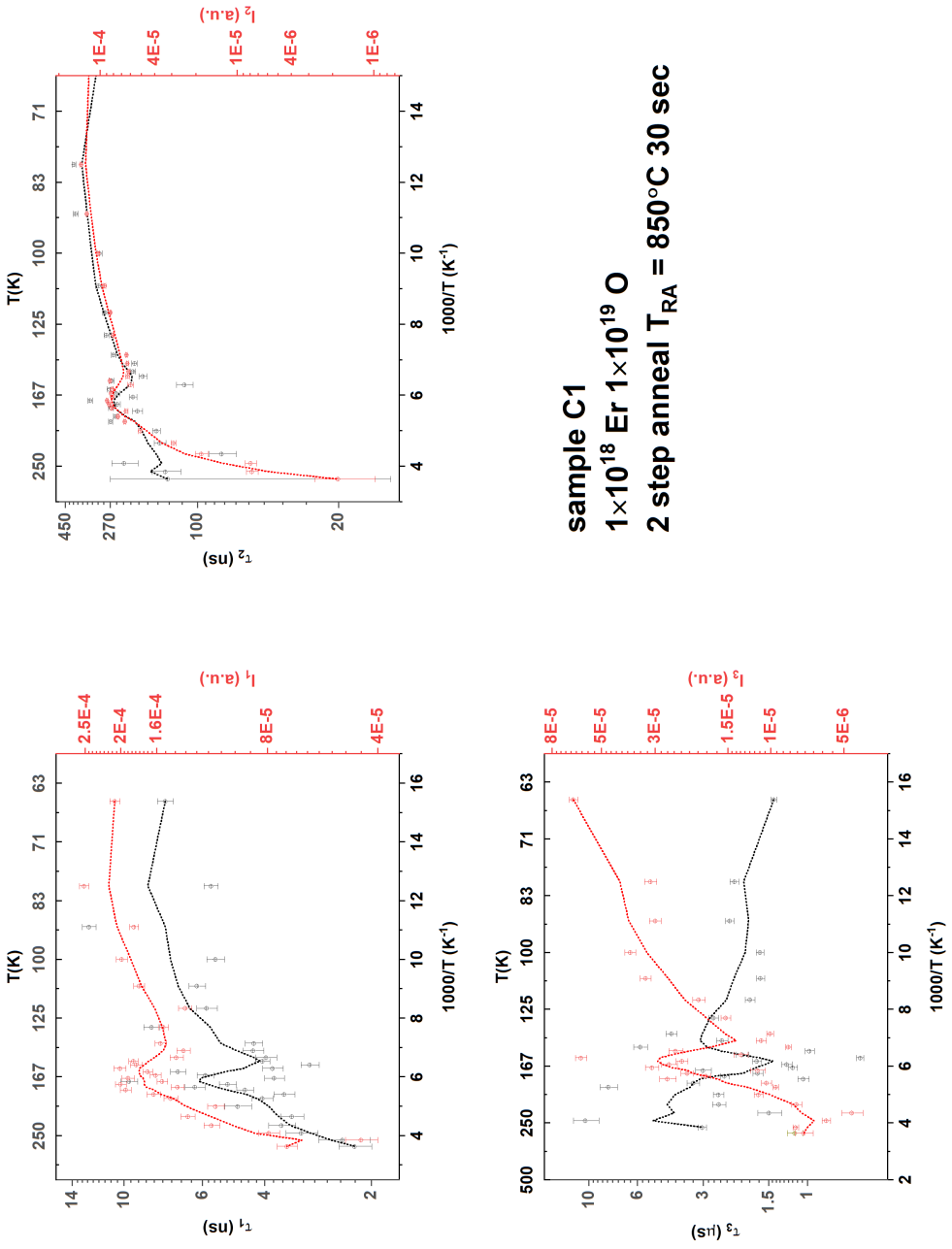

Figure 8.9: Extracted three-part exponential decay fit lifetime and amplitude components for sample C1

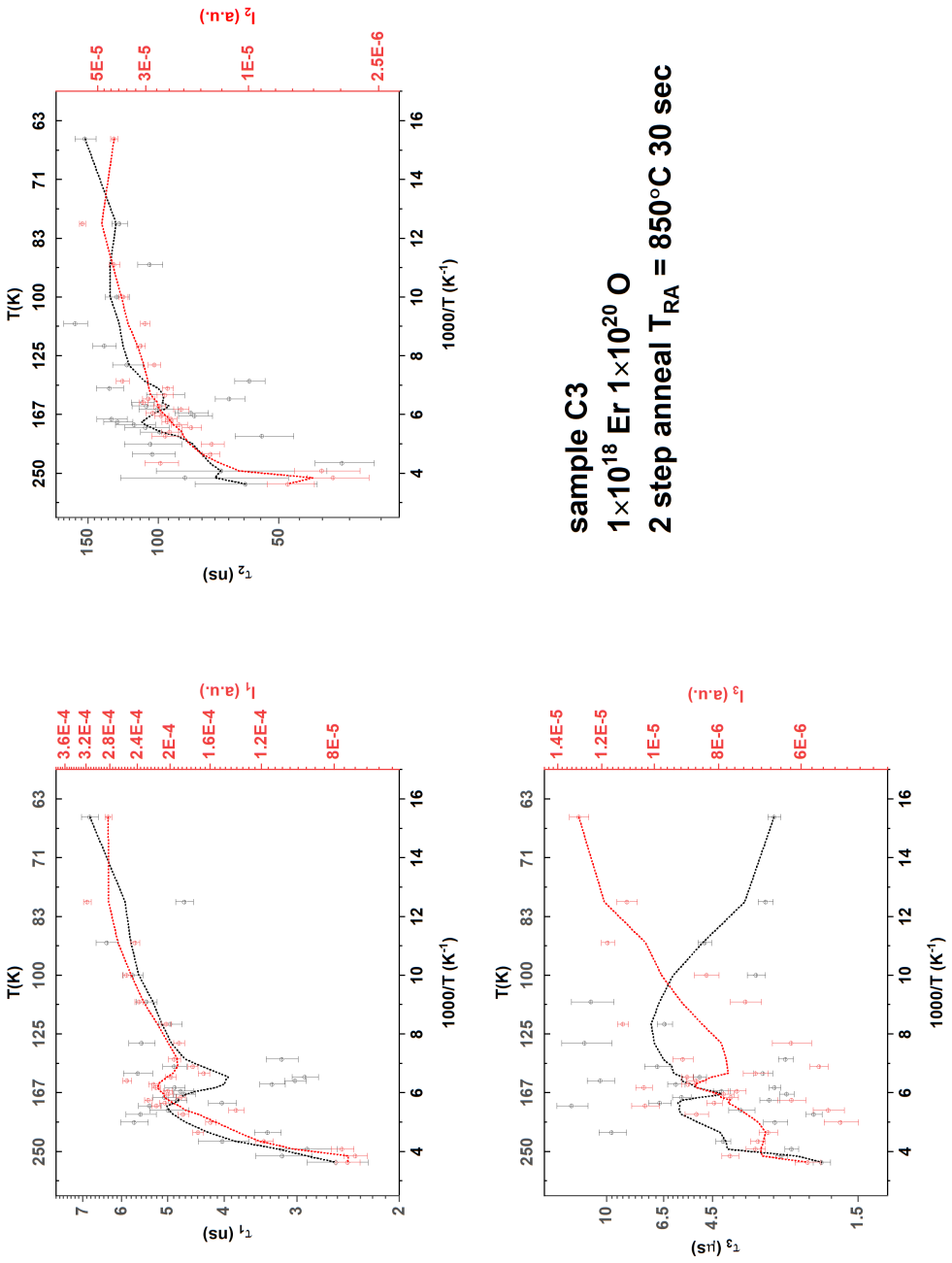

Figure 8.10: Extracted three-part exponential decay fit lifetime and amplitude components for sample C3

	Processing parameters		τ_1 (sec)	error τ_1 (sec)	τ_2 (sec)	error τ_2 (sec)	τ_3 (sec)	error τ_3 (sec)
three part	no RA		5.42E-09	3.23E-10	7.18E-08	3.98E-09	2.15E-06	8.40E-08
exponential		750	6.36E-09	2.32E-10	1.05E-07	3.93E-09	3.67E-06	1.37E-07
decay lifetime		800	**5.95E-09**	**3.70E-10**	**5.13E-08**	**3.29E-09**	**2.40E-06**	**8.09E-08**
output (in seconds)		850	**1.12E-08**	5.07E-10	**7.72E-08**	2.81E-09	**3.16E-06**	7.88E-08
		900	**4.39E-09**	**1.75E-10**	**8.24E-08**	**7.17E-09**	**3.00E-06**	**9.08E-08**
		950	7.10E-09	2.13E-10	2.14E-07	9.09E-09	2.19E-06	6.05E-08
			τ_1 (sec)	τ_2 (sec)	τ_3 (sec)			
continuous								
lifetime	no RA		**4.32E-09**	3.57E-08	1.03E-07	1.38E-06	6.92E-08	
distribution		750	5.51E-09	6.84E-08	4.68E-06			
output (in seconds)		8.00E+02	5.51E-09	**4.56E-08**	**2.44E-06**			
		8.50E+02	5.98E-09	1.46E-08	**8.05E-08**	**3.12E-06**	**1.03E-08**	
		9.00E+02	**4.32E-09**	**8.73E-08**	**2.88E-06**			
		9.50E+02	5.51E-09	2.96E-07	1.77E-06			
			amplitude component 1 (a1)	error a1	a2	error a2	a3	error a3
three part		750	1.73E-04	5.39E-06	6.02E-05	2.77E-06	1.37E-05	3.71E-07
exponential		800	1.80E-04	3.58E-06	5.01E-05	1.49E-06	9.76E-06	1.99E-07
decay amplitude		850	**1.22E-04**	**3.80E-06**	**4.51E-05**	**2.91E-06**	**9.59E-06**	**2.08E-07**
output		900	2.88E-04	6.72E-06	1.52E-04	6.10E-06	2.62E-05	3.85E-07
(in Volts)		950	**2.17E-04**	**4.78E-06**	**2.68E-05**	**1.80E-06**	**1.35E-05**	**2.49E-07**
			1.83E-04	3.27E-06	3.60E-05	8.33E-07	1.80E-05	4.45E-07

Figure 8.11: Comparison between the extracted lifetime components from the three part exponential fit and the centre of lifetime distribution from the continuous lifetime distribution model.